Frustrated Magnetism, Monopole Dynamics, and Non-Coplanar Ordering in Classical Spin Systems

Insights from Monte Carlo Simulations

Carl Martin Gembé

Dissertation

Frustrated Magnetism, Monopole Dynamics, and Non-Coplanar Ordering in Classical Spin Systems
Insights from Monte Carlo Simulations

Inaugural-Dissertation

zur

Erlangung des Doktorgrades

der Mathematisch-Naturwissenschaftlichen Fakultät

der Universität zu Köln

vorgelegt von

Carl Martin Gembé

aus Bonn

Köln 2023

Abstract

For decades, physicists have been fascinated by frustrated magnetism. Frustration arises when the pairwise interaction energies between localized magnetic moments in a system cannot be minimized simultaneously. This competition prevents the formation of long range magnetic order even at lowest temperatures and, eventually, leads to the hallmark of frustration in the form of a massive ground state degeneracy accompanied by a finite zero-point entropy. Thus, exotic magnetic analogs of ordinary fluids can be realized, where spins are highly correlated but remain strongly fluctuating. Such spin liquids are linked to remarkable unconventional collective phenomena, most notably emergent gauge fields and fractionalized quasi-particle excitations that can be conceived as magnetic monopoles. In this thesis, we study the dynamics of such quasi-monopoles in the presence of a magnetic field and address the question whether critical fluctuations at a phase transition always slow down equilibration or, conversely, can also help the system to thermalize. Employing large-scale dynamical Monte Carlo simulations, we show that the latter—a *critical speeding up*—can indeed be observed in two prototypical classical spin systems: dipolar spin ice in pyrochlore magnets and a Coulomb spin liquid in the triangular lattice Ising antiferromagnet. For the former, we also establish a relationship between Monte Carlo time and real time by comparing numerical and experimental data. Another part of this thesis is concerned with systems in which further-neighbor interactions stabilize certain non-coplanar magnetic orders. Such orders are particularly interesting because upon introducing quantum fluctuations, they may possibly melt into a chiral quantum spin liquid. To this end, we study two model systems that turn out to have non-coplanar classical ground states and are motivated by the recent synthesis of a number of Mott insulating square-kagome materials as well as of spin-1/2 maple-leaf lattice antiferromagnets. We explore the rich phenomenology of frustrated magnetism induced by these two lattice geometries, including extensive degeneracies and order-by-disorder mechanisms. For both models, we study an elementary, classical Heisenberg model with nearest-neighbor and additional cross-plaquette interactions and discuss a multitude of non-coplanar orders and spiral spin phases. Using extensive numerical simulations, we also discuss the thermodynamic signatures of these phases, which often show multi-step thermal ordering.

Kurzzusammenfassung

Seit Jahrzehnten übt frustrierter Magnetismus auf Physiker*innen eine ungebrochene Faszination aus. Frustration tritt auf, wenn die paarweisen Wechselwirkungsenergien zwischen lokalisierten magnetischen Momenten in einem System nicht gleichzeitig minimiert werden können. Diese Konkurrenz verhindert die Bildung einer langreichweitigen magnetischen Ordnung selbst bei tiefsten Temperaturen. Daraus resultiert schließlich das Hauptmerkmal von Frustration in Form einer massiven Grundzustandsentartung, die von einer endlichen Nullpunktsentropie begleitet wird. Auf diese Weise lassen sich exotische magnetische Gegenstücke zu gewöhnlichen Flüssigkeiten realisieren, in denen Spins zwar beträchtlich korreliert sind, aber dennoch stark fluktuieren. Diese Spinflüssigkeiten sind mit bemerkenswerten unkonventionellen kollektiven Phänomenen verbunden, insbesondere mit emergenten Eichfeldern und fraktionalisierten Quasiteilchenanregungen, die als magnetische Monopole aufgefasst werden können. In dieser Arbeit untersuchen wir die Dynamik solcher Quasi-Monopole in Anwesenheit eines Magnetfeldes und gehen der Frage nach, ob kritische Fluktuationen an einem Phasenübergang die Gleichgewichtsbildung immer verlangsamen oder umgekehrt auch zur Thermalisierung des Systems beitragen können. Mit Hilfe von groß angelegten dynamischen Monte-Carlo-Simulationen zeigen wir, dass das Letztere—ein *critical speeding up*—in zwei prototypischen klassischen Spinsystemen tatsächlich beobachtet werden kann: Dipolares Spin-Eis in Pyrochlor-Magneten und eine Coulomb-Spinflüssigkeit im Ising-Antiferromagneten auf dem Dreiecksgitter. Für das erstgenannte System stellen wir auch eine Beziehung zwischen der Monte-Carlo-Zeit und der realen Zeit her, indem wir numerische und experimentelle Daten vergleichen. Ein weiterer Teil dieser Arbeit befasst sich mit Systemen, in denen Wechselwirkungen zwischen weiter entfernten Spins bestimmte nicht-koplanare magnetische Ordnungen stabilisieren. Solche Ordnungen sind besonders interessant, weil sie durch das Einführen von Quantenfluktuationen möglicherweise zu einer chiralen Quantenspinflüssigkeit schmelzen können. Zu diesem Zweck untersuchen wir zwei Modellsysteme, die nichtkoplanare klassische Grundzustände aufweisen. Diese sind motiviert durch die jüngste Synthese einer Reihe von Mott-isolierenden Quadrat-Kagome-Materialien und von Spin-1/2-Ahornblatt-Gitter-Antiferromagneten. Wir erforschen die umfangreiche Phänomenologie des frustrierten Magnetismus, der durch diese beiden Gittergeometrien hervorgerufen wird, einschließlich extensiver Entartungen und Ordnung-durch-Unordnung-Mechanismen. Für beide Modelle untersuchen wir ein elementares, klassisches Heisenberg-Modell mit Wechselwirkungen zwischen nächsten Nachbarn sowie zusätzlichen plakettenübergreifenden Wechselwirkungen. Dabei behandeln wir eine Vielzahl von nicht-koplanaren Ordnungen und spiralförmigen Spinphasen. Anhand umfangreicher numerischer Simulationen erörtern wir zudem die thermodynamischen Eigenschaften dieser Phasen, die oft eine mehrstufige thermische Ordnung aufweisen.

Contents

'Frustration is the name of the game'—few could have imagined what an extraordinarily fascinating field of research was born when Nobel laureate P.W. Anderson wrote this on a blackboard in Aspen in 1976 [1]. Although not yet called *frustrated magnetism*, seminal studies of magnetic systems, in which competing interactions render it impossible to find a unique ground state, date back to as early as 1950[1]. At that time Wannier and Houtappel investigated the prototypical antiferromagnetic Ising model on the triangular lattice; they found that the system possesses an extensive residual ground state degeneracy and does not develop any long range order in a symmetry-breaking phase transition [4–6]. In another pioneering work, Anderson studied the problem of antiferromagnetically coupled Ising spins on what is now commonly known as the pyrochlore lattice [7]. Intriguingly, he linked it to the peculiar physics of proton ordering in common water ice, which leads to exactly the same macroscopic number of ground states and was explained by Pauling in 1935 [8, 9]. Since those early days, an exciting research area has evolved, giving rise to a plethora of novel concepts and sophisticated numerical and analytical tools that are now ubiquitous and indispensable in condensed matter physics.

Probably one of the most salient of these concepts is that of a *classical spin liquid* [10, 11]. This exotic phase of matter is a magnetic analog of an ordinary liquid: while in a magnetically ordered system the spins are in a fixed arrangement with static order (similar to the constituents of a conventional solid), in a spin liquid the constituent spins are highly correlated but remain strongly fluctuating even at lowest temperatures. This negative definition by the absence of magnetic order goes far beyond the prevailing Landau paradigm [12, 13], which distinguishes symmetry-broken from symmetry-preserving phases by a local order parameter. Instead, spin liquids often display unconventional *topological order*, which is characterized by the emergence of a gauge field, and exhibit non-local *fractionalized* quasi-particle excitations [14]. These concepts also carry over to the quantum counterparts of classical spin liquids, so-called *quantum spin liquids* [15–17]. The importance of such quantum phases of matter cannot be stressed enough, with possible practical applications all the way up to topological quantum computing [18, 19]. But classical spin liquids are no less valuable, as their study contributes to understanding the finite-temperature physics of real frustrated magnetic materials, and they often turn out to be parent states for quantum spin liquids [20, 21].

A poster child for the notions of fractionalization and topological order is a class of materials called *spin ice*, a system in which the spins can be thought of as classical vectors and which—like Anderson's pyrochlore Ising antiferromagnet—is frustrated in the same way as ordinary water

---

[1]In fact, the notion of *frustration* was introduced in the context of spin glasses [2, 3] where magnetic atoms are distributed randomly, but it is now inextricably linked to the study of localized magnetic moments on regular lattices where competing interactions cannot be satisfied simultaneously.

ice [22, 23]. A miraculous interplay of lattice geometry, crystal field effect, and dipolar interactions in spin ice ensures that its extensive ground state manifold is subject to a divergence-free constraint, giving rise to a gauge field governed by a Maxwell action. Elementary excitations in this incarnation of a Coulomb phase [24, 25] can be considered as emergent deconfined magnetic monopoles which, just like Dirac monopoles [26], carry magnetic charges and experience Coulomb interactions [27]. Notably, unlike Dirac's elusive original monopoles, the emergent monopoles in spin ice are actually experimentally observable [28–31], and their dynamics is a particularly important topic of ongoing research [32–35].

However, in some frustrated magnets, the massive ground state degeneracy can be partially or completely lifted. This occurs, for example, through the phenomenon of *order by disorder* [36], where soft modes in the fluctuation spectrum select a subset of ground states. This mechanism has long been established, e.g., in the classical Heisenberg antiferromagnet on the kagome lattice, where coplanar ground states are favored by thermal fluctuations [37, 38]. In other cases, competing interactions can even stabilize conventional types of order with broken spin symmetry. In particular, for non-Bravais lattices with further-neighbor interactions, this can lead to the formation of complex *non-coplanar* magnetic orders, for example with tetrahedral or cuboctahedral symmetry [39, 40]. Due to their finite spin chirality, such non-coplanar magnetic orders are of fundamental interest. Not only can they induce a spontaneous topological Hall effect [41–44], but they can also possibly melt into much sought-after chiral quantum spin liquid states when quantum fluctuations are introduced [45, 46]. In this way, non-coplanar magnetic orders provide an excellent starting point for the search for such spin liquid states.

The scope of this thesis is, on the one hand, the numerical study of the dynamics of magnetic monopoles in dipolar spin ice, where we put to the test the paradigm that critical fluctuations always lead to a *critical slowing down* of the dynamics [47]. On the other hand, we explore the formation of complex non-coplanar magnetic ground states of classical Heisenberg antiferromagnets on non-Bravais lattices with cross-plaquette interactions. In order to handle the exponentially large configuration space of the models at hand, the numerical means of choice are classical Monte Carlo simulations, which are provided with a dynamical flavor for the study of monopole relaxation rates.

To this end, the structure of this thesis is as follows. In **Part I**, we introduce the theoretical background relevant to this thesis. To do this, we begin in **Chapter 2** with a general introduction to frustrated magnetism, where we present the paradigmatic Heisenberg model and describe in detail the mechanisms that lead to the characteristic ground state degeneracy of frustrated magnets. We also discuss the phenomenon of order by disorder, by which this degeneracy can be partially lifted by fluctuations. Finally, we review the concept of a Coulomb phase and show how it gives rise to magnetic monopoles as elementary excitations. **Chapter 3** then sets the methodological stage of this thesis, where we start with the concept of Markov chains and their generation using the Metropolis algorithm and a parallel tempering scheme. We then outline the analysis of Monte Carlo data and its statistical errors as well as the influence of autocorrelations and the canonical phenomenon of critical slowing down. We also describe the dynamical Monte Carlo method, which allows us to measure non-equilibrium quantities such as the dynamical susceptibility.

In the following **Part II**, we discuss our numerical analyses of the dynamics of emergent magnetic monopoles in spin ice and spin liquids. **Chapter 4** begins with a detailed introduction to the

physics of spin ice. Subsequently, we show numerical results for the dynamical simulation of the dipolar spin ice model. The monopole relaxation times thus obtained are then compared with experimental results and a theory for the conversion between Monte Carlo time and real time is presented and tested for validity. In **Chapter 5**, we take a look at the prototype of a classical spin liquid, the triangular Ising antiferromagnet, and analyze its dynamics in comparison to a simple ferromagnet.

Part III of this thesis is devoted to the study of intricate, non-coplanar magnetic ground states of classical Heisenberg antiferromagnets on different lattice geometries. This is motivated in **Chapter 6**, which also introduces the Luttinger-Tisza method as well as various relevant non-coplanar orders such as spin spirals and so-called regular magnetic orders. Afterwards, in **Chapter 7**, we explore the classical Heisenberg model on the square-kagome lattice in great detail by means of large-scale Monte Carlo simulations complemented by a semi-analytical method. In addition to the classical spin liquid arising for the nearest-neighbor model, we discuss a large variety of coplanar and non-coplanar ground states for the extended model with cross-plaquette interactions. In **Chapter 8**, we use the same methods to briefly review the ground state phase diagram of a classical Heisenberg model on the maple-leaf lattice, which again provides a wealth of non-trivial ground states.

Finally, the thesis comes to an end with some general concluding remarks in **Chapter 9**. These summarize our results and give an outlook for possible future research.

Part I

Theoretical Foundation

Frustrated Magnetism

Frustration describes a situation where not all contributions to the energy of a physical system can be minimized simultaneously [2, 3]. The origin of the complex and exotic behavior of frustrated magnets can be illustrated remarkably simply by considering antiferromagnetically coupled Ising spins which can only point in two possible directions ($S_i^z = \pm 1$) and sit at the vertices of a triangle. While such spins can easily be antialigned with their neighbors on a square (as favored by the antiferromagnetic nature of their interaction), this is not possible on a triangle because of the odd number of connections (see Fig. 2.1(a) and (b)). By virtue of the conflict between the geometry of the lattice that the spins inhabit, and the preferred orientation of the spins due to their mutual interactions, the system is said to exhibit *geometric frustration*. The simplest basic building block of frustrated magnetic systems thus consists of spins arranged on triangular plaquettes. It is, therefore, not surprising that the prototypical example of such a system is the Ising antiferromagnet on the simple triangular lattice introduced by Wannier in 1950 [4, 5]. Another possible source of frustration is the presence of competing interactions that lead to so-called *exchange frustration*. This appears, e.g., in the celebrated and fundamental Kitaev model [48] on the honeycomb lattice (see Fig. 2.1(c)). There, the nearest-neighbor spin degrees of freedom interact via a strongly anisotropic Ising-like exchange so that the coupling of neighboring spins is highly dependent on the spatial direction of the bond, rendering a simultaneous minimization of all interactions impossible. As a consequence, frustration suppresses the build-up of conventional long range magnetic order and gives rise to exotic magnetic analogs of liquids and ice, where the spins are strongly fluctuating but highly correlated, and which exhibit a large residual zero-temperature entropy due to a degenerate
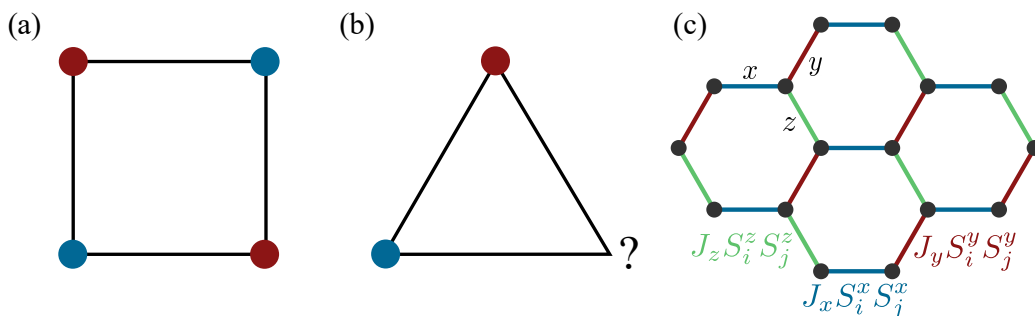
Figure 2.1 – **Sources of frustration.** (a) Unfrustrated Ising antiferromagnet on a square, where all four spins are antialigned with their neighbors (red and blue dots indicate spins pointing upwards and downwards, respectively). (b) On a triangle, this is not possible—three neighboring spins cannot be pairwise antialigned, and therefore, the system is frustrated due to the lattice geometry. (c) In the Kitaev model on the hexagonal lattice, exchange frustration arises since spins are coupled depending on the spatial direction of the bond. The x-components of neighboring spins are coupled along x-bonds (blue) via $J_x S_i^x S_j^x$, and the y-components and z-components are coupled analogously.

ground state manifold rather than a single stable ground state configuration. This chapter serves as an introduction to the rich phenomenology of such frustrated magnetic systems and provides the theoretical basis for this thesis. More detailed introductions can be found in the vast literature [49, 50].

2.1 Fingerprint of Frustration

Since frustration tends to suppress conventional magnetic order, strongly frustrated magnetic compounds have a characteristic fingerprint visible in the magnetic susceptibility χ, which at high temperatures in the conventional paramagnetic regime follows the Curie-Weiss law

$$\chi^{-1} \propto T - \Theta_{\mathrm{CW}}\,, \tag{2.1}$$

where Θ_{CW} is the Curie-Weiss temperature that characterizes the sign and strength of interactions. For antiferromagnets, Θ_{CW} is negative, and for unfrustrated systems, magnetic order appears below the Néel temperature $T_N \sim |\Theta_{\mathrm{CW}}|$, signaled by a cusp in χ. In the presence of frustration, on the other hand, the paramagnetic linear regime of χ^{-1} extends smoothly to temperatures $T_c \ll \Theta_{\mathrm{CW}}$, where some non-generic and compound-dependent freezing or frustration-relieving transition occurs (as schematically depicted in Fig. 2.2). The intermediate regime $T_c \lesssim T \lesssim \Theta_{\mathrm{CW}}$ is commonly termed *cooperative paramagnet* or *classical spin liquid* [51, 52]. Hence, a simple and widely used empirical measure of the degree of frustration is the frustration parameter [53, 54]

$$f = \frac{|\Theta_{\mathrm{CW}}|}{T_c}\,. \tag{2.2}$$

An ideal spin liquid with no ordering down to zero temperature would have $f \to \infty$. In real materials, however, degeneracy-breaking perturbative interactions ultimately lead to the development of long range order out of the spin liquid state at some critical temperature T_c. Materials with $f > 5$–10 are commonly called highly frustrated [10, 55].
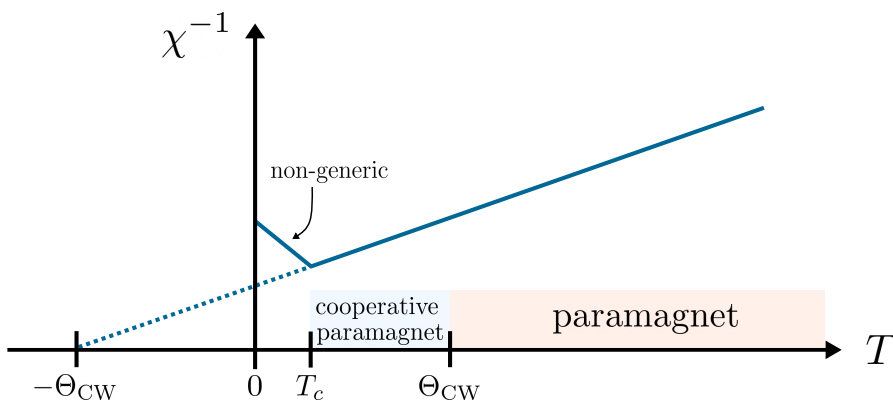
Figure 2.2 – **Fingerprint of frustration.** The inverse magnetic susceptibility follows the Curie-Weiss law at high temperatures in the paramagnetic regime, $\chi^{-1} \propto T - \Theta_{\mathrm{CW}}$. The Curie-Weiss temperature Θ_{CW} sets the scale for magnetic ordering in an unfrustrated material. In the presence of frustration, conventional ordering is suppressed and the linear behavior of χ^{-1} is extended to temperatures $T_c \ll \Theta_{\mathrm{CW}}$ in a cooperative paramagnetic, or classical spin liquid regime, where spins are highly correlated but strongly fluctuating. The width of this intermediate regime $T_c \lesssim T \lesssim \Theta_{\mathrm{CW}}$—typically expressed as the frustration parameter $f = |\Theta_{\mathrm{CW}}|/T_c$—is a widely used empirical measure of the degree of frustration in a material.

2.2 Paradigmatic Models

Theoretical models to describe classical localized moments in magnets typically start with the general Heisenberg Hamiltonian [56–58]

$$\mathcal{H} = \sum_{i,j} J_{ij} \mathbf{S}_i \cdot \mathbf{S}_j \,, \tag{2.3}$$

where $\mathbf{S}_i$ denotes a classical n-component spin vector of unit length and J_{ij} is the coupling strength between $\mathbf{S}_i$ and $\mathbf{S}_j$ that arises from their exchange interaction. This interaction is often (but not necessarily) restricted to nearest-neighbor pairs of spins with a single exchange constant J. For $n = 1$, 2, or 3 components of $\mathbf{S}_i$, one obtains the Ising, XY, and Heisenberg model, respectively.

With this starting point, models can be made increasingly complex to account for different physical contributions by adding more terms to the Hamiltonian. These could be, e.g., external magnetic fields, crystal field anisotropies that favor some specific easy axis [59], Dzyaloshinski-Moriya interactions that favor spin canting of otherwise parallel or antiparallel aligned spins [60–62], dipole-dipole interactions [63, 64], or bond-dependent anisotropies induced by spin-orbit coupling, where J_{ij} becomes a 3×3 exchange tensor with Kitaev, Γ, and Γ' terms [48, 65–68], just to name a few.

For $J_{ij} \equiv J < 0$, the basic Heisenberg Hamiltonian, Eq. (2.3), leads to ferromagnetic order, while a positive J can lead to antiferromagnetic Néel order provided the lattice structure allows it, i.e., if the lattice is bipartite. Then, the spins on each sublattice can be ordered ferromagnetically such that spins on one sublattice are antialigned with the spins on the other sublattice. For non-bipartite lattices, an antiferromagnetic J can lead to frustration, as already shown for three spins on a triangle. For this reason, particularly interesting models for the study of frustrated magnetism are those in which the spins are located on the vertices of lattices composed of elementary triangles. Besides the triangular lattice, important examples are the kagome lattice in two dimensions and the pyrochlore lattice in three dimensions (cf. Fig. 2.3).

(a)

(b)
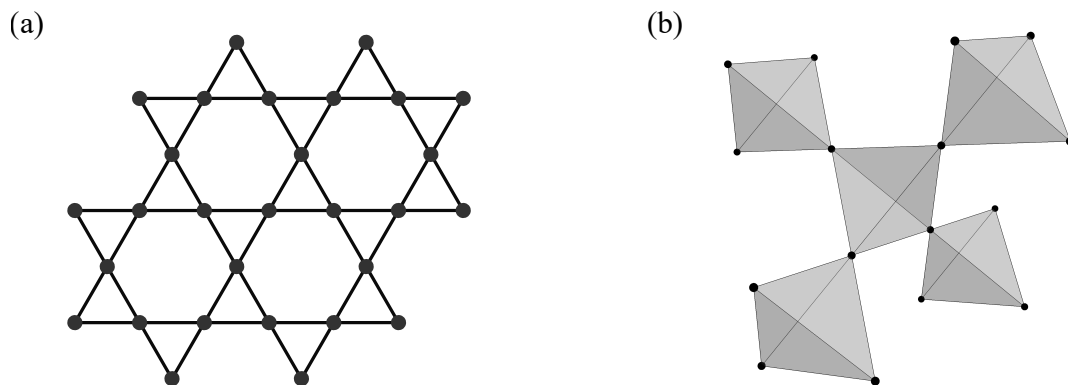
Figure 2.3 – **Lattices composed of elementary triangles.** (a) The two-dimensional kagome lattice consists of corner-sharing equilateral triangles. (b) A generalization of the kagome lattice to three dimensions is the pyrochlore lattice. It consists of corner-sharing regular tetrahedra.

2.3 Classical Ground State Degeneracy

Having shown that lattices of elementary triangular plaquettes can lead to frustration, we now want to understand the degeneracy of the ground state to quantify the degree of frustration with some accuracy. For a general arrangement of classical Heisenberg spins $\mathbf{S}_i$ on corner-sharing units of q sites (that is, $q = 3$ for the kagome lattice and $q = 4$ for the pyrochlore lattice), where each spin is coupled to its $q-1$ neighbors in each unit, the general Heisenberg Hamiltonian, Eq. (2.3), with $J_{ij} \equiv J$ can be rewritten as a sum over the N units forming the system as

$$\mathcal{H} = J \sum_{\langle i,j \rangle} \mathbf{S}_i \cdot \mathbf{S}_j = \frac{J}{2} \sum_{\alpha} |\mathbf{L}_\alpha|^2 + c \,, \tag{2.4}$$

where $\mathbf{L}_\alpha = \sum_{i \in \alpha} \mathbf{S}_i$ is the total spin in unit α and the constant $c = -JNq/2$ must be subtracted in order to account for the diagonal terms $\mathbf{S}_i^2$ in the expansion of $|\mathbf{L}_\alpha|^2$. For antiferromagnetic coupling $J > 0$, the energy is minimized for states in which $\mathbf{L}_\alpha = 0$ for all units α.

For a single unit with $q = 4$ spin vectors, we thus have $\mathcal{H} = J|\mathbf{L}|^2/2 + c$ and $\mathbf{L} = \mathbf{S}_1 + \mathbf{S}_2 + \mathbf{S}_3 + \mathbf{S}_4$. Such an arrangement with four spins that sum to zero is shown in Fig. 2.4(a). In addition to global rotations due to the O(3) symmetry of $\mathcal{H}$, the ground state of the system has two additional degrees of freedom—the angles θ and ϕ.

To understand how this accidental ground state degeneracy extends from a single unit to larger lattices, a counting argument introduced by James Clerk Maxwell in 1864 in the context of elastic systems [51, 69] can be used. The argument compares the number of degrees of freedom F in the system with the number of ground state constraints K that must be satisfied in order to determine the degrees of freedom in the ground state as

$$D_M = F - K \,. \tag{2.5}$$

A system of N_S classical Heisenberg spins has $F = 2N_S$, as each (unit length) spin is specified by two angles. Furthermore, a system consisting of N_C clusters has $K = 3N_C$, since $\mathbf{L}_\alpha$ must vanish for each cluster ($L_x = L_y = L_z = 0$). For the single cluster of four spins in Fig. 2.4(a) ($N_S = 4, N_C = 1$), this gives exactly the two extra angular degrees of freedom as $D_M = F - K = 2N_S - 3N_C = 8 - 3 = 5$, that is three global rotations plus the unconstrained two angles θ and ϕ.

We will stay with the example of $q = 4$, as in the pyrochlore lattice, as follows. There, four spins form one tetrahedron but each spin is part of two tetrahedra, such that $N_S = 2N_C$. This gives, for a pyrochlore lattice consisting of N_C tetrahedra, a number of degrees of freedom in the ground state of $D_M = 2N_S - 3N_C = N_C$, i.e. an *extensive* ground state degeneracy that grows proportional to the number of tetrahedra. In general, for lattices of corner-sharing units with q spins with n components, one obtains [51, 70]

$$D_M = N_C[n(q-2) - q]/2 \,. \tag{2.6}$$

The Maxwell counting relies on the assumption that all constraints are linearly independent. Therefore one may underestimate the true number of ground state degrees of freedom $D \geq D_M$ when this is not the case. An important example is the Heisenberg antiferromagnet on the kagome lattice, where the above estimate yields $D_M = 0$ (on each triangular unit the spins are

arranged such that they form mutual angles of 120°), but an extensive ground state degeneracy $D \propto N_C$ nonetheless arises, as an explicit ground state construction [71] shows, as illustrated in Fig. 2.4(b).

Ground state degeneracy due to geometrical frustration takes a different form for systems with Ising spins that take only discrete values. Unlike in the case of continuous spins, the number of ground states W is countable and can be used to define a residual entropy $S_0 = \ln W$ (with k_B being set to 1). A textbook example to illustrate this is the ground state degeneracy of the Ising antiferromagnet on the pyrochlore lattice. For a system of N_S Ising spins, there are 2^{N_S} different configurations in total. From the $2^4 = 16$ different configurations on a single tetrahedron, only $\binom{4}{2} = 6$ are ground states with $\mathbf{L}_\alpha = 0$, namely those, where two spins point up and two spins point down. A lattice consisting of N_S spins and hence $N_C = N_S/2$ tetrahedra has therefore $W = 2^{N_S}(6/16)^{N_S/2}$ possible ground states, leading to a residual ground state entropy per spin of

$$\frac{S_0}{N_S} = \frac{1}{2}\ln\frac{3}{2} \approx 0.203\,. \tag{2.7}$$

This estimate was already used by Pauling in 1935 in the description of water ice and the low-temperature ordering of protons therein [8, 9, 72]—the physics of proton ordering in water ice turns out to be locally equivalent to the physics of a frustrated pyrochlore antiferromagnet, as first noted by Anderson in 1956 [7].

A simple way to observe this residual entropy in experiments and simulations is to measure the specific heat c_V of the system as it is cooled down to temperatures at which only the ground states are accessible, and then to calculate the entropy ΔS released in this process. This in turn can be subtracted from the high temperature entropy of free spins that each can freely fluctuate between its two possible states, that is $S_f/N_S = \ln 2$. The entropy release between the high temperature T_f and the low temperature T_0 can easily be calculated directly by integrating

(a)

(b)
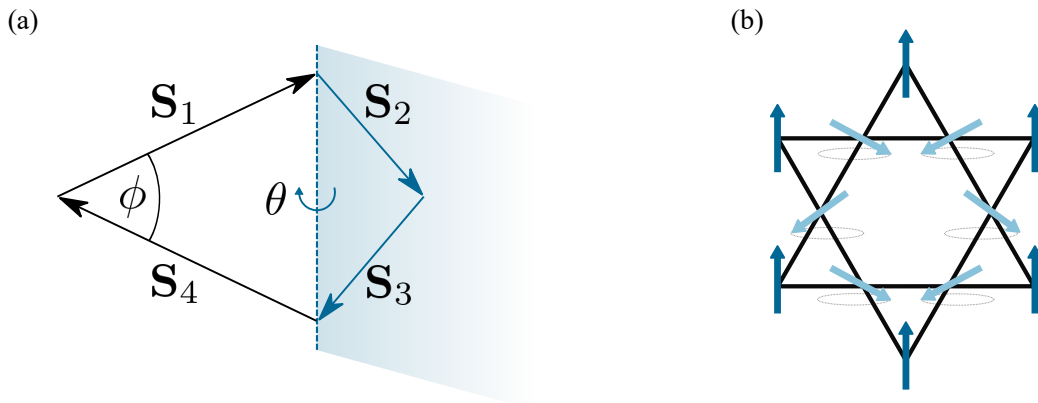
Figure 2.4 – **Ground state degeneracy.** (a) Four antiferromagnetically coupled classical Heisenberg spins that fulfill $\mathbf{L} = \sum_i \mathbf{S}_i = 0$. This constraint is fulfilled for arbitrary angles of ϕ between $\mathbf{S}_1$ and $\mathbf{S}_4$ and θ between the planes containing $\mathbf{S}_{1,4}$ and $\mathbf{S}_{2,3}$—the ground state has hence two extra degrees of freedom in addition to the three that arise from global rotations. (b) The ground state of the Heisenberg antiferromagnet on the kagome lattice is degenerate even though a single triangular unit has no intrinsic degrees of freedom—$\mathbf{L} = 0$ is only fulfilled when all three spins form mutual angles of 120°. Here, the (light blue) spins on the hexagon may be rotated all together about the axis defined by the (dark blue) outer spins, without leaving the ground state manifold.

c_V/T, thus the residual entropy is given by

$$\frac{S_0}{N_S} = \ln 2 - \Delta S = \ln 2 - \int_{T_0}^{T_f} \frac{c_V(T)}{T} \, \mathrm{d}T. \qquad (2.8)$$

Ground state degeneracy in frustrated systems is a striking result. It means that there are local degrees of freedom that can fluctuate independently without the system leaving its ground state manifold, preventing the formation of long range magnetic order.

2.4 Order by Disorder

Although massive ground state degeneracies are a key feature of frustrated magnets, they may be partially lifted by fluctuations, as they are not symmetry-protected but accidental in a technical sense. Therefore, the fluctuation spectrum about different degenerate ground states is expected to be different in some cases, and it is possible that states are selected because they minimize the free energy

$$\mathcal{F} = E - TS \qquad (2.9)$$

if they have the lowest excitation energy and hence have access to the largest part of the configuration space through thermal fluctuations and consequently have the highest entropy (cf. Fig. 2.5).

Villain et al. [36] introduced the concept of *order by disorder* (ObD), which describes exactly such an apparently paradoxical mechanism of degeneracy lifting, where fluctuations enhance order instead of suppressing it. In their model of a specific frustrated Ising model on a square lattice, at $T = 0$, the ground state has zero net magnetization and is disordered, but becomes ferromagnetically ordered at low temperatures when thermal fluctuations are introduced. It was also shown that a site dilution with random non-magnetic impurities leads to the same ordering pattern, hence the name order by disorder.

Whether a system explores its whole ground state manifold or not depends on its *soft modes* (i.e. quartic modes) in the harmonic spectrum. Specifically, ObD occurs when harmonic contributions to the partition function lead to a non-integrable divergence in the vicinity of the subset of configurations favored by fluctuations [70, 73]. To assess, whether this is the case, it is sufficient

(a)   (b)
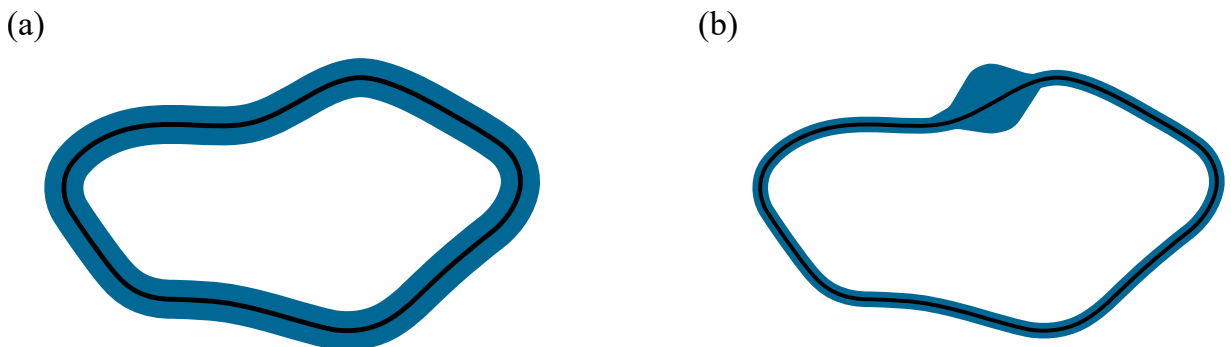
Figure 2.5 – **Order by disorder.** (a) A degenerate ground state manifold (black line) together with all thermally accessible states (blue region), where each ground state has the same number of accessible thermal excitations. (b) In contrast to (a), a subset of the ground state manifold can access more thermally excited states. The associated higher entropy minimizes the free energy and selects this subset of ground states over the rest of the ground state manifold.

to consider the criterion

$$D - S - M \leq 0 \,, \tag{2.10}$$

where D is the dimension of the ground state manifold, M is the number of soft modes, and S is the dimension of the submanifold where these soft modes occur. The dimension D of the ground state manifold can again be determined using the Maxwell counting argument introduced before as the difference of the total number of degrees of freedom in the system F and the number K of constraints that must be imposed to restrict the system to its ground state, that is $D_M = F - K$. Again, the Maxwell counting only provides a lower bound, $D \geq D_M$, as it assumes all constraints to be independent, but it serves a useful tool to estimate in advance the possibility of OdB.

Striking numerical evidence for the presence of ObD (in simulations of models with continuous degrees of freedom) can be found in the low-temperature limit of the specific heat c_V, since soft modes contribute to the specific heat with $k_B/4$, whereas harmonic modes contribute with $k_B/2$ according to the equipartition theorem. Therefore, in the presence of ObD, the low-temperature specific heat is diminished. This is the case, for example, in the kagome Heisenberg antiferromagnet with $c_V(T \to 0) = 11/12$ ($k_B = 1$), in perfect agreement with predictions by a mode counting analysis [74, 75]. In contrast, one finds $c_V(T \to 0) = 1$ for an unfrustrated Heisenberg model, where each spin is free to fluctuate about its ordered ground state in two orthogonal directions on the unit sphere and these two quadratic modes each contribute $1/2$ to the specific heat. The same low-temperature value of the specific heat of $c_V(T \to 0) = 11/12$ is found in the isotropic square-kagome Heisenberg antiferromagnet, that we discuss in detail in Part III of this thesis. An example curve of c_V for such a system that shows OdB is depicted in Fig. 2.6.
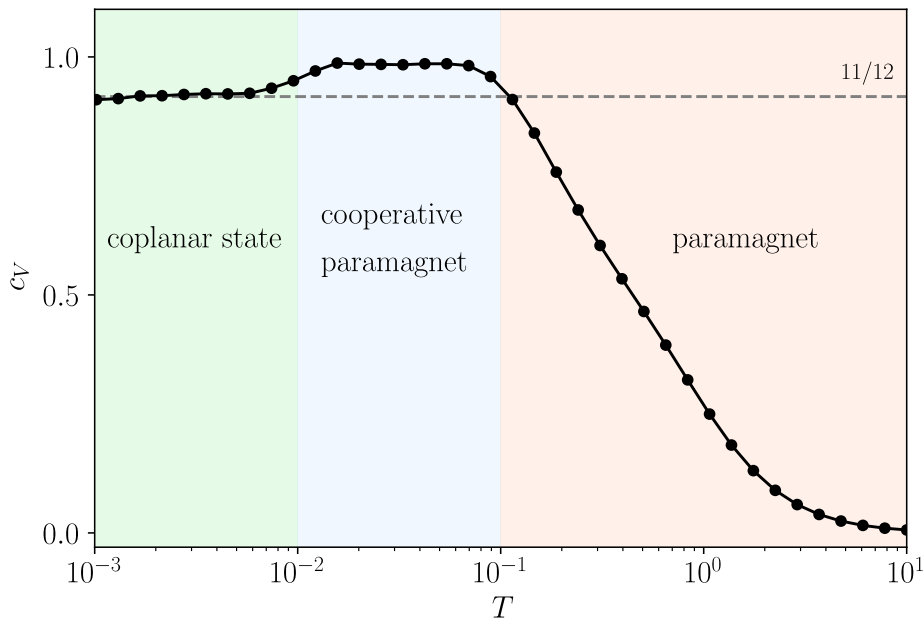
Figure 2.6 – **Signature of oder by disorder in the specific heat.** In the specific heat of the isotropic ($J = 1$) square-kagome Heisenberg antiferromagnet, one can clearly distinguish three different regimes. At high temperatures $T \geq 10^{-1}$, the system is in a paramagnetic state with only weak correlations. The intermediate regime $10^{-2} \leq T \leq 10^{-1}$ corresponds to the commonly known cooperative paramagnet or spin liquid state with a plateau $c_V \approx 1$, where the system fluctuates between the whole extensive number of possible ground states. Only at temperatures $T \leq 10^{-2}$, a globally coplanar subset of ground states is selected via an entropy-driven OdB mechanism due to the presence of one zero mode per triangle (and thus two zero modes per six-site unit cell) resulting in $c_V \to [10 \cdot (1/2) + 2 \cdot (1/4)]/6 = 11/12$ as $T \to 0$.

2.5 Ground State Correlations

In addition to the massive ground state degeneracy, the ground state condition of the squared Heisenberg Hamiltonian in Eq. (2.3) has another direct consequence. It turns out that despite the existence of local degrees of freedom, which can fluctuate independently, there are *long range* spin correlations.

This can again be easily shown using the condition that all elementary units forming a lattice have a vanishing total spin, that is $\mathbf{L}_\alpha = 0$ for all α. If we now look at the top layer z_1 of a lattice, as exemplified in Fig. 2.7 for the Heisenberg antiferromagnet on the kagome lattice, it has some finite magnetization of $\mathbf{m}(z_1) = \sum_{i \in z_1} \mathbf{S}_i = \mathbf{M}$. This magnetization is then perfectly correlated with the magnetization of the next layer z_2 since both layers together form a sheet of complete elementary units, that is, of units that fulfill $\mathbf{L}_\alpha = 0$. Consequently, the magnetization of the layer z_2 must be equal to $-\mathbf{M}$. The same argument can now be continued layer by layer, so that ultimately

$$\mathbf{m}(z_{i+n}) = (-1)^n \cdot \mathbf{m}(z_i) \tag{2.11}$$

for any n, which is indeed an indication of long range correlations. This simple argument already shows the existence of these correlations. In the following, we want to switch to the Coulomb phase theory in order to quantify these correlations for a class of models as well.
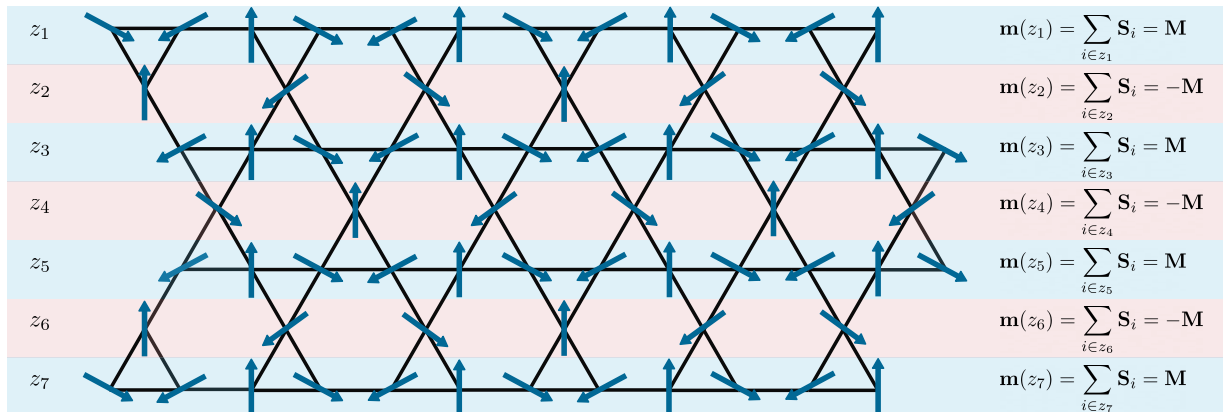
Figure 2.7 – **Long range correlations.** An immediate consequence of the ground state condition $\mathbf{L}_\alpha = 0$ for all units α (cf. Eq. (2.4)) is the build-up of long range correlations, as visualized here for a Heisenberg antiferromagnet on the kagome lattice. Let z_1 be the top layer of sites in the lattice. This layer then has some magnetization $\mathbf{m}(z_1) = \sum_{i \in z_1} \mathbf{S}_i = \mathbf{M}$. Consequently, the magnetization of the layer z_2 must be equal to $-\mathbf{M}$, since both layers together form a sheet of complete triangles, that is, of units that fulfill $\mathbf{L}_\alpha = 0$. In general, therefore, $\mathbf{m}(z_{i+n}) = (-1)^n \cdot \mathbf{m}(z_i)$ for any n, which is indeed a sign of long range correlations.

2.6 Coulomb Phase

In the theory of a Coulomb phase [25, 76, 77], a constrained spin configuration on some lattice $\mathcal{L}$ is mapped to a vector field $\mathbf{P}(\mathbf{r})$ on the *premedial* or *parent* lattice $\mathcal{B}$ of $\mathcal{L}$[1] such that the ground state constraint translates to the condition, that the resulting vector field has zero divergence, that is,

$$\nabla \cdot \mathbf{P}(\mathbf{r}) = 0 \,. \tag{2.12}$$

---

[1]That means that the elementary units of $\mathcal{L}$ sit on the vertices of $\mathcal{B}$ while the sites of $\mathcal{L}$ fall onto the bond midpoints of $\mathcal{B}$.

medial lattice $\mathcal{L}$ parent lattice $\mathcal{B}$
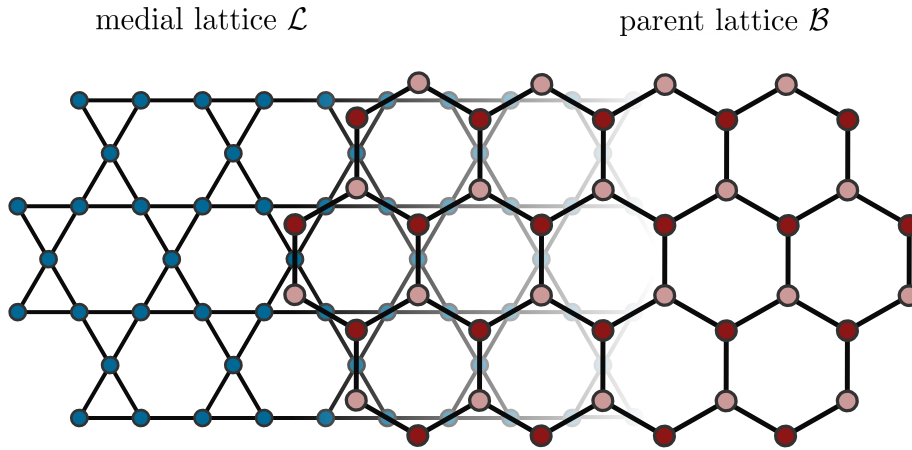
Figure 2.8 – **Parent and medial lattices.** The hexagonal lattice is the premedial or parent lattice $\mathcal{B}$ of its medial lattice $\mathcal{L}$, the kagome lattice. That is, the elementary triangular units of $\mathcal{L}$ sit on the vertices of $\mathcal{B}$ (red dots) while the sites of $\mathcal{L}$ (blue dots) fall onto the bond midpoints of $\mathcal{B}$.

The ground state constraint underlying the mapping can simply be the condition $\mathbf{L}_\alpha = 0$ of Eq. (2.3), or a more specific constraint (as for example in the case of kagome ice [78], see Fig. 2.9). For the mapping to be possible, the parent lattice must be bipartite, such as the hexagonal lattice, which is the parent lattice of the kagome lattice (cf. Fig. 2.8), or the diamond lattice, which is the parent lattice of the pyrochlore lattice. In this case, one can assign an orientation convention for the bonds from one sublattice of $\mathcal{B}$ to the other sublattice and thus translate the spin degrees of freedom on the sites of $\mathcal{L}$ into an arrangement of weighted lattice fluxes on the bonds of $\mathcal{B}$, such that the incoming and outgoing fluxes at each vertex sum to zero, as shown in Fig. 2.9 for kagome ice. The divergence-free emergent vector field $\mathbf{P}(\mathbf{r})$ is then the coarse-grained version of this arrangement of lattice fluxes that is averaged over some neighborhood larger than the lattice spacing but smaller than the system size and assumed to vary smoothly. Since each coarse-grained state of $\mathbf{P}(\mathbf{r})$ represents many different microscopic configurations, it should have an entropic weight that reflects this. Small field strengths of $\mathbf{P}(\mathbf{r})$ can be generated by a huge number of different microstates, while large field strengths are realized
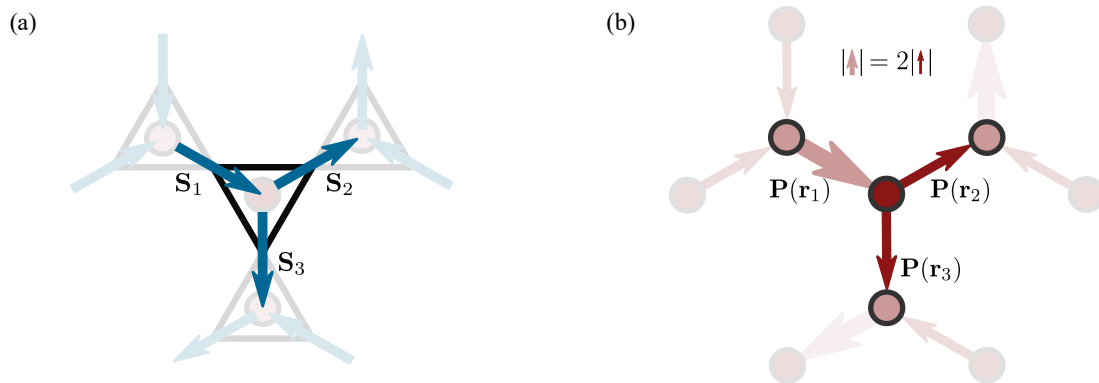
Figure 2.9 – **Coulomb phase in kagome ice**. (a) The ground state constraint of kagome ice is the rule, that on each elementary triangle of the kagome lattice $\mathcal{L}$ one spin points into the triangle and two spins point out (or vice versa) [78]. (b) Ground states of kagome ice can be mapped onto lattice flux configurations on the hexagonal parent lattice $\mathcal{B}$ by assigning fluxes starting from, say sublattice A (light red nodes), twice the weight of arrows starting from sublattice B (dark red nodes). In this way, the kagome ice rule is translated into the condition that at each node of $\mathcal{B}$ the sum of all weighted lattice fluxes is equal to zero.
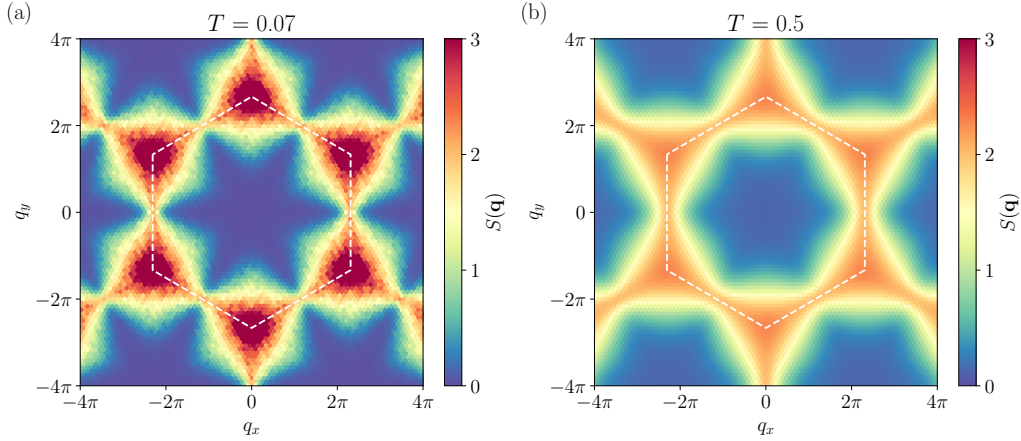
Figure 2.10 – **Pinch points in reciprocal space.** Structure factors from a Monte Carlo simulation of the Heisenberg antiferromagnet on the kagome lattice ($L = 24$) at (a) $T = 0.07$, and (b) $T = 0.5$ showing pinch point patterns on the edges of the extended Brillouin zone (dashed hexagon) that are characteristic for Coulomb phase correlations Eq. (2.16). As the temperature increases, the width of the pinch points widens.

only by very few microstates, suggesting [76, 79] a free energy as a function of $\mathbf{P}(\mathbf{r})$,

$$\frac{\mathcal{F}\left(\{\mathbf{P}(\mathbf{r})\}\right)}{T} = \frac{\kappa}{2} \int \mathrm{d}^3\mathbf{r}|\mathbf{P}(\mathbf{r})|^2 \tag{2.13}$$

with a single, dimensionless parameter, the stiffness κ. The name *Coulomb phase* comes from the similarity of this free energy and of the divergence-free constraint, Eq. (2.12), with a magnetic or electric field without monopoles. Both equations taken together indicate [77] that the probability distribution for the coarse-grained $\mathbf{P}(\mathbf{r})$ is the constrained Gaussian distribution

$$\mathrm{Prob}\left(\{\mathbf{P}(\mathbf{r})\}\right) \propto e^{-\mathcal{F}(\{\mathbf{P}(\mathbf{r})\})/T} \prod_{\mathbf{r}} \delta(\nabla \cdot \mathbf{P}(\mathbf{r})) \,. \tag{2.14}$$

By Fourier transforming the free energy, $\mathcal{F} = \frac{\kappa}{2}\sum_{\mathbf{q}}|\mathbf{P}(\mathbf{q})|^2$, and by applying equipartition, correlations can now be calculated as $S_{\mu\nu}(\mathbf{q}) = \langle P_\mu(-\mathbf{q})P_\nu(\mathbf{q})\rangle = (1/\kappa)\delta_{\mu\nu}$. However, it must also be taken into account that the divergence-free condition dictates that

$$\mathbf{q} \cdot \mathbf{P}(\mathbf{q}) = 0 \,. \tag{2.15}$$

Therefore, from the trivial result of equipartition for an unrestricted $\mathbf{P}(\mathbf{q})$, the longitudinal fluctuations must be projected out, leading to

$$S_{\mu\nu}(\mathbf{q}) = \langle P_\mu(-\mathbf{q})P_\nu(\mathbf{q})\rangle = \frac{1}{\kappa}\left(\delta_{\mu\nu} - \frac{q_\mu q_\nu}{|\mathbf{q}|^2}\right) \,. \tag{2.16}$$

These correlations give rise to sharp characteristic features in reciprocal space that resemble pinch points or bow ties [77, 79–82] and distinguish the structure factor $S_{\mu\nu}(\mathbf{q})$ of the frustrated system from the diffraction pattern of a magnetically ordered system or a paramagnet—cf. Fig. 2.10 for example structure factors from a Monte Carlo simulation of the Heisenberg antiferromagnet on the kagome lattice. When these correlations are Fourier transformed back to real space, one obtains

$$\langle P_\mu(0)P_\nu(\mathbf{r})\rangle = \frac{c_d}{\kappa r^d}\left(\delta_{\mu\nu} - d\hat{r}_\mu\hat{r}_\nu\right) \tag{2.17}$$

in d dimensions, where $\hat{\mathbf{r}} = \mathbf{r}/|\mathbf{r}|$ and c_d is a dimension-dependent constant ($c_3 = 4\pi$). Strikingly, the real space correlations are power-law decaying and in that sense critical and have the spatial dependence of a dipole-dipole interaction familiar from Maxwell magnetostatics.

2.7 Emergent Magnetic Monopoles

One of the most significant implications of a Coulomb phase comes to light when looking at possible excitations. As fundamental as the divergence-free condition, Eq. (2.12), for the ground state is, one can ask what happens when it is violated, for example by thermal fluctuations or by a magnetic field. Such a violation of the flux constraint $\nabla \cdot \mathbf{P}(\mathbf{r}) = 0$ leads to defects that can be labeled by their charge Q given by the net flux at a specific node of the parent lattice $\mathcal{B}$ [25].

The term *charge* is appropriate insofar as the Gauss law is fulfilled here, namely that the net flux through any hypothetical surrounding closed surface is equal to Q. This also has the consequence that charge is conserved—the net charge in some volume cannot be changed. In particular, such defects, or *magnetic monopoles*, are *fractionalized* and can only be created in pairs with opposite charges (one spin flip creates two defects, see sketch of monopole formation in kagome ice in Fig. 2.11).

Intriguingly, these monopoles are *deconfined* and may independently move trough the lattice further away from the origin of the monopole pair creation without any energy cost via subsequent flux inversions that restore a solenoidal flux arrangement on one node and violate the zero divergence on the next. Furthermore, the constraint $\nabla \cdot \mathbf{P}(\mathbf{r}) = 0$ immediately uncovers the existence of an emergent gauge field $\mathbf{A}(\mathbf{r})$ via $\mathbf{P}(\mathbf{r}) = \nabla \times \mathbf{A}(\mathbf{r})$, which is generally associated with *topological order* [83, 84].

The prime example of the formation of magnetic monopoles is that in spin ice [14, 27], which will be the subject of a more detailed discussion and the main topic in Part II of this thesis. However, before we go into this, we will first introduce the main method of this thesis, the Monte Carlo simulation technique, in the next chapter.
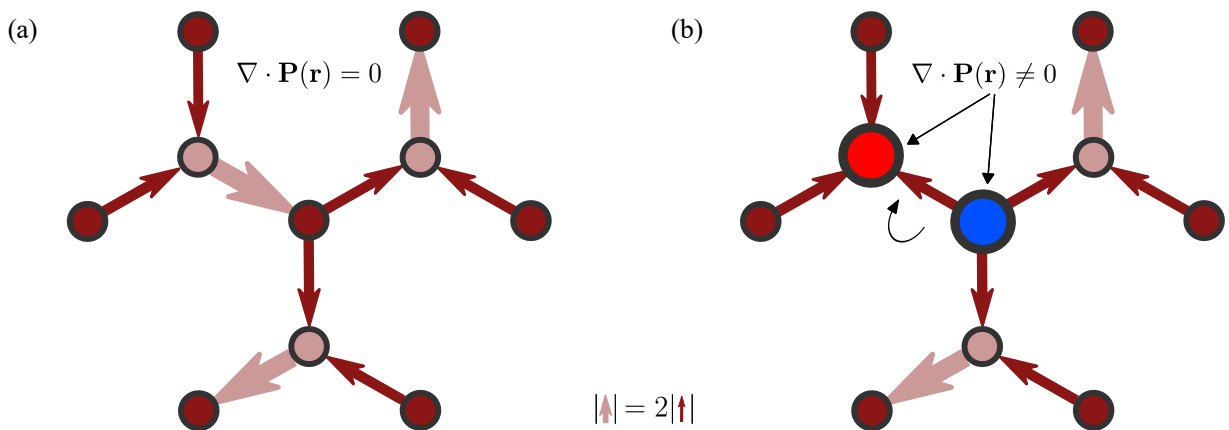
Figure 2.11 – **Formation of magnetic monopoles.** (a) A section of a lattice flux configuration on the hexagonal lattice that fulfills the zero divergence condition on every node. (b) By flipping a single spin, this condition is no longer fulfilled on two neighboring nodes. As a result, one node has a positive net flux (three incoming fluxes), that can be interpreted as a positive magnetic charge (red dot), while the other node has a negative magnetic charge (blue dot).

The Monte Carlo Method

The Monte Carlo method subsumes a class of statistical sampling techniques that use random numbers to solve hard problems. These problems are usually either too complex to be solved analytically or numerically too expensive to be solved deterministically. The underlying idea traces back to Stanislaw Ulam and John von Neumann in the early 1940s [85–87] and the first published work on the Monte Carlo method by Ulam and Metropolis in 1949 [88]. It has been applied to a vast range of problems in natural sciences, mathematics, engineering, or even finance and social sciences since then and is among the most powerful numerical tools at all. In this chapter, we give a brief introduction to Monte Carlo simulations of classical spin models, where the exponentially large configuration space often complicates analytical calculations, and numerical methods are, therefore, an invaluable important tool in the study of such systems.

3.1 Markov Chains

Most generally speaking, the primary objective of the Monte Carlo method is to draw unbiased and statistically relevant samples from some configuration space Ω, with the samples being distributed according to some probability distribution. The simplest application is the numerical evaluation of an integral by the Monte Carlo method, where the drawn samples are random coordinates $x_i \in \Omega$ with a suitably chosen distribution at which the function to be integrated can be evaluated. However, these random samples may also be more complex objects, such as spin configurations of a spin model. A set of such random samples $\{C_i\} \subset \Omega$—in the following referred to as configurations—is generated in a weighted random walk, and the resulting sequence of configurations

$$C_1 \to C_2 \to \cdots \to C_{i-1} \to C_i \to C_{i+1} \to \dots \tag{3.1}$$

is called a Markov chain, as the underlying process is Markovian, i.e., the next step in the chain only depends on the current configuration but is independent of any earlier configuration, which leads to the conditional probability

$$P(C_i|C_{i-1}, C_{i-2}, \dots, C_2, C_1) = P(C_i|C_{i-1}). \tag{3.2}$$

For the configurations to follow a given distribution p_C, this step has to fulfill certain conditions. The probability of the transition from some configuration C to some other configuration C' is given by the elements of a transition matrix $W_{CC'}$. As the probability of getting from one configuration C to any other configuration must be exactly 1, the first condition for the transition matrix is

1. **Normalization:** The columns of the transition matrix are normalized,

$$\sum_{C'} W_{CC'} = 1 \,. \tag{3.3}$$

This, by definition, makes the transition matrix a stochastic matrix and has the consequence that the largest eigenvalue of the transition matrix is equal to 1, with the corresponding eigenvector being an equilibrium distribution. For this stationary eigenvector to model the desired distribution p_C, the transition matrix must obey two additional properties. These are:

2. **Ergodicity:** Every configuration C' must be reachable from any other configuration C in a finite number of steps n,

$$\forall C, C' \; \exists n : (W^n)_{CC'} \neq 0 \,. \tag{3.4}$$

Ergodicity ensures that the Markov chain does not get trapped in a limited subset of the configuration space and thus the set of sampled configurations can never be statistically representative.

3. **Convergence to equilibrium:** The probability distribution at the nth Markov step, $p_C^{(n)}$, changes in each Markov step as $\sum_C p_C^{(n)} W_{CC'} = p_{C'}^{(n+1)}$ but converges to an equilibrium distribution,

$$\lim_{n \to \infty} p_C^{(n)} = p_C \,. \tag{3.5}$$

Since p_C is an eigenvector of the transition matrix with eigenvalue 1, the equilibrium condition is

$$\sum_C p_C W_{CC'} = p_{C'} \,, \tag{3.6}$$

or simply

$$\mathbf{p} \cdot \mathbf{W} = \mathbf{p} \,. \tag{3.7}$$

To fulfill the equilibrium condition, the so-called *detailed balance* condition is sufficient:

$$\frac{W_{CC'}}{W_{C'C}} = \frac{p_{C'}}{p_C} \,. \tag{3.8}$$

This can easily be checked by plugging Eq. (3.8) into the left hand side of the equilibrium condition in Eq. (3.7) and using the normalization of the columns of the transition matrix:

$$\sum_C p_C W_{CC'} \overset{(3.8)}{=} \sum_C p_{C'} W_{C'C} = p_{C'} \sum_C W_{C'C} \overset{(3.3)}{=} p_{C'} \,. \tag{3.9}$$

A sampling process that fulfills these conditions will yield a sequence of configurations that represents the probability distribution p_C.

3.2 Generation of Markov Chains

The rules stated above do not yet state how such a sequence can be generated in practice. Usually, this is done by employing the Metropolis algorithm [89, 90], which we outline in the following.

3.2.1 Metropolis Algorithm

To generate a Markov chain, an appropriate choice of weights $W_{CC'}$ must be made. One commonly used way to comply with the detailed balance condition is to choose so-called Metropolis weights

$$W_{CC'} = \min\left(1, \frac{p_{C'}}{p_C}\right). \tag{3.10}$$

That these fulfill the detailed balance condition, Eq. (3.8), can be demonstrated by considering the cases $p_{C'} > p_C$ and $p_{C'} > p_C$ separately. For the former, we find $W_{CC'} = 1$ and $W_{C'C} = \frac{p_C}{p_{C'}}$, whereas the latter yields $W_{CC'} = \frac{p_{C'}}{p_C}$ and $W_{C'C} = 1$, both leading to detailed balance.

After starting with some random initial configuration $C_i \in \Omega$, the iterative Monte Carlo step of the Metropolis algorithm then consists of the following steps:

1. Based on the current configuration C_i, propose some new configuration $\tilde{C}_{i+1}$.

2. Calculate the weight $\alpha = \frac{p_{\tilde{C}_{i+1}}}{p_{C_i}}$.

3. Generate a uniformly distributed random number $\gamma \in [0, 1]$.

4. The next configuration in the Markov chain is then given by

$$C_{i+1} = \begin{cases} \tilde{C}_{i+1} & \gamma \leq \alpha \\ C_i & \gamma > \alpha. \end{cases}$$

5. Based on C_{i+1}, restart from step 1.

One such single iteration is also called a Monte Carlo update (MCU). For a system of N random variables, a set of N MCU is called a Monte Carlo *sweep* (MCS), i.e., during one sweep, every random variable is (attempted to be) updated on average once.

Steps 2 to 4 simply implement the Metropolis weights of Eq. (3.10). The question of how to propose a new configuration in the first step, on the other hand, is nontrivial and depends strongly on the problem at hand. One simple update technique is to pick a randomly chosen spin and either flip it (Ising spins) or randomly rearrange it on the unit sphere (Heisenberg spins).

If the desired probality distribution is the Boltzmann distribution $p_C = \frac{1}{\mathcal{Z}} e^{-\beta \mathcal{H}(C)}$, where $\mathcal{H}(C)$ is the energy of configuration C (which is typically the case in statistical physics simulations), the weight α in step 2 simply becomes

$$\alpha = e^{-\beta(\mathcal{H}(\tilde{C}_{i+1}) - \mathcal{H}(C_i))} \equiv e^{-\beta \Delta E}. \tag{3.11}$$

The numerical expensive calculation of the partition function $\mathcal{Z} = \sum_C e^{-\beta \mathcal{H}(C)}$ in the denominator of p_C cancels out and the computational effort of step 2 reduces to finding the energy difference ΔE between the two configurations $\tilde{C}_{i+1}$ and C_i. A technical aspect that needs to be considered is equilibration. Due to the Boltzmann factor $e^{-\beta \Delta E}$ in the Metropolis weights, a proposed new configuration with a lower energy than the previous one is always accepted, while configurations with higher energy are accepted with exponentially small, but non-zero probability. These thermal fluctuations allow the system to overcome local energy minima and eventually reach a global energy minimum. Depending on the temperature $T = \beta^{-1}$ $(k_B = 1)$,

this can take a considerable number of sweeps. Therefore, it is essential to allow the system to *thermalize* to equilibrium for a certain number of sweeps before generating the Markov chain for later measurements.

3.2.2 Parallel Tempering

There are systems with complex and rough energy landscapes that have numerous local minima at low temperatures separated by energy barriers, such as spin glasses or frustrated spin systems. In such systems, conventional Monte Carlo methods can hardly relax to the true ground state. A solution to address this difficulty is the so-called *parallel tempering* or *replica exchange* Monte Carlo scheme [91–93].

The idea of this scheme is to simulate K independent replicas of the system simultaneously at different temperatures $\{T_1, T_2, \ldots, T_{i-1}, T_i, T_{i+1}, \ldots, T_K\}$ spanning from low to high temperatures. After a certain number of conventional Monte Carlo sweeps, a sequence of swap moves is suggested, where for each pair of neighboring replicas at temperatures T_i and T_{i+1} and with energies E_i and E_{i+1} the current configurations are interchanged with a probability

$$p(E_i, T_i \rightarrow E_{i+1}, T_{i+1}) = \min\left(1, e^{\Delta\beta\Delta E}\right), \tag{3.12}$$

where $\Delta\beta = 1/T_{i+1} - 1/T_i$ and $\Delta E = E_{i+1} - E_i$ are the differences between the inverse temperatures and energies of the two replicas, respectively. An accepted swap effectively corresponds to a global update and as a result, individual replicas make a random walk in temperature space and thus can escape local minima at low temperatures easily, since fluctuations occurring at higher temperatures are fed into systems at lower temperatures by warming up and cooling down each replica.

From a technical point of view it is important to choose the number of replicas and the temperature grid properly. The highest temperatures must be sufficiently large to enable all replicas to escape every local minimum. Also, one has to ensure that swap moves are accepted with a non-vanishing probability for all neighboring pairs of replicas. To this end, the probability distributions $p(E_i)$ and $p(E_{i+1})$ must have a finite overlap for all pairs $(i, i+1)$, as schematically depicted in Fig. 3.1. For the systems studied within this thesis, a logarithmically distributed temperature grid with 192 to 240 replicas between $T_{min}/J = 10^{-4}$ and $T_{max}/J = 10$ is used successfully. For other problems, different choices of temperature grids may be more efficient, for example, using a geometric progression of temperatures [94], adaptive temperature control schemes [95], or an adaptive feedback-optimized algorithm that minimizes the round-trip times of replicas moving between the lowest and highest temperatures [96].

3.3 Monte Carlo Data

Now that we have seen how Markov chains are constructed, we turn to the generation of physically relevant data from them. The following chapter describes how observables and their errors are measured and analyzed statistically and how successive measurements are correlated, which can lead to a *critical slowing down*.

3.3.1 Observables

The benefit of the outlined statistical sampling becomes particularly clear if one now considers a specific observable $\mathcal{O}$ in whose thermodynamic expectation value one is interested. In general, such an expectation value is given by

$$\langle \mathcal{O} \rangle = \sum_C p_C \mathcal{O}_C \,, \tag{3.13}$$

where the summation is performed over all possible configurations C of the system at hand, p_C is the probability of finding the system in configuration C, and $\mathcal{O}_C$ is specific the value of the observable $\mathcal{O}$ for the given configuration C. However, this summation turns out to be almost impossible to carry out due to an exponentially large configuration space—even in the simplest case, the Ising model with N spins, there are already 2^N different possible configurations.

Here, the Markov chain comes into play. With a set $\{C_i\}$ of $M \ll 2^N$ statistically relevant samples from the configuration space, the true expectation value can be approximated as a sample mean via

$$\langle \mathcal{O} \rangle \approx \bar{\mathcal{O}} = \frac{1}{M} \sum_{i=1}^{M} \mathcal{O}_{C_i} \,, \tag{3.14}$$

where $\mathcal{O}_{C_i} \equiv \mathcal{O}_i$ is the value of $\mathcal{O}$ for a given configuration C_i. Even though the expectation value $\langle \mathcal{O} \rangle$ is approximated by the arithmetic mean $\bar{\mathcal{O}}$, it is important to distinguish both quantities. Whereas the former is an expectation value and, therefore, a well-defined fixed numeric value, the latter is a random variable that fluctuates around the theoretical expectation value.

An important quantity is, therefore, its variance, which measures the squared deviation of $\bar{\mathcal{O}}$ from its expectation value:

$$\text{Var}(\bar{\mathcal{O}}) = \left\langle \left(\bar{\mathcal{O}} - \langle \bar{\mathcal{O}} \rangle \right)^2 \right\rangle = \langle \bar{\mathcal{O}}^2 \rangle - \langle \bar{\mathcal{O}} \rangle^2 \,. \tag{3.15}$$
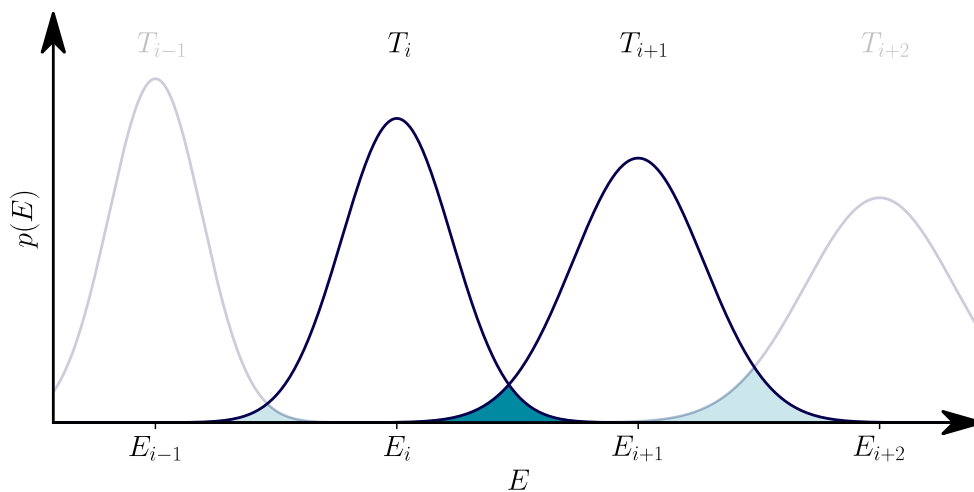
Figure 3.1 – **Energy histograms of replicas at different temperatures.** The distributions $p(E_i)$ and $p(E_{i+1})$ of replicas running at temperatures T_i and T_{i+1} must have a finite overlap in order to have a non-vanishing probability to exchange their configurations in an attempted swap move.

For M subsequent uncorrelated measurements, this variance is easily obtained by plugging Eq. (3.14) into Eq. (3.15):

$$
\begin{aligned}
\mathrm{Var}(\bar{\mathcal{O}}) &= \left\langle \left(\frac{1}{M} \sum_{i=1}^{M} \mathcal{O}_i \right)^2 \right\rangle - \left\langle \frac{1}{M} \sum_{i=1}^{M} \mathcal{O}_i \right\rangle^2 \\
&= \frac{1}{M^2} \sum_{i,j=1}^{M} \langle \mathcal{O}_i \mathcal{O}_j \rangle - \frac{1}{M^2} \sum_{i,j=1}^{M} \langle \mathcal{O}_i \rangle \langle \mathcal{O}_j \rangle \\
&= \frac{1}{M^2} \sum_{i=1}^{M} \left(\langle \mathcal{O}_i^2 \rangle - \langle \mathcal{O}_i \rangle^2 \right) + \frac{1}{M^2} \sum_{i \neq j}^{M} \left(\langle \mathcal{O}_i \mathcal{O}_j \rangle - \langle \mathcal{O}_i \rangle \langle \mathcal{O}_j \rangle \right) \\
&= \frac{1}{M} \mathrm{Var}(\mathcal{O}_i) \,,
\end{aligned}
\tag{3.16}
$$

where

$$
\mathrm{Var}(\mathcal{O}_i) = \frac{1}{M} \sum_{i=1}^{M} \langle \mathcal{O}_i^2 \rangle - \langle \mathcal{O}_i \rangle^2
\tag{3.17}
$$

and the summation in the third line of Eq. (3.16) is split into two parts, one with $i = j$ and one with $i \neq j$. The final step holds since the off-diagonal terms with $i \neq j$ vanish for uncorrelated measurements where $\langle \mathcal{O}_i \mathcal{O}_j \rangle = \langle \mathcal{O}_i \rangle \langle \mathcal{O}_j \rangle$. Also, assuming equilibrium, the quantity $\langle \mathcal{O}_i \rangle$ should be independent of the index i and Eq. (3.16) simplifies to

$$
\mathrm{Var}(\bar{\mathcal{O}}) = \frac{1}{M} \mathrm{Var}(\mathcal{O}) \,.
\tag{3.18}
$$

The variance of the arithmetic mean is thus proportional to the variance of the underlying distribution but becomes smaller the more Monte Carlo measurements are taken into account. This fact is rooted in the central limit theorem, which states that the distribution of a sum of independent and identically distributed random variables (here, Eq. (3.14)) becomes a normal distribution in the asymptotic limit of large M, that can be described only by its mean and its variance, no matter what the underlying distribution of the original random variables is[1]. The standard deviation $\sigma_{\bar{\mathcal{O}}} = \sqrt{\mathrm{Var}(\bar{\mathcal{O}})}$ is the width of this normal distribution and scales as $\frac{1}{\sqrt{M}} \cdot \sigma_{\mathcal{O}}$. The statistical error in a Monte Carlo simulation can therefore be well controlled by the sample size.

3.3.2 Autocorrelation Effects and Critical Slowing Down

Since each configuration in the Markov chain is generated by modifications of the previous configuration, successive measurements are usually correlated and not truly independent, and the off-diagonal term in Eq. (3.16) must be taken into account. To do so, we introduce the autocorrelation time τ, which is the typical time scale on which the correlations fall off. The correlations of two different measurements $\mathcal{O}_i$ and $\mathcal{O}_{i+\Delta}$ are found [98] to decay exponentially as

$$
\langle \mathcal{O}_i \mathcal{O}_{i+\Delta} \rangle - \langle \mathcal{O} \rangle^2 \propto \exp\left(-\tfrac{\Delta}{\tau} \right) \,.
\tag{3.19}
$$

---

[1]This is true as long as the underlying distribution has a well-defined expectation value and variance, which is always the case except for a few pathological distributions such as the Cauchy distribution [97].

An alternative way to express these correlations is via the integrated autocorrelation time

$$\tau_{\mathcal{O},\text{int}} = \frac{\sum_{\Delta=1}^{\infty} \left(\langle \mathcal{O}_i \mathcal{O}_{i+\Delta} \rangle - \langle \mathcal{O} \rangle^2 \right)}{\langle \mathcal{O}^2 \rangle - \langle \mathcal{O} \rangle^2} \,, \tag{3.20}$$

which becomes useful in the following calculation.

With the integrated autocorrelation time at hand, we can estimate how the correlations between subsequent measurements affect the variance of $\bar{\mathcal{O}}$ when the off-diagonal terms do not vanish:

$$\begin{aligned}
\text{Var}(\bar{\mathcal{O}}) &= \frac{1}{M} \text{Var}(\mathcal{O}) + \frac{1}{M^2} \sum_{i \neq j}^{M} \left(\langle \mathcal{O}_i \mathcal{O}_j \rangle - \langle \mathcal{O}_i \rangle \langle \mathcal{O}_j \rangle \right) \\
&= \frac{1}{M} \text{Var}(\mathcal{O}) + \frac{2}{M^2} \sum_{i=1}^{M} \sum_{\Delta=1}^{M-i} \left(\langle \mathcal{O}_i \mathcal{O}_{i+\Delta} \rangle - \langle \mathcal{O} \rangle^2 \right) \\
&\approx \frac{1}{M} \text{Var}(\mathcal{O})(1 + 2\tau_{\mathcal{O},\text{int}}) \,.
\end{aligned} \tag{3.21}$$

Here we used the symmetry $i \leftrightarrow j$ to reduce the summation $\sum_{i \neq j}^{M}$ to $2 \sum_{i=1}^{M} \sum_{\Delta=1}^{M-i}$ and translational invariance $\langle \mathcal{O}_i \rangle \leftrightarrow \langle \mathcal{O}_{i+\Delta} \rangle$ to rewrite the second term. From this we can conclude that the number of uncorrelated samples in the Markov chain is reduced by a factor of $1 + 2\tau_{\mathcal{O},\text{int}}$, or in other words, the statistical error of the Monte Carlo estimator, $\sigma_{\mathcal{O}}$, is enhanced by a factor $\sqrt{1 + 2\tau_{\mathcal{O},\text{int}}}$ due to the temporal correlations of subsequent measurements. The autocorrelation time τ is also related to the correlation length ξ by the dynamical exponent z,

$$\tau \propto \xi^z \,. \tag{3.22}$$

The correlation length, in turn, is the typical length scale of spatial correlations, or in other words, the typical size of clusters with the same spin orientation. Empirically, for the Metropolis algorithm for the 2D Ising model, the dynamical exponent is known to be $z_{\text{2D Ising}} \approx 2.17$ for local single spin flip updates [99]. This means that near the ferromagnetic phase transition, where fluctuations occur on all length scales and the correlation length diverges as $\xi \propto |T - T_c|^{-\nu}$ with the critical exponent $\nu > 0$, the autocorrelation time diverges as well, and the time between two uncorrelated configurations in the Markov chain becomes infinitely large—an effect that is known as *critical slowing down*.

The problem of critical slowing down can be circumvented by using cluster updates (as proposed, e.g., in the Swendsen-Wang algorithm [100] or the Wolff algorithm [101]), where clusters of spins are collectively flipped instead of local updates—techniques that we do not pursue in this thesis.

3.3.3 Numerical Estimation of Statistical Errors: Binning and Jackknife Analysis

Ignoring the intrinsic autocorrelation effects can lead to drastic underestimations of statistical errors. But since calculating $\tau_{\mathcal{O},\text{int}}$ via Eq. (3.20) is cumbersome, a common practice to cope with this and reliably determine autocorrelation times is a *binning analysis* [102], as outlined in the following. By grouping the M original measurements $\mathcal{O}_i$ into M_B bins of length k (i.e.,

$M = kM_B$),

$$\underbrace{\mathcal{O}_1, \mathcal{O}_2, \ldots, \mathcal{O}_k}_{\text{Bin } 1}, \underbrace{\mathcal{O}_{k+1}, \mathcal{O}_{k+2}, \ldots, \mathcal{O}_{2k}}_{\text{Bin } 2}, \ldots, \underbrace{\mathcal{O}_{(M_B-1)k+1}, \mathcal{O}_{(M_B-1)k+2}, \ldots, \mathcal{O}_{M_B k}}_{\text{Bin } M_B}, \tag{3.23}$$

one can form M_B different bin averages

$$\mathcal{O}_j^B = \frac{1}{k} \sum_{i=1}^{k} \mathcal{O}_{(j-1)k+i}. \tag{3.24}$$

The mean of all bin values evidently satisfies

$$\overline{\mathcal{O}^B} = \frac{1}{M_B} \sum_{j=1}^{M_B} \frac{1}{k} \sum_{i=1}^{k} \mathcal{O}_{(j-1)k+i} = \frac{1}{M} \sum_{i=1}^{M} \mathcal{O}_i \overset{(3.14)}{=} \bar{\mathcal{O}}, \tag{3.25}$$

while the bin averages, however, are less correlated than the original measurements. Upon increasing the bin size k, the variance of the bin averages also increases as

$$\text{Var}(\mathcal{O}^B) \approx \frac{1}{(M_B - 1)} \sum_{j=1}^{M_B} (\mathcal{O}_j^B - \overline{\mathcal{O}^B})^2, \tag{3.26}$$

but converges to the correct error estimate $\sigma_{\mathcal{O}}^2$ for sufficiently large k, when all bins become statistically independent. In order to determine for which k this is the case, the ratio

$$R_{\mathcal{O}} = \frac{\text{Var}(\mathcal{O}^B)}{\text{Var}(\mathcal{O})} \tag{3.27}$$

is measured as a function of the bin size k where the denominator is the unbinned sample variance, i.e. $\text{Var}(\mathcal{O}^B)$ for $k = 1$. If convergence is observed and $R_{\mathcal{O}}$ plateaus at a finite value $R_{\mathcal{O}}^{\text{plateau}}$, a reliable estimate for the autocorrelation time $\tau_{\mathcal{O}}$ is given by

$$\tau_{\mathcal{O}} = \frac{1}{2} \left(R_{\mathcal{O}}^{\text{plateau}} - 1 \right). \tag{3.28}$$

If no convergence of $R_{\mathcal{O}}$ can be observed, $\tau_{\mathcal{O}}$ is larger than the simulation time and much longer simulations must be performed in order to obtain reliable error estimates.

But even for uncorrelated data, error estimation can be problematic if an observable is not measured directly, but rather as a combination of different basic observables from the same time series—which, therefore, are not temporally but rather trivially statistically correlated. Important examples for which this is relevant are the specific heat $c_V = \beta^2(\langle E^2 \rangle - \langle E \rangle^2)$ or the magnetic susceptibility $\chi = \beta(\langle m^2 \rangle - \langle |m| \rangle^2)$, where different moments of the distribution of the energy and the magnetization, respectively, are involved. Instead of using the full machinery of calculating covariance matrices and correlation coefficients for multivariate variance estimates, a less tedious technique to handle this is the *jackknife method* [103, 104]. In this resampling method, instead of considering small bins of length k as in the binning method, one forms M_B large jackknife

blocks $\mathcal{O}_j^J$ that contain all measurements but the jth bin from the binning analysis,

$$\mathcal{O}_j^J = \frac{M\bar{\mathcal{O}} - k\mathcal{O}_j^B}{M - k}, \tag{3.29}$$

with $j = 1, \ldots, M_B$, such that each jackknife block consists of $N-k$ measurements. The jackknife estimates for mean and the variance are then given by [104]

$$\overline{\mathcal{O}^J} = \frac{1}{M_B} \sum_{j=1}^{M_B} \mathcal{O}_j^J, \tag{3.30}$$

$$\text{Var}(\mathcal{O}^J) = \frac{M_B - 1}{M_B} \sum_{j=1}^{M_B} \left(\mathcal{O}_j^J - \overline{\mathcal{O}^J}\right)^2. \tag{3.31}$$

3.4 Dynamical Monte Carlo

Up to this point, the Monte Carlo method, as described above, is used to study systems in equilibrium. Measurements of observables are taken after the system has equilibrated and the fluctuations in the configurations in the Markov chain can be thought of as thermodynamical fluctuations around some equilibrium configuration. In the following, we want to use and expand this framework to study dynamical phenomena and systems out of equilibrium, based on ideas of Takatsu et al. [105, 106].

3.4.1 Monte Carlo Time

The key idea is to interpret the sequence of configurations generated in the Markov chain not as a canonical ensemble of configurations but rather as the real time evolution of some initial configuration of the studied system, that is,

$$C_1 \to C_2 \to \cdots \to C_{i-1} \to C_i \to C_{i+1} \to \ldots \tag{3.32}$$

will be thought of as

$$C(t_1) \to C(t_2) \to \cdots \to C(t_{i-1}) \to C(t_i) \to C(t_{i+1}) \to \ldots . \tag{3.33}$$

This relation sets an elementary time scale that spans one Monte Carlo update (MCU). As such, the time passed in dynamical Monte Carlo, t_{MC}, can, in principle, be related to real time t_{real}, e.g., in an experimental system, by scaling with a factor A, that may depend on several external parameters such as temperature or magnetic field, which are a priori unknown but can be determined by comparison to experimental data, i.e.

$$t_{\text{MC}} = A(T, H, \ldots) \cdot t_{\text{real}}. \tag{3.34}$$

With this new time scale established, subsequent measurements of the observable $\mathcal{O}$ in a dynamical Monte Carlo simulation no longer contribute to a statistical mean but yield corresponding time-dependent measurement outcomes $\mathcal{O}(t_{\text{MC}})$. This time dependence can now be used to introduce time-varying parameters like an oscillating magnetic field and to consequently access dynamical measurements—previously unavailable in classical Monte Carlo studies. In particular,

as outlined in the next section, it can be used to numerically measure dynamic AC susceptibilities, which is a standard tool for probing magnetic dynamics in experiments [107–111].

At this point, we want to emphasize that the single spin-flip dynamics immanent in the local Monte Carlo updates is of great importance for the concept of dynamical Monte Carlo. Physically, one can interpret real time fluctuations in the Markov chain as phonons that shake the system and stochastically cause fluctuations of single spins. Based on this picture, it is logical that we use local updates instead of cluster update schemes, which are, therefore, not suitable to model single spin dynamics.

3.4.2 Dynamical Measurements

In contrast to static Monte Carlo simulations, our approach allows also for the calculation of dynamical observables such as the dynamical susceptibility $\chi_{\mathrm{AC}}(\omega)$. The dynamical (AC) susceptibility is a measure for the response to an alternating magnetic field

$$\mathbf{H}_{\mathrm{AC}}(t) = \mathbf{H}_0 \sin(\omega t) \,. \tag{3.35}$$

This magnetic field leads to a time-varying magnetization

$$\begin{aligned} \mathbf{M}(t) &= \mathbf{M}_0 \sin(\omega t - \delta) \\ &= \mathbf{M}' \sin(\omega t) + \mathbf{M}'' \cos(\omega t) \,, \end{aligned} \tag{3.36}$$

where $\mathbf{M}' = \mathbf{M}_0 \cos \delta$ is the in-phase component of the magnetization and $\mathbf{M}'' = -\mathbf{M}_0 \sin \delta$ the out-of-phase component. δ describes the dephasing between the magnetization and the magnetic field which originates in dissipation in the system which prevents the magnetization to follow the oscillations of the field. The associated AC susceptibility $\chi_{\mathrm{AC}}(\omega) = \mathbf{M}/\mathbf{H}_0 = \chi'(\omega) - i\chi''(\omega)$ can thus be calculated via

$$\chi'(\omega)\mathbf{H}_0 = \mathbf{M}_0 \cos(\delta) = \frac{2}{T} \int_0^T \mathbf{M}(t) \sin(\omega t) \mathrm{d}t \tag{3.37}$$

and

$$\chi''(\omega)\mathbf{H}_0 = \mathbf{M}_0 \sin(\delta) = \frac{2}{T} \int_0^T \mathbf{M}(t) \cos(\omega t) \mathrm{d}t \,. \tag{3.38}$$

For dynamical Monte Carlo simulations, where the Markov chain of successive configurations is interpreted as the real time evolution of the system, the alternating magnetic field in Eq. (3.35) can be implemented as a function of Monte Carlo time t_{MC} as

$$\mathbf{H}_{\mathrm{AC}}(t_{\mathrm{MC}}) = \mathbf{H}_0 \sin(\omega t_{\mathrm{MC}}) = \mathbf{H}_0 \sin\left(2\pi \frac{t_{\mathrm{MC}}}{t_{\mathrm{AC}}}\right) \,, \tag{3.39}$$

where $t_{\mathrm{AC}} = 2\pi/\omega$ is the period of the magnetic field in units of MCU. To measure the AC susceptibility, the integrals on the right hand sides of Eqs. (3.37) and (3.37) are then simply computed by averaging the integrands as usual in Monte Carlo simulations, that is,

$$\chi'(\omega)\mathbf{H}_0 = \frac{2}{N_{\mathrm{MC}}} \sum_{t_{\mathrm{MC}}=1}^{N_{\mathrm{MC}}} \mathbf{M}(t_{\mathrm{MC}}) \sin(\omega t_{\mathrm{MC}}) \tag{3.40}$$

for the real part of the dynamic susceptibility and

$$\chi''(\omega)\mathbf{H}_0 = \frac{2}{N_{\mathrm{MC}}} \sum_{t_{\mathrm{MC}}=1}^{N_{\mathrm{MC}}} \mathbf{M}(t_{\mathrm{MC}}) \cos(\omega t_{\mathrm{MC}}) \tag{3.41}$$

for its imaginary part, where $\mathbf{M}(t_{\mathrm{MC}})$ is the magnetization in the simulation cell measured at time t_{MC} and N_{MC} is the number of total MCU during the Monte Carlo simulation.

3.4.3 Example: Critical Slowing Down in a Ferromagnet

As a warm-up example of the dynamical Monte Carlo method, we want to probe the previously described effect of critical slowing down near a phase transition, where fluctuations occur on larger and larger and, eventually, system-spanning length scales and slow down the equilibration of the system dramatically.

To this end, we periodically drive the ferromagnetic Ising model on the triangular lattice with a sinusoidal magnetic field of the form of Eq. (3.35) and an amplitude of $|\mathbf{H}_0|/J = 0.01$. At zero DC field, this model is known to exhibit a symmetry-breaking phase transition at a critical temperature of $T_c = \frac{4}{\ln 3} \approx 3.64$ [112] and, therefore, is expected to show a drastic increase in correlation times near T_c. Assuming a simple exponential relaxation of the magnetization with a single relaxation time τ, linear response theory yields the Debye model for the AC susceptibility (for a derivation, see Appendix A),

$$\chi_{\mathrm{AC}}(\omega) = \frac{\chi_0}{1 + i\omega\tau} \, , \tag{3.42}$$

where the imaginary part $\chi''(\omega) = \omega\tau\chi_0 \left[1 + (\omega\tau)^2\right]^{-1}$ has a maximum at the *loss peak frequency* $\omega_p = 1/\tau$ [107]. Therefore, we measure spectra of $\chi_{\mathrm{AC}}(\omega)$ in a dynamical Monte Carlo scheme, fit the data to such a Debye relaxation, and use ω_{p} to determine the relaxation time τ, which we, in turn, interpret as the autocorrelation time of the system. This scheme is summarized in Fig. 3.2, where normalized spectra of the imaginary part of the AC susceptibility, $\chi''(\omega)/\chi_{\mathrm{max}}$, are shown for three different temperatures below, above, and near T_c. After fitting a Debye relaxation to several such data sets, the loss peak frequency ω_p can be plotted as a function of temperature (see inset Fig. 3.2). As expected, the canonical critical slowing down near the phase transition is successfully revealed as indicated by an exponential suppression of w_p corresponding to an exponential increase of $\tau = w_p^{-1}$. The method used in this fruitful example forms the basis for studies of the dynamics in other, more complex systems in the next part of this thesis, where the method, which is only briefly outlined here, is also presented in more detail.
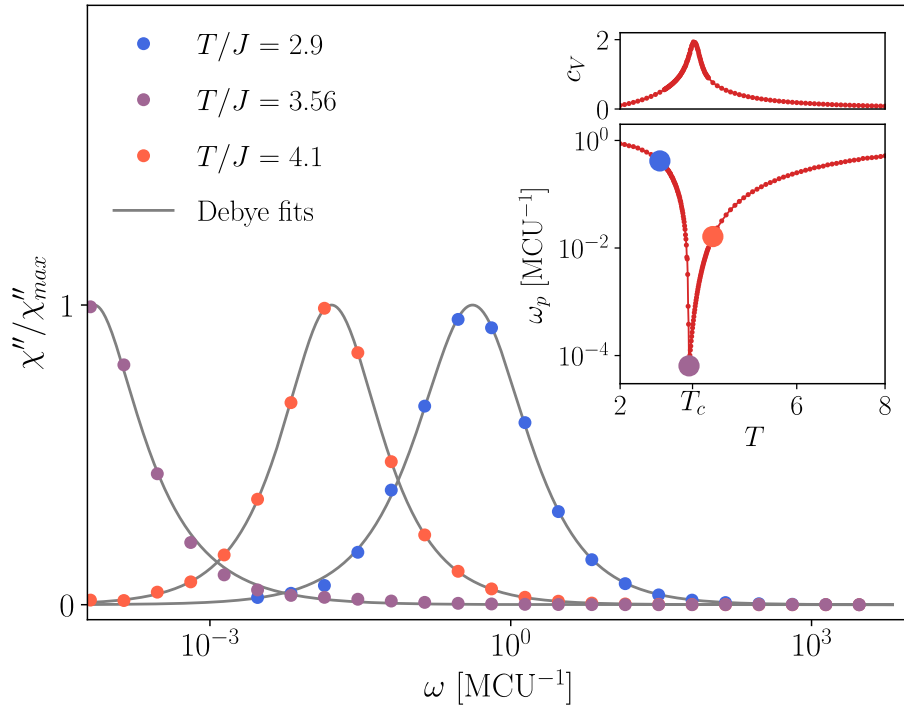
Figure 3.2 – **Numerical spectra of $\chi''(\omega)$.** Monte Carlo data of the (normalized) imaginary part of the AC susceptibility (Eq. (3.41)) and corresponding Debye fits (see Appendix A for details) for the triangular lattice Ising ferromagnet for three temperatures below, above, and near the phase transition at $T_c = \frac{4}{\ln 3} \approx 3.64$ [112]. Each curve has a distinct maximum at a peak frequency ω_p which is related to the relaxation time as $\tau = \omega_p^{-1}$. Inset: Upper panel shows the specific heat with the characteristic peak structure at $T = T_c$. The lower panel shows the temperature dependence of the peak frequency ω_p of the AC field response. The exponential suppression of ω_p is consistent with an exponential increase in correlation times near the phase transition, i.e., a critical slowing down. Figure taken from [U1].

Part II

Critical Speeding Up in Spin Ice and Spin Liquids

Monopole Dynamics in Spin Ice

Introduced 1997 by M. Harris, S. Bramwell, et al. [22], the term *spin ice* refers to a broad range [113] of magnetic rare earth oxides that exhibit remarkably similar physics to water ice with its characteristic zero point entropy [9]. These compounds are of the form $A_2B_2O_7$ where B^{4+} usually are non-magnetic ions of a transition metal and A^{3+} are magnetic rare earth ions that reside on the vertices of a face centered cubic network of corner-sharing tetrahedra commonly referred to as the pyrochlore lattice (cf. Fig. 2.3(b)). Well-established textbook members of this family of materials are holmium titanate ($Ho_2Ti_2O_7$) [22, 114] and dysprosium titanate ($Dy_2Ti_2O_7$) [115]. In this chapter, the basics of spin ice physics are introduced and the emergence of magnetic monopoles as elementary excitations in spin ice is discussed—for a much more comprehensive introduction to the topic of spin ice, the interested reader is referred to the extensive literature [23, 49, 50, 116, 117]. We will subsequently investigate the dynamics of such monopoles using dynamical Monte Carlo simulations.

4.1 Spin Ice Physics

In Part I we showed that tetrahedra are perfect geometric building blocks for frustrated systems and that antiferromagnetically coupled classical Ising spins on the pyrochlore lattice do not develop long range order, but have massively degenerate ground states leading to the residual Pauling entropy of Eq. (2.7). Intriguingly, the physics in spin ice can be mapped to this very same model due to a very strong axial crystal field on the rare earth ions that splits the free ion state such that an almost pure Ising doublet lies lowest in energy by several hundred Kelvin. This, in turn, gives rise to a strong single ion anisotropy that constrains the magnetic moments parallel to their local $\langle 111 \rangle$ quantization axes [118, 119]. That is, each spin behaves like a classical Ising spin parallel to the axis which connects the vertex with the center of its opposing triangular face (cf. Fig. 4.1) and thus can only either point into a tetrahedron or out of it.

Accordingly, each spin can be written as a product of its local axis $\hat{\mathbf{z}}_i$ and an Ising variable $\sigma_i \in \{-1, +1\}$,

$$\mathbf{S}_i = \sigma_i \hat{\mathbf{z}}_i \,, \tag{4.1}$$

where the four possible local axes are given by

$$\hat{\mathbf{z}}_1 = \frac{1}{\sqrt{3}} \left[1\bar{1}\bar{1} \right], \ \hat{\mathbf{z}}_2 = \frac{1}{\sqrt{3}} \left[\bar{1}1\bar{1} \right], \ \hat{\mathbf{z}}_3 = \frac{1}{\sqrt{3}} \left[\bar{1}\bar{1}1 \right], \ \hat{\mathbf{z}}_4 = \frac{1}{\sqrt{3}} \left[111 \right] \,. \tag{4.2}$$

Plugging this into a general nearest-neighbor Heisenberg Hamiltonian (Eq. (2.3)) with $J_{ij} \equiv J$ and using that $\hat{\mathbf{z}}_i \cdot \hat{\mathbf{z}}_j = -\frac{1}{3}$ for all neighboring i and j then yields the following effective Ising
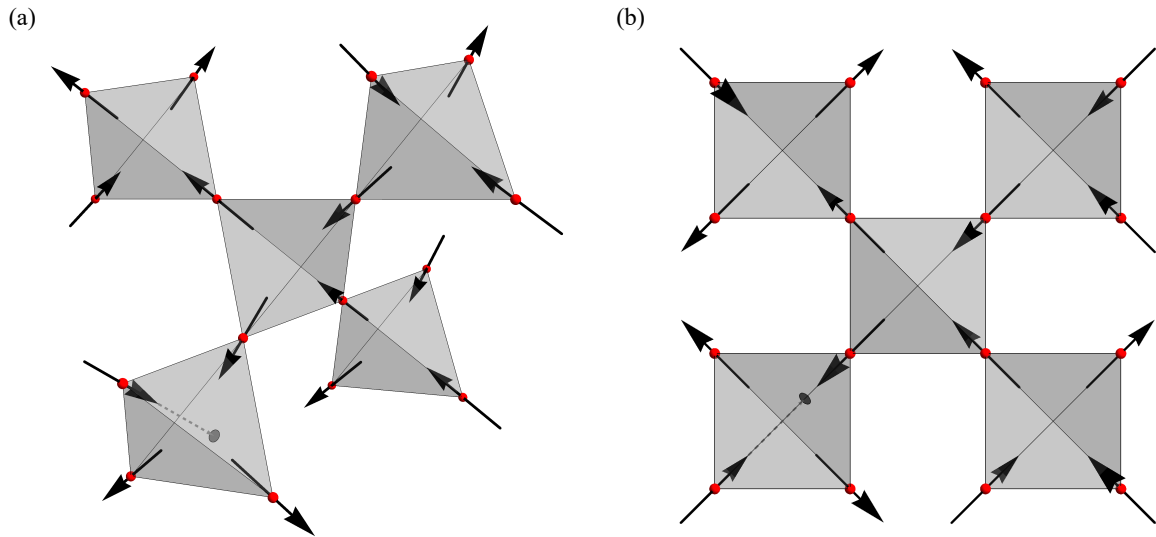
Figure 4.1 – **Pyrochlore lattice with Ising spins pointing along local ⟨111⟩ axes.** (a) In spin ice materials like $Dy_2Ti_2O_7$ or $Ho_2Ti_2O_7$, rare earth magnetic moments reside on the vertices of a network of corner-sharing tetrahedra. A strong single ion anisotropy due to crystal field effects forces the spins (indicated by arrows) to point along the axes that connect the vertices with the centers of the opposing triangular faces (example shown as dashed line). Each tetrahedron has two spins pointing inwards and two spins pointing outwards, according to the ice rule (see main text). (b) Shows a projection of (a) onto a two-dimensional plane for clarity.

Hamiltonian for nearest-neighbor spin ice (NNSI):

$$\mathcal{H}_{\text{NNSI}} = J \sum_{\langle i,j \rangle} \mathbf{S}_i \cdot \mathbf{S}_j = J \sum_{\langle i,j \rangle} \sigma_i \sigma_j (\hat{\mathbf{z}}_i \cdot \hat{\mathbf{z}}_j) = -\frac{J}{3} \sum_{\langle i,j \rangle} \sigma_i \sigma_j$$

$$= J_{\text{eff}} \sum_{\langle i,j \rangle} \sigma_i \sigma_j = \frac{J_{\text{eff}}}{2} \sum_{\alpha} |\mathbf{L}_\alpha|^2 + c \,. \tag{4.3}$$

This means that, due to the local single ion anisotropy, any coupling J is mapped to an effective coupling $J_{\text{eff}} = -J/3$. This reveals a first surprise in the physics of spin ice: while geometric frustration is generally associated with antiferromagnetism ($J > 0$), such a spin-spin coupling in spin ice yields only two ground states related by a global spin inversion symmetry with all spins pointing in or all out any reference tetrahedron ($\mathbf{L}_\alpha = \sum_{i \in \alpha} \sigma_i = \pm 4$), and, upon cooling the system, a second order phase transition in the unfrustrated three-dimensional Ising universality class occurs [49, 114].

In the particular case of spin ice, surprisingly, *ferromagnetism* ($J < 0$) leads to the minimal energy condition that $\mathbf{L}_\alpha = 0$ for all tetrahedra which ultimately causes massive frustration[1]. Indeed, the Curie–Weiss temperature of $Ho_2Ti_2O_7$ was found to be positive, $\Theta_{\text{CW}} \approx +1.9$ K, indicating overall ferromagnetic spin interactions, while no development of long range order was neither found in neutron scattering experiments down to a temperature four times lower [22] nor in muon spin relaxation (μSR) measurements down to 0.05 K [120].

---

[1] *'It would be no understatement to say that this observation came as a surprise; indeed, in the months after our initial discovery of spin ice both of us witnessed frequently the shock which this counter-intuitive result would cause in audiences, as we presented our findings.'*, S. Bramwell and M. Harris [117].

The condition $\mathbf{L}_\alpha = 0$ that requires two spins to point into each tetrahedron while the remaining two spins point out of it, leads to the same degree of frustration as already discussed in the context of water ice [9] and the Ising antiferromagnet on the pyrochlore lattice [7]. Therefore, following the heuristical reasoning of Pauling [9] in the case of water ice, one expects exactly the same residual entropy per spin in spin ice as in water ice: of all $2^4 = 16$ possible configurations on a single tetrahedron, $\binom{4}{2} = 6$ fulfill this condition, which is a fraction of $3/8$. This yields $W = 2^{N_S}(3/8)^{N_S/2}$ possible ground states for a lattice consisting of N_S spins and hence $N_C = N_S/2$ tetrahedra leading to a residual ground state entropy per spin of $S_0/N_S = \frac{1}{2}\ln\frac{3}{2}$. This exact correspondance to the physics of proton ordering in water ice with a macroscopic number of minimal energy configurations, where each oxide ion is tetrahedrally coordinated with two covalently bonded ("near") protons and two hydrogen bonded ("far") protons [72] (as visualized in Fig. 4.2), is why the 2-in/2-out rule in spin ice is also commonly called the *ice rule*.

Remarkably, A. Ramirez et al. found direct experimental evidence for exact this zero point entropy in the spin ice compound $Dy_2Ti_2O_7$ by measurements of the specific heat $c_V(T)$. They integrated the specific heat between $T_1 = 300$ mK in the spin ice regime and $T_2 = 12$ K in the paramagnetic regime, where the molar entropy is known to be $R\ln 2$ for two possible spin orientations per degree of freedom (where R is the molar gas constant). By applying Eq. (2.8), they were able to show that $Dy_2Ti_2O_7$ has, within a few percent [8], indeed the same zero point ground state entropy as water ice (cf. Fig. 4.3) and thus confirmed the existence of an ice rule obeying spin ice state in this compound [115, 121]. More recent specific heat measurements on $Dy_2Ti_2O_7$ lead to to a even better agreement between the experimental residual entropy and the Pauling estimate [122]. Similar evidence for $Ho_2Ti_2O_7$ is documented in Refs. [123, 124].
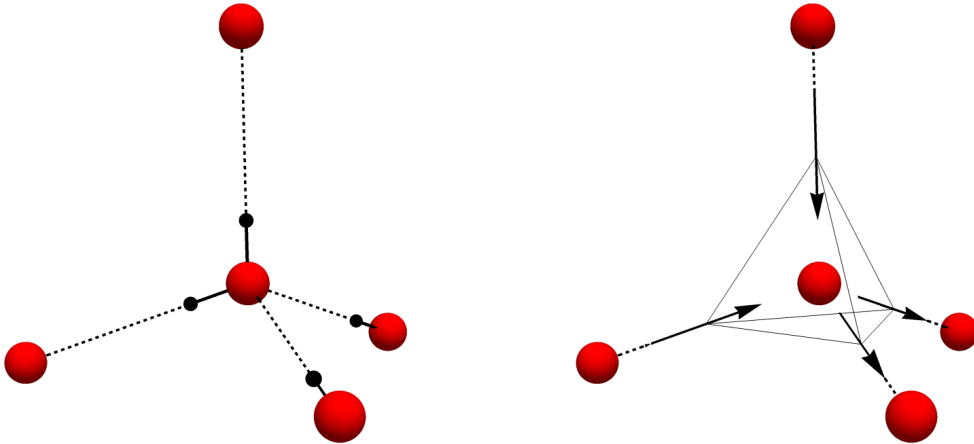
Figure 4.2 – **Analogy between water ice and spin ice.** Left: Low-energy configuration of water ice where each oxide ion (large red circles) is tetrahedrally coordinated with two covalently bonded ("near") protons (black dots connected by a solid black line) and two hydrogen bonded ("far") protons (connected by a dashed black line). Right: The left picture translates into the "two-in/two-out" ground state configuration in spin ice when the far protons are depicted as arrows pointing outwards and the near protons are depicted as arrows pointing inwards the tetrahedron spanned by the centers of the lines that connect two neighboring red circles [125].
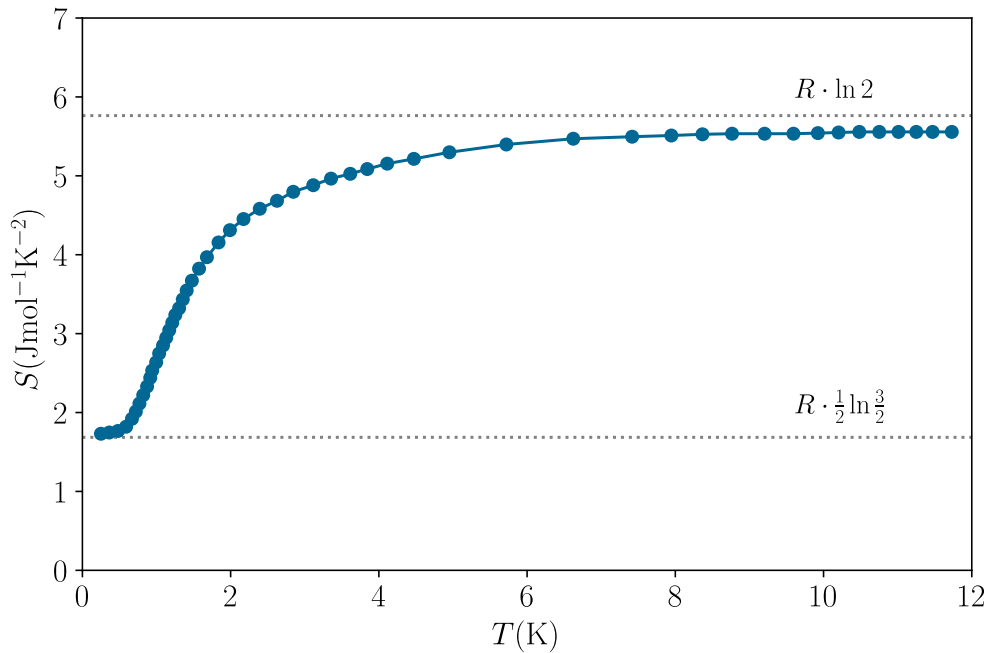
Figure 4.3 – **Entropy of the spin ice compound $Dy_2Ti_2O_7$.** The molar zero point entropy as found by integrating experimental specific heat data by A. Ramirez et al. coincides within a few percent with the entropy of water ice and the Pauling estimate $R \cdot \frac{1}{2} \ln \frac{3}{2}$ (Eq. (2.7)). The high temperature limit of $R \cdot \ln 2$ corresponds to independently fluctuating spins with two possible directions. Data extracted from [115] and figure reproduced with permission from Springer Nature.

4.2 Dipolar Spin Ice Model

We have shown that the nearest-neighbor spin ice model of Eq.(4.3) is already a surprisingly good approximation that is able to qualitatively explain the presence of spin ice phenomenology: the local $\langle 111 \rangle$ anisotropy due to the strong crystal field in combination with nearest-neighbor spin-spin interactions yields an effective Ising antiferromagnet with a macroscopic residual Pauling entropy as well as the ferromagnetic sign of the experimentally observed Curie-Weiss constant.

However, it turns out that both, Ho^{3+} and Dy^{3+}, carry large magnetic moments μ of approximately $10\,\mu_B$ [126]. Therefore, these systems have a magnetic dipole-dipole interaction of about

$$D = \frac{\mu_0 \mu^2}{4\pi r_{nn}^3} \tag{4.4}$$

with $D \approx 1.41$ K at the nearest-neighbor distance $r_{nn} \approx 3.5$ Å, which is comparable to Θ_{CW} and the same order of magnitude as the exchange energy.

Thus, it surprises that the long range, proportional to r^{-3} decaying, and complex nature of the dipolar interactions does not lift the ground state degeneracy in spin ice and induce long range order at some critical temperature $T_N \sim D$. Siddharthan et al. were the first to emphasize their influence, suggesting the dipolar origin of the effective ferromagnetic nearest-neighbor coupling in $Ho_2Ti_2O_7$, with the exchange coupling between Ho^{3+} ions actually being antiferromagnetic, which in themselves would indeed drive the system into a long range ordered state [127]. To see how this is possible, we introduce the dipolar spin ice model (DSI) [126, 128, 129],

which adds a long range dipolar interaction part $\mathcal{H}_{\mathrm{DD}}$ to the NNSI model:

$$\mathcal{H}_{\mathrm{DSI}} = \mathcal{H}_{\mathrm{NNSI}} + \mathcal{H}_{\mathrm{DD}} = J \sum_{\langle i,j \rangle} \mathbf{S}_i \cdot \mathbf{S}_j + D r_{\mathrm{nn}}^3 \sum_{i,j} \left[\frac{\mathbf{S}_i \cdot \mathbf{S}_j}{|\mathbf{r}_{ij}|^3} - \frac{3(\mathbf{S}_i \cdot \mathbf{r}_{ij})(\mathbf{S}_j \cdot \mathbf{r}_{ij})}{|\mathbf{r}_{ij}|^5} \right] . \tag{4.5}$$

where $\mathbf{r}_{ij}$ is the vector connecting spins $\mathbf{S}_i$ and $\mathbf{S}_j$, and $\mathbf{S}_i = \sigma_i \hat{\mathbf{z}}_i$ are, again, three component unit vectors composed of a local $\langle 111 \rangle$ axis $\hat{\mathbf{z}}_i$ and an Ising variable σ_i, and with a magnetic moment $\mu_i = \mu \mathbf{S}_i$, whose magnitude μ is absorbed in the definition of the dipolar interaction strength D. Rewritten in terms of the Ising variables σ_i and using that $\hat{\mathbf{z}}_i \cdot \hat{\mathbf{z}}_j = -\frac{1}{3}$ for all neighboring i and j as well as $(\hat{\mathbf{z}}_i \cdot \mathbf{r}_{ij})(\hat{\mathbf{z}}_j \cdot \mathbf{r}_{ij}) = -\frac{2}{3} r_{\mathrm{nn}}^2$, the DSI Hamiltonian can be split into an effective nearest-neighbor part and a part in which all dipole-dipole interactions beyond the nearest-neighbor distance r_{nn} are absorbed:

$$\mathcal{H}_{\mathrm{DSI}} = \mathcal{H}_{\mathrm{DSI}}^{\mathrm{nn}} + \mathcal{H}_{\mathrm{DSI}}^{> \mathrm{nn}} \tag{4.6}$$

with

$$\mathcal{H}_{\mathrm{DSI}}^{\mathrm{nn}} = \left(-\frac{J}{3} + \frac{5D}{3} \right) \sum_{\langle i,j \rangle} \sigma_i \sigma_j = J_{\mathrm{eff}} \sum_{\langle i,j \rangle} \sigma_i \sigma_j , \tag{4.7}$$

where

$$J_{\mathrm{eff}} = J_{\mathrm{nn}} + D_{\mathrm{nn}} \tag{4.8}$$

is the effective nearest-neighbor coupling consisting of an exchange part $J_{\mathrm{nn}} = -J/3$ and a dipolar part $D_{\mathrm{nn}} = 5D/3$ with positive D. This reveals a second surprise in the physics of spin ice: remarkably, this means that the dipolar interactions are not only compatible with the existence of spin ice phenomenology, but in fact they appear to be *responsible* for it, given the antiferromagnetic ($J > 0$ and $J_{\mathrm{nn}} < 0$) exchange interaction in $Dy_2Ti_2O_7$ and $Ho_2Ti_2O_7$—provided the effective interaction is ferromagnetic ($J_{\mathrm{eff}} > 0$) overall. The condition

$$J_{\mathrm{eff}} > 0 \Leftrightarrow 5D > J \tag{4.9}$$

is thus a simple criterion to weigh up whether a system displays a degenerate spin ice state, or one has two unique Néel ordered ground states related by global spin inversion that correspond to all spins pointing in or out each tetrahedron. This criterion is fulfilled by both reference spin ice materials, $Dy_2Ti_2O_7$, and $Ho_2Ti_2O_7$, respectively (see Table 4.1). Note that taking into account the dipolar interactions in the DSI model only up to a finite truncation radius r_{trunc} may lead to a degeneracy lifting. But calculations using mean-field theory [130–132] as well as Monte Carlo simulations [129]—carefully including the infinite range of dipolar interactions by the Ewald method (cf. Appendix B)—have shown that by going from the effective nearest-neighbor DSI

Compound	J	J_{nn}	D	D_{nn}	J_{eff}	μ/μ_B
$Dy_2Ti_2O_7$ [126]	3.72	-1.24	1.41	2.35	1.11	9.866
$Ho_2Ti_2O_7$ [123]	1.56	-0.52	1.41	2.35	1.83	9.866

Table 4.1 – **Interactions strengths.** Exchange and dipolar interactions as well as effective nearest-neighbor energy scales in $Dy_2Ti_2O_7$ and $Ho_2Ti_2O_7$ given in Kelvin, and the respective magnetic moments in units of μ_B.

to true long range dipole-dipole interactions, spin ice degeneracy is almost completely recovered as $r_{trunc} \to \infty$ by some kind of self-screening mechanism of the dipolar interactions. These calculations also showed that the threshold between systems with long range order and spin ice is only slightly modified to approximately $4.53D = J$ in the limit of infinitely long range dipolar interactions. That means that the full beyond-nearest-neighbor interaction, $\mathcal{H}_{DSI}^{>nn}$, acts only very weakly to stabilize Néel order to the detriment of the degenerate spin ice manifold.

Finally we would like to point out that the relevance of the DSI eventually became clear not least because it successfully accounts for discrepancies between experimental neutron scattering patterns and calculated scattering intensities in the NNSI model, as illustrated in Fig. 4.4. What is remarkable about the DSI model is that it can not only elegantly explain the surprising qualitative success of the NNSI model in understanding spin ice physics through the interplay of antiferromagnetic nearest-neighbor exchange and effectively ferromagnetic nearest-neighbor dipole-dipole interactions, but at the same time it also shows that the long range dipolar interactions are indispensable for the quantitative understanding of various aspects of spin ice.
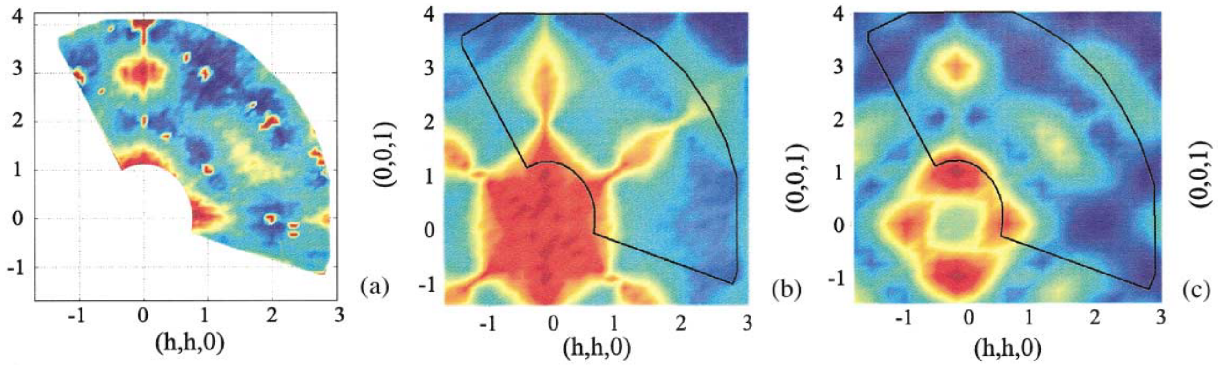
Figure 4.4 – **Neutron scattering patterns of $Ho_2Ti_2O_7$.** (a) Experimental neutron scattering results at $T = 50$ mK with dark blue regions representing low intensity and red regions representing high intensity. Main features are intense scattering around $(0, 0, 0)$ and $(0, 0, 3)$ and a broad region with weaker scattering around $(3/2, 3/2, 3/2)$, connected by narrow necks that resemble bow-ties. Interestingly, qualitatively similar scattering patterns have been observed in water ice [133]. (b) and (c) show numerically calculated neutron scattering intensities for the NNSI model Eq. (4.3), and the DSI model Eq. (4.5), respectively (the solid line indicates the region of experimental data in (a)). The main features of the experimental pattern are reproduced successfully by both models, but the DSI model reproduces the features qualitatively and quantitatively much better. Reprinted with permission from Ref. [123]. Copyright (2001) by the American Physical Society.

4.3 Magnetic Monopoles in Spin Ice

So far we have only considered spin ice with globally obeyed ice rules, that is two spins pointing in and two spins pointing out each and every tetrahedron. One of the most impressive and interesting aspects of spin ice, however, is revealed when one asks what excitations are in this system. It turns out that spin ice is a prime example of a Coulomb phase (see Sec. 2.6), where the local constraint leading to the zero divergence condition of the emergent flux vector field $\mathbf{P(r)}$ is precisely the ice rule, that is, each node of $\mathcal{B}$ carries two incoming and two outgoing fluxes[2].

---

[2]Recall from Sec. 2.6 that $\mathbf{P(r)}$ is defined on the parent diamond lattice $\mathcal{B}$ that is formed by the midpoints of the tetrahedra of the medial pyrochlore lattice $\mathcal{L}$

If now a single spin is flipped, one of this fluxes is reversed, breaking the ice rule in the two adjacent tetrahedra the spin belongs to, and thus creating two defects in form of nodes on $\mathcal{B}$ with three ingoing and one outgoing flux and vice versa. The defects are therefore sources and sinks of the flux field $\mathbf{P}(\mathbf{r})$. Notably, these fractionalized defects are *deconfined*: flipping further spins along a *Dirac string* separates the defects without further energy costs, connected by a Dirac string (cf. Fig. 4.5). Remarkably, the defects can be considered effective magnetic monopoles.

In the above defect picture, we did not refer to the magnetic moment μ of the spins. Adding these is conveniently best done pictorially similar to the way an electric dipole is composed of two electric charges: by replacing the dipole moment of a spin situated on the vertices of the pyrochlore lattice $\mathcal{L}$ by two separated *magnetic* charges sitting on the nodes of the diamond lattice $\mathcal{B}$. In order to reproduce the value of the magnetic moment μ of the rare earth ions correctly in this *dumbbell model* [14, 27], the magnetic charges need to take values of $q = \pm\mu/r_D$ where r_D is the distance between two neighboring charges. Consequently, each center of a tetrahedron is occupied by four charges, which either sum up to a total magnetic charge of $Q = 0$ when the ice rule is fulfilled, or to $Q = \pm 2\mu/r_D$, when a spin is flipped such that three spins point into the tetrahedron and one out, or vice versa. Intriguingly, since the spins in the DSI model interact with each other through dipolar interactions, the magnetic charges at the centres of the tetrahedra in the dumbbell picture must interact through an effective magnetic Coulomb interaction and behave like classical magnetic monopoles. Therefore, for pairs of monopoles with charges Q_α and Q_β (sitting on the nodes α and β of the diamond lattice formed by the midpoints of the tetrahedra), separated by a distance $r_{\alpha\beta}$ through subsequent flips of neighboring spins, the energy of the system can be described (up to corrections $\mathcal{O}(r^{-5})$) [27] by translating the DSI Hamiltionian to

$$\mathcal{H} = \frac{\mu_0}{4\pi} \sum_{\alpha < \beta} \frac{Q_\alpha Q_\beta}{r_{\alpha\beta}} + \frac{\nu_0}{2} \sum_\alpha Q_\alpha^2. \tag{4.10}$$
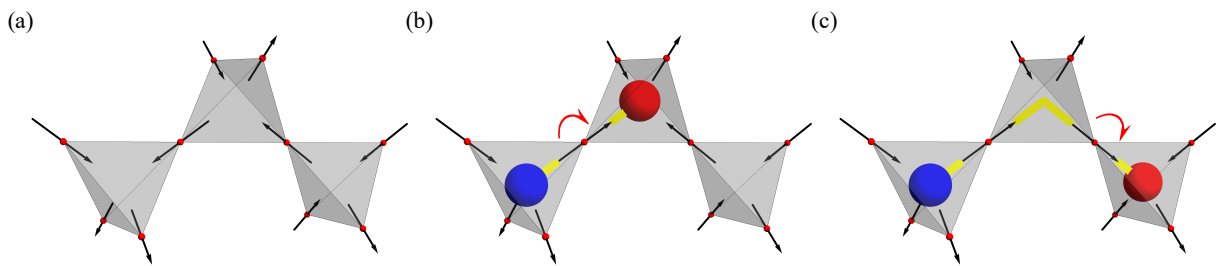
Figure 4.5 – **Emergent monopoles in spin ice.** (a) A section of a pyrochlore lattice obeying the ice rules in each tetrahedron. (b) The spin sitting on the vertex connecting the left and the middle tetrahedron is flipped leading to a 1-in/3-out configuration on the left tetrahedron and a 3-in/1-out configuration on the middle tetrahedron, both violations of the ice rule and therefore of the divergence-free condition of the flux vector field. This can be interpreted as an emerging pair of magnetic monopoles sitting at the centers of the two neighboring tetrahedra connected by the spin that was flipped. (c) The same situation as before, but now with a second spin being flipped, namely the one sitting on the vertex connecting the middle and the right tetrahedron. This spin flip restores the ice rule on the middle tetrahedron but leads to a violation of it (3-in/1-out) on the right tetrahedron. As both configurations have the same energy, this process can be interpreted as deconfined magnetic monopoles moving apart without energy cost, connected by a Dirac string (yellow line) [125].
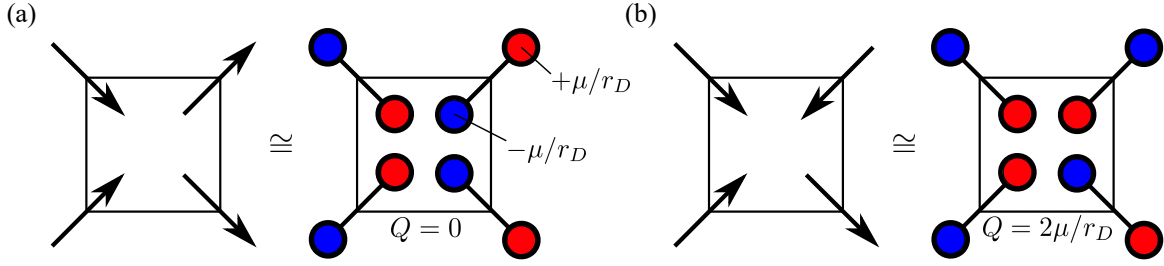
Figure 4.6 – **Dumbbell model of magnetic charges.** (a) Left: Schematic projection of a tetrahedron obeying the ice rule. Right: Each magnetic moment μ can be decomposed into two magnetic charges $q = \pm \mu / r_D$ sitting on the ends of a dumbbell. In the case of two spins pointing inwards and two outwards, the four charges in the tetrahedron sum up to $Q = 0$. (b) If one spin is flipped such that three spins point inwards, the tetrahedron is no longer charge neutral, but has a net magnetic charge of $Q = 2\mu / r_D$.

Here, the second term with

$$\nu_0 \left(\frac{\mu}{r_D} \right)^2 = \frac{J}{3} + \frac{4}{3} \left(1 + \sqrt{\frac{2}{3}} \right) D \tag{4.11}$$

is added in order to include the nearest-neighbor exchange interaction correctly [14]. Note, that large enough ν_0 enforces $Q_\alpha = 0$ for all α which is simply a reformulation of the ice rule.

We have thus seen that the dipolar spin ice model and the dumbbell model both reconstruct spin ice physics and that topological defects in the former can be viewed as emerging magnetic monopoles via the latter—which can ultimately even be observed in experiments [24, 28–31]. We will now see how the density of such monopoles can be tuned by an external magnetic field and what effects this entails.

4.4 Magnetic Field Effects: Kagome Ice and Monopole Liquid-Gas Transition

In this section we briefly want to review how an externally applied magnetic field can act as a chemical potential favoring the creation of magnetic monopoles. To that end, we add a magnetic field $\mathbf{H} = H\hat{\mathbf{n}}$ to the DSI Hamiltonian of Eq. (4.5) via

$$\mathcal{H}_{\mathrm{H}} = -\mu \sum_i \mathbf{S}_i \cdot \mathbf{H} \,. \tag{4.12}$$

Due to the strong single ion anisotropy, an external magnetic field can couple in various different ways to the rare earth magnetic ions depending on its orientation. Magnetic fields along the principal axes [100] and [110] break the macroscopic ground state degeneracy and remove the residual entropy of the spin ice state at $H = 0$ relatively quickly [134–137] by forming long range ordered $\mathbf{q} = 0$ and $\mathbf{q} = X$ states, respectively, both satisfying the ice rules [129], as illustrated in Fig. 4.7.

Of particular interest, on the other hand, it is to consider the case of $\hat{\mathbf{n}} \parallel$ [111]. To get a better idea of what happens when a magnetic field is applied along the global [111] crystal direction, it is convenient to think of the pyrochlore lattice as an assembly of stacked kagome layers along that very crystal direction, with alternating triangular layers in between, so that

(a)

[100]

(b)

[110]

q = 0

q = X
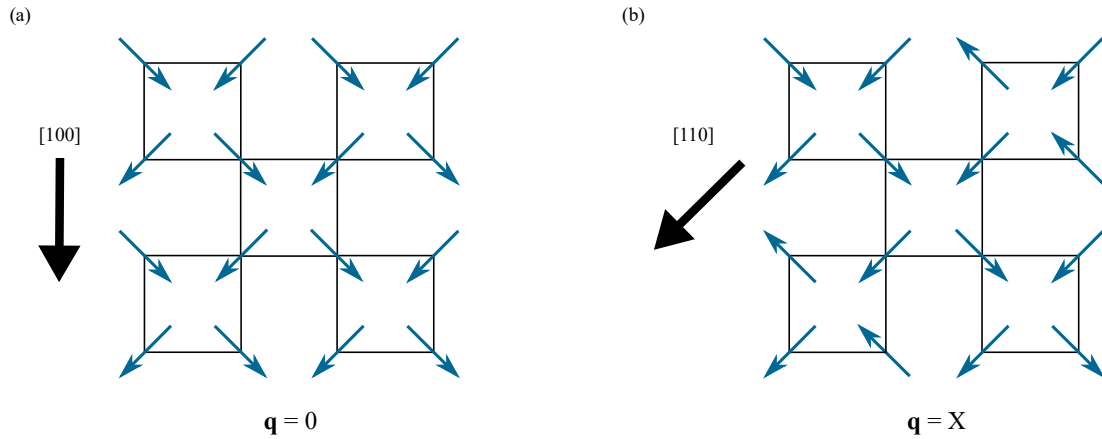
Figure 4.7 – **q** = 0 **and q** = X **states.** Schematic projections of the pyrochlore unit cell down the z-axis. For external magnetic fields applied along the principal axes (a) [100], and (b) [110], spin ice has unique, ice rule obeying ground states.

each triangle of a kagome plane is decorated with an extra spin from a triangular layer above or below, which together form exactly one tetrahedron of the pyrochlore lattice, cf. Fig. 4.8.

If a field is applied along the global [111] axis, all spins couple to the field, i.e., they have a non-zero dot product in Eq. (4.12), whereby the local anisotropy axes of a quarter of the spins—namely of those on the triangular layers—and the magnetic field are collinear while the remaining spins have a component of the magnetic moment along the [111] field direction a third smaller. As a result, spin ice evolves to a fully polarized state in two steps.

Firstly, these triangular layer spins are subject to the highest Zeeman energy and will align with the magnetic field first upon increasing the magnetic field strength, whereas the other spins remain free to fluctuate on the effectively decoupled kagome layers such that the ice rule will still be satisfied globally for intermediate fields, where a competition between the exchange, dipolar, and the magnetic field part in the Hamiltonian is expected.

[111]

Kagomé layer

Triangular layer

Kagomé layer

Triangular layer
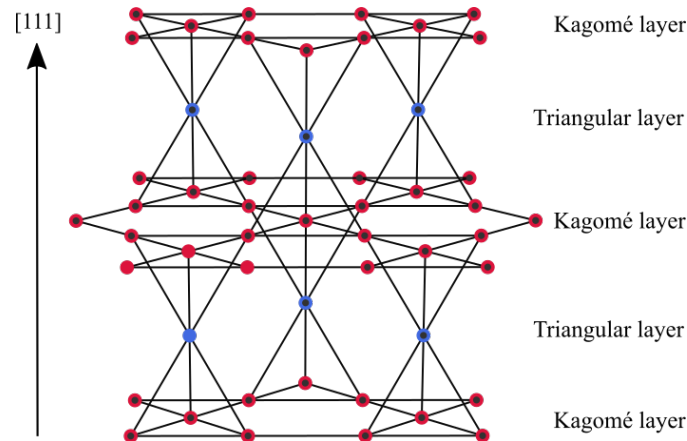
Kagomé layer

Figure 4.8 – **The pyrochlore lattice as an assembly of stacked kagome layers** (red) along along the global cubic [111] direction, with alternating triangular layers (blue) in between, so that each triangle of a kagome plane is decorated with an extra spin from a triangular layer above or below, which together form exactly one tetrahedron of the pyrochlore lattice [125].

From the discussion in Sec. 2.6 we know that a single kagome layer consists of corner-sharing triangles and for the ice rule being obeyed, the triangles may either have a 1-in/2-out configuration or a 2-in/1-out configuration, each being threefold degenerate. This *modified* ice rule can be mapped to the problem of covering the hexagonal lattice with hardcore dimers, which allows an analytical calculation of the reduced residual entropy of this state of about 40% of the zero-field spin ice state [138, 139], in good agreement with experimental results [140]. Under projection of the intra-layer spins onto the kagome layers, the planar system is equivalent to the two-dimensional kagome ice model presented by Wills, Ballou, and Lacroix [78], hence giving this macroscopically degenerate state its name *kagome (spin) ice* (KI).

The magnetization per spin m along the [111] direction in this regime can be easily derived by considering a single tetrahedron with its triangular layer spin pinned by the magnetic field plus two kagome layer spins having components aligned with the field and one spin with component aligned against it. Using the definition of the local anisotropy axes from Eq. (4.2), this yields a magnetization plateau with a value of

$$
\begin{aligned}
m_{\mathrm{KI}} &= \frac{\mu}{4}\left(+\hat{\mathbf{z}}_1 - \hat{\mathbf{z}}_2 - \hat{\mathbf{z}}_3 + \hat{\mathbf{z}}_4\right) \cdot \hat{\mathbf{z}}_{[111]} \\
&= \frac{\mu}{4\sqrt{3}}\left(+[1\bar{1}\bar{1}] - [\bar{1}1\bar{1}] - [\bar{1}\bar{1}1] + [111]\right) \cdot \frac{1}{\sqrt{3}}[111] \\
&= \frac{\mu}{3}\,.
\end{aligned}
\tag{4.13}
$$

In a second step, at larger field strengths (of about 1 T for $Dy_2Ti_2O_7$ [141] and 1.7 T for $Ho_2Ti_2O_7$ [82]), when the Zeeman energy dominates the exchange and dipolar interactions, the ice rules will eventually be broken into 3-in-1-out configurations (or vice versa) since then all spins will have a positive projection onto the field. The resulting state is fully ordered with maximal polarization along the field. Thus the residual ground state entropy is expected to disappear and the magnetization per spin can be calculated as

$$
\begin{aligned}
m_{\mathrm{polarized}} &= \frac{\mu}{4}\left(-\hat{\mathbf{z}}_1 - \hat{\mathbf{z}}_2 - \hat{\mathbf{z}}_3 + \hat{\mathbf{z}}_4\right) \cdot \hat{\mathbf{z}}_{[111]} \\
&= \frac{\mu}{4\sqrt{3}}\left(-[1\bar{1}\bar{1}] - [\bar{1}1\bar{1}] - [\bar{1}\bar{1}1] + [111]\right) \cdot \frac{1}{\sqrt{3}}[111] \\
&= \frac{\mu}{2}\,.
\end{aligned}
\tag{4.14}
$$

Both, the saturation of the magnetization and the disappearance of the residual entropy, have been confirmed experimentally [124, 136, 142]. As we have seen before, breaking the ice rule leads to magnetic point defects. Hence going from the kagome ice to the fully polarized phase is accompanied by a drastic increase of the magnetic monopole density—which is also well illustrated by the monopole density per tetrahedron from Monte Carlo simulations as a function of temperature and magnetic field shown in Fig. 4.9(c). Therefore, an external magnetic field along the crystallographic [111] axis can indeed be considered as an chemical potential for the magnetic monopoles

To illustrate this two step evolution from spin ice via kagome ice to a fully polarized state, we show results of Monte Carlo simulations of the DSI model Eq. (4.5), with model parameters of $Dy_2Ti_2O_7$ (cf. Tab. 4.1), where the full dipolar interactions are carefully taken into account by using the Ewald simulation technique (see Appendix B for details), in Fig. 4.9.
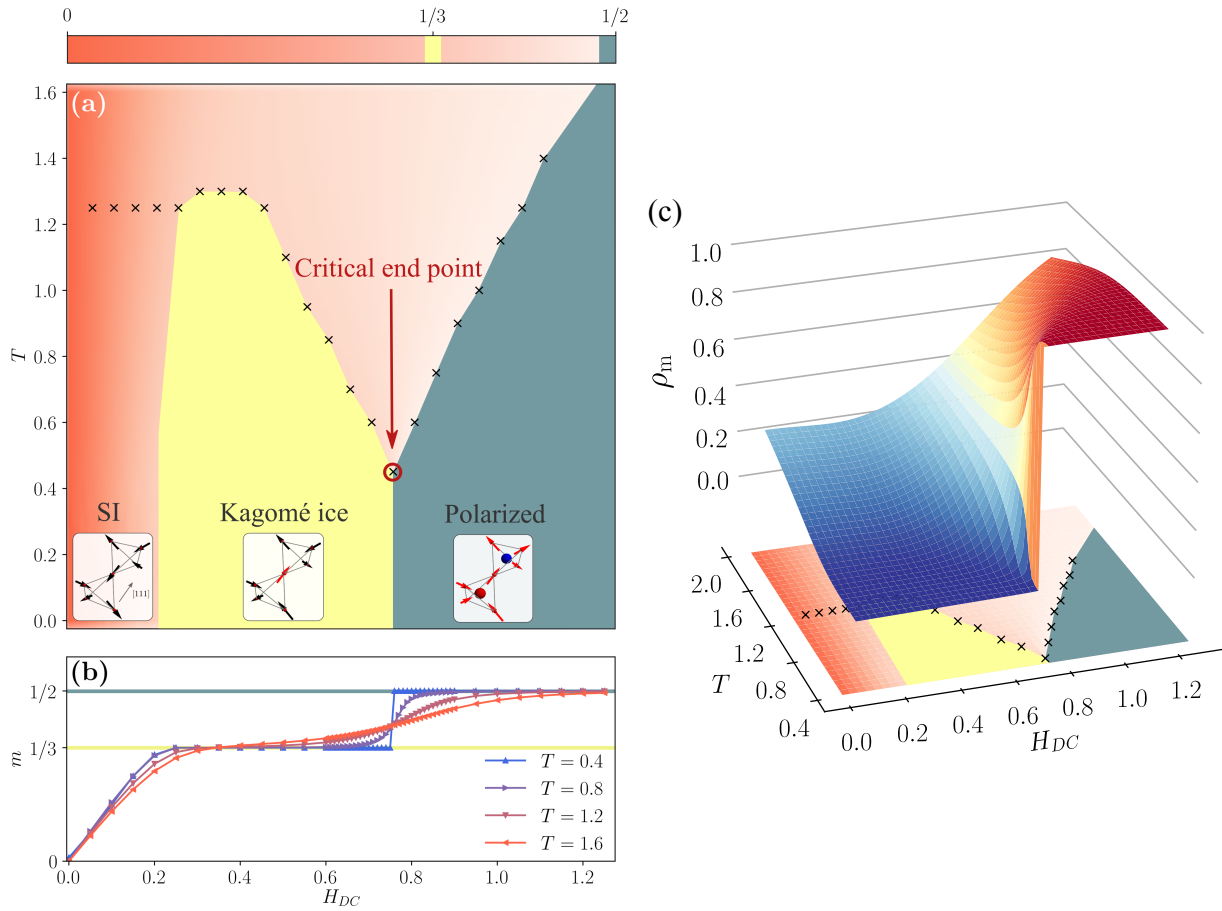
Figure 4.9 – **Phase diagram and monopole density of spin ice in a magnetic field.** (a) Monte Carlo data of spin ice in a static external magnetic field along the crystallographic [111] direction (in units of Tesla) shows a rich phase diagram. The colormap encodes magnetization data (in units of μ) whereas black crosses indicate peaks in the specific heat. At low temperatures, two magnetization plateaus can be observed which correspond to the kagome ice phase ($m = 1/3$) and the polarized phase ($m = 1/2$). The transition from the spin ice phase (at $H_{DC} = 0$) into the kagome ice phase can be described by aligning one of the four spins (see red spin in inset) on each tetrahedron with the external field while still preserving the ice rules. A further increase in field breaks the ice rules and aligns all spins with the external field, yielding the polarized phase. This sequence is also depicted in the insets of panel (a) where spins that are pinned by the magnetic field are colored in red. The transition between kagome ice and the polarized phase is of first order up to a critical end point above which the transition occurs in a crossover. This change of behavior can also be seen in panel (b) where cuts of the magnetization are shown as function of the external field. (c) The corresponding monopole density per tetrahedron ρ_m as a function of temperature and magnetic field. Figure taken from [U1].

In line with previous experimental [136, 141, 143, 144] and numerical [27] results, the magnetization and specific heat data shown in Fig. 4.9 reveal a rich phase diagram. For low field strengths, the triangular spins start to align with the field and the magnetization immediately starts to build up up to the first plateau value of the KI regime, m_{KI}. Furthermore, and even more remarkably, we see that the ice rule-breaking spin flip that turns kagome ice to the fully polarized phase occurs in a liquid-gas type transition: below some critical temperature T_c, the magnetization as a function of the external magnetic field strength along the [111] direction, H_{DC}, jumps from the KI regime value, m_{KI}, to the value of the fully polarized phase, $m_{\mathrm{polarized}}$. This line of first order transitions ends at a critical end point $(H_{\mathrm{DC}}, T_c)_{\mathrm{MC}} \approx (0.75, 0.48)$ which slightly deviates from the experimental values $(H_{\mathrm{DC}}, T_c)_{\mathrm{exp}} \approx (0.91, 0.36)$ which can be attributed to finite size effects in numerics and further-neighbor interactions in real materials [27]. At higher tempera-

tures, there is a continuous crossover regime between the low monopole density KI ("gas") phase and the high monopole density polarized ("liquid") phase, implying that there is no symmetry breaking between the two phases. This makes spin ice one of the the very few experimentally known instances of such a transition in localized spin systems [144].

4.5 Monopole Dynamics in Spin Ice

Now that we have established the general phase diagram of spin ice with its low- and high-monopole density phases with a magnetic field applied along the [111] crystallographic direction, we can turn to the main topic of this chapter—the dynamics of these magnetic monopoles in a magnetic DC field. As a final preparation for this, we briefly summarize what is known about dynamics in spin ice so far and what is ultimately the motivation for the studies carried out within the framework of this thesis.

In addition to various possible experimental methods such as neutron scattering [145], muon spin resonance (μSR) [146], or nuclear magnetic resonance (NMR) [147], the main method of choice for gaining insights into spin dynamics is AC susceptibility measurements. This method has been applied numerous times to $Ho_2Ti_2O_7$ and $Dy_2Ti_2O_7$ [148–159], revealing a quite unique behavior of the zero DC field relaxation time $\tau(T)$ which can be roughly described by three different temperature regimes. At high temperatures above 12 K, the relaxation can effectively be explained by an Arrhenius law $\tau(T) = \tau_0 \exp(E/T)$ with an energy barrier $E = 200 - 300$ K due to thermal excitations of higher crystal field levels [160]. For intermediate temperatures between approximately 2 and 10 K, the spin relaxation time flattens and is almost constant. This regime is described in terms of annihilation and creation of monopoles and their diffusive motion [29]. Below 2 K, $\tau(T)$ increases again as spin ice is formed. In this regime, spin relaxation can again be described by an Arrhenius law, but with a much lower energy ($E \approx 6.6$ K for $Dy_2Ti_2O_7$ [35]). Finally, below about 0.6 K—which is above T_c of the critical end point—spin ice freezes and relaxation becomes too long to be measured experimentally and also numerically. Fig. 4.10 illustrates this typical profile of $\tau(T)$ between 0.8 and 17 K on the example of $Dy_2Ti_2O_7$.
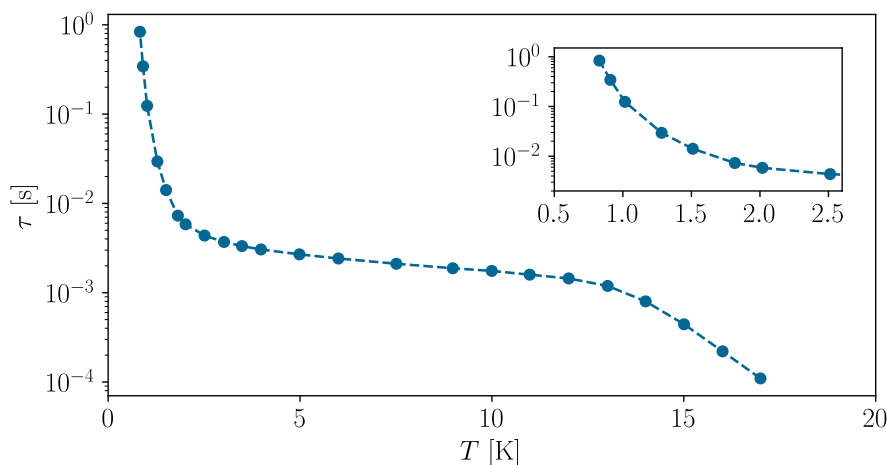

Figure 4.10 – **Experimental spin relaxation time.** Temperature dependence of $\tau(T)$ in the spin ice compound $Dy_2Ti_2O_7$ obtained by AC susceptibility measurements. The temperature regime of spin ice relevant for this thesis is shown in the inset. Data taken and figure reproduced with permission from Ref. [153]. Copyright (2004) by the American Physical Society.

Much less is known about the dynamics of spin ice in DC magnetic fields, especially near the critical field so that the critical end point has not been approached very closely by AC susceptibility measurements. Takatsu et al. studied the dynamics of $Dy_2Ti_2O_7$ in a magnetic DC field applied along the [111] direction, where excitations can be regarded as monopoles restricted to effective two-dimensional kagome layers [34, 106]. The motion of these monopoles was studied by AC susceptibility measurements in an additional magnetic AC field along the [11$\bar{2}$] direction, i.e. perpendicular to [111]. Their measurements at $T = 1$ K $\gg T_c \approx 0.36$ K showed that the relaxation strongly depends on the DC field strength. While in the crossover of spin ice to kagome ice between 0 T and 0.4 T the monopole dynamics is slowed down, relaxation becomes significantly faster—beyond the measurement limit—upon approaching the critical field from either side, signifying a *critical speeding up* of monopole dynamics that can be interpreted as a change from independent diffusive monopole motion to a collective phenomenon or as diffusively moving monopoles with highly increased hopping rate.

The fact that there is ultimately more information about the monopole dynamics near the critical end point is due to an important consequence of the existence of emergent magnetic monopoles, that was pointed out by D. Khomskii [161] after some early experimental indications [162]: a redistribution of the electric charge depending on the spin configuration causes the formation of spontaneous electric dipole moments in the case of 3-in-1-out or 1-in-3-out tetrahedra, i.e. in the presence of magnetic monopoles. A different mechanism for the formation of electric dipole moments in the presence of magnetic monopoles was proposed in Ref. [163]. Both explanations lead to the same striking consequence that magnetic monopole dynamics contribute to the dielectric response function $\epsilon(\nu)$ [164]. Grams et al. [165] have taken advantage of this and performed spectroscopic measurements of $\epsilon(\nu)$ in $Dy_2Ti_2O_7$ in a magnetic DC field along the [111] direction down to 200 mK. Fig. 4.11 shows the temperature and magnetic field dependence of the loss peak frequency $\nu_p = (2\pi\tau)^{-1}$ of the relaxation spectrum, which is fastest at the critical end point of the monopole liquid gas transition and forms a fan-shaped region above the critical end point.
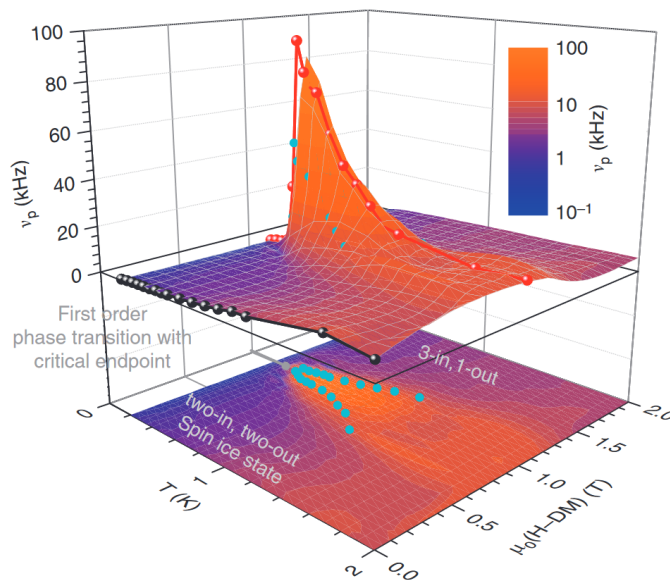
Figure 4.11 – **Peak frequency of the dielectric loss spectra.** Loss peak frequency obtained by spectra of the dielectric function as a function of temperature and magnetic field exposing a sharp peak at the critical point. Figure taken from [165] and reprinted with permission from Springer Nature.

We recall (see discussion in Sec. 3.3.2) that the relaxation time is related to the correlation length by some dynamical exponent z as $\tau \propto \xi^z$, and that at the critical field the correlation length diverges as $\xi \propto |T - T_c|^{-\nu}$ with a positive exponent $\nu > 0$. Combining these relations leads to

$$\left. \frac{1}{\tau(T)} \right|_{H=H_c} = 2\pi \nu_{\mathrm{p}}(T) \Big|_{H=H_c} \propto |T - T_c|^{\nu z} \, . \tag{4.15}$$

Therefore, the sharp peak in ν_{p} signifies a negative dynamical exponent ($\nu z \approx -0.7$ [165]) quite contrary to the usual positive dynamical exponent leading to the canonical behavior of critical slowing down, which, similar to the results of Ref. [106], implies a critical speeding up of the dynamics close to the liquid-gas transition.

4.6 Dynamics in Spin Ice: Numerical Results

Having reviewed what is known about dynamics in spin ice experimentally, we will now move on and discuss the results of dynamical Monte Carlo simulations of spin ice and whether they can reproduce the experimentally observed critical slowing down. To that end, we simulate the DSI model of Eq. (4.5) with model parameters of $Dy_2Ti_2O_7$ (as in Tab. 4.1), where the full dipolar interactions are again incorporated via the Ewald simulation technique (cf. Appendix B). In addition, we add a magnetic field that consists of a static part and an AC part,

$$\mathbf{H}(t_{\mathrm{MC}}) = \mathbf{H}_{\mathrm{DC}} + \mathbf{H}_{\mathrm{AC}}(t_{\mathrm{MC}}) = H_{\mathrm{DC}}\hat{\mathbf{n}}_{\mathrm{DC}} + H_{\mathrm{AC}}\sin(\omega t_{\mathrm{MC}})\hat{\mathbf{n}}_{\mathrm{AC}} \, , \tag{4.16}$$

in order to measure spectra of the AC susceptibility as described in Sections 3.4.2 and 3.4.3, for DC fields from zero beyond the critical field (fixed along $\hat{\mathbf{n}}_{\mathrm{DC}} = [111]$) and AC fields with an amplitude of $H_{\mathrm{AC}} = 0.1$, to map out the AC susceptibility across the whole phase diagram of Fig. 4.9(a). As already briefly described before, this technique measures the response

$$\chi_{\mathrm{AC}}(\omega) = \frac{\mathbf{M}}{\mathbf{H}_{\mathrm{AC}}} = \chi'_{\mathrm{AC}}(\omega) - i\chi''_{\mathrm{AC}}(\omega) \, , \tag{4.17}$$

to an applied magnetic AC field $\mathbf{H}_{\mathrm{AC}}(t_{\mathrm{MC}})$ that oscillates with angular frequency $\omega = 2\pi\nu$. Formally—for a derivation see Appendix A—the AC susceptibility has the form of a Debye relaxation,

$$\chi_{\mathrm{AC}}(\omega) = \frac{\chi_0}{1 + i\omega\tau} \, , \tag{4.18}$$

and its real and imaginary parts are, therefore, given by

$$\chi'_{\mathrm{AC}}(\omega) = \frac{\chi_0}{1 + (\omega\tau)^2} \, , \tag{4.19}$$

and

$$\chi''_{\mathrm{AC}}(\omega) = \frac{\omega\tau\chi_0}{1 + (\omega\tau)^2} \, , \tag{4.20}$$

respectively. Since the imaginary part is a symmetric function in logarithmic scale with a maximum when $\omega\tau = 1$, one can extract the characteristic spin relaxation time as

$$\tau = \frac{1}{\omega_{\mathrm{p}}} \, . \tag{4.21}$$
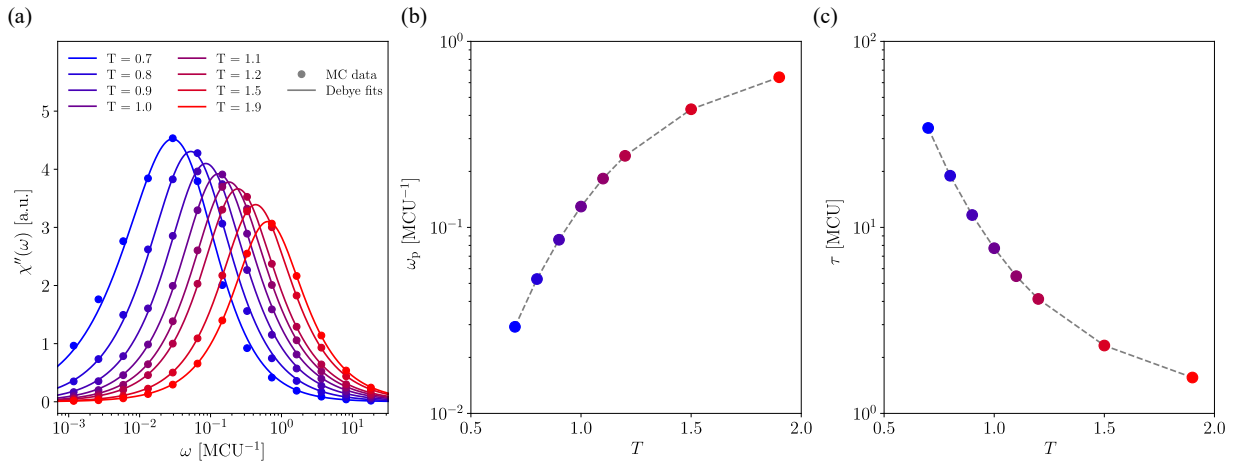
Figure 4.12 − **Numerical spectra of $\chi''_{\mathrm{AC}}(\omega)$ and extraction of the relaxation time $\tau(T)$.** (a) Monte Carlo spectra of the imaginary part of the AC susceptibility of the spin ice compound $\mathrm{Dy_2Ti_2O_7}$ in zero magnetic DC field for temperatures between $T = 0.7$ and $T = 1.9$ with corresponding (generalized) Debye fits (Eq. (4.22)). (b) From the curves in (a), one can extract the loss peak frequency ω_{p} as a function of temperature. (c) The resulting spin relaxation time $\tau(T) = 1/\omega_{\mathrm{p}}(T)$.

An example of this workflow for the study of dynamics in spin ice is illustrated in Fig. 4.12. Panel (a) of this Figure shows raw Monte Carlo spectra of $\chi''_{\mathrm{AC}}(\omega)$ for zero DC field and temperatures between 0.7 K and 1.9 K with $\hat{\mathbf{n}}_{\mathrm{AC}} = [1\bar{1}0]$ (i.e. perpendicular to [111] and parallel to the kagome planes), together with corresponding fits to the imaginary part of a Havriliak-Negami function [166]

$$\chi_{\mathrm{AC}}(\omega) = \frac{\chi_0}{[1 + (i\omega\tau)^{1-\alpha}]^\beta} \, . \tag{4.22}$$

This is a generalized Debye relaxation that takes into account a spread of relaxation times in real materials caused by interaction effects by introducing the real parameters $0 \leq \alpha, \beta \leq 1$ (cf. Appendix A). Panel (b) of Fig. 4.12 shows the resulting loss peak frequency ω_{p}, where $\chi''(\omega)_{\mathrm{AC}}$ has its maximum, as a function of temperature. Finally, panel (c) shows the corresponding relaxation time $\tau(T) = 1/\omega_{\mathrm{p}}(T)$, which is very similar to the experimental low temperature relaxation time in the inset of Fig. 4.10. In the same way we will now proceed to study the dynamics over the whole range of relevant magnetic fields and temperatures.

4.6.1 Speeding Up vs. Slowing Down

We start with applying the magnetic AC field along the $[1\bar{1}0]$ direction, that is, parallel to the kagome planes and *transversal* to the cubic [111] direction of the DC field. Fig. 4.13(a) depicts the resulting loss peak frequency of the numerical AC susceptibility for static fields up to 1.27 T and temperatures between 0.4 K and 2.0 K. Intriguingly, we observe a maximum of ω_{p} towards the critical field of the monopole liquid-gas transition ($H_c \approx 0.75$ T), that can be attributed to the critical speeding up of the monopole dynamics, in line with the experimental results [106, 165]. Noteworthy is the deviation from experiment (cf. Fig. 4.11) that the peak frequency does not fall back to zero beyond the critical field, but remains on a plateau. Also, the ridge along the temperature direction around the critical field does not drop off exponentially, but is rather temperature independent. These similarities and differences show that some aspects of monopole dynamics in spin ice are already well reproduced by dynamical Monte Carlo simulations of the DSI model, but others are not. The latter must therefore be compensated for by a conversion

(a) $\mathbf{H}_{AC}\|[1\bar{1}0]$ (transversal) (b) $\mathbf{H}_{AC}\|[111]$ (longitudinal)
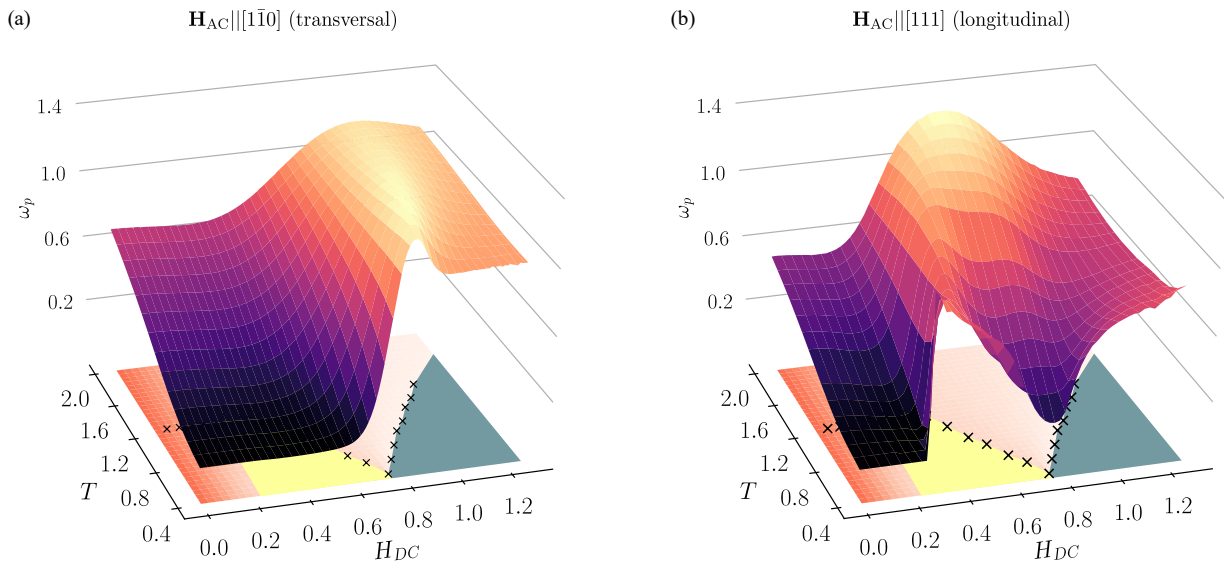
Figure 4.13 – **Speeding up versus slowing down in dipolar spin ice.** (a) Shown is the loss peak frequency ω_p of the AC susceptibility of dipolar spin ice with transversal AC field, obtained from dynamical Monte Carlo simulations with an alternating field $H_{AC} \parallel [1\bar{1}0]$ and amplitude of the AC field $H_0 = 0.1$ T. For orientation, the phase diagram from Fig. 4.9 is plotted below the susceptibility data. Peak frequencies of the AC response show a characteristic ridge towards the critical end point but no sign of (exponential) suppression. Along the magnetic field direction, a critical speeding up of the dynamics is revealed towards the critical field. (b) As (a), but with an alternating field $H_{AC} \parallel [111]$. Peak frequencies of the AC response show a stark suppression towards the critical end point, consistent with a slowing down of the critical dynamics. Figure taken from [U1].

factor between Monte Carlo time and real time, which we will examine in detail later. We also checked the case $H_{AC} \parallel [11\bar{2}]$, which is parallel to the kagome planes as well, and obtained exactly the same results as for $H_{AC} \parallel [1\bar{1}0]$ (not shown here). Therefore, in both cases we speak synonymously of the *transversal* case and later on, we will use experimental data for both cases as a comparison to our numerical data.

We now compare the transversal field data to the results for the case $H_{AC} \parallel [111]$, that is *longitudinal* to the cubic [111] direction. As depicted in Fig. 4.13(b), it turns out that in this case the dynamics are subject to a conventional slowing down near the critical end point. Fig. 4.14 demonstrates how the slowing down is gradually transformed into the speeding up by varying AC field direction from [111] to [1$\bar{1}$0] at 0.6 K.

In both cases, transversal and longitudinal AC field, the zero DC field cut of ω_p shows an increase towards higher temperatures consistent with experimental results [150, 153, 159]. Building on the qualitatively already good agreement with experiments, we want to investigate the connection between Monte Carlo and real time in the later course of this thesis by combining detailed comparisons with various experimental results and theoretical considerations about the nature of this conversion.

4.6.2 Spin Flips

In order to understand which spins mainly carry the speeding up of the dynamics in a transversal AC field, we take a look at the fluctuations of the different types of spins grouped according to their local Ising axes (cf. sketch in Fig. 4.15). The plots on the r.h.s. of Fig. 4.15 show these
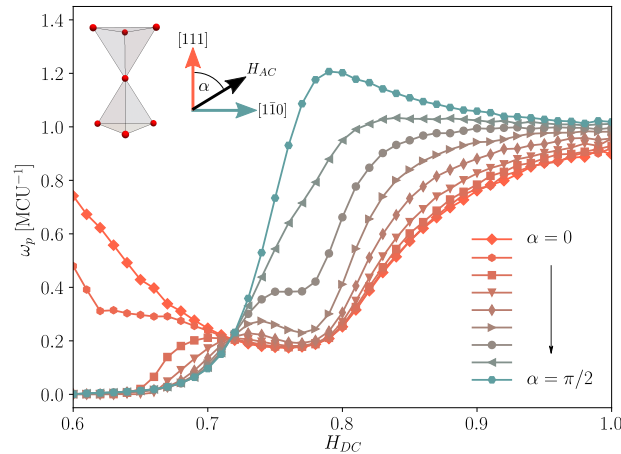
Figure 4.14 – **Tuning between slowing down and speeding up.** Monte Carlo data of the loss peak frequency ω_p of the AC susceptibility in dipolar spin ice close to the critical end point. Data shows cuts for constant $T = 0.6$ upon tilting of the AC magnetic field. The behavior of the switches from a characteristic decrease of ω_p near H_c for a longitudinal AC field $H_{\mathrm{AC}} \parallel [111]$ (red curve) to a speeding up for a transversal AC field $H_{\mathrm{AC}} \parallel [1\bar{1}0]$ (turquoise curve). Figure taken from [U1].

spin fluctuations, ordered by spin type and for both cases, longitudinal and transversal AC field. In the longitudinal case (upper four plots on the right of Fig. 4.15), all three types of spins in the kagome planes ($\mathbf{S}_1$, $\mathbf{S}_2$, and $\mathbf{S}_3$) fluctuate equally independent of the magnetic field strength. The fluctuations of $\mathbf{S}_4$ drop rapidly to zero as soon as the system enters the KI phase above 0.2 T where these spins are pinned by the static DC field, whereas the fluctuations of the remaining spins do not drop until above the critical field when the system becomes fully polarized. This also seems logical, because spins of type $\mathbf{S}_1$, $\mathbf{S}_2$, and $\mathbf{S}_3$ are geometrically equivalent with respect to the magnetic field axis which happens to coincide with the local axes of $\mathbf{S}_4$. Moreover, the fluctuations of all spins are largely independent of the frequency of the AC field.

For the transversal case, on the other hand, it is revealed (lower four plots on the right of Fig. 4.15) that with increasing driving frequency, fluctuations of $\mathbf{S}_3$ are enhanced just below the critical field while those of $\mathbf{S}_1$ and $\mathbf{S}_2$ are suppressed compared to a static setup. In this scenario, $\mathbf{S}_3$ is geometrically distinct from $\mathbf{S}_1$ and $\mathbf{S}_2$.

4.7 Comparison to Experimental Data

Having shown the qualitative agreement of Monte Carlo data and experimental results in terms of the prevalent spin dynamics close to the critical point, a natural question to ask is to what extent the observables can be matched quantitatively. In the following section, we demonstrate that the Monte Carlo dynamics can indeed be compared to the dynamics of the real system by employing a systematical mapping. To this end, a conversion factor is introduced which maps the timeline of updates in the Monte Carlo simulation to the real time passing in the experiment. We show that this conversion not only gives qualitative but also quantitative agreement for certain regions of the phase diagram.

4.7.1 Conversion Factor

In our Monte Carlo Markov chain, configurations succeed each another by means of single-spin flip Monte Carlo updates (MCU) in each of which the flip of an individual spin is accepted or rejected based on the thermal Metropolis weights. One typically groups N of those updates together to form a so-called Monte Carlo *sweep* (MCS), a unit of Monte Carlo time which is consequently independent of system size and which can be roughly understood as the average time for any given spin to be updated. However, despite this grouping spin flips still occur sequentially and not in parallel.

In contrast to our Monte Carlo simulation, however, a real material exhibits spontaneous thermal spin flips, e.g., induced by phonon activity, which are not sequential but occur at any given place within the sample simultaneously. One therefore is usually discussing quantities of a single spin which is again (mostly) independent of sample size.

Let us consider the two systems individually. In the experimental system, the number of spin flips that occur in a given time interval Δt_{real}, measured in seconds, is given by

$$N_{\mathrm{SF}}^{\mathrm{real}} = \tilde{\alpha}\, n_{\mathrm{ph}}\, \Delta t_{\mathrm{real}} \tag{4.23}$$

where $\tilde{\alpha}$ is a material constant, amounting for coupling between phonons and spins as well as the total amount of spins and n_{ph} describes the density of phonons present in the system which can couple to the spins.

In the Monte Carlo system, the number of spin flips in a given time interval Δt_{MC}, measured in Monte Carlo updates, can be given far more explicit, it is

$$N_{\mathrm{SF}}^{\mathrm{MC}} = p_{\mathrm{acc}}\, \Delta t_{\mathrm{MC}}\,, \tag{4.24}$$
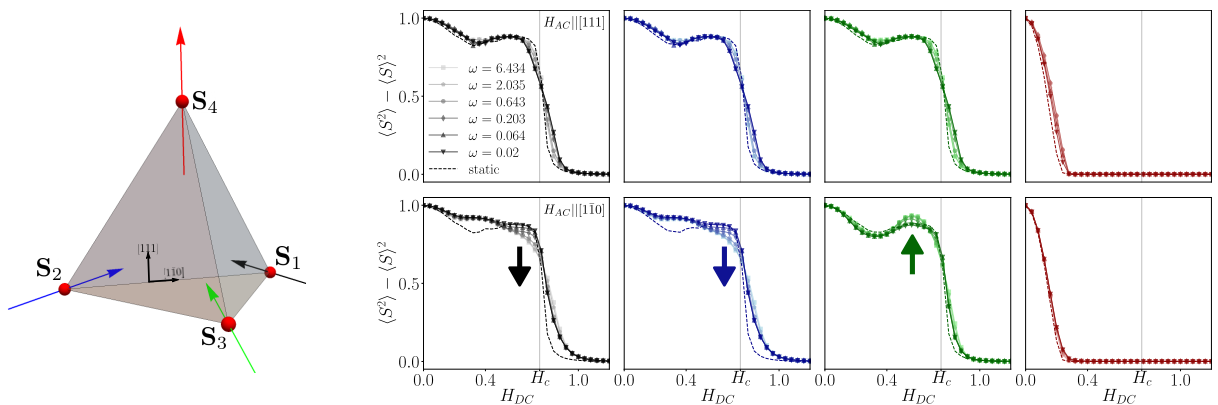
Figure 4.15 – **Spin fluctuations in spin ice.** Panels show the variance of different types of spins in each tetrahedron as function of external magnetic field for $T = 0.6$ K. The colors of the variance plots match the respective type of spin in the sketch. For the two distinct cases $H_{AC} \parallel [111]$ (upper four plots) and $H_{AC} \parallel [1\bar{1}0]$ (lower four plots), qualitatively different behavior in the vicinity of the critical field can be observed: Whereas for $H_{AC} \parallel [111]$, $\mathbf{S}_1, \mathbf{S}_2, \mathbf{S}_3$ remain equally fluctuating for all magnetic fields, fluctuations in these spins are pronounced differently in the vicinity of the critical field for the transversal case, where fluctuations of $\mathbf{S}_3$ are enhanced near $H_{\mathrm{DC}} = H_c$. Figure taken from [U1].

which only includes the length of time interval, Δt_{MC}, as well as the update acceptance probability p_{acc} which emerges from the Monte Carlo update scheme.

In order to compare time scales between the real system and the Monte Carlo system, time intervals Δt_{MC} and Δt_{real} are compared in which both systems perform one *spin flip per spin* as illustrated in Fig. 4.16, i.e.

$$\frac{N_{\mathrm{SF}}^{\mathrm{real}}}{N_{\mathrm{S}}^{\mathrm{real}}} = \frac{N_{\mathrm{SF}}^{\mathrm{MC}}}{N_{\mathrm{S}}^{\mathrm{MC}}} \overset{!}{=} 1 \, . \tag{4.25}$$

If one uses this and equates Eqs. (4.23) and (4.24), then it follows that

$$\alpha \, n_{\mathrm{ph}} \, \Delta t_{\mathrm{real}}[\mathrm{s}] = \frac{p_{\mathrm{acc}}}{N_{\mathrm{SF}}^{\mathrm{MC}}} \, \Delta t_{\mathrm{MC}}[\mathrm{MCU}] \tag{4.26}$$

with some new constant $\alpha = \tilde{\alpha}/N_{\mathrm{SF}}^{\mathrm{real}}$ which is now independent of the size of the real system.

This identification leads to relating real and Monte Carlo time intervals in the form of

$$\Delta t_{\mathrm{MC}}[\mathrm{MCS}] = A \cdot \Delta t_{\mathrm{real}}[\mathrm{s}] \tag{4.27}$$

with a conversion factor A. Such a conversion factor between Monte Carlo time and real time has already been introduced by Takatsu and et al. [105]—however, the factor was only introduced phenomenologically and only its temperature dependence was investigated, which was explained with a simple Arrhenius law, that is, $A(T) \propto \exp{-\Delta/T}$ with $\Delta \approx 4$ K. But with the previous discussion, this factor can now be theoretically identified as

$$A = \frac{\alpha \, n_{\mathrm{ph}}}{p_{\mathrm{acc}}} \, . \tag{4.28}$$

For a typical phonon system underlying the spin system one can make further general assumptions. The phonon occupation has in general a thermal dependence $n_{\mathrm{ph}}(T)$ which can be expressed as a Bose function of typical energy scale E_{ph} as

$$n_{\mathrm{ph}}(T) \sim \frac{1}{e^{E_{\mathrm{ph}}/k_{\mathrm{B}}T} - 1} \, . \tag{4.29}$$

This Bose form of the phonon occupation explicitly has two relevant limits. For high temperatures $k_{\mathrm{B}}T \gg E_{\mathrm{ph}}$, the function is roughly given as $n_{\mathrm{ph}}(T) \sim T$ whereas for small temperatures $k_{\mathrm{B}}T \ll E_{\mathrm{ph}}$, the function is roughly given as $n_{\mathrm{ph}}(T) \sim e^{-\frac{E_{\mathrm{ph}}}{k_{\mathrm{B}}T}}$.

Extracting the conversion factor for the purpose of spin ice (and in general) can hence be done from two different perspectives. First and foremost, having access to experimental AC susceptibility data allows to compare the peak frequencies between Monte Carlo and experiment according to Eq. (4.27), directly yielding the factor A as a function of external parameters. Secondly, the theoretical approach of Eq. (4.28) can be used, employing the numerical acceptance rates while still containing estimates or fits for the phonon contributions.
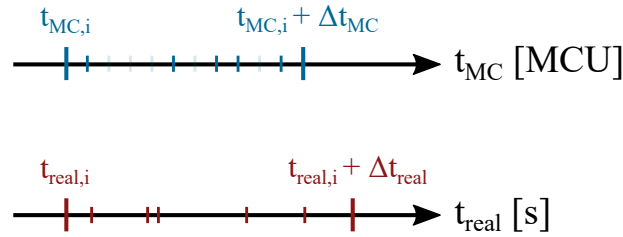
Figure 4.16 – **Time scale comparison between Monte Carlo and real time.** In the time it takes the Monte Carlo system a certain number of proposed updates (light and dark blue ticks), Δt_{MC}, the experimental system progresses by a time interval Δtreal. These time intervals can be related if they include the same number of spin flips (dark blue and dark red ticks, respectively) per spin in both systems as outlined in the main text. The final result is that for one update in a Monte Carlo system of N spins, the real time progresses by Δtreal $\sim p_{\mathrm{acc}}/(n_{\mathrm{ph}}N)$.

In the following, both methods are compared by first calculating the actual conversion from experimental to Monte Carlo time and then fitting Eq. (4.28) to the resulting $A(H, T)$.

Note, that in Eq. (4.28), the acceptance rates of the Monte Carlo process enter as p_{acc} and the only fit parameters are the global prefactor α as well as the phonon energy E_{ph}, entering the phonon density term n_{ph}. The Monte Carlo update probability p_{acc} as a function of magnetic DC field and temperature is shown in Fig. 4.17. As expected, p_{acc} goes to zero for low temperatures, making the conversion factor A large and indispensable for conversion between real time and Monte Carlo time. Note also, that the precise form of phonon contribution can be extracted from this comparison and is separately compared to the estimated n_{ph} given by Eq. (4.29). Overall, comparisons are limited by the availability of experimental data, which is the reason for combining data from different sources and concentrating on certain regions of the phase diagram, namely zero field, the KI regime, and slightly below or at H_c.
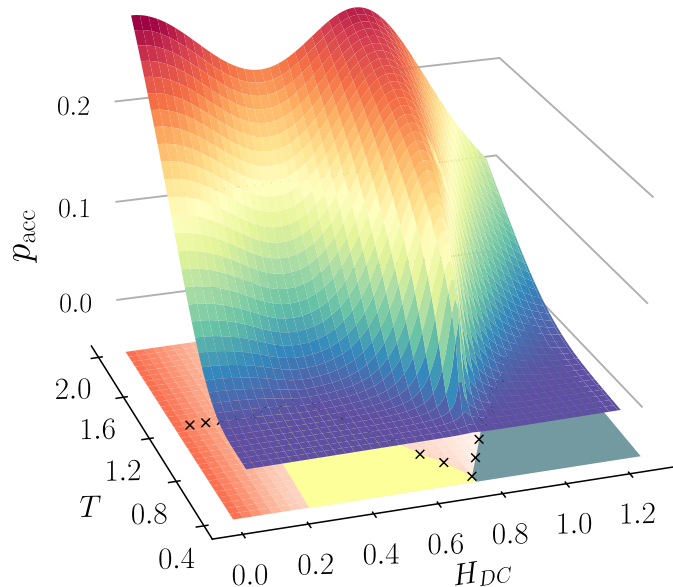
Figure 4.17 – **Monte Carlo acceptance probability.** The probability of accepted updates p_{acc} in the Monte Carlo simulation of spin ice in a magnetic field enters the conversion between real time and Monte Carlo time according to Eq. (4.28).

4.7.2 Transversal AC Field

Let us start by investigating the conversion between time scales for an alternating magnetic field $H_{AC} \parallel [1\bar{1}0]$ which is perpendicular to the static magnetic field and thus compatible with accelerated dynamics. First, we focus on the temperature behavior below 2 K in the spin ice and kagome ice phases with data shown in Fig. 4.18. Here, we compare experimental susceptibility data for $H_{DC}/H_c = 0.0$ [158] and for $H_{DC}/H_c = 0.54$ [34] against our Monte Carlo data obtained at the same parameter values—the scaling of the magnetic field is due to the slightly different values of the critical field between experiment ($H_c \approx 0.91$ T) and Monte Carlo simulation ($H_c \approx 0.75$ T). This data features frequency-resolved AC susceptibilities for multiple temperatures at a fixed magnetic field. Overall, a bare comparison of the experimental peak frequencies in panels (a) and (e) to the numerical peak frequencies in panels (b) and (f) shows a
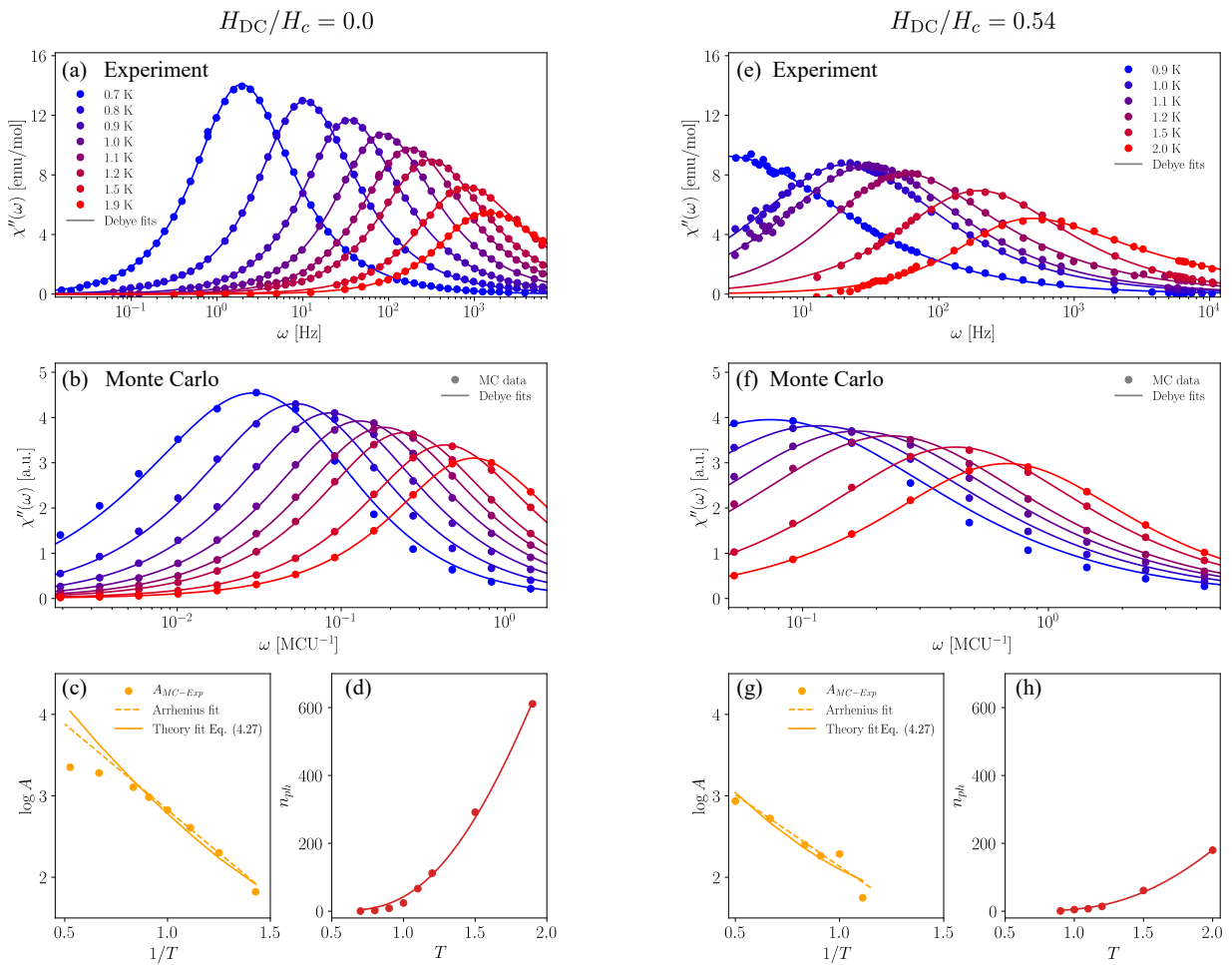
Figure 4.18 – **Comparison of experimental and numerical AC susceptibilities for transversal H_{AC}.** Experimental AC susceptibilities (panels (a) and (e)) are compared to Monte Carlo data (panels (b) and (f)) for the case of AC field $\perp$ DC field. A direct comparison of peak frequencies leads to a conversion of time scales with a factor A depicted in panels (c) and (g), respectively. Overall, the conversion factor is compatible with an Arrhenius-like behavior for low temperatures. The factor contains contributions from both the experimental as well as the Monte Carlo side. Removing the latter by explicitly taking the Monte Carlo specifics into account yields a remaining phonon contribution depicted in panels (d) and (h), which is consistent with our estimates. Experimental data in panel (a) is taken from Ref. [158] for $H_{DC}/H_c = 0.0$, experimental data in panel (e) is taken from Ref. [34] which describes $H_{DC}/H_c = 0.54$. Figure taken from [U1].

good qualitative resemblance. Both the order of peak frequencies as well as the relative heights of peaks agree on a qualitative level. Fitting the extracted conversion factors $A_{\text{MC-exp}} = \omega_{\text{p}}^{\text{real}}/\omega_{\text{p}}^{\text{MC}}$ with the theoretical prediction from Eq. (4.28), displayed in panels (c) and (g), reveals a good agreement to the a priori predictions especially for low temperatures. Furthermore, extracting only the phonon part of the conversion by multiplying with p_{acc}, one can observe in panels (d) and (h) that this is well reproduced by the expected n_{ph} given by Eq. (4.29).

If the conversion factor is considered only phenomenologically, it shows the same Arrhenius-like behavior as already shown by Takatsu et al. [105], as indicated by the dashed line in panel (c) of Fig. 4.18. However, it should be noted that this Arrhenius law is purely descriptive whereas the fit to Eq. (4.28) is based on theoretical considerations.

Increasing the static field further, let us compare the dynamics in the cone above the critical end point where the critical speeding up occurs. In experiment, this speeding up can be measured as a drastic increase in peak frequency upon lowering the temperature towards the critical end point, as displayed in Fig. 4.19 which shows data similar to that published in reference [165] (see also Fig. 4.11) and has been provided by the Hemberger group at University of Cologne. As visualized in Fig. 4.13(a), our Monte Carlo data has a similar feature in terms of a ridge which does not show any signs of a critical slowing down towards the critical end point.

Fig. 4.20 compares frequency-resolved AC susceptibility data at the critical field for various temperatures between experiment and Monte Carlo simulation. A qualitative comparison between experimental data in panel (a) and numerical data in panel (b) shows a good agreement, especially when comparing again to the data of Figure 4.18. In this comparison, especially the narrow spread of peak frequencies seems to be reproduced by the numerics accurately. However, upon closer inspection, the behavior for higher temperatures differs between experimental and numerical data. Whereas peak frequencies are observed to drop significantly at higher tem-

Figure 4.19 – **Critical speeding up in experiment** – Experimental data for the magnetic AC susceptibility with transversal AC field. The cone-like structure at $H_{\text{DC}}/H_c = 1.0$ indicates increased response frequencies close to the critical end point. Data has been provided by the Hemberger group at University of Cologne and is similar to that published in reference [165].
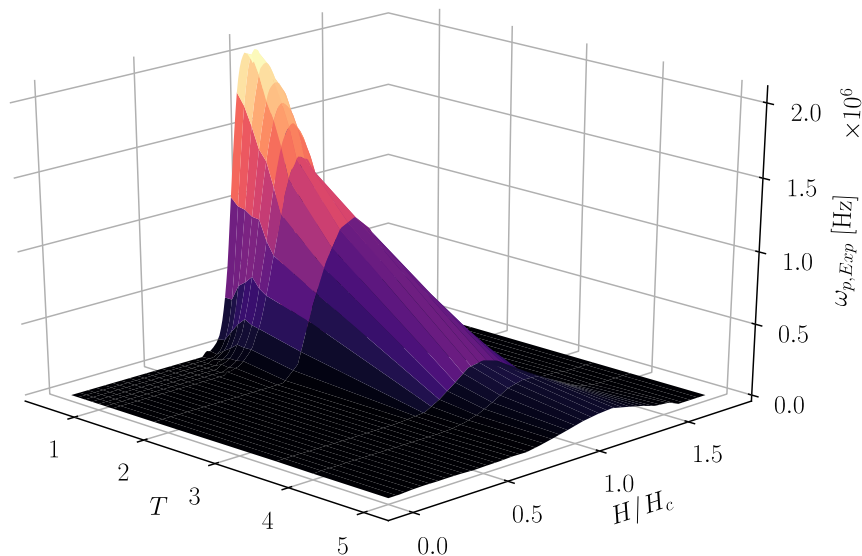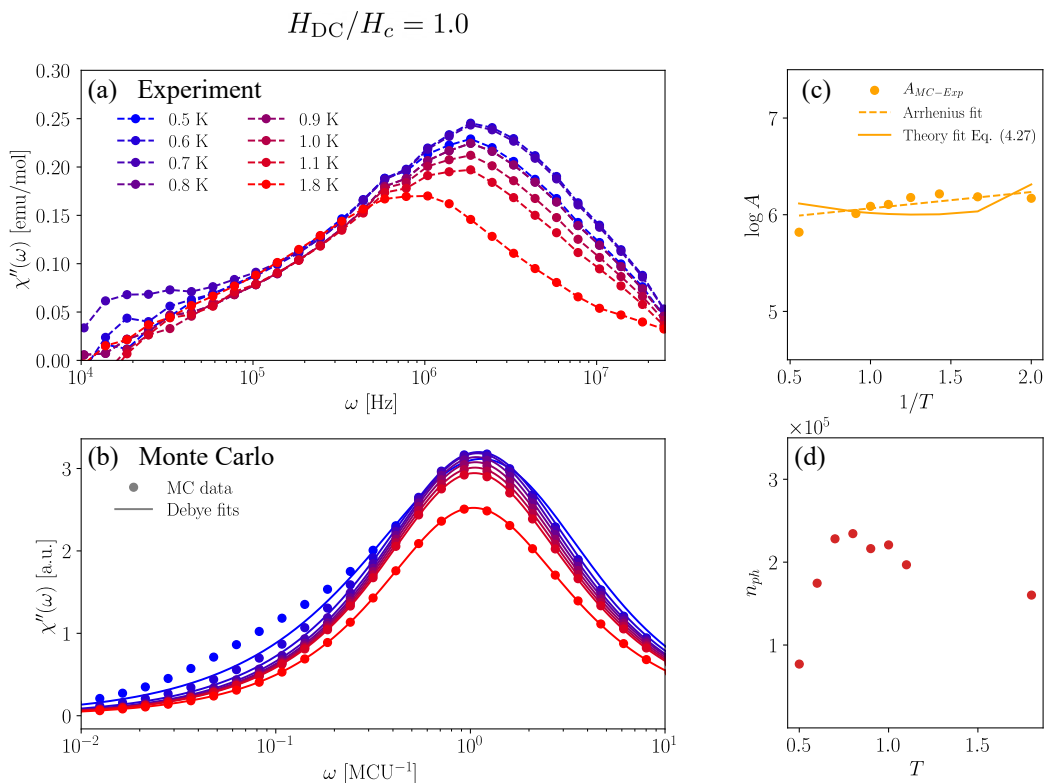
$$H_{\mathrm{DC}}/H_c = 1.0$$

Figure 4.20 – **Comparison of experimental and numerical AC susceptibilities for transversal H_{AC}.** Experimental AC susceptibilities (panel (a)) are compared to Monte Carlo data (panel (b)) for the case of AC field ⊥ DC-field similar to Fig. 4.18. Data is shown for the static field tuned to the critical point and different temperatures above the critical temperature. A comparison of time scales between experiment and Monte Carlo simulations reveals the absence of the typical Arrhenius-like behavior (panel (c)) as well as a strange and unphysical phonon contribution (panel (d)). Experimental data in panel (a) has been provided by the Hemberger group at University of Cologne and is similar to that published in reference [165]. Figure taken from [U1].

peratures in the experiment, the Monte Carlo data does not seem to follow this trend as peak frequencies tend to group up and show no signs of variation. This is replicated in the atypical behavior of the conversion factor, displayed in panel (c), and the lack of a clear phonon contribution form, displayed in panel (d). We thus conclude that the theoretical ansatz of Eq. (4.28) does not hold up close to the critical magnetic DC field.

4.7.3 Longitudinal AC Field

Let us switch the AC field direction to $H_{AC} \parallel [111]$ which is parallel to the static magnetic field and where the raw Monte Carlo data (cf. Fig. 4.14) shows a slowing down of the critical dynamics close to the critical end point.

We start by investigating the dynamics in the spin ice and kagome ice phases as displayed in Figure 4.21. Again, experimental frequency-resolved AC susceptibility data [167] is compared along cuts of constant field. Overall, there is a good qualitative agreement between the experimental datasets [167] in panels (a) ($H_{DC}/H_c = 0.0$) and (e) $H_{DC}/H_c = 0.4$ and the numerically obtained susceptibilities in panels (b) and (f), respectively. This agreement is also reflected in a well-fitted conversion factor, displayed in panels (c) and (g), which is well described by the theoretical estimates of Eq. (4.28). Also, the extracted phonon contribution fits well to its theoretical estimate, complementing the overall conversion.
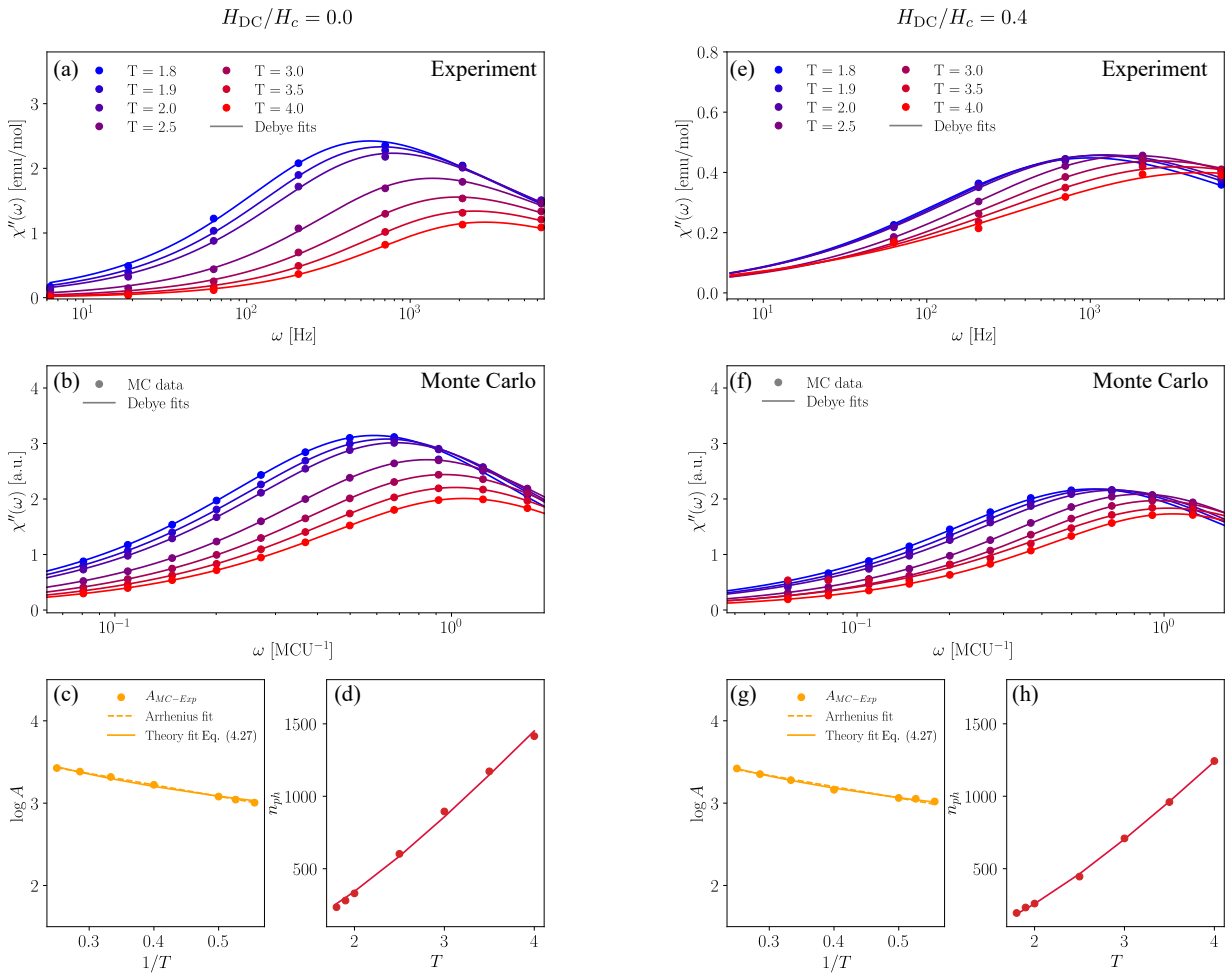

Figure 4.21 – **Comparison of experimental and numerical AC susceptibilities for longitudinal H_{AC}.** Experimental AC susceptibilities (panels (a) and (e)) are compared to Monte Carlo data (panels (b) and (f)) for the case of AC field $\parallel$ DC field. For both field strengths, the calculated conversion factors between numerical and experimental time scales feature an theoretically predicted behavior and a phonon contribution consistent with our theoretical expectations. Experimental data was provided by the Hemberger group at University of Cologne [167]. Figure taken from [U1].

Increasing the static field further and probing the region right below the critical slowing down ($H_{DC}/H_c = 0.7$) yields the comparison displayed in Figure 4.22. Similar to the case of perpendicular AC field, the experimental and Monte Carlo data seem to differ here. Whereas a general agreement in terms of relative peak heights and overall spread of the peak frequencies can be observed, the order of peak frequencies seems to mismatch. This is again reflected in a anomalous conversion factor and phonon factor, depicted in panel (c) and (d).

Overall, Fig. 4.23 summarizes the quality of conversion between experimental and numerical data for the longitudinal AC field. Here it can be seen that the qualitative and non-monotonous dependency of A on the static field H_{DC}, predicted by theoretical estimates along Eq. (4.28), is reproduced qualitatively by the true conversion factor obtained by directly comparing numerical and experimental relaxation times. It is further possible to assign a single phonon energy E_{ph} to large regions of the phase diagram, further solidifying the shape of the conversion.

$$H_{DC}/H_c = 0.7$$
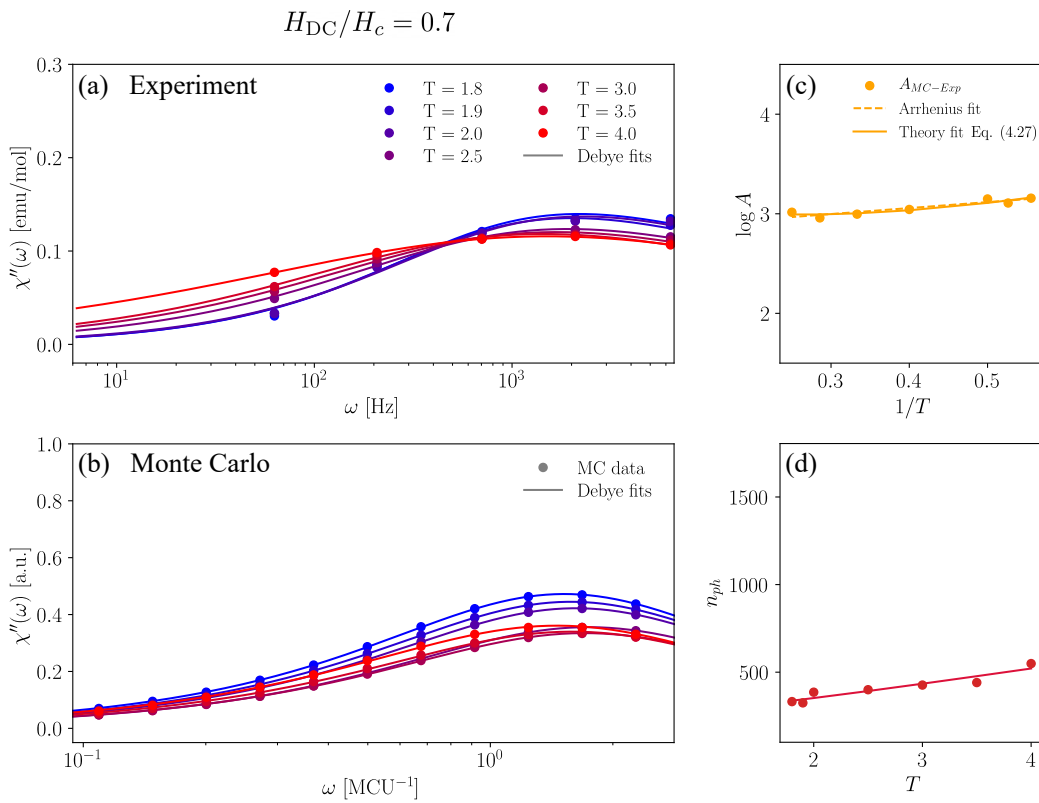
Figure 4.22 – **Comparison of experimental and numerical AC susceptibilities for longitudinal H_{AC}.** Experimental AC susceptibilities (panels (a)+(e)) are compared to Monte Carlo data (panels (b)+(f)) for the case of AC field ∥ DC field. Upon increasing the static magnetic field, the conversion factor (panel c) show no longer Arrhenius-like behavior, but has a positive slope yielding an unphysical phonon factor (panel d) with negative phonon energy. Experimental data was provided by the Hemberger group at University of Cologne [167]. Figure taken from [U1].

4.8 Discussion and Outlook

We have extensively studied the dynamics of monopole-like excitations in spin ice based on dynamical Monte Carlo simulations. This revealed several interesting features already on a raw numerical level without comparison to experimental results and conversion between Monte Carlo
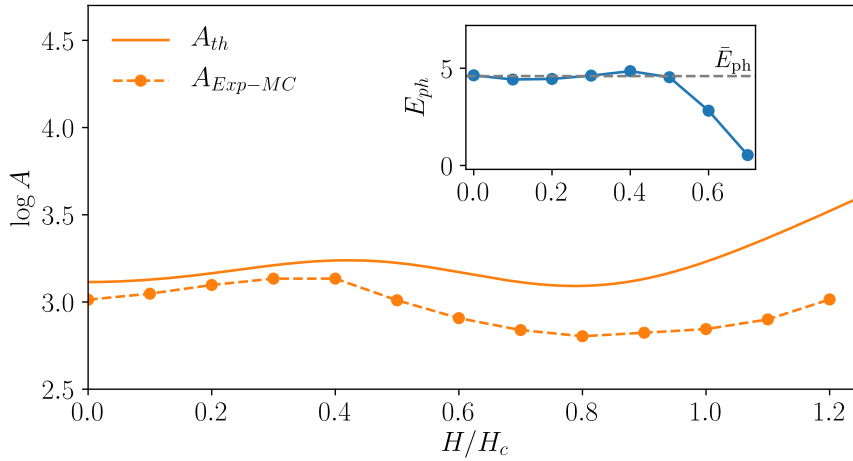
Figure 4.23 – **Conversion factor for longitudinal** H_{AC}**.** Comparison of the measured (Eq. (4.27)) and expected (Eq. (4.28)) conversion factors between experimental and numerical data. The factor is shown as a function of static field for an alternating field $H_{AC}||$[111] for a fixed temperature of 1.8 K. Dashed curve shows the measured factor A, obtained by comparing peak frequencies in experimental and numerical Monte Carlo data. The solid curve shows the prior expectation based solely on a phonon factor with constant phonon energy $\bar{E}_{\mathrm{ph}}$ and the numerical Monte Carlo acceptance rates. The constant phonon energy $\bar{E}_{\mathrm{ph}}$ in this curve is given by the average of the fit parameter E_{ph} of the fit to n_{ph} as in Fig. 4.21(d)+(h) for fields between $H_{\mathrm{DC}}/H_c = 0.0$ and $H_{\mathrm{DC}}/H_c = 0.5$ (inset). Overall, the non-monotonic behavior of the conversion factor is captured by the theoretical approach. Figure taken from [U1].

time and real time. The purely numerical results show that the dynamics of spin ice depend very sensitively on the direction along which the alternating magnetic field oscillates: while for a longitudinal field along [111] the dynamics slows down near the critical end point of the monopole liquid-gas transition, for a transverse field along [1$\bar{1}$0] signs of a critical speeding up become apparent, in complete contrast to the prevailing paradigm that critical fluctuations always slow down equilibrium.

Subsequently, we established the connection between our numerical simulations with various experiments on the dynamics in spin ice and made statements about the conversion between Monte Carlo time and real time based on a profound theory for the conversion factor A. For parts of the phase diagram—from zero field to well into the KI regime—the conversion based on our theory works well and reproduces the actual conversion as well as the previously purely phenomenological introduced Arrhenius-like relationship between t_{MC} and t_{real}, which allows to better understand the microscopic origin of this conversion than before.

However, this theoretical conversion breaks down before the critical field is reached. For further research, it would therefore be important to understand how the conversion can also be theoretically substantiated for strong magnetic DC fields. But the prerequisite for this is, of course, corresponding experimental data for fields exceeding H_c. On a purely numerical level, a worthwhile goal would be to understand what is the microscopic origin of the field direction dependence of the dynamics, i.e. why the dynamics becomes slow for a longitudinal AC field and fast for a transverse field.

Monopole Dynamics in a Classical Spin Liquid

Having seen from the dynamics of monopoles in spin ice that critical fluctuations can lead to a speeding up of the dynamics, and that dynamic Monte Carlo simulations can capture these dynamics considerably well, we now want to use the same method to consider an even more fundamental system than spin ice, namely a classical spin liquid arising from the Ising antiferromagnet on the triangular lattice. After reviewing the basics of this model in a static setup, we proceed with analyzing the dynamics due to an applied magnetic AC field.

The motivation for this chapter stems from a bachelor thesis supervised by the author of this thesis [168], the content of which has been taken up and substantially expanded by the author of this thesis in preparation of [U1].

5.1 Introduction

As already mentioned in the very beginning of Chapter 2, the prototypical example of an frustrated system is the triangular lattice Ising antiferromagnet (TIAFM) as introduced by Wannier in 1950 [4, 5]. In Fig. 2.1(b) we showed how frustration arises geometrically on an elementary, triangular plaquette. The Hamiltonian of the TIAFM is simply given by

$$\mathcal{H} = J \sum_{\langle i,j \rangle} \sigma_i \sigma_j \,, \tag{5.1}$$

where $\sigma_i = \pm 1$ denote standard Ising variables, $\langle i, j \rangle$ indicates summation over pairs of nearest neighbors, and $J > 0$ is the isotropic antiferromagnetic coupling constant. The energy is therefore minimal for all configurations that fulfill the constraint that each elementary triangular plaquette has exactly two up spins ($\sigma = +1$) and one down spin ($\sigma = -1$), or vice versa. Only two of the three bonds on such a plaquette can, therefore, be satisfied simultaneously, which leads to a massive ground state degeneracy.

A snapshot of one specific ground state is shown in Fig. 5.1(a). Looking at this Figure, the ground state degeneracy becomes immediately clear when one realizes that there exist spins that can be flipped without energy cost, e.g., the grey encircled spin. The resulting residual entropy can be calculated analytically by mapping the ground state spin configuration to a hardcore dimer covering on the dual hexagonal lattice (see Fig. 5.1(b)). This is done by placing a dimer on each bond of the hexagonal lattice that crosses an unsatisfied bond of the original triangular lattice, that is, a bond connecting two parallel spins. The resulting dimer covering is such that
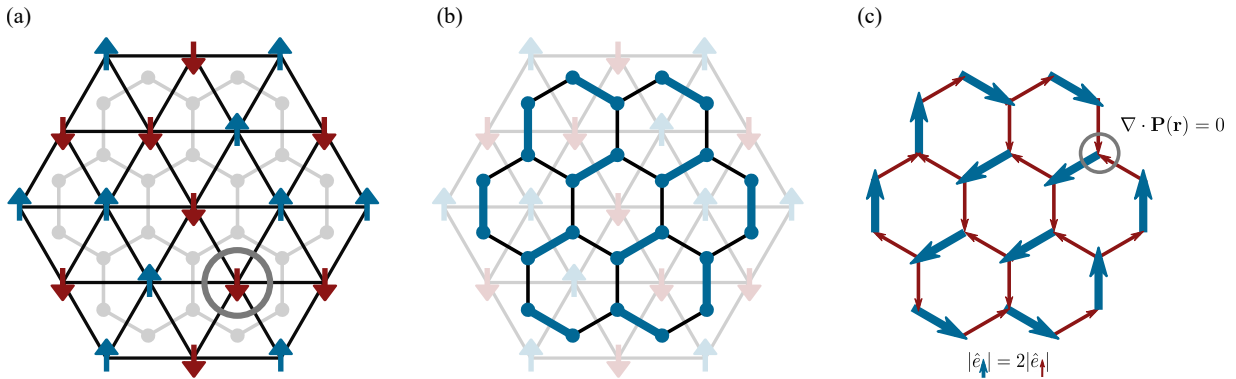
Figure 5.1 – **Triangular Ising antiferromagnet.** (a) A snapshot of one specific ground state of the triangular AFM on the triangular lattice. Each triangle hosts two up spins and one down (or vice versa). The grey encircled spin is an example of a spin that can be flipped without energy cost. In the background, the hexagonal dual lattice to the triangular lattice, can be seen in transparent. (b) Here, the hexagonal dual lattice is now in focus. The ground state configuration of (a) can be mapped to a dimer covering an the dual hexagonal lattice such that those bonds are covered by dimers that cross unsatisfied bonds in the original triangular lattice and every site is part of precisely one dimer. (c) This in turn can be mapped to a divergence-free flux field $\mathbf{P}(\mathbf{r})$ by identifying the bonds of the hexagonal lattice with lattice fluxes where each dimer-covered bond has (minus) twice the weight of an uncovered bond. Each node has then zero net (incoming minus outgoing) flux.

each dimer covers exactly two hexagonal lattice sites and each hexagonal lattice site is occupied by precisely one dimer. The number of ground state configurations on the triangular lattice then translates to the number of possible different dimer coverings on the hexagonal lattice—a problem that has been addressed in the early 1960s [169, 170], yielding an exact value for the zero point entropy per spin of

$$S_0/N = 0.323. \tag{5.2}$$

This is in stark contrast to the unfrustrated ferromagnetic ($J < 0$) Ising model on the triangular lattice, which exhibits a thermal phase transition from a paramagnet to an unique ferromagnetic ground state (up to global spin inversion) at some critical temperature $T_c = 4/\ln 3 \approx 3.6403$ [112, 171] and, therefore, has no residual entropy.

In Fig. 5.2, we show a comparison of antiferromagnetic (AFM) and ferromagnetic (FM) triangular lattice Ising model by their specific heat and residual entropy, both calculated in Monte Carlo simulations. Whereas the FM shows a sharp peak in the specific heat at T_c, the AFM displays a crossover regime and no sign of a symmetry breaking phase transition. The numerical curves of the residual entropy also show the expected behavior with the respective limiting values for $T \to 0$ of 0.323 and 0, respectively.

This is already a quite interesting result and makes the TIAFM a prototypical cooperative paramagnet, or classical spin liquid. But the mapping to a hardcore dimer covering opens up yet another perspective. Starting from the dimer covering in Fig. 5.1(b), the system can then be mapped to a divergence-free flux field $\mathbf{P}(\mathbf{r})$, as visualized in Fig. 5.1(c). Similar to the mapping of kagome ice to a Coulomb phase presented in Sec. 2.6, weighted fluxes are placed on the bonds of the hexagonal lattice such that bonds, that are occupied by a dimer, have twice the weight of an unoccupied bond. This results in the sum of all incoming and outgoing fluxes being equal at each node of the hexagonal lattice, i.e. there is no net flux, which is exactly the divergence-free condition of $\mathbf{P}(\mathbf{r})$. The TIAFM is thus also a prime example of a Coulomb phase with all the consequences described in Sec. 2.6, in particular long range algebraic correlations that decay
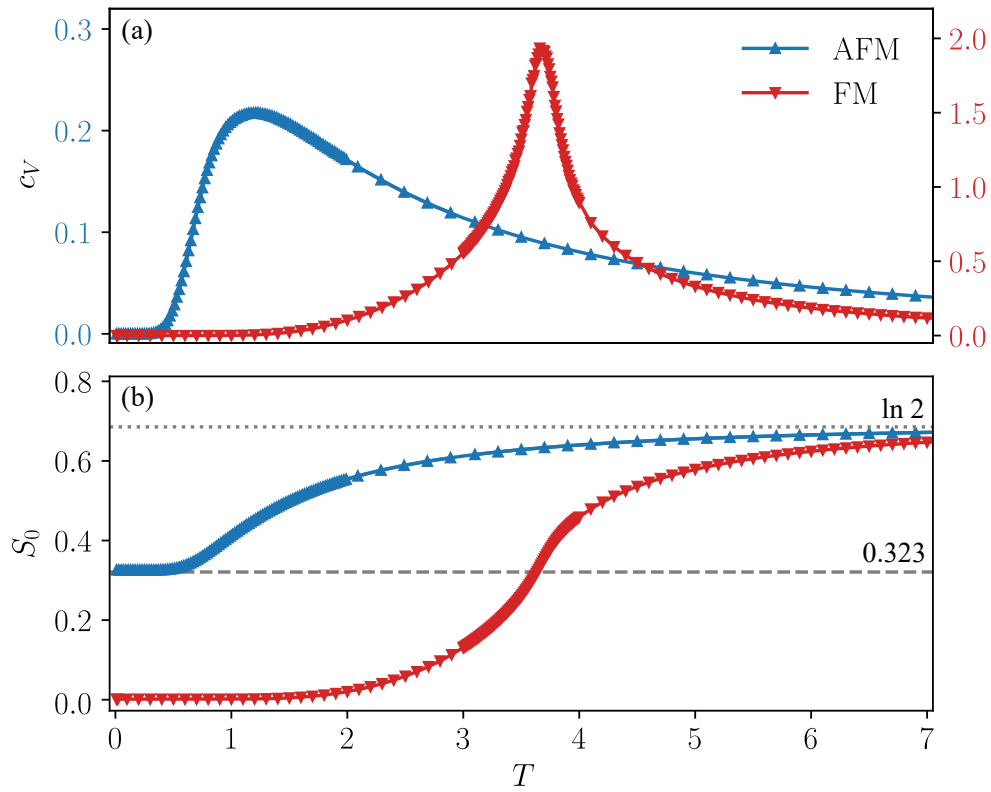
Figure 5.2 – **Triangular Ising AFM vs. FM.** (a) Specific heat of AFM and FM Ising model on the triangular lattice. The latter shows a distinct peak at the ferromagnetic phase transition at the critical temperature $T_c = 3.6403$ [112, 171]. (b) Residual entropy per spin showing a finite zero-temperature entropy only in the AFM, indicating a highly degenerate ground state.

with the distance r as $1/r^2$ and possible defects, that can be interpreted as emerging magnetic monopoles.

5.2 TIAFM in a Magnetic Field

Applying a static magnetic DC field to the TIAFM leads to a similarly rich phase diagram as it is the case for spin ice in a magnetic field along the cubic [111] direction [172–175]. In order to implement the magnetic field, the term

$$\mathcal{H}_H = -H \sum_i \sigma_i \tag{5.3}$$

is added to the TIAFM Hamiltonian of Eq. (5.1). If the magnetic field is now switched on, the system enters into a non-degenerate ordered phase with a magnetization per spin $m = 1/3$ where the spins on one sublattice are aligned along one direction whereas the spins on the other two sublattices point in the opposite direction.

This can be nicely illustrated by considering the triangular lattice as a centred hexagonal lattice [176], as visualized in Fig. 5.3. A first approximation to the zero field ground state of the TIAFM is then a Néel ordered state on the hexagons with one degree of freedom per hexagonal plaquette, namely the spin in its centre. That this is only an approximation of the ground state
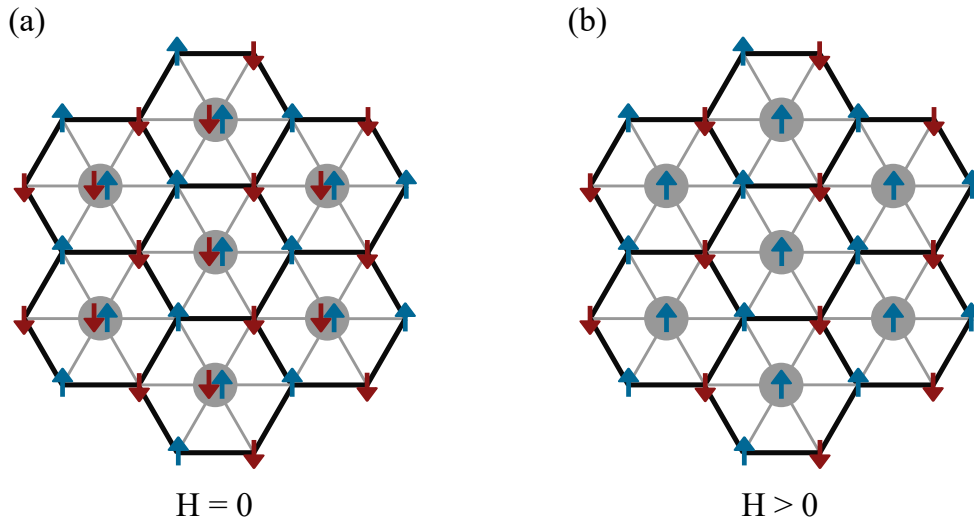
Figure 5.3 – **First approximation to the TIAFM ground state and magnetization plateau.** (a) By considering the triangular lattice as a centred hexagonal lattice (thick black lines), the (zero field) ground state of the TIAFM can be understood in a first approximation as a Néel ordered state on the hexagons with one degree of freedom per hexagonal plaquette, namely the spin in its centre. (b) An infinitely small magnetic field lifts the degeneracy and aligns the spins on the centres of the hexagonal plaquettes. Consequently, two sublattices of the triangular lattice are aligned with the field, while the third sublattice is antialigned, leading to a magnetization per spin of $m = 1/3$.

is reflected in the fact a one Ising degree of freedom per hexagonal plaquette leads to a too low residual entropy of $S_0/N = (1/3) \ln 2 \approx 0.231 < 0.323$, since each spin belongs to three hexagons and, therefore, a lattice with N spins hosts $N/3$ hexagonal plaquettes. Nevertheless, this approximation explains the magnetization step very well: when an infinitely small magnetic field is applied, all spins in the centres of the hexagonal plaquettes immediately align with it, such that the degeneracy is lifted and two sublattices are aligned with the magnetic field while the third one is antialigned, leading to the magnetization plateau with a magnetization per spin of $m = 1/3$. In this respect, the plateau is very similar to the kagome ice regime in spin ice—but it is also different because, unlike the kagome ice regime, it has no reduced residual entropy. This magnetization plateau exists at temperatures below approximately $T = 1.3$ and magnetic fields up to $H_c = 6J$ (for $T = 0$). The value of the critical field is determined by the fact that each spin that is antiparallel to the field is surrounded by six spins that are parallel to the field. For larger fields, the system becomes fully polarized and magnetic defects in the divergence-free flux field picture emerge. The polarized phase is thus quite similar to the polarized phase in spin ice.

The full phase diagram in the H_{DC}-T plane, obtained by Monte Carlo simulations, is depicted in Fig. 5.4(a)—the previously described strongly correlated spin liquid phase is indicated as the small blue region for zero DC field. The extension of this region up to temperatures of about 0.3 K results from the residual entropy data (Fig. 5.2(b)), which drops to its zero temperature value of $S_0/N = 0.323$ at this temperature. Fig. 5.4(b) depicts the corresponding specific heat in the H_{DC}-T plane and reveals that the transition to the magnetization plateau is quite sharp.

Taken together, the phase diagram of the TIAFM compares very well with that of spin ice in a magnetic field (Fig. 4.9): in addition to an extensively degenerate phase at zero field, there is a phase characterised by a magnetization plateau that globally satisfies the ground state constraint
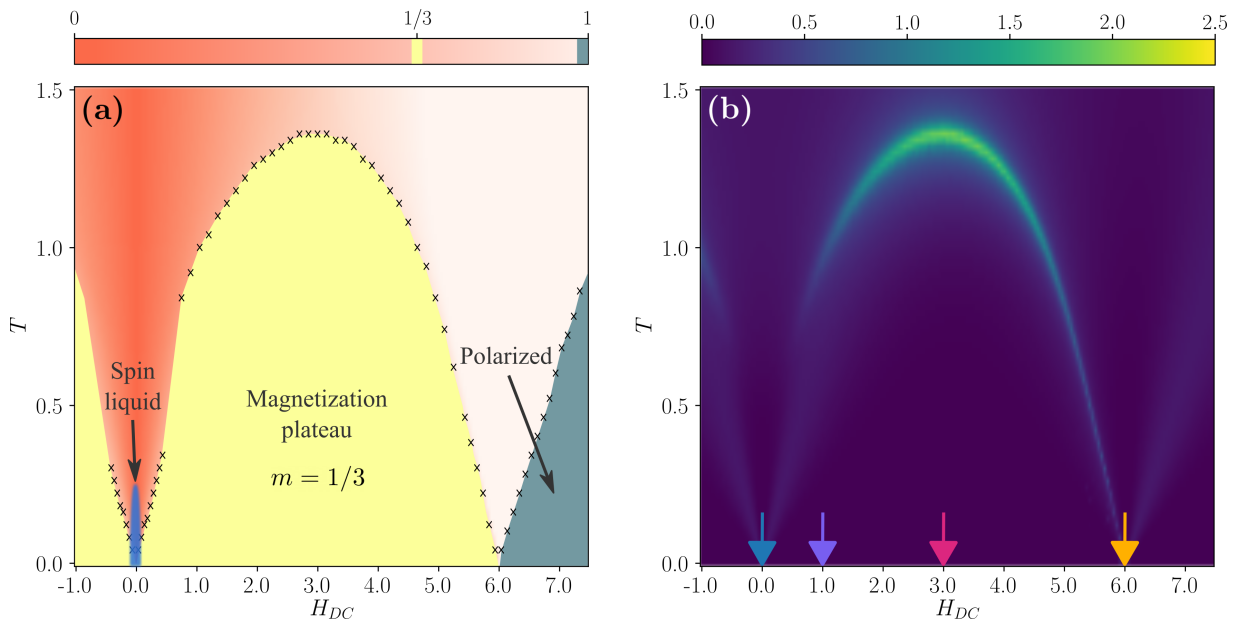
Figure 5.4 – **Triangular Ising AFM.** (a) Phase diagram of the triangular lattice Ising antiferromagnet with colorcoded magnetization data and crosses indicating peak positions of the specific heat, obtained by Monte Carlo simulations. For zero field and $T \lesssim 0.3$, the system is in the classical spin liquid regime, where a divergence-free condition is obeyed (blue region). For finite magnetic field, the system exhibits a $m = 1/3$ magnetization plateau which is extended in both directions, magnetic field and temperature (yellow region). Within this plateau, the divergence-free condition of the classical spin liquid phase is still obeyed. For fields $H_{DC} > 6$, the system becomes polarized and monopoles emerge (dark green region). (b) Specific heat of the TIAFM throughout the phase diagram. Colored arrows indicate vertical cuts in Fig. 5.7. Figure taken from [U1].

at intermediate fields, followed by a fully polarized phase that is accompanied by a proliferation of defects that can be understood as emergent monopoles in the Coulomb phase picture. As in the case of spin ice, we will now proceed and study the dynamics in the whole temperature and magnetic field range of the phase diagram.

Before we do that, however, we would like to conclude this section with a brief comment on possible other magnetic field strengths of importance besides $H_c = 0^+$ and $H_c = 6J$, since these play a role in the discussion of later results. In the first approximation that we used to explain the $1/3$ magnetization plateau, we considered the TIAFM ground state a Néel ordered state on the hexagonal lattice with one degree of freedom in the centre of each hexagonal plaquette (as visualized in Fig. 5.3(a)). But this approximation can actually be improved simply by taking into account possible *tripod* configurations, as shown in Fig. 5.5. Panel (b) of this Figure shows an isolated tripod, whose center spin belongs to the hexagonal sublattice. The consequence of such an isolated tripod is that the spins in the centres of the three hexagonal plaquettes neighboring the tripod have four antiparallel nearest neighbors. Therefore, the critical field to flip these spins is $H_c = 2J$. An even further approximation is displayed in Fig. 5.5(c), where a configuration with three connected tripods is shown. In this case, the spins in the centres of the affected hexagonal plaquettes have five antiparallel neighbors, which leads to a critical field of $H_c = 4J$. Additional critical fields through further approximations are not possible, because up to here all possible numbers of antiparallel neighbors between one and six are already covered. This approximation scheme was set up [176, 177] in order to explain the experimental magnetization curves in $Ca_3Co_2O_6$, which is a compound that consists of ferromagnetically coupled spin
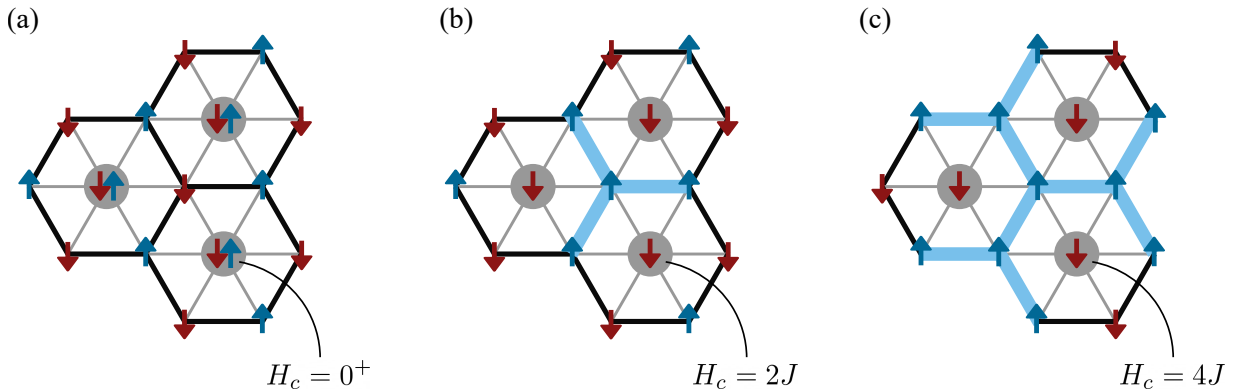
Figure 5.5 – **Further approximations to the TIAFM ground state.** (a) First approximation of the TIAFM ground state: Néel order on a hexagonal lattice with one degree of freedom in the centre of each hexagonal plaquette. (b) This approximation can be improved by including tripod configurations (blue star). The consequence of such an isolated tripod is that the spins in the middles of the three hexagonal plaquettes neighboring the tripod have four antiparallel nearest neighbors and hence the critical field to flip these spins is $H_c = 2J$. (c) An even further approximation is to include configurations with three connected tripods. In this case, the spins in the centres of the affected hexagonal plaquettes have five antiparallel neighbors, which leads to a critical field of $H_c = 4J$.

chains arranged on a triangular lattice with antiferromagnetic inter-chain coupling, and displays a equidistant multi-step magnetization rather than a two-step magnetization [178–182]. In numerical simulations, however, it depends subtly on the thermalization scheme whether the additional magnetization plateaus occur or not, which shows that the states into which the plateau is split are metastable and do not correspond to states in equilibrium [183–185]. Throughout this thesis, the simulated systems were thermalized with the magnetic field switched on and over a period of 10^6 MCU, yielding the equilibrium $1/3$ magnetization plateau for all fields between $H = 0^+$ and $H = 6J$ (and appropriate temperatures), as indicated in the phase diagram Fig. 5.4(a).

5.3 Dynamics in the TIAFM: Numerical Results

To study the dynamics, we proceed as before. We simulate the TIAFM (Eq. (5.1) with $J = 1$) including a magnetic field via Eq. (5.3), where we add a sinusoidal time varying part in addition to the static magnetic DC field, that is

$$H(t_{\mathrm{MC}}) = H_{\mathrm{DC}} + H_{\mathrm{AC}}(t_{\mathrm{MC}}) = H_{\mathrm{DC}} + H_{\mathrm{AC}} \sin(\omega t_{\mathrm{MC}}) . \tag{5.4}$$

Again, we measure numerical spectra of the AC susceptibilities $\chi_{\mathrm{AC}}(\omega)$, fit Debye relaxations to them, and determine the peak frequency ω_{p} as a function of temperature and magnetic field to obtain information about the relaxation time $\tau = 1/\omega_{\mathrm{p}}$.

A temperature cut of ω_{p} for zero DC field is shown in Fig. 5.6 where it is compared to the loss peak frequency data of the triangular Ising ferromagnet that we have already shown in the warm-up example in Sec. 3.4.3. While the FM, as we have seen, exhibits a critical slowing down at the critical temperature T_c, the loss peak frequency of the TIAFM behaves completely differently and has a maximum in the crossover regime which implies a speeding up of the dynamics. Only below approximately $T = 0.3$ upon entering the classical spin liquid regime, the dynamics of the TIAFM slows down.
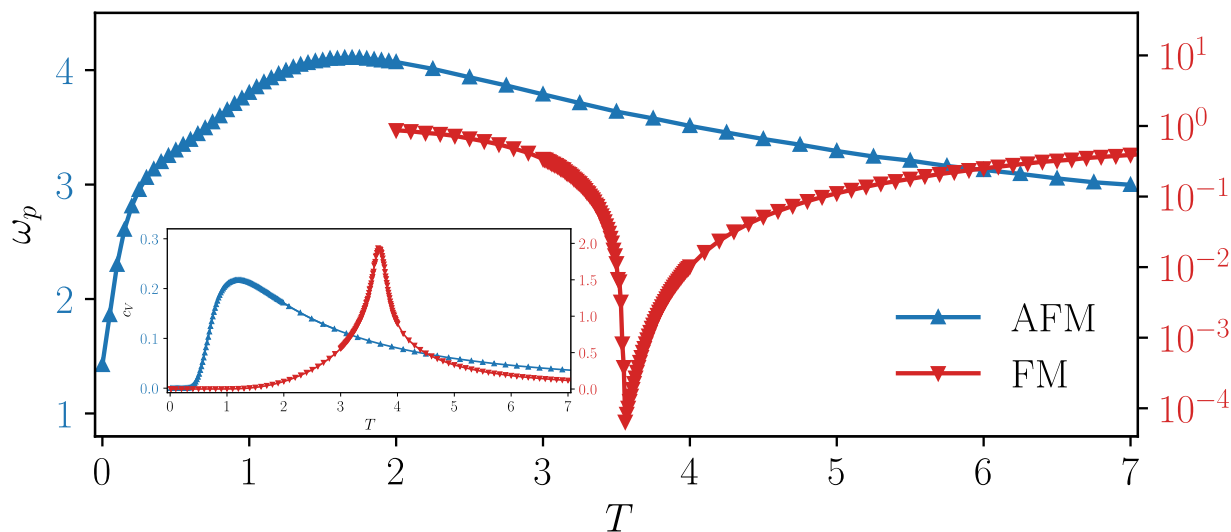
Figure 5.6 – **Loss peak frequency of the TIAFM.** AC susceptibility loss peak frequency of TIAFM (blue) and FM (red) at zero magnetic DC field. The FM displays a significant decrease of ω_p at the critical temperature ($T_c \approx 3.64$ [112, 171]—see also specific heat data in the inset for orientation), signaling a critical slowing down. The TIAFM, on the other hand, has a maximum in the crossover regime, indicative of no slowing down effect taking place, but a speeding up of the dynamics.

In the next step we switch on a static magnetic field in order to probe the dynamics for different magnetic fields. Fig. 5.7 shows specific heat, residual entropy and loss peak frequency for cuts along fixed $H_{DC} = 0, 1, 3$, and 6. For $H_{DC} = 6$, the system behaves similar as at $H_{DC} = 0$ in terms of a broad crossover regime in the specific heat and a non-zero residual entropy that is even slightly higher than the residual entropy at zero field, in line with previous results [174, 186].

Within the magnetization plateau, at $H_{DC} = 1$ and $H_{DC} = 3$, the specific heat shows rather sharp peaks beyond which the residual entropy drops to zero, indicating an ordering transition. The loss peak curves (panel (c)) behave similar for $H_{DC} = 0$ and $H_{DC} = 6$ as they both show a maximum in the crossover regime and only drop off again at low temperatures, thus displaying a speeding up of the dynamics at the crossover that only slows down upon going to very low temperatures below approximately $T = 0.3$. In contrast, the curves for $H_{DC} = 1$ and $H_{DC} = 3$ within the magnetization plateau, show a canonical slowing down of the dynamics above $T = 1$ at the ordering transition when the magnetization plateau is entered.

A three-dimensional surface plot of the resulting loss peak frequency for the whole H_{DC}-T phase diagram with temperatures up to $T = 5$ and magnetic fields between $H_{DC} = -1$ and $H_{DC} = +7$ as well as cuts for different fixed temperatures are shown in Fig. 5.8—the grey cut-off area is due to noisy data, as in this area the response to the AC magnetic field is too small to measure meaningful spectra of $\chi_{AC}(\omega)$ so that these gray values do not correspond to actually measured loss peak frequencies. One can see well in it that inside the magnetization plateau and the polarized phase, the dynamics are relatively slow.

Outside of these regions, the dynamics speed up showing several features that we will discuss in the following. To explore the dynamics at the transition from the spin liquid regime to the magnetization plateau and from the magnetization plateau to the polarized phase, we take a closer look at cuts for fixed temperatures (cf. Fig. 5.8 (b) and (c)). It turns out that for lower temperatures, ω_p has distinct peaks exactly at $H_{DC} = 0$ and at $H_{DC} = 6$ which indicate a critical
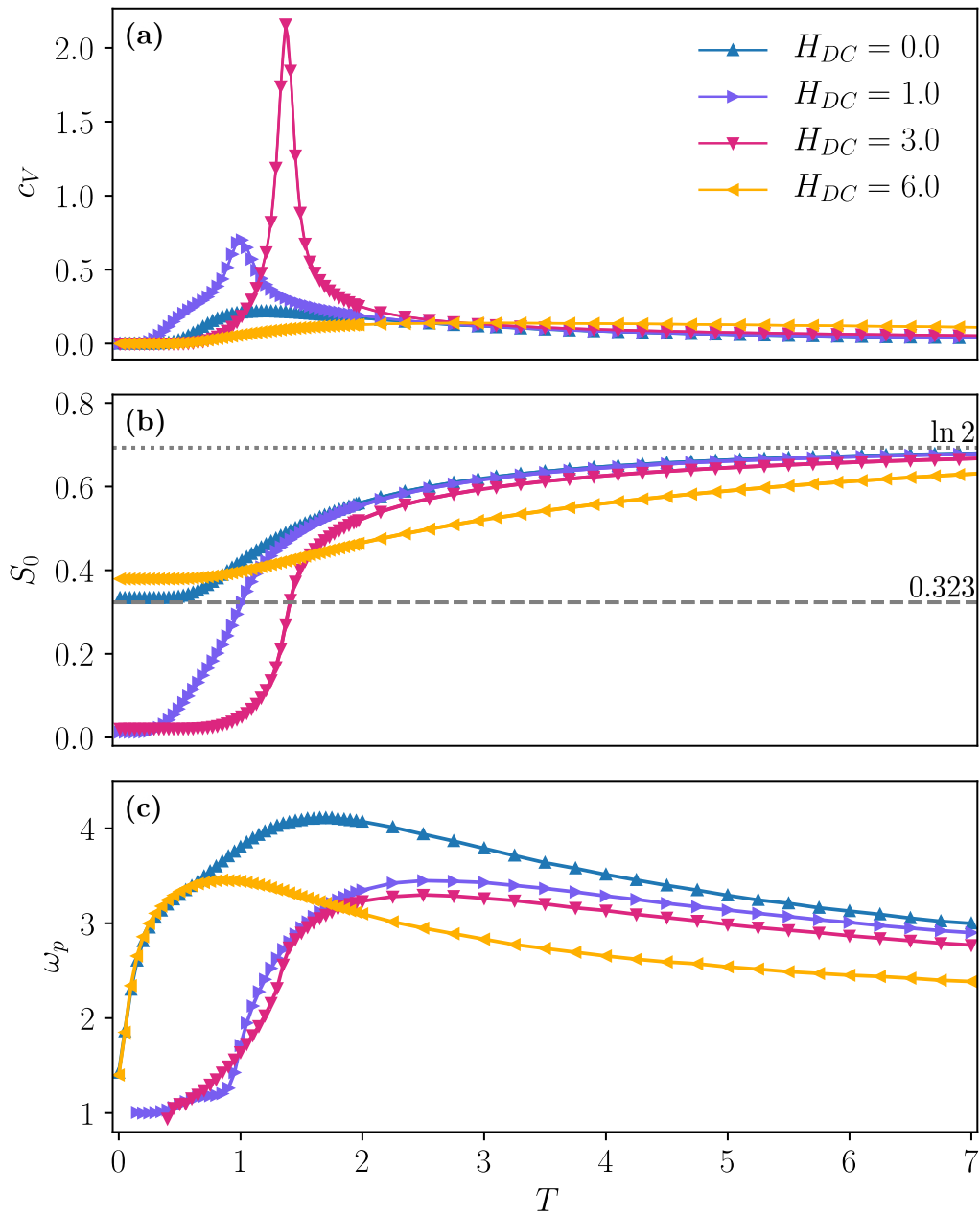
Figure 5.7 – **Cuts for constant DC field.** Panels show specific heat (a), entropy (b) and loss peak frequency of the AC susceptibility (c) of the TIAFM for cuts at static magnetic fields indicated by arrows in Fig. 5.4(b). While for $H_{DC} = 1$ and $H_{DC} = 3$, within the 1/3 magnetization plateau, all curves behave similar in terms of a vanishing residual entropy (panel (b)) and a slowing down of the dynamics (panel (c)) at the ordering transition, for $H_{DC} = 0$ and $H_{DC} = 6$, one can observe a non-zero residual entropy and a speeding up of the dynamics in the crossover regime. Figure taken from [U1].

speeding up at these points. In addition, one can see a tiny bump right in the middle of the magnetization plateau exactly at $H_{DC} = 3$. For temperatures that lie above the magnetization plateau, ripples emerge in the structure of ω_p with additional peaks at $H_{DC} = 2$ and at $H_{DC} = 4$. Intriguingly, that is exactly at the critical field strengths at which spins surrounded by isolated and connected tripod configurations are being flipped (see Sec. 5.2). The inset of Fig. 5.7(c) shows how the valleys of this structure vanish with increasing temperature.
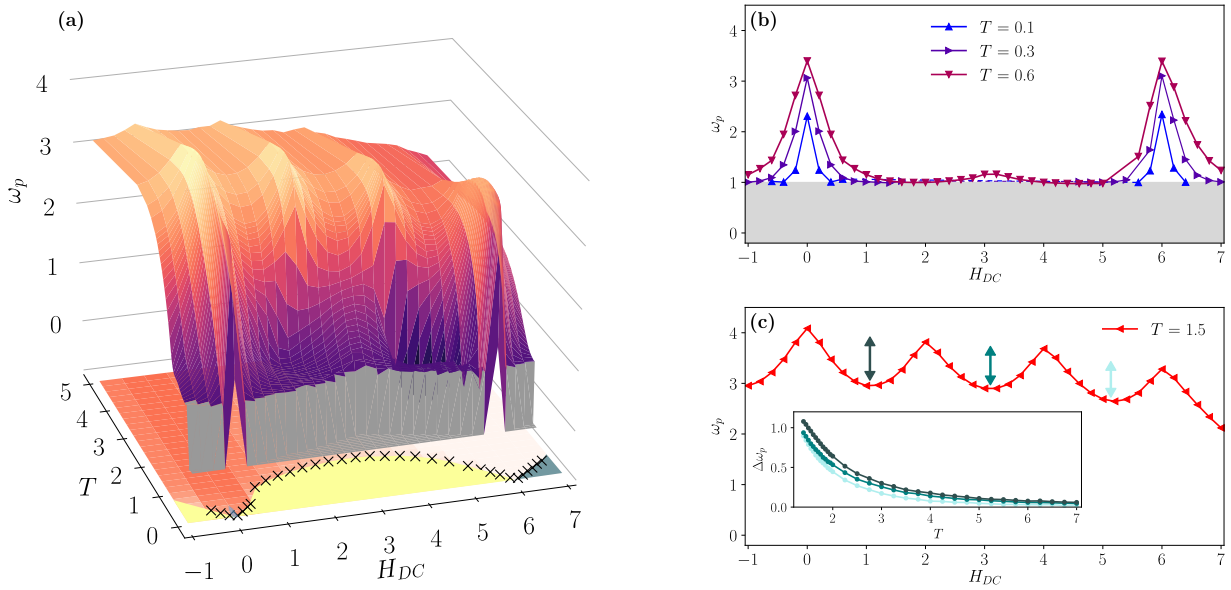
Figure 5.8 – **Loss peak frequency of the TIAFM.** (a) Three-dimensional plot of the loss peak frequency ω_p of the AC susceptibility, measured by dynamical Monte Carlo, superimposed on top of the static phase diagram of Fig. 5.4. In the gray region right above the magnetization plateau and the polarized phase at low temperatures, the AC response is too weak to fit a Debye relaxation so that these values do not correspond to actually measured loss peak frequencies. Panels (b) and (c) show cuts at constant temperature through the magnetization plateau. For temperatures above the magnetization plateau, ripples emerge in the structure of ω_p, whose amplitude decreases for large temperatures (inset panel (c)). Figure taken from [U1].

5.4 Discussion and Outlook

We have studied the dynamics of magnetic monopole-like excitations in the simplest and most basic model of a classical spin liquid, the triangular Ising antiferromagnet. Even without a magnetic field, the dynamics in this model differ drastically from its ferromagnetic cousin: while the latter exhibits a phase transition at a critical temperature T_c and experiences a canonical critical slowing down near T_c, no magnetic long range order builds up in the TIAFM and the dynamics experiences a speeding up in the crossover to the classical spin liquid regime.

In an applied magnetic DC field, the TIAFM possesses a similarly rich phase diagram as spin ice, including a magnetization plateau and a fully polarized phase. While the system undergoes an ordering transition into the magnetization plateau at $H_{\mathrm{DC}} = 1$ and $H_{\mathrm{DC}} = 3$ where the dynamics slows down and the residual entropy vanishes for $T \to 0$, a behavior similar to zero field is found at $H_{\mathrm{DC}} = 6$—the critical field where the system enters the fully polarized phase—namely a non-zero residual entropy and a speeding up of the dynamics.

The magnetic field dependence of the dynamics also displays interesting features. Here, for temperatures in which the magnetization plateau exists ($T < 1.2$), maxima in ω_{p}, i.e. signs of a speeding up of the dynamics, appear exactly at $H_{\mathrm{DC}} = 0$ and $H_{\mathrm{DC}} = 6$. For higher temperatures, ripples in ω_{p} emerge by two additional peaks at $H_{\mathrm{DC}} = 2$ and $H_{\mathrm{DC}} = 4$—exactly the magnetic field strengths relevant for flipping spins neighboring meta-stable tripod configurations (see remark in Sec. 5.2 and Fig. 5.5). With regard to the magnetic field dependence, a comparison with experimental results of the relaxation time in $Ca_3Co_2O_6$ seems interesting, a compound that exhibits a multi-step magnetization with equidistant steps in a magnetic field [178–182].

Due to its ferromagnetically coupled spin chains that are arranged on a triangular lattice with antiferromagnetic inter-chain couplings, it was logical to explain these steps with precisely the tripod configurations in the TIAFM mentioned before [176, 177]. Remarkably, measurements of the relaxation time in $Ca_3Co_2O_6$ [181, 182] show a similar behavior of the dynamics at exactly the magnetic field strengths relevant for these steps, just as in our numerical results for the TIAFM, see Fig. 5.9(c) and (d). Also the dip of τ at $H_{DC} = 0$, appears both numerically in the TIAFM and experimentally in $Ca_3Co_2O_6$, cf. Fig. 5.9(a) and (b).

The experimental results in $Ca_3Co_2O_6$ were explained [181, 182] by *quantum tunneling of magnetization* [187], a phenomenon which has been observed, for example, in Mn_{12} [188, 189] or ferritin [190, 191], where at specific resonant values of H_{DC}, magnetization steps occur and spin relaxation is enhanced by resonant quantum tunneling, signaled by a phenomenologically similar relaxation behavior as observed in $Ca_3Co_2O_6$. Future efforts should therefore be directed towards investigating the connection between quantum tunneling of magnetization on the one hand, and the characteristic profile of spin relaxation inherent in dynamical Monte Carlo simulations of the TIAFM on a classical level on the other.
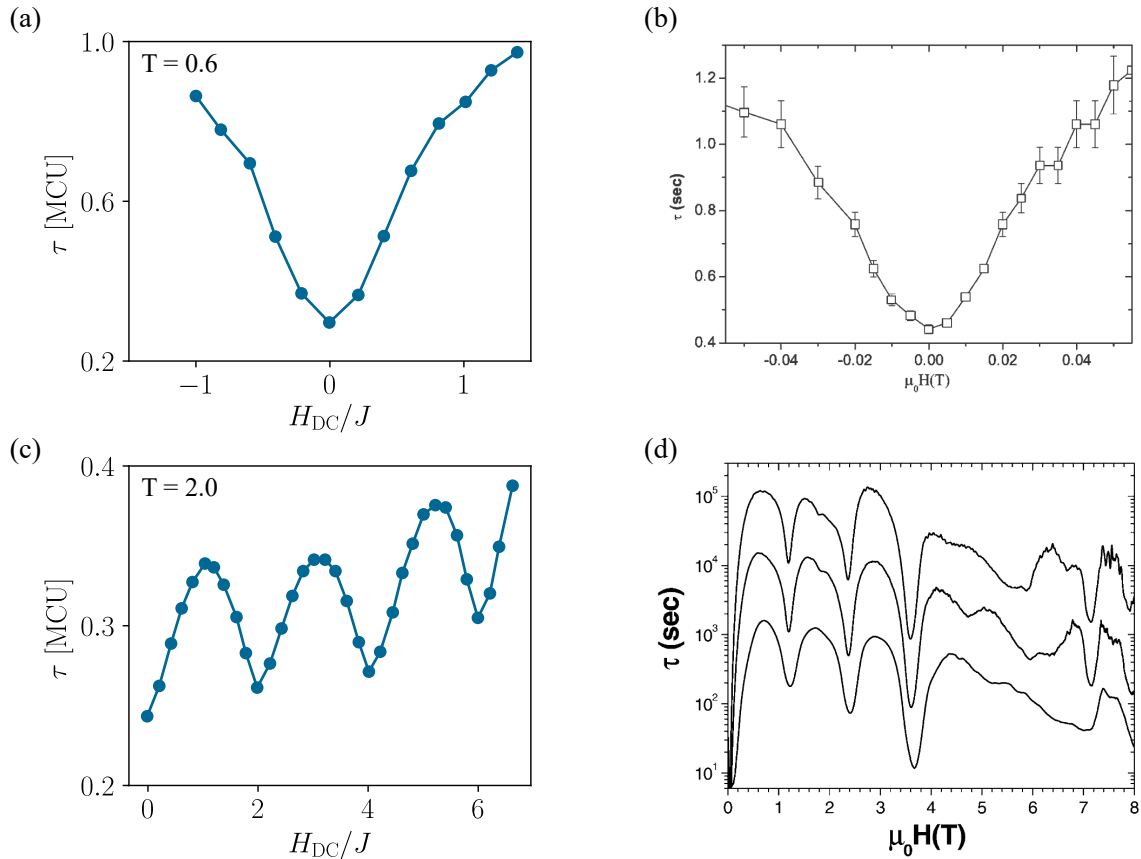
Figure 5.9 – **Numerical relaxation times of the TIAFM and experimental relaxation times in $Ca_3Co_2O_6$.** (a) and (c) show numerical relaxation times $\tau = 1/\omega_p$ and their field dependence for $T = 0.6$ and $T = 2.0$, respectively, extracted from the data shown in Fig. 5.8. (b) Experimental relaxation times in $Ca_3Co_2O_6$ at $T = 2.0$, showing the same dip structure around $H = 0$ as in (a). Reprinted with permission from [182]. Copyright (2004) by the American Physical Society. (d) Experimental relaxation times in $Ca_3Co_2O_6$ at $T = 2.0$ for different sweep rates (top to bottom: 0.01 T min^{-1}, 0.1 T min^{-1}, and 1 T min^{-1}), showing qualitatively the same variations as in (c). Used with permission of the Royal Society of Chemistry, from [181], permission conveyed through Copyright Clearance Center, Inc.

Part III

Non-Coplanar Magnetic Orders in Classical
Antiferromagnets

Although magnetic orders can theoretically be arbitrarily complex, the magnetic orders found in nature are mostly simple, such as collinear orders like ferromagnetic order or antiferromagnetic Néel order. However, more complicated forms of magnetic order can also occur, including coplanar orders or even non-coplanar orders up to complex spin spirals. Such intricate textures are highly relevant in many respects, as will be motivated below.

This part of the thesis focuses on the study of non-coplanar magnetic orders in classical antiferromagnets. To this end, we study two model systems that turn out to have non-coplanar classical ground states and are motivated by the recent synthesis of a number of Mott insulating square-kagome materials and of spin-1/2 maple-leaf lattice antiferromagnets. We explore the rich phenomenology of frustrated magnetism, including extensive degeneracies and order-by-disorder mechanisms, induced by these lattice geometries, namely square-kagome antiferromagnets in Chapter 7 and maple-leaf antiferromagnets in Chapter 8. For both models, we study an elementary, classical Heisenberg model with nearest-neighbor and additional cross-plaquette interactions and discuss a multitude of non-coplanar orders, as well as a number of spin spiral phases.

The following introductory chapter serves as the basis for both subsequent chapters and provides the motivation and fundamentals relevant to both models examined.

6.1 Motivation

Non-coplanar magnetic orders can lead to non-trivial and exotic topological effects and unconventional transport properties. These phenomena arise since non-coplanar orders are typically associated with a non-zero scalar spin chirality

$$\chi_{ijk} = \mathbf{S}_i \cdot (\mathbf{S}_j \times \mathbf{S}_k) \ . \tag{6.1}$$

The scalar spin chirality χ_{ijk} is proportional to the volume of the parallelepiped spanned by the three spins $\mathbf{S}_i$, $\mathbf{S}_j$, and $\mathbf{S}_k$, and thus also to the solid angle Ω subtended by these three spin vectors (see sketch in Fig. 6.1). Consequently, it is non-zero if the three spins are non-coplanar.

As a consequence, non-coplanar magnetic orders can induce a spontaneous *topological Hall effect* (THE) by virtue of their finite spin chirality, as has recently been shown [41–44], making them very interesting for spintronic applications [192, 193]. In the ordinary Hall effect that arises in a normal conductor in a perpendicular magnetic field, the Lorentz force acting on the charge carriers induces a transverse Hall resistivity that scales linearly with the applied magnetic field [194]. Furthermore, in ferromagnets there is a much higher additional component of Hall re-

(a)

(b)

$\Omega \sim \chi_{123}$

$\mathbf{S}_3$

$\mathbf{S}_2$

$\mathbf{S}_1$

$\mathbf{S}_3$
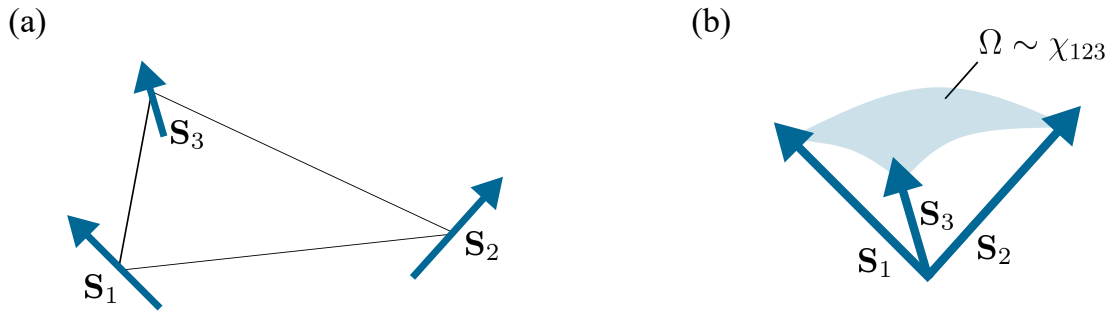
$\mathbf{S}_1$ $\mathbf{S}_2$

Figure 6.1 – **Scalar spin chirality.** (a) Three spins on the vertices of a triangle that are arranged non-coplanar. (b) The corresponding scalar spin chirality $\chi_{123} = \mathbf{S}_1 \cdot (\mathbf{S}_2 \times \mathbf{S}_3)$ is proportional to the solid angle Ω subtended by the three spin vectors—and hence zero for coplanar spins. Figure inspired by Ref. [195].

sistivity resulting from the internal magnetization of the ferromagnetically ordered spins. This *anomalous Hall effect* is ascribed to spin-orbit interactions and can occur even in the absence of a magnetic field when time-reversal symmetry is spontaneously broken [196]. The THE, on the other hand, arises from the fact that a conduction electron, that hops along a loop of non-coplanar spin sites, picks up an additional quantum-mechanical Berry phase, which acts as an emergent magnetic field that scales with the scalar spin chirality [195]. This emergent magnetic field then can generate a contribution to the Hall resistivity in antiferromagnets without internal magnetization and external magnetic field [197]. Such a THE has been observed, e.g., in frustrated pyrochlore magnets [198]. Conversely, the THE can also be used as a powerful probe to detect unconventional non-coplanar magnetic orders [199].

Closely related to this, non-coplanar magnetic orders are also particularly interesting in another respect. Upon introducing quantum fluctuations, for instance by going to small spins such as $S = 1/2$, such orders can melt into *chiral quantum spin liquids* (CSLs) [45, 46]. CSLs are a class of spin liquids with macroscopically broken time-reversal and mirror symmetries as well as non-zero expectation value of the scalar spin chirality. They were originally proposed in the late 1980s [200, 201], but their experimental realization and observation remains challenging so far. Therefore, due to the possible melting of classical non-coplanar magnetic orders to a CSL, such orders are an excellent starting point in the search for the latter.

Now that we have shown that non-coplanar orders are interesting in various ways, we will introduce some examples of such magnetic orders (as special cases of non-collinear orders) that are relevant in the course of this thesis.

6.2 Types of Non-Collinear Magnetic Order

In this section, we briefly review classical non-collinear ground states of frustrated Heisenberg models, including three-dimensional, non-coplanar generalizations of spin spirals and regular magnetic orders. Since the criterion for the formation of spin spirals can be well understood in the Luttinger-Tisza framework, we start by introducing this method.

6.2.1 The Luttinger-Tisza Method

The Luttinger-Tisza (LT) method [202, 203] is a powerful approach to determine the ordering wave vector that characterizes the ground state of classical Heisenberg models. Initially lim-

ited to Bravais lattices, the method was soon extended to non-Bravais lattices by Lyons and Kaplan [204]. To discuss the LT method, we follow Refs. [205, 206] and start with the general Heisenberg Hamiltonian of Eq. (2.3) and rewrite it as a sum over real-space coordinates by using $\mathbf{S}_i = \mathbf{S}(\mathbf{r}_i)$ and $J_{ij} = J(\mathbf{R}_{ij})$, where $\mathbf{r}_i$ is the position of $\mathbf{S}_i$ and $\mathbf{R}_{ij} = \mathbf{r}_i - \mathbf{r}_j$ is the distance between sites i and j:

$$\mathcal{H} = \sum_{i,j} J(\mathbf{R}_{ij})\mathbf{S}(\mathbf{r}_i) \cdot \mathbf{S}(\mathbf{r}_j) \,. \tag{6.2}$$

The problem of solving for the energy minimum and finding the ground state under the *strong constraint*

$$|\mathbf{S}_i|^2 = 1 \; \forall \; i \tag{6.3}$$

is in general non-trivial. The key idea of the LT approach is to soften this constraint and to demand, that it is only fulfilled on average, leading to the much less restrictive *weak constraint*

$$\sum_i |\mathbf{S}_i|^2 = N \,, \tag{6.4}$$

where N is the total number of spins. Since all solutions that satisfy the strong constraint necessarily meet the weak constraint, one can solve the problem for solutions under the weak constraint and then check whether the found solutions additionally satisfy the strong constraint. This softening of the spin length constraint allows to solve the minimization problem by diagonalizing the symmetric interaction matrix with entries $J(\mathbf{R}_{ij})$. The problem is then simplified by making use of the translational variance of $J(\mathbf{R}_{ij})$ and transforming the problem to Fourier space, leading to the quadratic form

$$\mathcal{H} = \sum_{\mathbf{q}\in\text{BZ}} \sum_{\mu,\nu} \tilde{J}_{\mu\nu}(\mathbf{q})\tilde{\mathbf{S}}_\mu(\mathbf{q}) \cdot \tilde{\mathbf{S}}_\nu(-\mathbf{q}) \,. \tag{6.5}$$

Here, the following definitions of the Fourier transform are being used:

$$\tilde{\mathbf{S}}_\mu(\mathbf{q}) = \frac{1}{\sqrt{N/\Gamma}} \sum_{i\in\mu} \mathbf{S}(\mathbf{r}_i)e^{-i\mathbf{q}\cdot\mathbf{r}_i}, \tag{6.6}$$

$$\tilde{J}_{\mu\nu}(\mathbf{q}) = \sum_{j\in\nu} J(\mathbf{R}_{i\in\mu,j})e^{i\mathbf{q}\cdot\mathbf{R}_{i\in\mu,j}} \,, \tag{6.7}$$

where the lattice is assumed to have Γ sites per unit cell, that is, $\mu = 1,\ldots,\Gamma$ and N/Γ is the number of spins per sublattice. The summation over $i \in \mu$ in the definition of $\tilde{\mathbf{S}}_\mu(\mathbf{q})$ then runs over all spins of sublattice μ while the notation $i \in \mu$ in the definition of $\tilde{J}_{\mu\nu}(\mathbf{q})$ refers to an arbitrary but fixed site belonging to sublattice μ. $\tilde{J}_{\mu\nu}(\mathbf{q})$ are the elements of the $\Gamma \times \Gamma$ matrix $\tilde{\mathbf{J}}(\mathbf{q})$ that contains all interactions between sublattices μ and ν. $\tilde{\mathbf{J}}(\mathbf{q})$ is hermitian and has, therefore, real eigenvalues $\lambda_\mu(\mathbf{q})$, and the corresponding normalized eigenvectors $\mathbf{u}_\mu(\mathbf{q})$ form an eigenbasis of the underlying Γ-dimensional vector space. Thus, Eq. (6.6) can be rewritten in this eigenbasis as

$$\tilde{\mathbf{S}}_\mu(\mathbf{q}) = \sum_{\nu=1}^{\Gamma} \mathbf{w}_\nu(\mathbf{q})u_\mu^\nu(\mathbf{q}) \,, \tag{6.8}$$

where $\mathbf{w}_\nu(\mathbf{q})$ are three-dimensional coefficients that determine the components of $\tilde{\mathbf{S}}_\mu(\mathbf{q})$. Inserting this into Eq. (6.5) leads to

$$\mathcal{H} = \sum_{\mathbf{q} \in \text{BZ}} \sum_{\nu=1}^{\Gamma} \lambda_\nu(\mathbf{q}) |\mathbf{w}_\nu(\mathbf{q})|^2 \,. \tag{6.9}$$

Furthermore, using the inverse Fourier transform

$$\mathbf{S}(\mathbf{r}_{i \in \mu}) = \frac{1}{\sqrt{N/\Gamma}} \sum_{\mathbf{q} \in \text{BZ}} \tilde{\mathbf{S}}_\mu(\mathbf{q}) e^{i\mathbf{q} \cdot \mathbf{r}_i} \,, \tag{6.10}$$

allows to express the weak spin length constraint of Eq. (6.4) in Fourier space as

$$\sum_{\mathbf{q} \in \text{BZ}} \sum_{\nu=1}^{\Gamma} |\mathbf{w}_\nu(\mathbf{q})|^2 = N \,. \tag{6.11}$$

Combining this with Eq. (6.9) yields the lower limit for the energy of the true ground state as

$$\mathcal{H} \geq N \lambda_{\text{LT}} \,, \tag{6.12}$$

where $\lambda_{\text{LT}} = \min\{\lambda_\nu(\mathbf{q})\}$ is the minimal eigenvalue of $\tilde{\mathbf{J}}(\mathbf{q})$. The wave vector that corresponds to λ_{LT} is the optimal Luttinger-Tisza ordering wave vector $\mathbf{q}_{\text{LT}}$.

6.2.2 Spin Spirals

Having found the lower limit for the ground state energy and the associated ordering wave vector, one might be interested in the corresponding ground state spin configuration in real space. According to Eq. (6.9), the energy can be minimized by allowing $\mathbf{w}_\nu(\mathbf{q})$ to be non-zero only for the values $\pm \mathbf{q}_{\text{LT}}$ and ν_{LT} for which $\lambda_\nu(\mathbf{q})$ is minimal, that is

$$|\mathbf{w}_\nu(\mathbf{q})|^2 = \begin{cases} \frac{N}{2} & \text{if } (\mathbf{q}, \nu) = (\mathbf{q}_{\text{LT}}, \nu_{\text{LT}}) \,, \\ 0 & \text{otherwise} \,. \end{cases} \tag{6.13}$$

With these coefficients, the weak spin length constraint is met by construction. The inverse Fourier transform of Eq. (6.8) then yields

$$\mathbf{S}(\mathbf{r}_{i \in \mu}) = \frac{1}{\sqrt{2\Gamma}} \sum_{\mathbf{q} = \pm \mathbf{q}_{\text{LT}}} \hat{\mathbf{w}}(\mathbf{q}) u_\mu^{\text{LT}}(\mathbf{q}) e^{i\mathbf{q} \cdot \mathbf{r}_i} \,, \tag{6.14}$$

where $\hat{\mathbf{w}}(\mathbf{q})$ is the unit vector along $\mathbf{w}_{\nu_{\text{LT}}}(\mathbf{q})$ and $u_\mu^{\text{LT}}(\mathbf{q})$ is the μth component of the eigenvector that corresponds to λ_{LT}. From this, physical solutions that fulfill the strong spin length constraint arise in form of *coplanar spin spirals* [207]

$$\mathbf{S}(\mathbf{r}_i) = \begin{pmatrix} \cos(\mathbf{q}_{\text{LT}} \cdot \mathbf{r}_i) \\ \sin(\mathbf{q}_{\text{LT}} \cdot \mathbf{r}_i) \\ 0 \end{pmatrix} \,, \tag{6.15}$$

which are described by a single propagation vector $\mathbf{q}_{\text{LT}}$ that indicates direction and pitch of the spiral. A sketch of such a coplanar spin spiral in shown in Fig. 6.2.

(a)
(b)
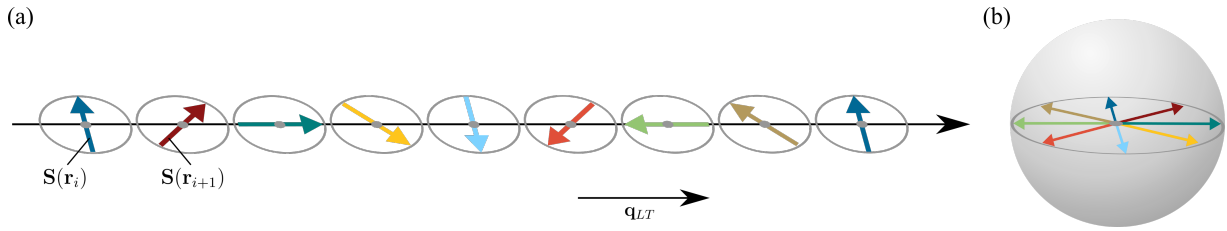
Figure 6.2 – **Spin spiral.** (a) A coplanar spin spiral as described by a single propagation vector $\mathbf{q}_{LT}$. The spin vectors $\mathbf{S}(\mathbf{r}_i)$ rotate in a single plane (indicated by the grey ellipses) and the propagation vector determines direction and pitch of the spiral. (b) A common origin plot, where all spin vectors of the spiral are plotted on a single unit sphere. For coplanar spin spirals, the spins lie on a great circle.

Due to the $O(3)$ symmetry of the isotropic Heisenberg Hamiltonian, every rotation of this solution is a possible solution as well. This method is exact for monoatomic lattices, where $u_\mu^{\mathrm{LT}}(\mathbf{q}) = 1$. This is sometimes also referred to as the *spiral theorem*, which states that every classical Heisenberg Hamiltonian with one spin per unit cell has a spiral spin state in its ground state manifold [208, 209]. It can also be shown [205] that the LT method is exact for all bipartite lattices, but it may also hold in certain cases of non-bipartite lattices. In the case of multiple equivalent minimal eigenvalues λ_{LT}, the set of corresponding wave vectors $\{\mathbf{q}_{\mathrm{LT}}\}$ describes degenerate spin spiral ground states in form of a manifold of propagation vectors in the Brillouin zone, which can appear in the shape of points, lines, surfaces, or even volumes [210]. If, on the other hand, no physical solution can be found, the method only gives a lower bound for the true ground state energy in form of Eq. (6.12).
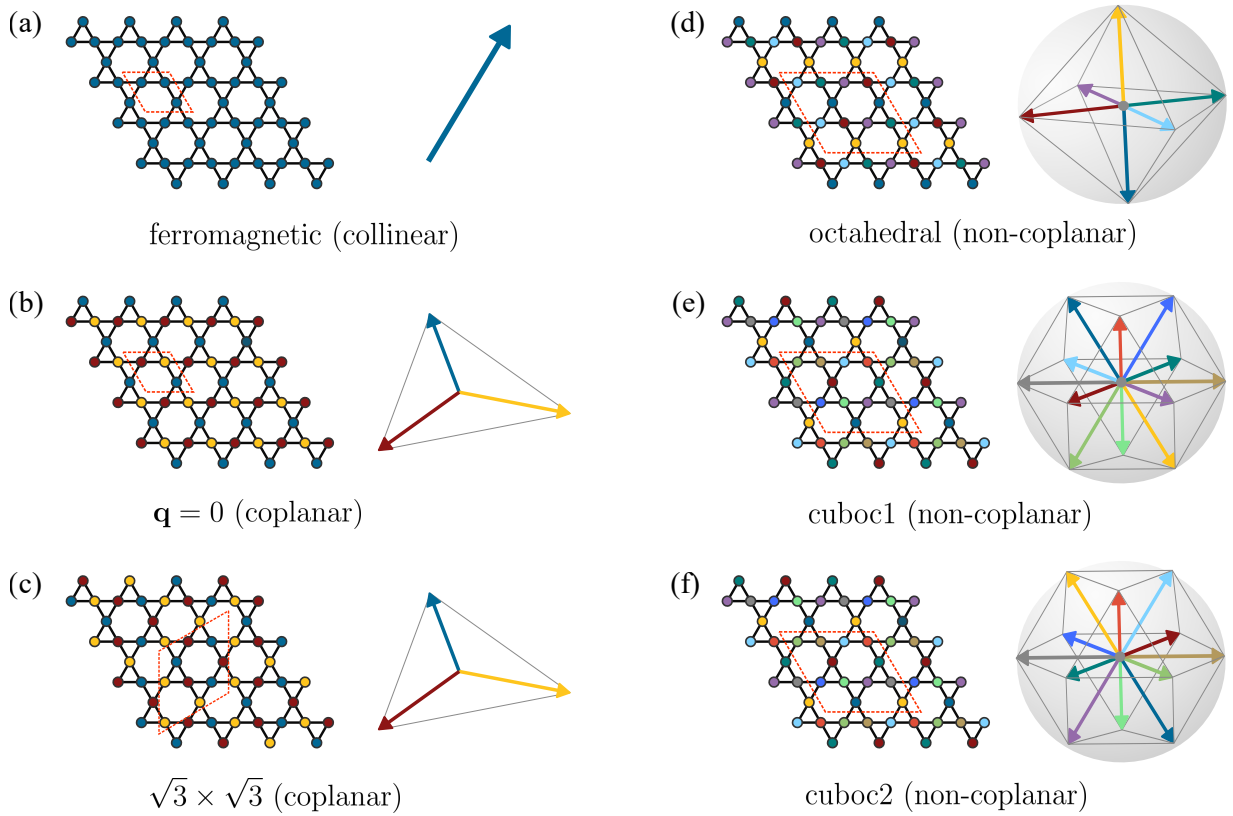
Possible spiral ground states are not limited to two dimensions, however. It is straightforwardly possible to find three-dimensional, non-coplanar spin spirals as possible ground state solutions in a generalization of the LT framework [211]. From the above discussion it is clear that a necessary, but not sufficient requirement to find non-coplanar ground states with the LT method is that the underlying lattice is non-Bravais [212].

6.2.3 Regular Magnetic Orders

We have seen that in the special cases of quadratic Heisenberg Hamiltonians on monoatomic Bravais lattices and bipartite lattices, the Luttinger-Tisza method can construct exact ground states. In general, however, the problem of finding the ground state of a generic spin model with global $O(3)$ spin symmetry on non-Bravais lattices or in the presence of multiple-spin interactions (that is, beyond the Heisenberg model), is remarkably challenging and there is no analytical method for doing so.

To facilitate this, Messio et al. introduced a class of spin configurations called *regular magnetic orders* (RMOs), which are good variational ground state candidates [39]. These RMOs preserve all lattice symmetries modulo global $O(3)$ spin transformations (i.e., rotations and spin inversions) and can be constructed explicitly via a group-theoretical approach in a systematic way for any lattice geometry and independent of the spin interactions.

RMOs include both simple collinear magnetic orders as well as more complex orders up to non-coplanar magnetic structures. For example, the two- (three-) sublattice Néel order on the square (triangular) lattice is an RMO, since each lattice symmetry operation can be compensated by global spin rotations of angle 0 or π $(0, \pm 2\pi/3)$. In Fig. 6.3, we present as an example all RMOs

(a)

ferromagnetic (collinear)

(b)

$\mathbf{q} = 0$ (coplanar)

(c)

$\sqrt{3} \times \sqrt{3}$ (coplanar)

(d)

octahedral (non-coplanar)

(e)

cuboc1 (non-coplanar)

(f)

cuboc2 (non-coplanar)

Figure 6.3 – **Regular magnetic orders on the kagome lattice.** Shown are the RMOs on the kagome lattice as constructed by Messio et al. [39] with their real-space arrangement and the corresponding spin vectors. (a) The simplest RMO on the kagome lattice is the ferromagnetic state where all spins point in the same direction. The unit cell (red rhomb) contains the three basis sites of the underlying triangular lattice. (b) and (c) show the coplanar $\mathbf{q} = 0$ and $\sqrt{3} \times \sqrt{3}$ orders, with three-site, and nine-site magnetic unit cells, respectively. In both cases, the spins on the three sublattices form mutual angles of $120°$. For both orders there are also non-coplanar umbrella states that interpolate between the ferromagnetic state and the respective $120°$ order (not shown here). (d) The non-coplanar octahedral state has a 12-site magnetic unit cell with six sublattices of spins that point to the corners of a regular octahedron. (e) and (f) show the non-coplanar cuboctahedral states cuboc1 and cuboc2. In both cases, the magnetic unit cell contains 12 sites and the 12 sublattices of spins point to the corners of a cuboctahedron. While in the cuboc1 state the nearest-neighbor pairs of spins form angles of $120°$, in the cuboc2 state the angle is $60°$. Figure inspired by Ref. [39].

that were constructed for the kagome lattice [39]. Besides a collinear ferromagnetic order, these include the prominent coplanar $\mathbf{q} = 0$ and $\sqrt{3} \times \sqrt{3}$ orders, as well as various non-coplanar orders. Messio et al. also showed that large parts of the ground state phase diagram of a J_1-J_2-J_3-J_3' Heisenberg model on the kagome lattice with further-neighbor cross-plaquette interactions host these RMOs and thus that RMOs are indeed extremely good ground state candidates.

Finally, it should be mentioned that it is precisely such non-coplanar RMOs that are expected to melt into chiral spin liquids upon the introduction of quantum fluctuations [46], making them natural candidates for the parent states of such spin liquids. Now that we have motivated *where* to look for non-coplanar magnetic orders and *why*, we do so by studying the non-Bravais square-kagome and maple-leaf lattices with further-neighbor interactions via large-scale Monte Carlo simulations in the following chapters.

Square-Kagome Antiferromagnets

Motivated by the recent synthesis of a series of Mott insulators based on the square-kagome lattice, the potential of this geometry to accommodate intricately structured magnetic ground states or quantum spin liquid phases is currently under intense investigation [213–219]. Indeed, no sign of long range magnetic order down to 50 mK has been observed in the spin $S = 1/2$ Cu^{2+} based compounds $KCu_6AlBiO_4(SO_4)_5Cl$ [213] and $Na_6Cu_7BiO_4(PO_4)_4[Cl,(OH)]_3$ [216] despite having large negative Curie-Weiss temperatures of -237 K and -212 K, respectively. On the other hand, their sister compounds $KCu_7(TeO_4)(SO_4)_5Cl$ and $NaCu_7(TeO_4)(SO_4)_5Cl$ develop antiferromagnetic order [217, 218], while related compounds $Rb_7(TeO_4)(SO_4)_5Cl$ and $Cs_7(TeO_4)(SO_4)_5Cl$ do not show any sign of magnetic order down to 2 K [218]. In the following, we provide a comprehensive discussion of the physics of square-kagome antiferromagnets on a classical level by investigating ground states and the thermodynamics of the classical Heisenberg model on this lattice in the presence of nearest-neighbor couplings as well as additional cross-plaquette interactions.

This chapter is largely based on publication [P1], to which the author of this dissertation has contributed the major part, namely almost all numerical simulations, all figures, and large parts of the text. The latter are, therefore, partly adopted one-to-one when it comes to the technical description of the results. If there are contributions of co-authors involved, they will be marked as such in the appropriate places.
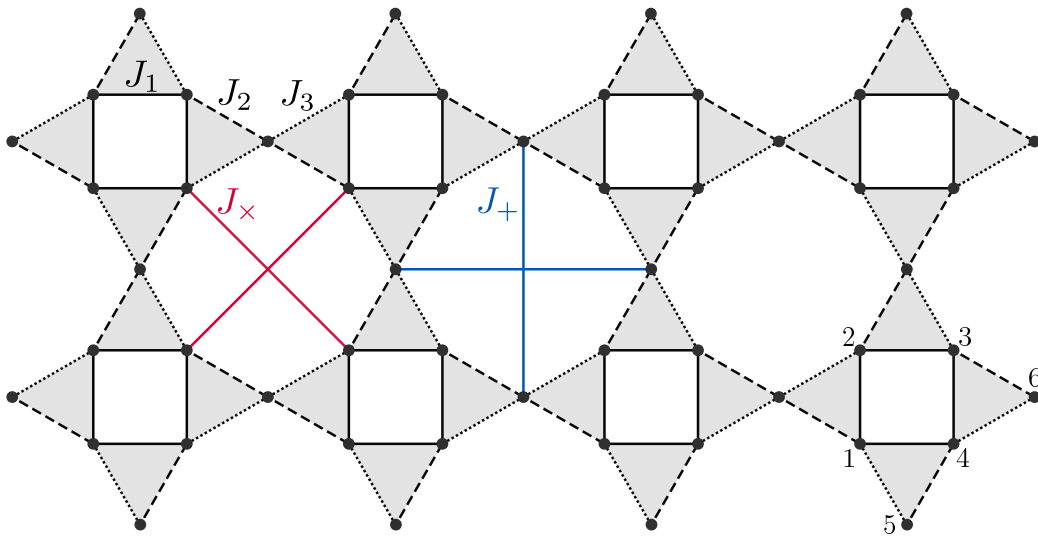
7.1 Square-Kagome Heisenberg Model

The square-kagome lattice [220]—in the literature also referred to as the squagome or shuriken lattice—is a non-Bravais lattice that consists of a two-dimensional network of corner-sharing triangles with alternating square and octagon plaquettes in between, as depicted in Fig. 7.1. The lattice can be described by a square lattice with unit vectors

$$\mathbf{a}_1 = (1, 0)\,, \qquad\qquad \mathbf{a}_2 = (0, 1)\,,$$

and a unit cell comprising six sites with relative coordinates

$$\delta_1 = \left(-\frac{1}{4}, -\frac{1}{4}\right)\,, \qquad\qquad \delta_2 = \left(-\frac{1}{4}, \frac{1}{4}\right)\,,$$

$$\delta_3 = \left(\frac{1}{4}, \frac{1}{4}\right)\,, \qquad\qquad \delta_4 = \left(\frac{1}{4}, -\frac{1}{4}\right)\,,$$

$$\delta_5 = \left(0, -\frac{1}{2}\right)\,, \qquad\qquad \delta_6 = \left(\frac{1}{2}, 0\right)\,.$$

Figure 7.1 – **Square-kagome lattice and interactions.** The square-kagome lattice, also referred to as the squagome or shuriken lattice in the literature, consists of two sets of topologically distinct sites – square sites and bow-tie sites. Nearest-neighbor interactions are referred to as J_1 (square) and J_2, J_3 (bow-tie), respectively. Additionally, we introduce further-neighbor cross-plaquette J_+-bonds ($J_\times$-bonds) as indicated in blue (red). The unit cell contains six spins (labeled 1 to 6), namely the four square sites and two bow-tie sites of a single shuriken star. Figure taken and modified from [P1].

The resulting lattice is *non-Archimedean* since it has two topologically distinct types of sites, namely those forming the square plaquettes (basis sites 1 to 4) and those forming the bow-ties (basis sites 5 and 6).

For this reason, but also because some synthesized square-kagome materials have symmetry inequivalent couplings [213], we allow our classical Heisenberg model Eq. (2.3) to host three different nearest-neighbor couplings, J_a with $a = \{1, 2, 3\}$, on the sides of the elementary triangles, as indicated in Fig. 7.1.

Furthermore, we allow for further-neighbor interactions, J_+ and $J_\times$, across the octagonal plaquettes. Similar interactions across the hexagons in the kagome lattice are known to stabilize non-coplanar spin structures [39, 40, 221, 222], as motivated earlier. These further-neighbor interactions, therefore, give good reason to expect similar results on the square-kagome lattice.

To tackle this model numerically, we employ large-scale Monte Carlo simulations over a wide range of parameters. Our Monte Carlo simulations are performed on finite lattices of $L \times L$ unit cells, i.e. $N = 6L^2$ spins, with periodic boundary conditions. Unless explicitly stated otherwise, we choose $L = 12$ ($N = 864$).

In order to resolve the thermal selection of ground states by subtle thermal order-by-disorder effects at very low temperatures, we employ a parallel tempering/replica exchange Monte Carlo scheme (see Sec. 3.2.2) such that after every 10th (consisting of N local update attempts), spin configurations of neighboring replicas are attempted to be exchanged. For ground state properties, 192 logarithmically spaced temperature points between $T_{\min} = 10^{-4}$ and $T_{\max} = 10$ are simulated simultaneously. In some cases, which are pointed out separately, a conventional Monte Carlo scheme without parallel tempering and 192 linearly spaced temperature points between $T_{\min} = 0.1$ and $T_{\max} = 0.5$ is employed. In all cases, measurements are performed over $5 \cdot 10^8$

sweeps after a thermalization period of 10^8 sweeps. In some cases, our Monte Carlo simulations are complemented by a semi-analytical method, which we will described in detail later. With this in mind, let us now turn to our results.

7.2 Nearest-Neighbor Model

Before we consider the further-neighbor cross-plaquette interactions in more detail, we will first look at the nearest-neighbor Heisenberg model. With just nearest-neighbor interactions the square-kagome model shares much of the same physics as the nearest-neighbor kagome Heisenberg model. Below, we briefly summarize some of the known results for the ground states of the square-kagome model that can be inferred from the conventional kagome antiferromagnet. We then move on to discuss its finite temperature physics and explore critical fluctuations, going beyond what has been studied for the conventional kagome scenario.

The Hamiltonian with nearest-neighbor couplings can be written as

$$\mathcal{H} = \sum_{\langle i,j \rangle \in a} J_a \, \mathbf{S}_i \cdot \mathbf{S}_j \,, \tag{7.1}$$

where $a = \{1, 2, 3\}$ runs over the three different types of bonds, as in Fig. 7.1. However, its properties can be more easily understood by rewriting it as

$$\mathcal{H} = \sum_{i,j,k \in \triangle} \left[\frac{1}{2} \left(\sqrt{\frac{J_1 J_3}{J_2}} \mathbf{S}_i + \sqrt{\frac{J_1 J_2}{J_3}} \mathbf{S}_j + \sqrt{\frac{J_2 J_3}{J_1}} \mathbf{S}_k \right)^2 - \frac{1}{2} \left(\frac{J_1 J_3}{J_2} + \frac{J_1 J_2}{J_3} + \frac{J_2 J_3}{J_1} \right) \right] \,, \tag{7.2}$$

where the sum is now over all four types of elementary triangles of the lattice and we have assumed all couplings to be antiferromagnetic, $J_a > 0$ (such that all of the arguments of the square roots are positive). The Hamiltonian of the kagome Heisenberg model can be written in the same form, but with a key distinction being the number and nature of elementary triangles that are summed over. The new form of the Hamiltonian allows us to easily construct a special class of classical ground states. These are the states that satisfy the constraint

$$\left(\sqrt{\frac{J_1 J_3}{J_2}} \mathbf{S}_i + \sqrt{\frac{J_1 J_2}{J_3}} \mathbf{S}_j + \sqrt{\frac{J_2 J_3}{J_1}} \mathbf{S}_k \right) = 0 \,. \tag{7.3}$$

where $\mathbf{S}_i, \mathbf{S}_j$ are the spins on the squares and $\mathbf{S}_k$ is the spin on the centers of the bow-ties. To see that such states are indeed ground states, note that the Hamiltonian, for a given set of parameters, is the sum of a squared term, which is always positive, and a constant term. The minimal possible energy is thus obtained when the squared term is precisely zero, i.e., the constraint above. However, there is the additional constraint that the spins at each site are all properly normalized, $|\mathbf{S}_i| = 1 \, \forall \, i$. Satisfying both of these constraints is only possible within a restricted region of parameter space, namely

$$-2 \leq \frac{J_2 J_3}{J_1^2} - \left(\frac{J_2}{J_3} + \frac{J_3}{J_2} \right) \leq +2 \,. \tag{7.4}$$

Thus, within this parameter region, all spin configurations satisfying the constraint of Eq. (7.3) on each and every triangle are guaranteed to be bona fide ground state spin configurations. This includes both globally coplanar and non-coplanar spin configurations as, though the three spins in each triangle are constrained to lie within the same plane, it is not necessary that the planes for different triangles are the same.

The resulting unusual and highly degenerate phase is the classical spin liquid indicated in the phase diagram of Fig. 7.2(a) and previously reported in Ref. [223], which shares the same qualitative physics as the classical spin liquid found in the distorted kagome version of the model [224–227]. At the isotropic point, $J_1 = J_2 = J_3$, the spins in each triangle lie within the same plane at an angle of exactly 120° away from one another. On the other hand, away from the isotropic point, e.g. along the diagonal line $J_2 = J_3$, the coplanar spin configuration for a single triangle obeying the constraint can be written as

$$
\begin{aligned}
\mathbf{S}_i &= (-J_2/(2J_1), -\sqrt{4 - (J_2/J_1)^2}/2, 0), \\
\mathbf{S}_j &= (-J_2/(2J_1), +\sqrt{4 - (J_2/J_1)^2}/2, 0), \\
\mathbf{S}_k &= (1, 0, 0),
\end{aligned}
\tag{7.5}
$$

where we have fixed the spins to lie in the xy-plane for simplicity. As one increases J_2 from $J_2 = 0$ to $J_2 = 2J_1$, the angle θ between $\mathbf{S}_k$ (the spin on the bow-tie) and the other two spins (on the squares) increases from $\pi/2$ to π, passing through $2\pi/3$ exactly at the isotropic point $J_2 = J_1$ [228]. For globally coplanar spin configurations, which are the relevant configurations at the lowest temperatures as we will see in the next section, as well as the constraints already mentioned, there is one additional form of constraint [224]. It is related to how the spins in the triangles around the square and octagonal plaquettes of the lattice are arranged. For globally coplanar ground state spin configurations, we can define on each triangle a chirality variable, $\eta_a = \pm 1$, which encodes whether the spins rotate clockwise or anti-clockwise as one goes from say i to j to k [229] (keep in mind that the angles between the spins in each triangle are fixed, e.g. all three angles are fixed to $2\pi/3$ at the isotropic point).
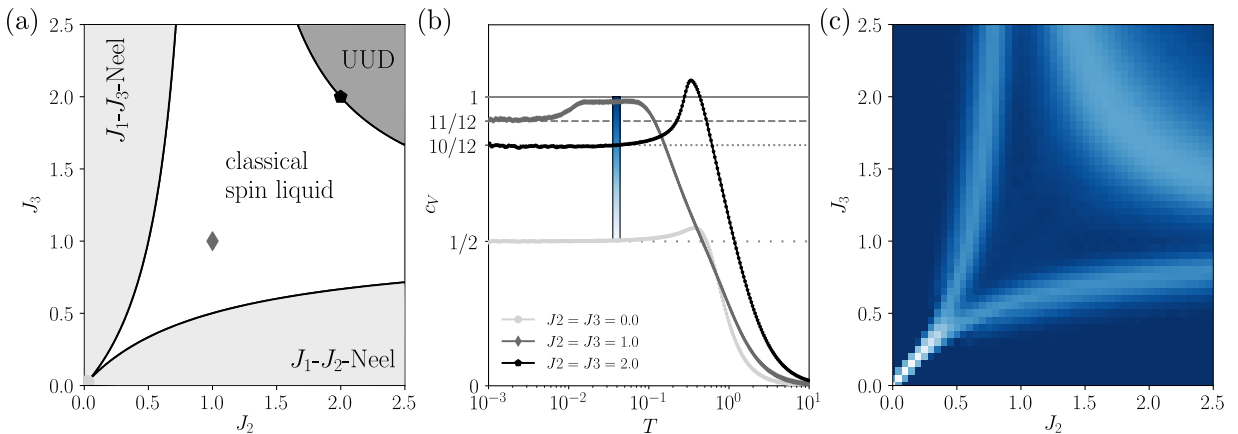
Figure 7.2 – **The nearest-neighbor model.** (a) Zero-temperature phase diagram as a function of nearest-neighbor couplings J_2 and J_3, reproduced from Ref. [223] via Eq. (7.4). (b) Specific heat traces obtained from Monte Carlo simulations for three representative points along the $J_2 = J_3$ diagonal in the phase diagram of panel (a). The one for the isotropic point, $J_1 = J_2 = J_3 = 1$, closely resembles the well-studied specific heat trace of the kagome AFM [37, 38]. (c) Specific heat scan across the phase diagram of panel (a) at fixed, low temperature of $T = 0.04$ (in units of $J_1 = 1$). Figure taken from [P1].

Now, starting from an initial spin which points in some specific direction, if one travels in a closed loop on the lattice then one must return back to that same initial spin pointing in that same specific direction. However, as one travels along each bond the chirality variables dictate in which direction the spins rotate, and so in order to get back to the same initial spin there is a constraint on the sum of the chirality variables along the closed loop. At the isotropic point, we require $\sum_a \eta_a = 0$ for the four triangles surrounding a square, and $\sum_a \eta_a = 0, \pm 6$ for the eight triangles surrounding an octagon. Away from the isotropic point there will in general be more stringent constraints as the angle between spins is no longer $2\pi/3$, but instead some angle incommensurate with respect to 2π. This results, for a given lattice size, in a smaller number of allowed coplanar ground state spin configurations, just as in the analogous kagome case [224].

Outside of the classical spin liquid region there are two distinct Néel states in the phase diagram of of Fig. 7.2(a), depending on whether J_2 or J_3 dominates. In each phase, spins are arranged antiferromagnetically along the bonds with the dominant coupling, and ferromagnetically along the weaker bonds. On the other hand, for dominant $J_2 = J_3$, there is an up-up-down (UUD) state, sometimes also referred to as a Lieb ferrimagnet [230], in which the spins on the squares point along one direction while the spins on the bow-ties point in the opposite direction (this can be seen from Eq. (7.5) with $J_2 = 2J_1$, the critical point between the classical spin liquid and UUD state).

7.2.1 Finite-Temperature Physics

The unusual nature of the classical spin liquid phase is naturally revealed by examining how the specific heat behaves as a function of temperature. For two-dimensional Heisenberg models with finite-range exchange interactions, true long range magnetic order cannot set in at any non-zero temperature, as laid out in the Mermin-Wagner theorem [231]. However, it is possible for quasi-long-range order to develop, signaled by a peak in the specific heat. Our discussion, in the following, of such quasi-long-range "orders" is based on an analysis of the symmetry of spin-spin correlations. In the case of non-coplanar, i.e., chiral orders, however, a true thermal phase transition associated with the breaking of discrete symmetries occurs.

As briefly discussed in Sec. 2.4, at the lowest temperatures, one generically expects that, in the thermodynamic limit, the specific heat per site $c_V \to 1$ as $T \to 0$. This is because each spin is free to fluctuate about its ordered ground state in two orthogonal directions on the unit sphere. These two quadratic modes each contribute $(1/2) \cdot T$, as dictated by classical equipartition, to the energy and thus $1/2$ to the specific heat (setting $k_B = 1$). However, as first discussed in the context of the kagome antiferromagnet [74], this simple counting breaks down within the classical spin liquid region, as well as in an extended finite temperature fan about the critical lines in the phase diagram. The breakdown is due to the entropic selection of a subset of ground state spin configurations, those which carry the largest entropy and thus the lowest free energy at finite temperature. Classical fluctuations about this favored subset include one or more zero modes at the harmonic level, which contribute $1/4$ (i.e. they are quartic modes), rather than $1/2$, to the specific heat. The deviation of the low-temperature specific heat from $c_V \to 1$ thus serves as a signature of this phenomenon of thermal order by disorder. In Fig. 7.2(b), we show the specific heat as a function of temperature for three special parameter points along the diagonal line $J_2 = J_3$, with a number of curves in between shown in Fig. 7.3(a) and (b).
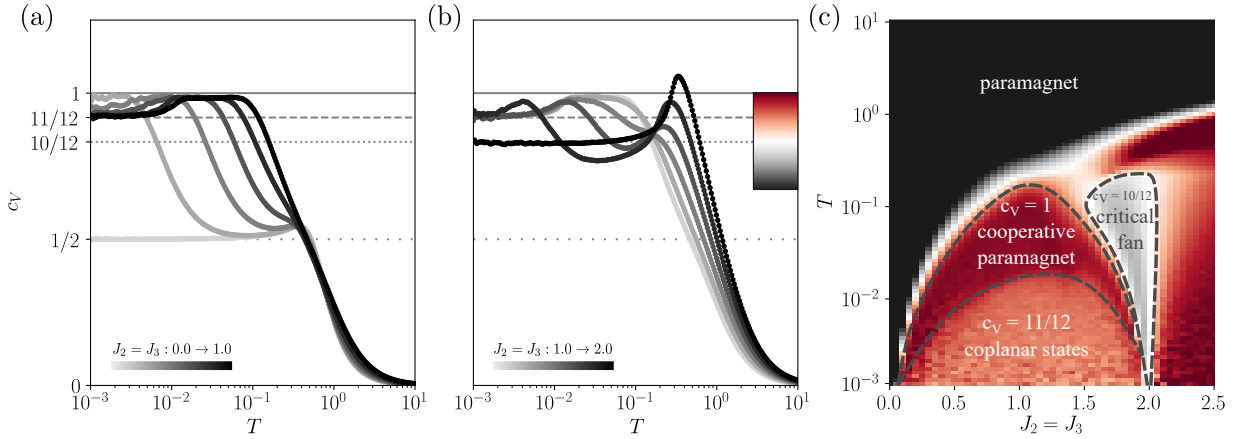
Figure 7.3 – **The nearest-neighbor model II.** (a) Specific heat traces from Monte Carlo simulations for $0.0 \leq J_2 = J_3 \leq 1.0$ (in steps of 0.2). (b) Specific heat traces for $1.0 \leq J_2 = J_3 \leq 2.0$. Of special interest is the curve for $J_2 = J_3 = 2.0$ which is the only one which converges to a value of $c_V = 10/12$. (c) Finite temperature specific heat along the diagonal $J_2 = J_3$ illustrating the $c_V = 1$ plateau of the cooperative paramagnet (dark red area), the coplanar phase with $c_V = 11/12$ (light red area), the critical fan with $c_V \leq 10/12$ (grey area), and the paramagnetic phase (black region). Figure taken from [P1].

(i) First, starting with $J_2 = J_3 = 0$, we have the trivial limit of fully disconnected squares. Alternatively, one can think of this limit as consisting of decoupled four-site periodic Heisenberg chains. The spins order in a simple antiferromagnetic arrangement within each square. There are 8 quadratic modes per square, minus two due to the global rotational symmetry of the antiferromagnetic moment. This leaves us with 6 independent quadratic modes, and a contribution to the specific heat per site as $c_V \rightarrow [6 \cdot (1/2)]/6 = 1/2$ as $T \rightarrow 0$ [232]. (ii) At the isotropic point, there are three distinct regimes, which share the same physics as the isotropic kagome model at finite temperatures [38] (the similarity even extends to the spin-1/2 quantum case [233]). There is the usual high-temperature paramagnetic region, followed by a cooperative paramagnetic regime and finally a coplanar state at the lowest temperatures. These three regimes can be observed throughout the classical spin liquid phase. The cooperative paramagnet is clearly distinguished by a plateau in the specific heat with $c_V \approx 1$. Within this temperature window, the system fluctuates between the full (extensive) number of states within the ground state manifold that satisfy the constraint in Eq. (7.3). At lower temperatures, within the coplanar states, fluctuations select the subset of globally coplanar states within the ground state manifold via the entropic-driven order-by-disorder mechanism. This is accompanied by $c_V \rightarrow [10 \cdot (1/2) + 2 \cdot (1/4)]/6 = 11/12$ as $T \rightarrow 0$ due to the presence of one zero mode per triangle (thus two zero modes per unit cell) within the spectrum of classical harmonic fluctuations (very similar to the conventional kagome case [74]). (iii) At $J_2 = 2J_1$ we have the transition between the classical spin liquid and UUD state. Precisely at this critical point an additional zero mode per triangle leads to $c_V \rightarrow [8 \cdot (1/2) + 4 \cdot (1/4)]/6 = 10/12$ as $T \rightarrow 0$.

The evolution of the specific heat between these three special points, as one increases $J_2 = J_3$, is shown in Fig. 7.3(c). Starting from the trivial limit, $J_2 = J_3 = 0$, the width of the plateau that develops at $c_V \approx 1/2$ shrinks as the interaction scale that couples squares, $J_2 = J_3$, grows. At low temperatures, the characteristic two temperature regimes emerge, with the cooperative paramagnet and coplanar regimes giving rise to plateaus at $c_V = 1$ and $11/12$, respectively. The $1/2$-feature disappears completely at the isotropic point. As one moves past the isotropic point, the width of the cooperative paramagnet plateau starts to decrease, until it eventually disappears completely at the critical point $J_2 = 2J_1$.

At the same time, in the temperature regime above the cooperative paramagnet, there is a substantial drop in the specific heat as a result of increasing fluctuations on approaching the critical point (which damps the entropy loss in this temperature regime and thus the specific heat). This can be more clearly seen in Fig. 7.3(c), where the drop manifests itself as a *finite temperature fan*, emanating from the zero-temperature critical point—reminiscent of the fan-like structure at quantum critical points [234].

We conclude this section by presenting the finite size scaling behaviour of the previously discussed c_V data for $J_2 = J_3 \in [0.0, 1.0, 2.0]$. Fig. 7.4 shows that for three different system sizes, $L = 8, 12, 16$, the curves fall onto each other. This indicates that the observed behaviour is universal and independent of system size.

## 7.2.2 Spin-Spin Correlations

To explore the formation of quasi-long-range order and cooperative paramagnetic phases in the absence of any true thermal phase transitions, we turn to the static spin structure factor, i.e. the Fourier transform of the equal-time real-space spin-spin correlations, that is,

$$S(\mathbf{q}) = \frac{1}{N} \sum_{i,j=1}^{N} \langle \mathbf{S}_i \cdot \mathbf{S}_j \rangle e^{i\mathbf{q} \cdot (\mathbf{r}_i - \mathbf{r}_j)} , \tag{7.6}$$

where N is the number of lattice sites, $\mathbf{q}$ is a momentum inside the extended Brillouin zone, and $\mathbf{r}_i$ denotes the position of site i.

Sharp peak-like features in $S(\mathbf{q})$ indicate the formation of quasi-long-range order, while the tell-tale signatures of cooperative paramagnets are pinch points in momentum space, which map
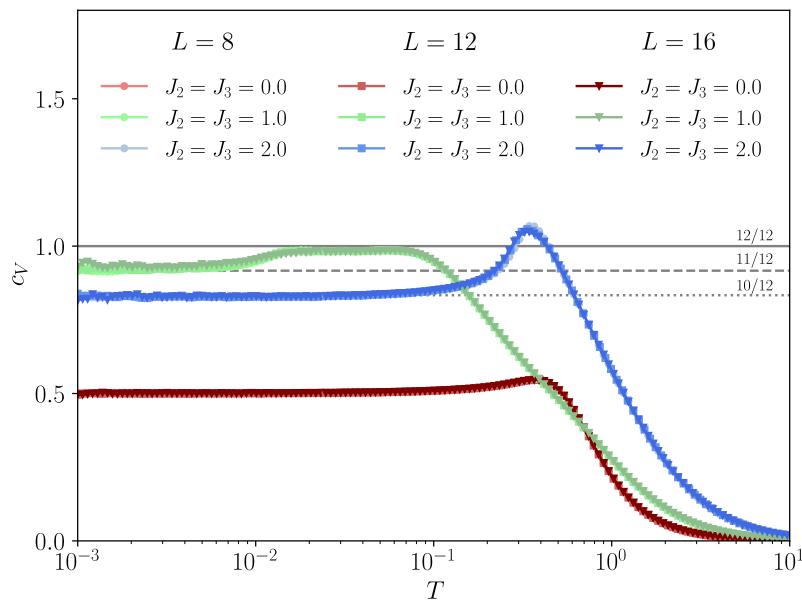
Figure 7.4 – **Finite-size scaling of c_V for selected parameters in the nearest-neighbor model.** Specific heat traces from Monte Carlo simulations for $J_2 = J_3 = 0.0, 1.0, 2.0$ for different system sizes $L = 8, 12, 16$, showing no system size dependence. Figure taken from [P1].

to algebraically decaying correlations in real space, as discussed in Sec. 2.6.

In Fig. 7.5, we provide a comprehensive overview of the static structure factor over a wide range of temperatures and parameter points. In some cases, such as rows (g) and (h), the ground state is quasi-long-range-ordered and sharp peaks are clearly visible at the corresponding ordering wavevectors. In other cases, i.e. within the classical spin liquid parameter region, we observe a complex redistribution of spectral weight as the system passes through the three distinct finite temperature regimes.

For the isotropic point ($J_2 = J_3 = 1.0$), the $S(\mathbf{q})$ at the highest temperature shown in Fig. 7.5(b) only displays a broad diffuse profile corresponding to a weakly correlated thermal paramagnet. Inside the cooperative paramagnetic regime, at $T = 0.1$ and 0.05, pinch points (with a finite-width set by the inverse correlation length) appear between the square and lobed shaped regions of stronger relative intensity. Their presence signifies the approximate fulfillment of the $\mathbf{S}_\triangle = 0$ constraint of Eq. (7.3) and thus the onset of strong correlations between spins within triangular plaquettes.

Upon cooling further, at $T = 0.03$ and 0.02, the intensity is redistributed to the centers of squares and lobes located at $\mathbf{q} = (4\pi, 0)$ and $\mathbf{q} = (2\pi, 2\pi)$ (and symmetry related points), respectively. Since one is still in the cooperative paramagnetic regime characterized by a dipolar $\sim 1/r^2$ decay of spin-spin correlations (at distances smaller than the correlation length), these high intensity features do not correspond to Bragg peaks.

Finally, once order by disorder kicks in at $T \lesssim 0.01$ selecting coplanar states, we notice the disappearance of spectral weight at the location of the pinch point as well as the absence of narrow necks connecting the squares with the lobes. The presence of well-defined maxima at the aforementioned points indicates enhanced correlations of the 120° $\mathbf{q} = \mathbf{0}$ type order [215, 235], in contrast to the conventional kagome antiferromagnet which favors $\sqrt{3} \times \sqrt{3}$ correlations [236–238]. While the kagome antiferromagnet develops long range dipolar magnetic order of the $\sqrt{3} \times \sqrt{3}$ type in the limit $T \to 0$ [238], it remains to be established on the square-kagome lattice whether true long range $\mathbf{q} = \mathbf{0}$ dipolar ordering of 120° type asymptotically develops as $T \to 0$.

Away from the isotropic point, but still on the line $J_2 = J_3$, we first note that the cooperative paramagnetic and coplanar temperature regimes are pushed down to smaller T and shrink in extent (see Fig. 7.3). At $J_2 = J_3 = 0.5$, within the cooperative paramagnetic regime ($0.008 \lesssim T \lesssim 0.05$), the pinch points are seen to be present, and with the principal spectral weight at the center of the lobes $\mathbf{q} = (2\pi, 2\pi)$ (and symmetry related points) which progressively increases, together with a relatively weaker signal at the centers of the squares $\mathbf{q} = (4\pi, 0)$ (and symmetry related points) (see Fig. 7.5(a)).

However, upon entering the coplanar regime, at $T = 0.003$, an equally strong maximum develops at the $\mathbf{q} = (4\pi, 0)$ type points, but in contrast to the isotropic point, these are not indicative of enhanced $\mathbf{q} = \mathbf{0}$ correlations of the 120° type. Similar observations hold true at $J_2 = J_3 = 1.5$ (see Fig. 7.5(c)) with the noticeable difference being the presence of a finite spectral weight at the Brillouin zone centre, being more pronounced in the intermediate temperature, i.e., cooperative paramagnetic regime. Moving away from the symmetric line, i.e., $J_2 \neq J_3$ but still inside the degenerate manifold region, one observes that the $S(\mathbf{q})$ are only rotationally invariant possibly reflective of the underlying symmetries of the incipient magnetic order in the limit $T \to 0$.
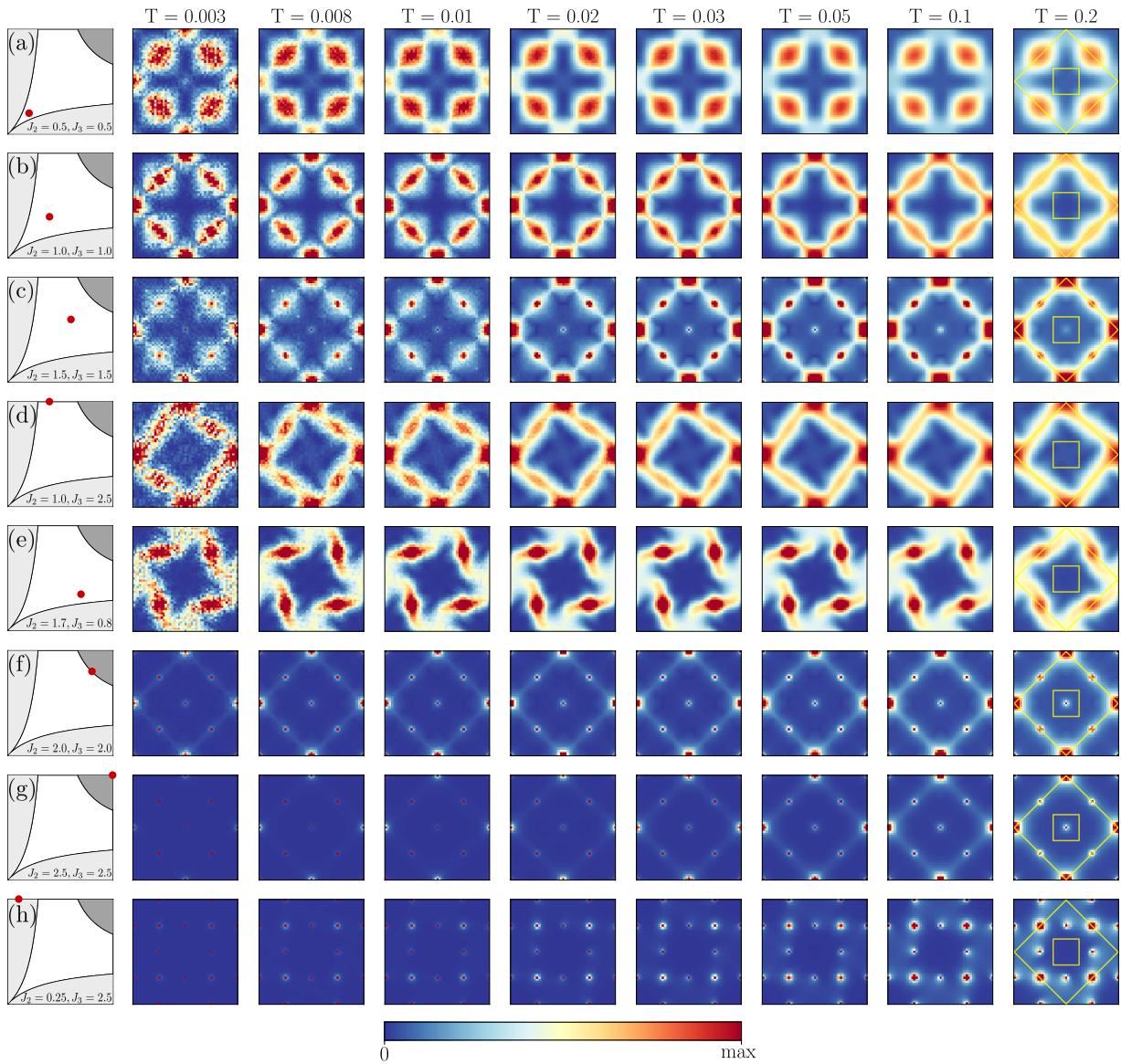
Figure 7.5 – **Structure factors of the J_1-J_2-J_3 model.** Structure factors from Monte Carlo simulations for different temperatures between T = 0.003 and T = 0.2 (left to right) and for different values of J_2 and J_3 as indicated in the phase diagram in the left column (top to bottom). The shown squares extent in reciprocal space from -4π to 4π in both dimensions. Rows (a) to (c) show structure factors on the diagonal $J_2 = J_3$ within the classical spin liquid regime, especially for the isotropic point $J_1 = J_2 = J_3 = 1.0$ in row (b), which agrees well with the result obtained via large-N analysis in [215]. Rows (d) and (e) as well show structure factors in the classical spin liquid regime, but off the diagonal with different values for J_2 and J_3. All structure factors within the classical spin liquid regime show sharp pinch point-like features upon entering the cooperative paramagnetic regime at around $T = 0.01$, which broaden with increasing temperature. The statistical noise at lower temperatures is due to freezing in Monte Carlo sampling. The lower three rows (f) to (h) display structure factors outside the classical spin liquid regime, namely directly on the transition line to the UUD phase, $J_2 = J_3 = 2.0$, in (f), within the UUD phase, $J_2 = J_3 = 2.5$, in (g), and in the J_1-J_3-Néel ordered phase, $J_2 = 0.25$ and $J_3 = 2.5$, in (h). Figure taken from [P1].

Upon cooling, a progressive redistribution of spectral weight occurs leading to the appearance of new soft maxima in the coplanar regime at $(J_2, J_3) = (1.0, 2.5)$ (see Fig. 7.5(d)) while at $(J_2, J_3) = (1.7, 0.8)$ (see Fig. 7.5(e)) interestingly a similar intensity distribution prevails across all temperatures. Finally, inside the magnetically ordered regions, the $S(\mathbf{q})$ become more sharply peaked, as expected, and interestingly the $S(\mathbf{q})$ at $(J_2, J_3) = (2.0, 2.0)$ (see Fig. 7.5(f)) and $(J_2, J_3) = (2.5, 2.5)$ (see Fig. 7.5(g)) resemble those inside the disordered regime at $(J_2, J_3) = (1.5, 1.5)$ seen in Fig. 7.5(c) along the $J_2 = J_3$ axis as if pre-empting the UUD order which onsets for $J_2 = J_3 \geq 2.0$. Inside the Néel phase at $(J_2, J_3) = (0.25, 2.5)$, in Fig. 7.5(h) there is no spectral weight at the centre of the Brillouin zone as expected, and instead we find dominant peaks at the $(2\pi, 2\pi)$ (and symmetry related) points, and subdominant peaks at $(2\pi, 0)$ (and symmetry related) points.

7.3 Octagon-Plaquette Interactions

We now augment the nearest-neighbor model, discussed in the previous Section, with the cross octagon-plaquette interactions J_+ and $J_\times$ (cf. Fig. 7.1), which microscopically arise upon the inclusion of longer-range Heisenberg couplings. Conceptually, they are interesting as they are expected to stabilize non-coplanar magnetic orders, akin to the cross-hexagonal interactions in the conventional kagome case, and in distinction to square-diagonal couplings.

Indeed, we find that the cross octagon-plaquette interactions induce a plethora of non-coplanar orders as summarized in the global phase diagram of Fig. 7.6. One can, in fact, distinguish *ten* different phases (labeled I to X), indicated by the different colors in the phase diagram, as one varies the relative coupling strength of the two couplings, J_+ and $J_\times$, starting from an isotropic nearest-neighbor model (i.e. for fixed $J_1 = J_2 = J_3 = 1$). The distinct nature of these phases can be easily visualized by representative common origin plots for each phase, i.e. the collapse of an extended ground state real-space configuration of spins to a single unit sphere by placing all spins at a joint origin. These are shown around the phase diagram. In addition, we show their respective spin structure factors. Let us briefly go through these phases here, before providing a much more detailed description in the remainder of this Section. Following this detailed description, the results are later summarized once again in Table 7.1.

The only phases with coplanar order come in the form of a 120° ordered phase (VI) in the lower left quadrant, i.e. for ferromagnetic J_+ and $J_\times$ (indicated by dark gray in Fig. 7.6), as well as a distorted version of this 120° order (VII) for slightly positive $J_\times$ (indicated by light gray in the phase diagram). In the plain-vanilla 120° ordered phase spins on elementary triangles form mutual angles of $2\pi/3$, while this angle is increased beyond $2\pi/3$ in the distorted phase as discussed in Sec. 7.3.2. All other phases of the phase diagram exhibit non-coplanar order, which come in commensurate and incommensurate forms[1]. The simpler, commensurate variant of such non-coplanar order is the extended phase with cuboctahedral order (I) in the upper right quadrant and a distorted version of this (II), which we discuss in depth in Sec. 7.3.3. Somewhat more complex non-coplanar orders come in incommensurate spin spiral order, which we find for the remaining six phases (III-V and VIII-X). Remarkably, however, these can still be described by a semi-analytical ground state construction [239–245], which we describe in Sec. 7.3.4.

---

[1] A magnetic order is said to be *incommensurate* when its periodicity cannot be matched to the periodicity of the underlying lattice.
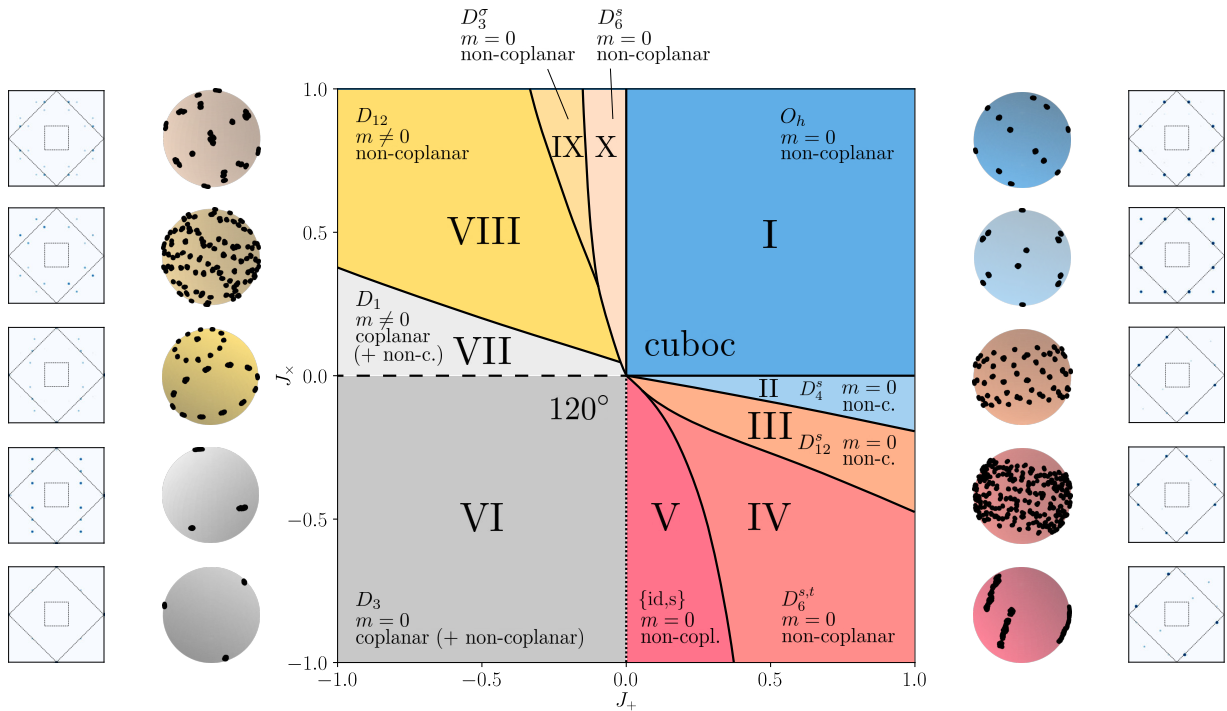
Figure 7.6 – **Phase diagram in the presence of cross-octagonal couplings.** At the center we show the phase diagram with ten different phases (labeled I to X) as a function of J_+ and $J_\times$ for a nearest-neighbor model with isotropic, antiferromagnetic interactions, i.e. $J_1 = J_2 = J_3 = 1$. (A companion phase diagram for ferromagnetic nearest-neighbor couplings is later shown in Fig. 7.23.) Besides indicating the phase boundaries (solid, dashed and dotted lines), the phases are described by symmetry (with D_n referring to the dihedral group of order n and O_h to full octahedral symmetry), coplanarity, and magnetization of their ground states. As a quick visualization of their distinct nature, we show common origin plots and spin structure factors for each phase left and right around the phase diagram. The only coplanar orders are found in form of 120° order (VI) in the lower left quadrant, i.e. ferromagnetic J_+ and $J_\times$ (darker gray phase), as well as a distorted version of this (VII) for sligthly positive $J_\times$ (lighter gray phase). All other phases are non-coplanar, which besides a rigid phase with cuboctahedral order (I) in the upper right quadrant and a distorted version of this (II) include a variety of different spirals (III-V and VIII-X). Phase boundaries of special interest are found upon exiting the coplanar 120° order, indicated by the dashed and dotted lines, along which the low temperature specific heat $c_V(T \to 0)$ takes values of 11/12 and 23/24, respectively (cf. Fig. 7.7). Figure taken from [P1].

7.3.1 Physics on the Axes

Before we dive into the various magnetic orders that can be stabilized by the combined effects of cross octagon-plaquette interactions, we first consider their exclusive effect, i.e. we consider the horizontal and vertical axes in the middle of the phase diagram of Fig. 7.6. Adding *only one* of the two cross octagon-plaquette interactions ($J_\times$ or J_+ only), it turns out that it is still possible to locally satisfy the constraint of Eq. (7.3) provided that the added interaction is ferromagnetic in nature.

For FM J_+, the spins located on the bow-ties become locked together and are all ferromagnetically aligned, meaning that $\mathbf{S}_k$ in the constraint Eq. (7.3) is fixed in each and every triangle to be the same. Denoting this fixed direction by $\mathbf{M}$, the remaining two spins (located on the squares) are thus subject to the local constraint on each triangle

$$\mathbf{S}_i + \mathbf{S}_j = -\mathbf{M}. \tag{7.7}$$

87

This results in a global spin configuration in which 1/3 of the spins point along **M** while the other 2/3 point along a ring at an angle of $2\pi/3$ away from **M**. This removes the possibility of having an extensive number of both globally coplanar and globally non-coplanar ground states, and thus there are only two distinct finite temperature regimes. In other words, entropic-driven selection of globally coplanar configurations would result in a regular 120° ordered state. At high temperatures there is the usual paramagnetic regime, and at low temperatures a crossover into the ground state manifold with an accompanying specific heat $c_V \to 11/12$ as $T \to 0$, due to the continued existence of one zero mode per triangle. This is precisely what we find in finite-temperature Monte Carlo simulations as shown in Fig. 7.7. For FM $J_\times$, the spins within each octagon coupled by $J_\times$ become locally ferromagnetically aligned, but the spins from one octagon to the next are not. This locks neighboring triangles together, resulting in one zero mode per unit cell, as opposed to one zero mode per triangle, and thus a low-temperature specific heat $c_V \to [11 \cdot (1/2) + 1 \cdot (1/4)]/6 = 23/24$ as $T \to 0$. This, again, is in perfect agreement with finite-temperature Monte Carlo simulations as shown in Fig. 7.7. Corresponding finite size scaling data to the data of Fig. 7.7 is shown in Fig. 7.8. For $J_+ = 0.0, J_\times = -1.0$ ($J_2 = J_3 = 1.0$), the curves, again, fall onto each other for all system sizes. In the case $J_+ = -1.0, J_\times = 0.0$, the feature at higher temperatures scales with increasing system size, while the feature at lower temperatures does not.

In comparison to the spin structure factors, summarized for the nearest-neighbor model in Fig. 7.5, the spin-spin correlations discussed above lead to a deformation of $S(\mathbf{q})$ as shown in Fig. 7.9. The $S(\mathbf{q})$ for ($J_+ = -1.0, J_\times = 0.0$) show maxima at positions where the Bragg peaks of the incipient $\mathbf{q} = \mathbf{0}$ order of the 120° type would show up as $T \to 0$ [215]. In contrast, for ($J_+ = 0.0, J_\times = -1.0$), the $S(\mathbf{q})$ display maxima at the expected locations for $\sqrt{3} \times \sqrt{3}$ order [215].
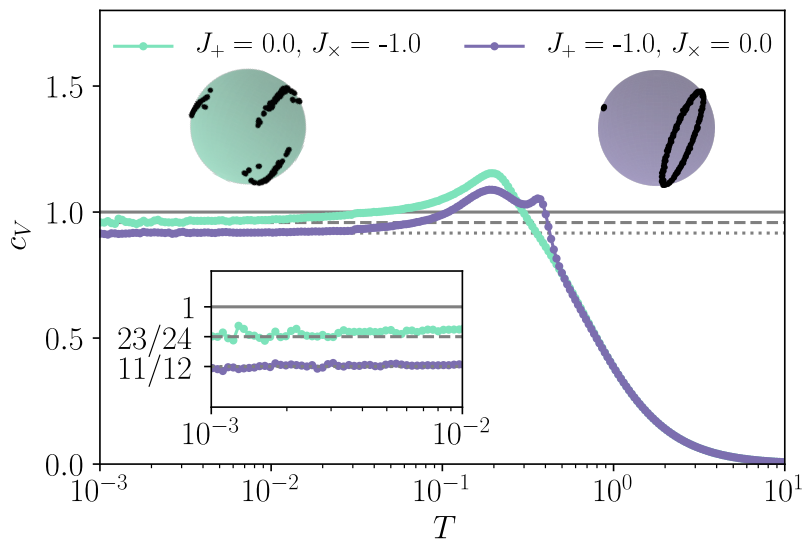
Figure 7.7 – **Specific heat and ground states of the extended model on the axes.** For either only J_+ or $J_\times$ turned on and being ferromagnetic, one again finds special values of $c_V(T \to 0)$ that differ from 1. For For $J_\times = 0.0, J_+ < 0.0$, the value is 11/12 (cf. purple curve with $J_+ = -1.0$), and for $J_+ = 0.0, J_\times < 0.0$, we find a value of 23/24 (cf. mint curve with $J_\times = -1.0$). The upper insets show common origin plots of the corresponding ground states. Figure taken from [P1].
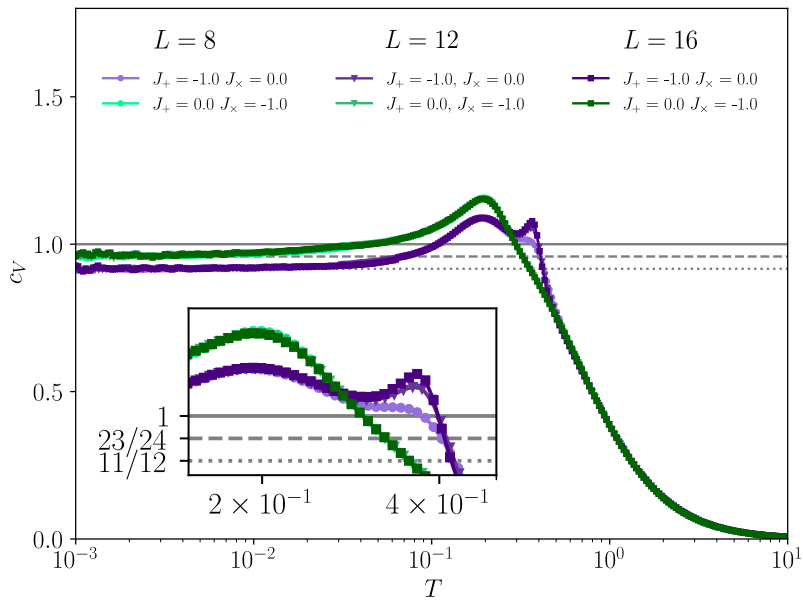
Figure 7.8 – **Finite-size scaling of c_V on the axes of the extended model.** Specific heat traces for $J_+ = -1.0, J_\times = 0.0$ and $J_+ = 0.0, J_\times = -1.0$ ($J_2 = J_3 = 1.0$) for different system sizes $L = 8, 12, 16$. Figure taken from [P1].
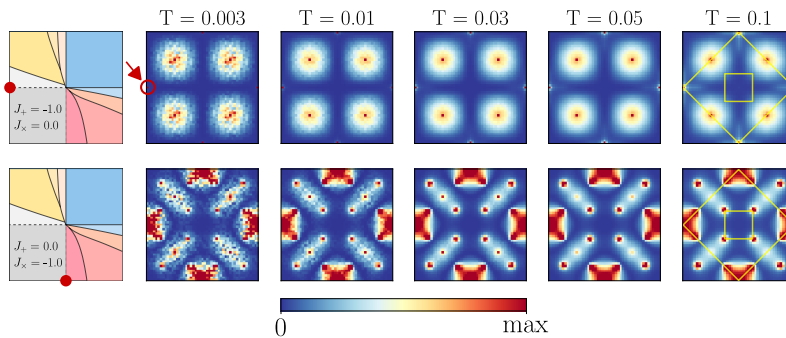

Figure 7.9 – **Structure factors of the extended model on the axes.** Structure factors for different temperatures between T = 0.003 and T = 0.1 (left to right) on the axes ($J_+ = -1.0, J_\times = 0.0$ on the top and $J_+ = 0.0, J_\times = -1.0$ on the bottom). Note the sharp maxima at $(-4\pi, 0)$ and symmetry related momenta in the top row (indicated by red circle). The shown squares extent in reciprocal space from -4π to 4π in both dimensions. For $T = 0.1$, the first Brillouin zone and the extended Brillouin zone are indicated. Figure taken from [P1].

7.3.2 120° Order

Turning to the magnetically ordered states of our phase diagram in Fig. 7.6, we start with the 120° order found in the lower left quadrant where both cross octagon-plaquette couplings are ferromagnetic. While at zero temperature the ground state is degenerate and coplanar states as well as non-coplanar states with the same energy exist, this degeneracy is lifted at small, finite temperatures and coplanar states are selected over non-coplanar states by a thermal order-by-disorder mechanism. Therefore, we start our discussion concentrating on these coplanar states, whereas the non-coplanar states are discussed afterwards.

Coplanar States

For the square-kagome lattice geometry at hand, one can, in principle, distinguish three different types of $120°$ coplanar orders, each with three sublattices where the spins on each sublattice point to a different corner of an equilateral triangle such that each neighboring pair of spins forms an angle of $2\pi/3$. As illustrated in Fig. 7.10, the magnetic unit cell coincides either with the geometric 6-site unit cell as in the regular $\mathbf{q} = 0$ order shown in Fig. 7.10(a), or contains either 12 sites and is two times larger than the geometric unit cell for the type shown in Fig. 7.10(b), or 24 sites for the type in Fig. 7.10(c), with the difference between the two latter types coming down to the bow-tie spins. While these bow-tie spins are all pointing in the same direction in the order of Fig. 7.10(b) forming a bow-tie ferromagnet, the bow-tie spins in the second type of $120°$ order form stripy antiferromagnets with alternating rows/columns of up and down-pointing
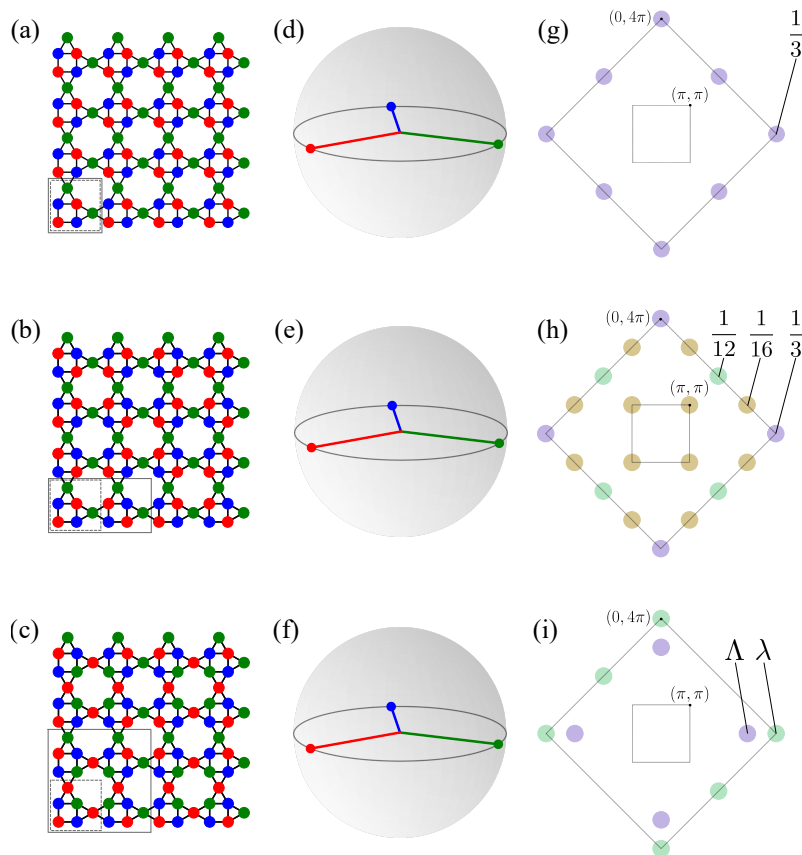

Figure 7.10 – **Coplanar** $120°$ **orders.** (a), (b), and (c) show real space arrangements of spins in the three different coplanar $120°$ ordered states, with (a) corresponding to regular $\mathbf{q} = (0,0)$ order, (b) corresponding to $\mathbf{q} = (0,0)$ and $\mathbf{q} = (\pi,\pi)$ and (c) having no $\mathbf{q}$ vectors at all . The states have either a 6-site magnetic unit cell that coincides with the geometric unit cell (a), a 12-site magnetic unit cell (large gray square), which is two times larger than the geometric unit cell (small square) (b), or a 24-site magnetic unit cell (c), respectively. The magnetization of the square-diagonal spins, m_{diag}, is 1.0 for state (a), 0.5 for state (b), and 0.25 for state (c). (d)+(e)+(f) There are each three sublattices (each one corresponding to one color). Each sublattice of spins points towards a different corner of an equilateral triangle such that each neighboring pair of spins forms an angle of $2\pi/3$. (g)+(h)+(i) First and extended Brillouin zones of the square-kagome lattice showing the positions of the corresponding dominant and subdominant Bragg peaks. In (i), the ratio of the weight of the subdominant peaks λ to the weight of the dominant peaks Λ is $\lambda/\Lambda \approx 85\%$. Arising from these three coplanar orders, there are three one-parameter families of non-coplanar orders, whose details are shown later in Fig. 7.12. Figure taken from [P1].

spins as shown in Fig. 7.10(c). The magnetization of the spins on the main diagonal of the squares, m_{diag}, is different for all three types of order with $m_{\mathrm{diag}} = 1.0$ for order Fig. 7.10(a), $m_{\mathrm{diag}} = 0.5$ for order Fig. 7.10(b), and $m_{\mathrm{diag}} = 0.25$ for order Fig. 7.10(c) (see also Fig. 7.11). A schematic of the static spin structure factors corresponding to these types of real-space $120°$ order is shown for an extended Brillouin zone of the square-kagome lattice in Fig. 7.10(g), (h), and (i), respectively. All three spin configurations exhibit the symmetry of the dihedral group D_3. Their net magnetization vanishes, $m = 0$, and the energy per site can be calculated as

$$E_{120°} = -1 + \frac{1}{3}(J_+ + J_\times)\,, \tag{7.8}$$

for varying strengths of the two couplings.

To elucidate the thermodynamics associated with these $120°$ orders we show, in Fig. 7.11, specific heat traces for the point in the lower left corner, $J_+, J_\times = -1$ (i.e. deep in the phase), for different system sizes between $L = 8$ and $L = 32$.
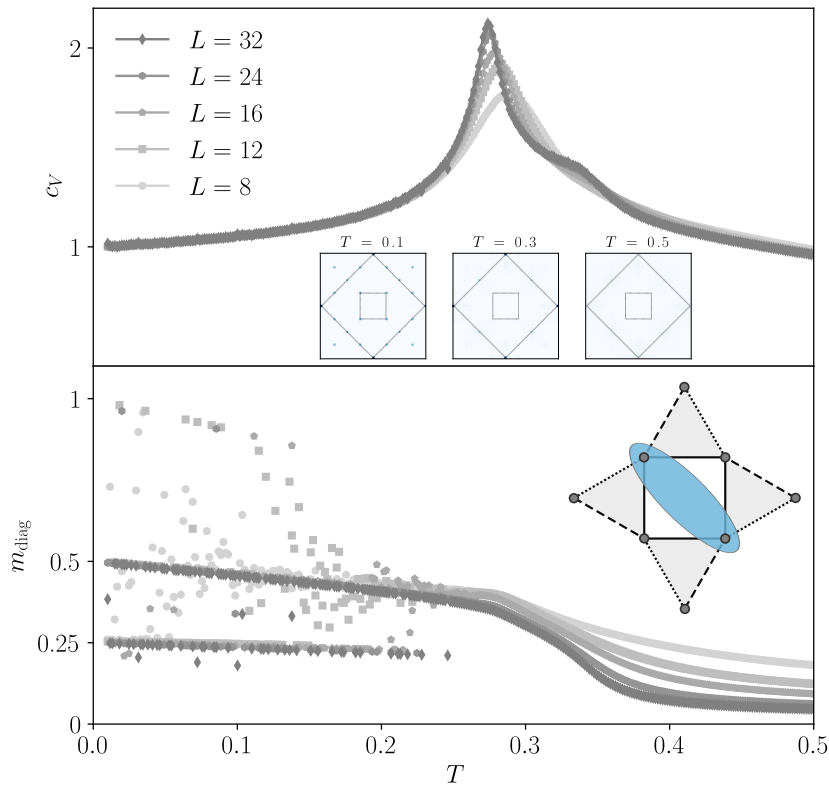
Figure 7.11 – **Thermodynamics of** $120°$ **order.** (top) The specific heat (obtained via Monte Carlo simulations without parallel tempering) of the $120°$ phase shows a sharp feature at $T = 0.27(3)$ and a subtle bump at $T = 0.33(2)$. The subtle bump can be associated with the build-up of $120°$ order, whereas at the sharp feature a specific $120°$ order is selected – in the example shown the structure factor at $T = 0.1$ (inset) coincides with the analytical structure factor in Fig. 7.10(h), whereas the intermediate structure factor can be obtained by averaging the real space correlations of all possible $120°$ orders, i.e. those shown in Fig. 7.10(g)+(h)+(i) plus all possible rearrangements with the same order. The bottom panel shows the magnetization of the square-diagonal spins m_{diag}, i.e., the two spins on the main diagonal of the square of each unit cell (inset). The displayed square-diagonal magnetization starts to build up right at the bump-like feature slightly above $T = 0.3$. Below $T = 0.3$, at the sharp peak in the specific heat, the square-diagonal magnetization splits up into different branches that converge to the values of $m_{\mathrm{diag}} = 1.0$, $m_{\mathrm{diag}} = 0.5$, and $m_{\mathrm{diag}} = 0.25$, corresponding to the $120°$ orders shown in Fig. 7.10(a), (b), and (c), respectively. Figure taken from [P1].

Next to a sharp peak at $T = 0.27(3)$, there is a second, more subtle feature at $T = 0.33(2)$. This smaller bump can, in fact, be associated with the build-up of quasi-long-range $120°$ order—but without selecting one of the types of $120°$ order. Accordingly, the structure factor for the regime between the two features in the specific heat c_V, e.g., for $T = 0.3$, can be obtained by averaging the real space correlations of the possible $120°$ order arrangements. Also, the net magnetization of the square-diagonal spins, shown in the lower panel of Fig. 7.11, builds up at this feature at higher temperatures. The lower temperature peak at $T = 0.27(3)$ then corresponds to the spontaneous selection of one of the types $120°$ orders, resulting in a sharp feature in the specific heat.

Non-Coplanar States

The $120°$ order found for ferromagnetic J_+ and $J_\times$ possesses a rather complex ground state manifold, with three distinct families of non-coplanar configurations connected via the three coplanar configurations just described. Here, we give a more detailed description of the non-coplanar states[2]. The three coplanar ground states (a), (b) and (c) described in Fig. 7.10 all satisfy the following two rules:

1. $120°$ rule: any two spin vectors of adjacent squagome sites form angles of $120°$.

2. Pairing rule: lattice sites with FM octagon-plaquette interactions (i. e. $J_+, J_\times < 0$) are occupied by identical spin vectors.

Conversely, any spin configuration obeying these rules has an energy of $E_{120°}$ given by Eq. (7.8) and thus represents a ground state. However, in addition to the above three coplanar ground states, these rules are also satisfied by certain one-parameter families of, in general, non-coplanar spin configurations. These can be further characterized by the fact that the sequence of spin vectors in the squares of unit cells is either of the form $(\mathbf{a}, \mathbf{b}, \mathbf{a}, \mathbf{b})$ (1st family) or $(\mathbf{a}, \mathbf{b}, \mathbf{a}, \mathbf{c})$ (2nd family) or $(\mathbf{a}, \mathbf{b}, \mathbf{c}, \mathbf{d})$ (3rd family). It turns out that the 1st family connects the coplanar ground states (a) and (b) of Fig. 7.10, the 2nd one the coplanar ground states (b) and (c), and the third family loops (c) with itself, as summarized in Fig. 7.12 pictorially.

The first one-parameter family can be described by five spin vectors that depend on a single angle α as

$$\mathbf{S}_1^\alpha = \left(-\frac{\sqrt{3}}{2}, 0, \frac{1}{2}\right),$$

$$\mathbf{S}_2^\alpha = \left(\frac{\sqrt{3}}{2}, 0, \frac{1}{2}\right),$$

$$\mathbf{S}_3^\alpha = \left(-\frac{\sqrt{3}}{2}\cos\alpha, -\frac{\sqrt{3}}{2}\sin\alpha, \frac{1}{2}\right),$$

$$\mathbf{S}_4^\alpha = \left(\frac{\sqrt{3}}{2}\cos\alpha, \frac{\sqrt{3}}{2}\sin\alpha, \frac{1}{2}\right),$$

$$\mathbf{S}_5^\alpha = (0, 0, -1) . \tag{7.9}$$

---

[2]The derivation and description of the non-coplanar $120°$ orders was done by Heinz-Jürgen Schmidt (co-author of publication [P1]).

For $\alpha = 0$, this yields the coplanar 120° order of Fig. 7.10(a). For $\alpha = \pi$, on the other hand, one obtains the coplanar order Fig. 7.10(b). For arbitrary values of α between 0 and π one obtains the non-coplanar 120° orders depicted in Fig. 7.12(a).
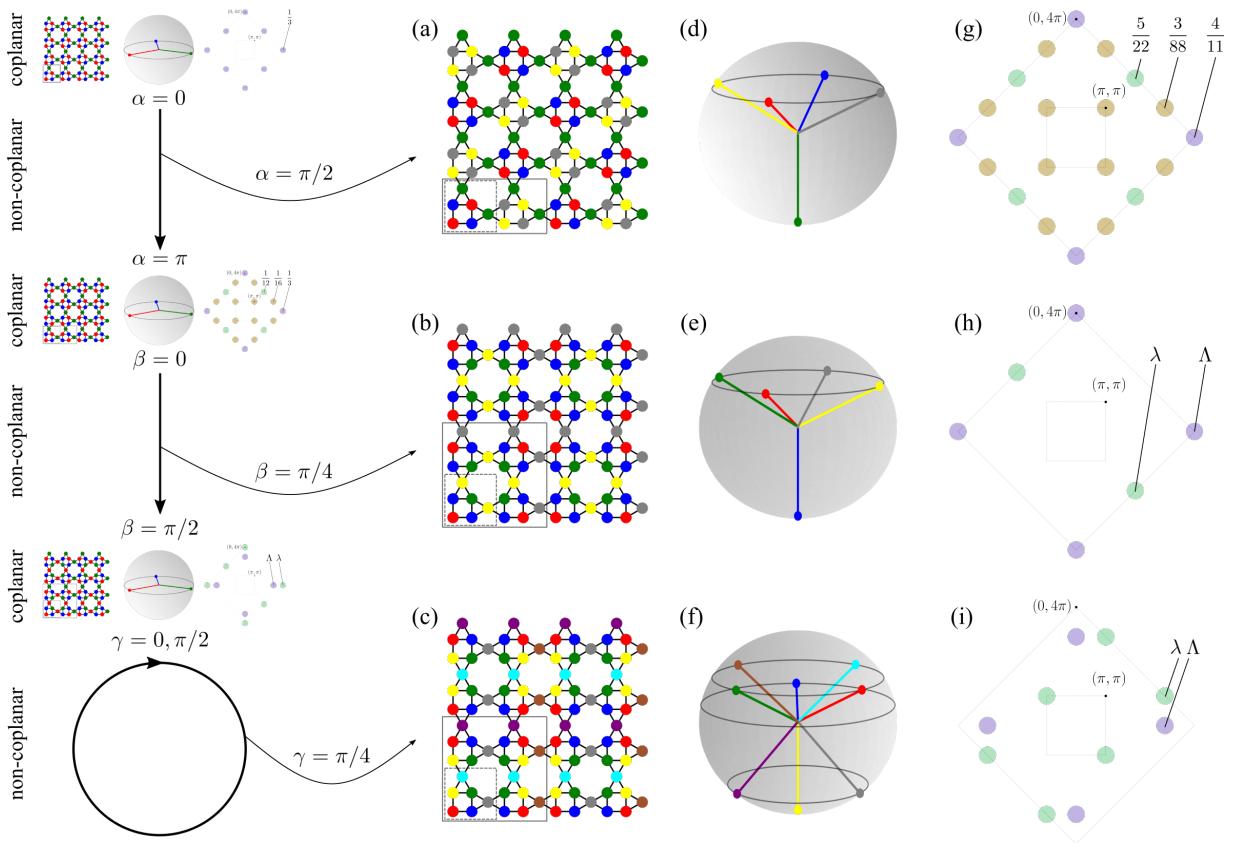
The second one-parameter family can be described by five spin vectors that depend on a single angle β as

$$\mathbf{S}_1^\beta = \left(-\frac{\sqrt{3}}{2} \cos\beta, -\frac{\sqrt{3}}{2} \sin\beta, \frac{1}{2} \right),$$

$$\mathbf{S}_2^\beta = \left(-\frac{\sqrt{3}}{2} \cos\beta, \frac{\sqrt{3}}{2} \sin\beta, \frac{1}{2} \right),$$

$$\mathbf{S}_3^\beta = \left(\frac{\sqrt{3}}{2} \cos\beta, -\frac{\sqrt{3}}{2} \sin\beta, \frac{1}{2} \right),$$

$$\mathbf{S}_4^\beta = \left(\frac{\sqrt{3}}{2} \cos\beta, \frac{\sqrt{3}}{2} \sin\beta, \frac{1}{2} \right),$$

$$\mathbf{S}_5^\beta = (0, 0, -1) . \tag{7.10}$$

For $\beta = 0$, these vectors describe the coplanar 120° order of Fig. 7.10(b). For $\alpha = \pi/2$, they reproduce the coplanar order Fig. 7.10(c). For other values of β between 0 and $\pi/2$ one obtains the non-coplanar 120° orders depicted in Fig. 7.12(b).

Finally, the third one-parameter family of non-coplanar orders can be described by eight spin vectors that depend on a single angle γ:

$$\mathbf{S}_1^\gamma = \left(-\frac{\sqrt{3}}{2} \cos\gamma, -\frac{\sqrt{3}}{2} \sin\gamma, \frac{1}{2} \right),$$

$$\mathbf{S}_2^\gamma = \left(-\frac{\sqrt{3}}{2} \cos\gamma, \frac{\sqrt{3}}{2} \sin\gamma, \frac{1}{2} \right),$$

$$\mathbf{S}_3^\gamma = \left(\frac{\sqrt{3}}{2} \cos\gamma, -\frac{\sqrt{3}}{2} \sin\gamma, \frac{1}{2} \right),$$

$$\mathbf{S}_4^\gamma = \left(\frac{\sqrt{3}}{2} \cos\gamma, \frac{\sqrt{3}}{2} \sin\gamma, \frac{1}{2} \right),$$

$$\mathbf{S}_5^\gamma = \left(-\frac{4\sqrt{3}\cos\gamma}{5 + 3\cos\gamma}, 0, \frac{1 + 3\cos 2\gamma}{5 + 3\cos 2\gamma} \right),$$

$$\mathbf{S}_6^\gamma = \left(\frac{3\sqrt{3}\cos\gamma\sin^2\gamma}{5 + 3\cos 2\gamma}, -\frac{\sqrt{3}}{2}\sin\gamma, -\frac{7 + 9\cos 2\gamma}{10 + 6\cos 2\gamma} \right),$$

$$\mathbf{S}_7^\gamma = \left(\frac{3\sqrt{3}\cos\gamma\sin^2\gamma}{5 + 3\cos 2\gamma}, \frac{\sqrt{3}}{2}\sin\gamma, -\frac{7 + 9\cos 2\gamma}{10 + 6\cos 2\gamma} \right),$$

$$\mathbf{S}_8^\gamma = (0, 0, -1) . \tag{7.11}$$

Figure 7.12 – **Three families of non-coplanar orders arising from coplanar $120°$ order.** In the $120°$ phase, there are three one-parameter families of non-coplanar states, each described by a single angle α, β, or γ, whose limiting cases yield the coplanar orders presented in Fig. 7.10, as sketched on the left. The first family, here depicted in (a)+(d)+(g) by its real space arrangement, a schematic common origin plot, and its structure factor, respectively, for $\alpha = \pi/2$, interpolates between the coplanar **q** = 0 state in Fig. 7.10(a)+(d)+(g) (limit $\alpha = 0$) and the coplanar state Fig. 7.10(b)+(e)+(h) (limit $\alpha = \pi$). The second family, here depicted in (b)+(e)+(h) by its real space arrangement, a schematic common origin plot, and its structure factor, respectively, for $\beta = \pi/4$, interpolates between the coplanar state in Fig. 7.10(b)+(e)+(h) (limit $\beta = 0$) and the coplanar state Fig. 7.10(c)+(f)+(i) (limit $\beta = \pi/2$). The ratio of the weight of the subdominant peaks λ to the weight of the dominant peaks Λ in the structure factor is $\lambda/\Lambda = 40\%$. The third family, here depicted in (c)+(f)+(i) by its real space arrangement, a schematic common origin plot, and its structure factor, respectively, for $\gamma = \pi/4$, has the coplanar state in Fig. 7.10(c)+(f)+(i) for both limits $\gamma = 0$ and $\gamma = \pi/2$ and non-coplanar states in between. The ratio of the weight of the subdominant peaks λ to the weight of the dominant peaks Λ in the structure factor is $\lambda/\Lambda \approx 39\%$. Figure taken from [P1].

These vectors reproduce the coplanar order Fig. 7.10(c) for $\gamma = 0$ and $\gamma = \pi/2$, but yield the non-coplanar orders Fig. 7.12(c) in between. However, all these non-coplanar orders do not occur as actual ground states, as we show next.

### Order-by-Disorder Selection of Coplanar States

We briefly discuss the thermal order-by-disorder effect that selects the coplanar configurations at finite temperatures. The energy of the three families of non-coplanar ground states, as well as the three coplanar ground states, are all identical. However, as these spin configurations are not related by a symmetry of the Hamiltonian, the relevant quantity that needs to be minimized at finite temperature, their free energy, will not be identical. The selection of a subset of ground states via such a thermal order-by-disorder mechanism is a well-studied phenomenon within the

context of frustrated magnets (cf. Sec. 2.4).

By expanding to quadratic order in classical fluctuations about a particular ordered ground state one can compute the lowest-order correction to the entropy. With the free energy $F = E - TS$, the states with the highest entropy will be selected at finite temperatures which, as shown in Fig. 7.13, are precisely the three coplanar states[3].

Interestingly, these all possess the exact same correction at this lowest quadratic order, meaning that the ultimate selection of the (coplanar) ground state must be via higher-order non-linear corrections. To avoid such involved calculations, we apply a numerical approach to determine the preferred ground state.

The three different coplanar $120°$ orders, shown in Fig. 7.10, each have a distinct value of m_{diag}. In Fig. 7.14, we show histograms from Monte Carlo timeseries showing the equilibrium distribution of m_{diag} within the $120°$ phase ($J_+ = J_\times = -1.0$) for different system sizes at different temperatures. Below the phase transition at $T = 0.27$ (cf. Fig. 7.11), the distribution of m_{diag} splits up into three distinct peaks, corresponding to the three different coplanar $120°$ orders. At the lowest temperature, $T = 0.05$, and for $L = 24$, the probability of $\mathbf{q} = 0$ order (Fig. 7.10(a)) is 2%, whereas the orders Fig. 7.10(b) and (c) have probabilities of 88% and 10%, respectively. We thus suspect that the order in (b) is the likely spin configuration favored by thermal fluctuations at finite temperatures, on the largest system sizes. Only for smaller system sizes, $\mathbf{q} = 0$ order occurs with significant probability. Overall, the probabilities only slightly change between $T = 0.05$ and $T = 0.15$.
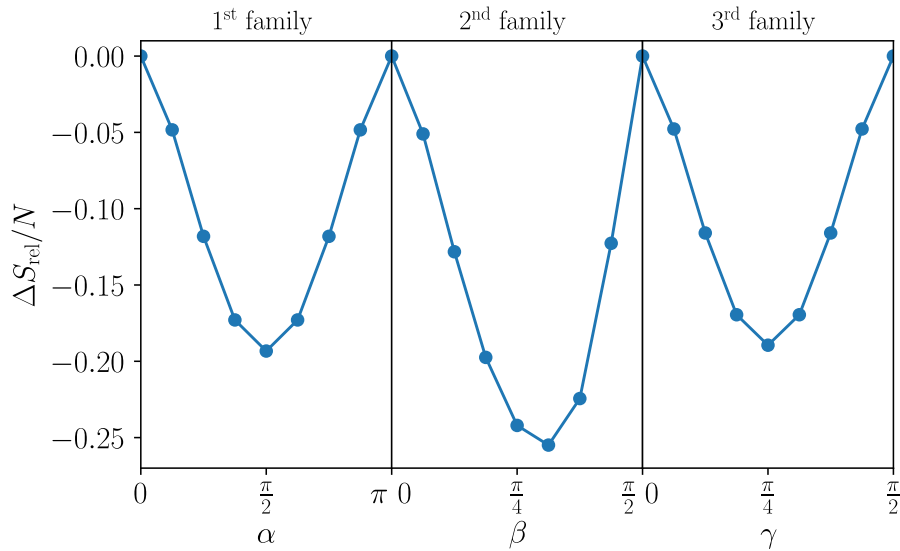
Figure 7.13 – **Order-by-disorder correction.** The entropy correction ΔS_{rel} relative to the coplanar correction for the three one-parameters families of non-coplanar order in the $120°$ phase as a function of the parameters α, β, and γ shows that the entropy is maximal for the coplanar $120°$ orders ($\alpha = 0, \pi; \beta = 0, \pi/2; \gamma = 0, \pi/2$). Figure taken from [P1].

---

[3]The calculation of the OdB correction was not carried out by the author of this dissertation, but by Ciarán Hickey (co-author of publication [P1]).
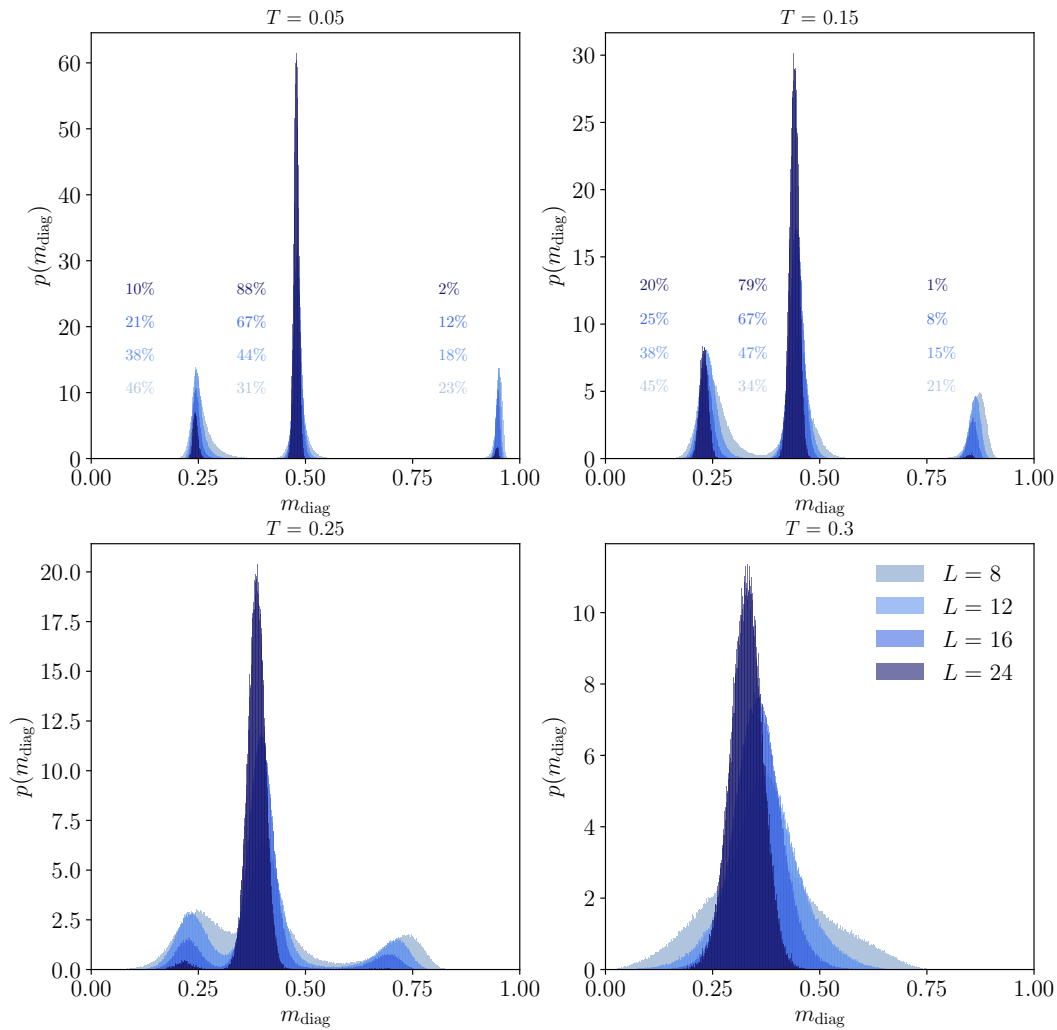
Figure 7.14 – **Square-diagonal magnetization distribution in the** $120°$ **phase.** Histograms from Monte Carlo timeseries showing the equilibrium distribution of m_{diag} in phase VI ($J_+ = J_\times = -1.0$) for different system sizes at different temperatures. The square-diagonal magnetization of the coplanar orders Fig. 7.10(a), (b), and (c) takes values of $m_{\mathrm{diag}} = 1.0$, 0.5, and 0.25, respectively. Slightly lower values of m_{diag} in these histograms are due to thermal fluctuations. Figure taken from [P1].

Deformed Coplanar States

A deformed version of the $120°$ order, henceforth termed $120°$-d, exists in a small region touching the conventional $120°$ ordered phase in the upper left quadrant of the phase diagram, indicated as phase VII in Fig. 7.6. As in the non-deformed case, there exist non-coplanar states and coplanar states with the same energy, with the latter being selected by thermal order by disorder at small, but finite temperature, in a similar way as in the non-deformed $120°$ order. Therefore, the following discussion concentrates on the coplanar deformed $120°$ order.

Its deformation—two of the three mutual angles between neighboring spins take a value of $\alpha > 2\pi/3$, while the third one becomes smaller than $2\pi/3$—can be seen in the common origin plot of Fig. 7.6. It can be derived by elementary geometric considerations: for instance, let the angle between the blue and the red sublattices and between the blue and the green sublattices shown in Fig. 7.10 increase to $\alpha > 2\pi/3$, while the third angle, between the red and the green sublattices, becomes $2\pi - 2\alpha < 2\pi/3$. The angle α is found to vary as $\cos \alpha = -(2 + J_\times)^{-1}$ and the ground state energy per site takes the value

$$E_{120°\text{-d}} = -\frac{6 + J_\times^2 - 2J_+ - J_\times(J_+ - 4)}{3(J_\times + 2)}. \tag{7.12}$$

The ground state symmetry is reduced to the symmetry of the dihedral symmetry group D_1 and has a non-zero, yet small magnetization $m_{120°\text{-d}} = \frac{J_\times}{3(2+J_\times)}$, which only depends on the values of $J_\times$ (see also Fig. 7.25).

7.3.3 Cuboc1 Order

Let us now turn to the first instance of exclusively non-coplanar order and consider the cuboctahedral (cuboc) order found in the upper right quadrant of the phase diagram, where both cross-octagon plaquette couplings are antiferromagnetic.

In real-space this order is described by 12 sublattices where the spins on each sublattice point towards a different corner of a cuboctahedron, as illustrated in Fig. 7.15(b). The order has zero magnetization, $m = 0$, and its energy per site is given by

$$E_{\text{cuboc}} = -1 - \frac{1}{3}(J_+ + J_\times). \tag{7.13}$$

The underlying magnetic unit cell contains 24 sites and is thus four times larger than the geometric unit cell, see Fig. 7.15(a). All neighboring spins form an angle of $2\pi/3$, which corresponds to the *cuboc1* state discussed for the kagome lattice with cross-hexagonal couplings [39, 221] and introduced earlier (cf. Fig. 6.3(e)).
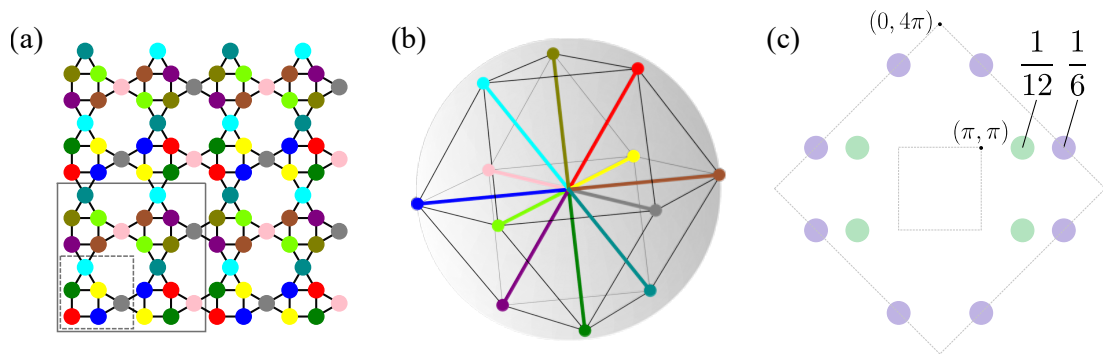
Figure 7.15 – **Cuboctahedral order *cuboc1*.** (a) Real space arrangement of spins in a cuboctahedral (cuboc) ordered state. There are 12 sublattices (each one corresponding to one color) with a 24-site magnetic unit cell (large gray square), which is four times larger than the geometric unit cell (small square). (b) Each sublattice of spins points towards a different corner of a cuboctahedron such that each neighboring pair of spins forms an angle of $2\pi/3$. This order corresponds to the *cuboc1* state in [39]. (c) First and extended Brillouin zones of the square-kagome lattice showing the positions and the fractions of total spectral weight of the corresponding Bragg peaks. The order breaks C_4 symmetry. Figure taken from [P1].

There are eight different possibilities to set up cuboc1 order on the square-kagome lattice, each of which breaks C_4 rotation symmetry, as visualized in Fig. 7.16. The remaining symmetry of this ordered state is the full octahedral symmetry group O_h. The real-space correlations of the cuboc1 order give rise to a spin structure factor as schematically visualized for one of the eight possible real-space configurations in Fig. 7.15 (c), which shows the positions of the corresponding Bragg peaks within the extended Brillouin zone of the square-kagome lattice together with the associated fraction of total spectral weight. Averaging over the real-space correlations of all eight possible cuboc1 arrangements restores C_4 symmetry in the structure factor (cf. Fig. 7.16(f)).

The different cuboc1 realizations can be best described by dividing the 24-site magnetic unit cell into four building blocks, each encompassing one geometric unit cell, with some specific fixed arrangement of spins—indicated as blue, green, yellow, and red squares in Fig. 7.16. These building blocks can be arranged clockwise or anti-clockwise, each in four different ways. The order parameter to distinguish between clockwise and anti-clockwise arrangements of blue-green-yellow-red is

$$\mathcal{O} = \frac{1}{M} \sum_{\bowtie} \mathcal{O}_{ijkl} \tag{7.14}$$

where

$$\mathcal{O}_{ijkl} = \frac{1}{\sqrt{2}} \mathbf{S}_i \cdot [(\mathbf{S}_j - \mathbf{S}_k) \times (\mathbf{S}_l - \mathbf{S}_m)] \tag{7.15}$$

is summed over all skew bow-ties as shown in the inset of the lower panel of Fig. 7.17 and M is the number of skew bow-ties.
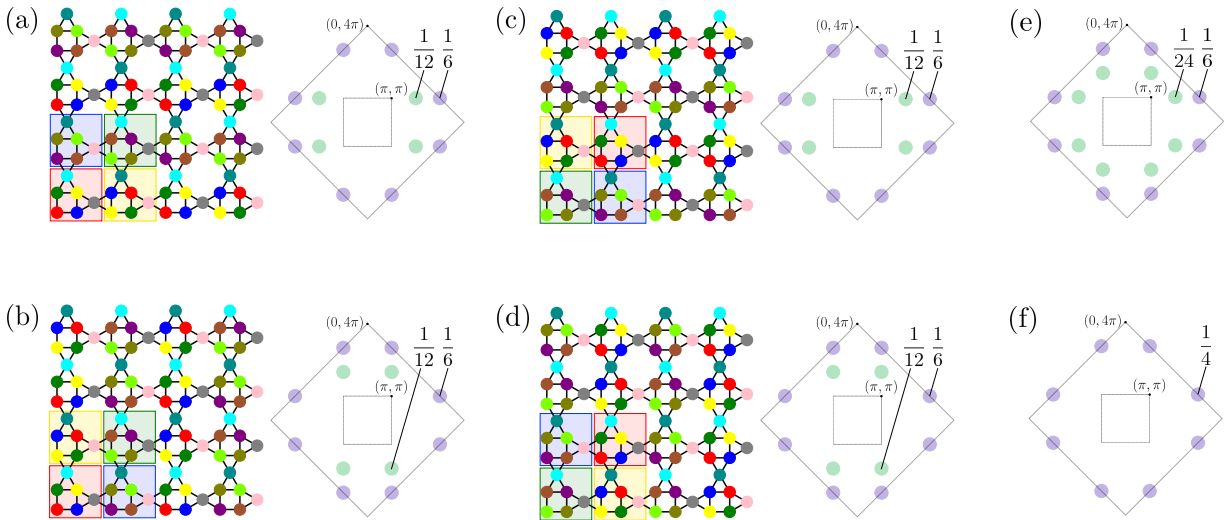
Figure 7.16 – **Variants of cuboc1 order on the square-kagome lattice.** (a)-(d) show four of the eight different possible arrangements of cuboc1 order on the square-kagome lattice, each with its corresponding structure factor. The arrangement in (a) corresponds to the arrangement shown in Fig. 7.15 and has a clockwise placement of the building blocks highlighted in blue, green, yellow, and red, in the magnetic unit cell. The arrangement in (c) also has this clockwise placement, but in a different order, and has the same structure factor as (a). The other two arrangements, (b) and (d), on the other hand, have an anti-clockwise placement of blue, green, yellow, and red, resulting in a structure factor that is rotated by $\pi/2$ (two additional arrangements are possible in each case, but not explicitly shown). (e) Averaging the real space correlations of a clockwise and an anti-clockwise arrangement results in a structure factor with twice as much subdominant peaks. (f) The averaged real space correlations of all possible cuboc1 orders yields a structure factor with only main peaks on the edges of the extended Brillouin zone without further subdominant peaks. Figure taken from [P1].

For cuboc1 order with a clockwise (anti-clockwise) arrangement of blue-green-yellow-red, $\mathcal{O}$ yields $+1$ (-1). The associated susceptibility is given by

$$\chi_{\mathcal{O}} = \frac{M}{T} \left(\langle \mathcal{O}^2 \rangle - \langle |\mathcal{O}| \rangle^2 \right). \tag{7.16}$$

Turning to the thermodynamics of the cuboc phase, we show, in Fig. 7.17, the specific heat, the cuboc1 order parameter $\mathcal{O}$ (and its absolute value, $|\mathcal{O}|$), as well as its associated susceptibility $\chi_{\mathcal{O}}$ for different system sizes between $L = 8$ and $L = 32$.

The specific heat displays a clearly visible double-peak structure which, similar to our discussion of the coplanar $120°$ order, can be rationalized by the coexistence of multiple possible cuboc1 arrangements on the square-kagome lattice: at the high-temperature peak in c_V (at $T = 0.371$), the system builds up cuboc1 order, but does not select a specific arrangement out of the eight possible realization, as can be seen from the C_4 symmetric structure factor in the inset. At the low-temperature peak (at $T = 0.256$) a specific cuboc1 order is then spontaneously selected. At this temperature, the order parameter $\mathcal{O}$ (Eq. (7.14)), which takes values of ± 1 for different specific cuboc1 arrangements, builds up and the corresponding susceptibility $\chi_{\mathcal{O}}$ (Eq. (7.15)) diverges as shown in the lowest panel of Fig. 7.17.

Deformed Cuboc Order

A deformed version of cuboc1 order (denoted as phase II in our phase diagram Fig. 7.6), termed cuboc-d, extends to a part of the lower right quadrant in the phase diagram with $J_\times < 0$ and $J_+ \geq 0$. In this cuboc-d phase, the antipodal squares of the cuboctahedron are deformed into antipodal squares with modified z-values while the square in the equatorial plane remains undeformed. Its symmetry is thereby reduced to the symmetry of the dihedral symmetry group D_4^s where the superscript s denotes additional mirror symmetry on the xy-plane, i.e. $s = \mathrm{diag}(1, 1, -1)$. The ground state energy per site can be calculated to be

$$E_{\text{cuboc-d}} = \frac{3 + J_\times^2 + J_+ - J_\times(J_+ + 3)}{3(J_\times - 1)}. \tag{7.17}$$

The cuboc-d ground state still has zero magnetization, $m = 0$.

7.3.4 Spiral Orders

The upper left and lower right quadrant of our phase diagram are occupied by spin spiral phases, coming in the form of six different variants (labeled III-V and VIII-X, respectively). The complexity of these incommensurate, non-coplanar orders becomes immediately clear when looking at their common origin plots next to the phase diagram in Fig. 7.6, whose intricate patterns point to magnetic unit cells of hundreds of spins. This renders any direct analytical description of these phases rather elusive, but it turns out that one can, in fact, deduce a *semi-analytical description* [239–245] of these phases from low-temperature numerical simulation data. As we will discuss below, this approach provides us with a symmetry-optimized description of these spin spirals including explicit expressions of their ground state energy as function of the coupling parameters. The latter then allows us to establish sharp phase boundaries between these complex spin spiral phases as depicted in the phase diagram of Fig. 7.6.
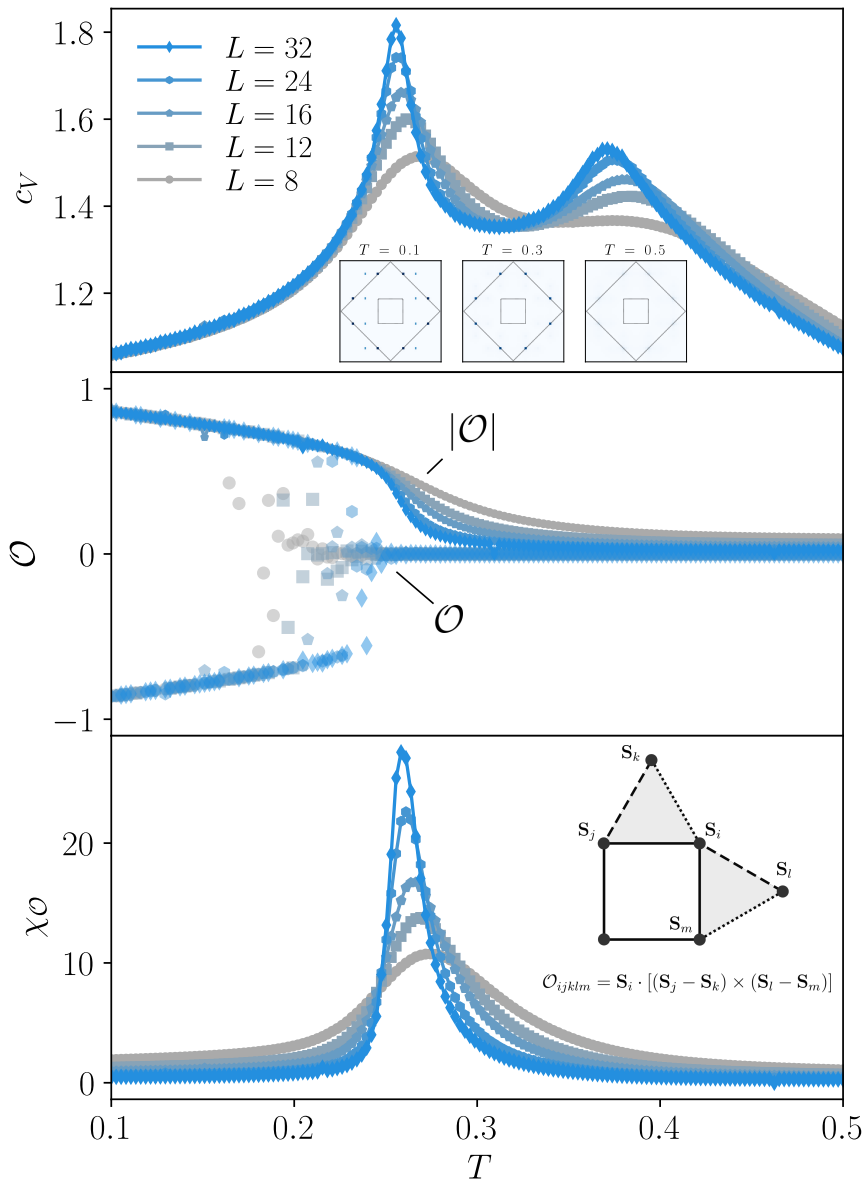
Figure 7.17 – **Thermodynamics of cuboc1 phase.** Top panel: the specific heat (obtained from Monte Carlo simulations without parallel tempering) of the cuboc1 phase displays a double-peak structure. The high-temperature peak at $T = 0.371$ can be associated with the initial build-up of coexisting cuboc1 orders. At the low-temperature peak (at $T = 0.256$), one specific realization of cuboc1 order is selected. This can be seen from the structure factors (inset). While the structure factor at $T = 0.1$ corresponds to one specific realization of cuboc1 order, the intermediate structure factor at $T = 0.3$ coincides with the analytical structure factor of the superposition of all possible cuboc1 order realizations. Middle and bottom panels show the cuboc1 order parameter $\mathcal{O}$ (Eq. (7.14)), and the corresponding susceptibility $\chi_{\mathcal{O}}$ (Eq. (7.15)). The lower inset shows how $\mathcal{O}_{ijkl}$ is being calculated on a single skew bow-tie. This quantity is then averaged over all skew bow-ties in order to calculate $\mathcal{O}$. Figure taken from [P1].
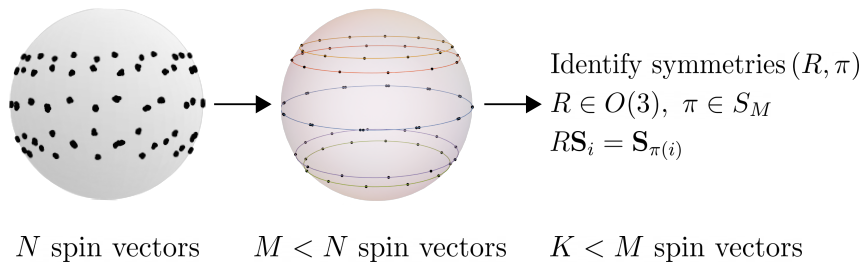
Semi-Analytical Approach

The starting point of our semi-analytical approach is numerical data in the form of a common origin plot of the N spin vectors of a ground state spin configuration sampled in Monte Carlo simulations at ultra-low temperatures $T = 10^{-4}$. Example input for the spin spiral phase III in the lower right quadrant is shown on the left in the schematic illustration of Fig. 7.18.

In a second step, we then identify a smaller number of $M < N$ unique spin vectors by grouping spins in the initial common origin plot that point approximately in the same direction, see the middle panel of Fig. 7.18. In practice, we say that two spins $\mathbf{S}_i$ and $\mathbf{S}_j$ point approximately in the same direction if $\mathbf{S}_i \cdot \mathbf{S}_j \geq \gamma$, where the exact value of γ slightly varies from case to case, but typically $\gamma \approx 0.995$.

Finally, for these M spin directions we then identify all possible symmetries, which allows us to further reduce the number of unique spin vectors to $K < M$. A symmetry in the aforementioned sense is a tuple (R, π) with $R \in O(3)$ and $\pi \in S_M$ where S_M is the permutation group of M elements, such that $R\mathbf{S}_i = \mathbf{S}_{\pi(i)}$ for all spin vectors $\mathbf{S}_i$. From the remaining K spin vectors, all spin vectors can be generated by applying these symmetries. In total, this approach allows us to describe the ground state by at most $2K - 1$ parameters – maximally two parameters per spin minus one parameter due to a global rotation around the symmetry axis, but less if some polar or azimuthal angles of the ground state assume fixed values[4].

Having such an analytical representation at hand, we can then explicitly calculate various observables such as the magnetization or ground state energy for arbitrary couplings J_+ and $J_\times$ for all phases, which in turn allows us to determine the phase boundaries shown in the phase diagram Fig. 7.6. Several cross-checks can be used to validate this approach, including a comparison of the analytical ground state energy and the Monte Carlo result as well as the determination of the phase boundaries, which we compare to scans of derivatives of the Monte Carlo energy, as shown later in Sec. 7.3.7.

$$\text{Identify symmetries}\,(R, \pi)$$
$$R \in O(3),\ \pi \in S_M$$
$$R\mathbf{S}_i = \mathbf{S}_{\pi(i)}$$

N spin vectors $M < N$ spin vectors $K < M$ spin vectors

Figure 7.18 – **Semi-analytical scheme for spin spiral phases.** Starting point is a common origin plot of the N spin vectors of a ground state spin configuration sampled in Monte Carlo simulations at ultra-low temperatures $T = 10^{-4}$, as shown on the left. In a second step, we identify $M < N$ unique spin directions by grouping spins that point approximately in the same direction (middle). From these unique spin vectors, we then identify symmetries that further reduce the number of unique spin vectors to $K < M$ and allow us to describe the spiral phase analytically (right). The data shown is for spin spiral phase III of the lower right quadrant with couplings $J_+ = +1$ and $J_\times = -0.2$. The initial common origin plot has $N = 864$ spins corresponding to a system size of $L = 12$. The initial reduction leads to $M = 72$ points on five circles (as indicated in the middle panel). The symmetry group G of the example is generated by rotations of $\pi/6$ about the vertical symmetry axis as well as by a reflection at the equatorial plane, i.e. $G = D_{12}^s$, and therefore $K = 4$. Figure taken from [P1].

---

[4]The second and third steps of the semi-analytical approach were carried out by Heinz-Jürgen Schmidt (co-author of publication [P1]), to whose idea the method can also be traced back.

In the following we present explicit results of this semi-classical approach for all six spin spiral phases. In all cases, the nearest-neighbor couplings are set to $J_1 = J_2 = J_3 = 1.0$ and the numerical Monte Carlo ground states are taken at a temperature of $T = 10^{-4}$.

Spiral Phase III with D_{12}^s Symmetry

We start with spiral phase III in the lower right quadrant of the phase diagram Fig. 7.6 for $J_+ = +1$ and $J_\times = -0.2$ (our schematic illustration of the semi-classical approach in Fig. 7.18 uses this example). The common origin plot on the left consists $N = 864$ spin vectors of the numerical ground state of a system of linear length $L = 12$. By grouping spins that point to the same direction, using the criterion $\mathbf{S}_i \cdot \mathbf{S}_j \geq 0.999$, we find that there are only $M = 72$ unique spin directions which are shown in the middle panel. Performing a symmetry analysis, one finds that the symmetry group G of this state is generated by rotations of $\pi/6$ about the vertical symmetry axis as well as by a reflection at the equatorial plane, i.e. $G = D_{12}^s$. This leaves us with just $K = 4$ representative spins that describe the entire spin spiral configuration—one on each of the upper circles as well as two on the equator shown in Fig. 7.18. This is a significant reduction compared to the $N = 864$ spins in the original real-space configuration. The $K = 4$ representative spins can be written as functions of three parameters α, z_1, z_2 in the following way

$$\mathbf{S}_1 = \left(0, \sqrt{1 - z_1^2}, z_1 \right) ,$$

$$\mathbf{S}_2 = \left(\frac{\sqrt{1 - z_2^2}}{\sqrt{2}}, \frac{\sqrt{1 - z_2^2}}{\sqrt{2}}, z_2 \right) ,$$

$$\mathbf{S}_{3,4} = \left(\cos\left(\frac{\pi}{4} \pm \alpha \right), \sin\left(\frac{\pi}{4} \pm \alpha \right), 0 \right) . \tag{7.18}$$

With this compact representation at hand, the energy per site can now be explicitly calculated as

$$
\begin{aligned}
E_{\mathrm{III}} =& \frac{1}{12} \left[J_\times \cos 2\alpha + \sqrt{3} J_\times \sin 2\alpha - 2\left(\sqrt{3} J_+ - (\sqrt{3} - 2) J_+ z_1^2 + 4 z_1 z_2 \right. \right. \\
& \left. + (\sqrt{6} - \sqrt{2}) \sqrt{(1 - z_1^2)(1 - z_2^2)} + J_\times (2 z_2^2 - 1) + 2\left(\sqrt{3 - 3 z_2^2} - \sqrt{2 - 2 z_1^2} \right) \sin \alpha \right. \\
& \left. \left. + 2\left(\sqrt{2 - 2 z_1^2} + \sqrt{1 - z_2^2} \right) \cos \alpha \right） \right] . \tag{7.19}
\end{aligned}
$$

Numerical minimization of this energy with $J_+ = +1$ and $J_\times = -0.2$ then leads to a ground state energy of $E_{\mathrm{III,semi\text{-}analytical}} = -1.34515$ which is in excellent agreement with and slightly below the Monte Carlo result $E_{\mathrm{III,MC}} = -1.345$, which is shifted upwards by finite-temperature fluctuations commensurate with a temperature of $T = 10^{-4}$.

Spiral phase IV with $D_6^{s,t}$ Symmetry

We consider the ground state for $J_+ = J_\times = -0.2$. On the left of Fig. 7.19(a), a common origin plot of the $N = 864$ ($L = 12$) spin vectors of the numerical ground state is shown. After grouping those spins that point to the same direction, we are left with $M = 228$ unique spin directions which are shown on the right of Fig. 7.19(a). The symmetry group G of this state is generated by two reflections and rotations of $\pi/3$ about the symmetry axis i.e. $G = D_6^{s,t}$, where the superscripts imply additional mirror symmetries on the xy-plane and the yz-plane,
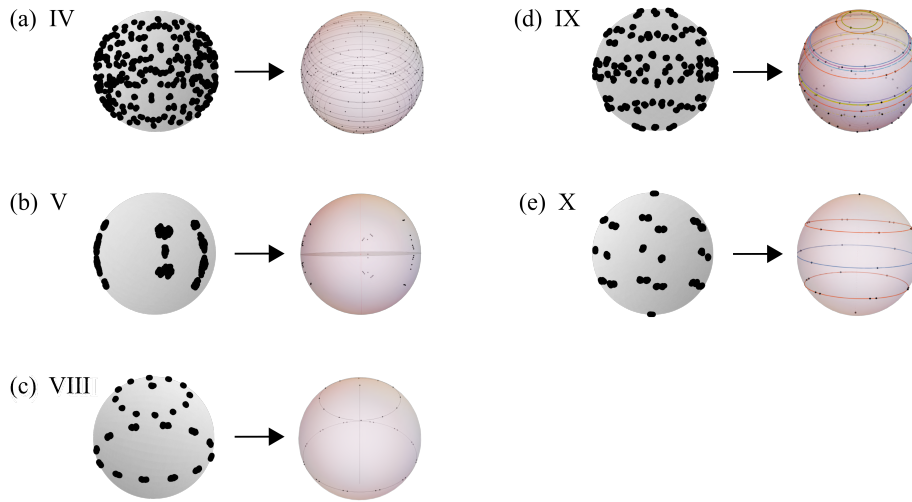
Figure 7.19 – **Spin spiral phases.** Shown are common origin plots (left column) of the numerical Monte Carlo ground states of spiral phases IV (a), V (b), VIII (c), IX (d), and X (e), at $T = 10^{-4}$. Each common origin plot depicts the spin direction of all $N = 864$ spins on the unit sphere. The right column shows the result of reducing the number of spin directions by grouping spins that point to the same direction which eventually allows for the symmetry analysis and analytical description outlined in the text. Figure taken from [P1].

i.e. $s = \mathrm{diag}(1, 1, -1)$ and $t = \mathrm{diag}(-1, 1, 1)$. The energy per site can eventually be described as a function of 19 parameters (which is too long to be specified here) and numerical minimization of this energy with $J_+ = -0.2$ then leads to $E_{\mathrm{IV,semi\text{-}analytical}} = -1.10525$ in accordance with the Monte Carlo result $E_{\mathrm{IV,MC}} = -1.1051(4)$ for the same parameters.

Spiral phase V with $\{\mathrm{id}, s\}$ Symmetry

For $J_+ = 0.2$ and $J_\times = -1.0$, there are $M = 47$ unique spin vectors left after grouping the $N = 864$ ground state spin vectors according to unique directions (cf. Fig. 7.19(b)). There is no exact rotation symmetry but a reflection symmetry with respect to the equatorial plane, thus the symmetry group of this phase is {id,s}. The energy per spin then is a function of 48 parameters and yields, after minimization, $E_{\mathrm{V,semi\text{-}analytical}} = -1.36719$ in accordance with the Monte Carlo result $E_{\mathrm{V,MC}} = -1.367(1)$ for the same parameters.

Spiral phase VIII with D_{12} Symmetry

The ground state for $J_+ = -1.0$ and $J_\times = 1.0$ (Fig. 7.19(c)) can be constructed depending on two polar angles α and β and one azimuthal angle γ as follows. Let $\mathbf{S}_i$ $(i = 1, \ldots, 6)$ be the six spin vectors of the primitive unit cell with $\mathbf{S}_1$ and $\mathbf{S}_2$ being the bow-tie spins. One can define

$$
\begin{aligned}
\mathbf{S}_1 &= (0, 0, 1), \\
\mathbf{S}_2 &= (\sin\alpha, 0, \cos\alpha), \\
\mathbf{S}_3 &= (\sin\beta\cos\gamma, \sin\beta\sin\gamma, \cos\beta), \\
\mathbf{S}_4 &= (\sin\beta\cos\gamma, -\sin\beta\sin\gamma, \cos\beta), \\
\mathbf{S}_5 &= (-\sin\beta\cos\gamma, \sin\beta\sin\gamma, \cos\beta), \\
\mathbf{S}_6 &= (-\sin\beta\cos\gamma, -\sin\beta\sin\gamma, \cos\beta).
\end{aligned} \tag{7.20}
$$

With $\mu = (m, n, i)$ denoting the general index of a spin site on the lattice, any spin of the ground state can thus be written as $\mathbf{S}_\mu = \sigma^n \rho^m \mathbf{S}_i$ with

$$\sigma = \begin{pmatrix} -1 & 0 & 0 \\ 0 & -1 & 0 \\ 0 & 0 & 1 \end{pmatrix}, \quad \rho = \begin{pmatrix} \cos\frac{\pi}{6} & \sin\frac{\pi}{6} & 0 \\ -\sin\frac{\pi}{6} & \cos\frac{\pi}{6} & 0 \\ 0 & 0 & 1 \end{pmatrix}. \tag{7.21}$$

The ground state energy per spin of this state is given as

$$\begin{aligned} E_{\mathrm{VIII}} = \frac{1}{12}\Big[& 2J_+(1 + \cos^2\alpha) + 8\cos\beta(1 + \cos\alpha) + 4(2 + J_\times)\cos^2\beta + \sqrt{3}J_+ \sin^2\alpha \\ & + 8\cos\gamma\sin\alpha\sin\beta + 2\sqrt{3}J_\times\cos^2\gamma\sin^2\beta + 4J_\times\cos\gamma\sin^2\beta\sin\gamma \\ & - 8\sin^2\beta\sin^2\gamma - 2\sqrt{3}J_\times\sin^2\beta\sin^2\gamma \Big]. \end{aligned} \tag{7.22}$$

Specific heat traces for this spiral phase and for spiral phase IV for different system sizes are shown Fig. 7.20. However, due to the incommensurability of these spin spirals there are significant finite-size effects, making it hard to narrow down the location of the finite-temperature transition.
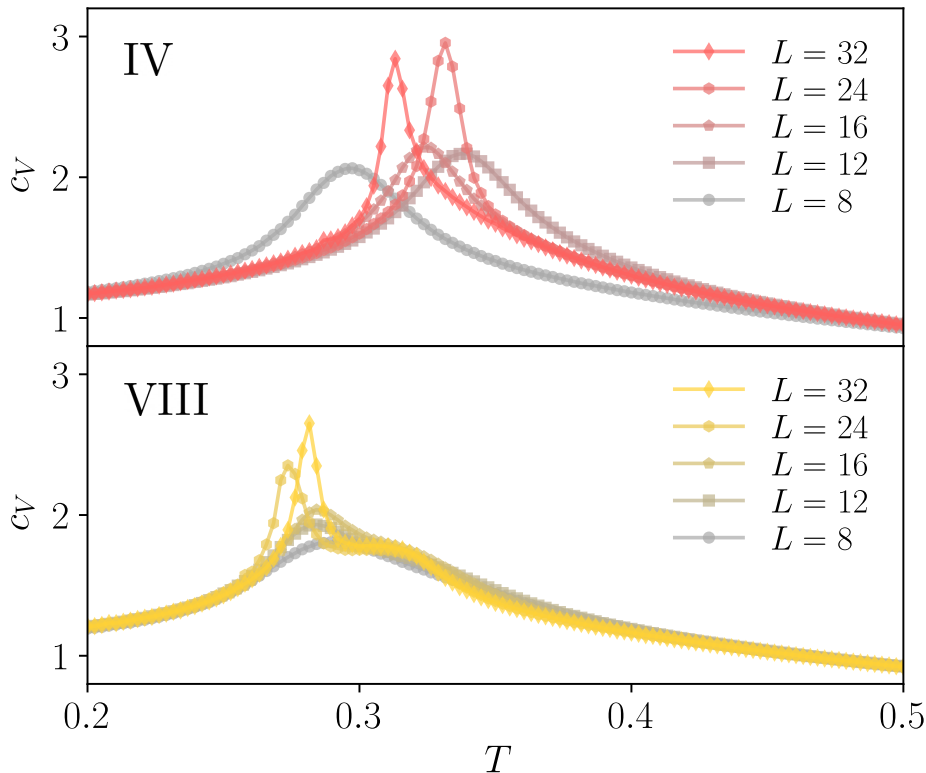
Figure 7.20 − **Specific heat of spiral phases IV and VIII.** To exemplify the complicated behaviour of the specific heat of the spiral phases, we show c_V traces from Monte Carlo simulations (without parallel tempering) for the spiral phase IV (top) and VIII (bottom). In both cases, the specific heat qualitatively changes drastically with the system size which indicates that the spiral ground state depends very sensitively on the system size. Figure taken from [P1].

Spiral phase IX with D_3^σ Symmetry

For $J_+ = -0.2$ and $J_\times = 1.0$ (Fig. 7.19(e)), grouping the $N = 864$ ground state vectors according to their direction leaves us with $M = 108$ unique spin vectors. These can be reduced further by identifying the symmetry group G of this state, which is generated by a point reflection and rotations of $2\pi/3$ about the symmetry axis, i.e. $G = D_3^\sigma$, where the superscript σ implies additional point reflection symmetry, i.e. $\sigma = \mathrm{diag}(-1, -1, -1)$. The energy per spin is then given by a function of 26 variables and minimization yields $E_{\text{IX,semi-analytical}} = -1.3272$ as compared to the Monte Carlo result $E_{\text{IX,MC}} = -1.327(1)$ for the same parameters.

Spiral phase X with D_6^s Symmetry

For $J_+ = -0.05$ and $J_\times = 0.4$ (Fig. 7.19(e)), there are $M = 32$ unique spin directions left after identifying the numerical ground state spin vectors that are close to each other. The symmetry group of this state is generated by a point reflection and by rotations of $\pi/3$ about the symmetry axis.

The energy per site can be expressed as a function of three variables α_1, α_2, z as

$$
\begin{aligned}
E_{\text{X}} = \frac{1}{36} \Bigg[& 8J_\times \left(z^2 - 1\right) \sin\left(\pi\left(-\alpha_1 + \alpha_2 + \frac{1}{6}\right)\right) + 2J_\times \left(z^2 - 1\right) \cos\left(\pi\left(\alpha_1 - \alpha_2 - \frac{5}{3}\right)\right) \\
& + 2J_\times \left(z^2 - 1\right) \cos\left(\pi\left(\alpha_1 - \alpha_2 + \frac{1}{3}\right)\right) - 12 J_\times z^2 - 2\sqrt{1 - z^2} \cos\left(\pi\left(\alpha_1 + \frac{2}{3}\right)\right) \\
& + 2\sqrt{1 - z^2} \cos\left(\pi\left(\alpha_1 + \frac{5}{3}\right)\right) - 3J_+ + 2\left(z^2 - 1\right) \cos\left(\frac{1}{3}\pi(3\alpha_1 - 3\alpha_2 - 4)\right) \\
& + 6\left(z^2 - 1\right) \cos\left(\frac{1}{3}\pi(3\alpha_1 - 3\alpha_2 + 2)\right) + 2\left(z^2 - 1\right) \cos\left(\pi\left(\alpha_1 - \alpha_2 - \frac{4}{3}\right)\right) \\
& + 2\left(z^2 - 1\right) \cos\left(\pi\left(\alpha_1 - \alpha_2 + \frac{2}{3}\right)\right) + 4\sqrt{1 - z^2}\left(\sqrt{3}\sin(\pi\alpha_1) + \cos(\pi\alpha_1)\right) \\
& + 12\sqrt{1 - z^2}\cos(\pi\alpha_2) + 12z^2 - 24z - 12 \Bigg].
\end{aligned}
\tag{7.23}
$$

Minimization of this expression gives $E_{\text{X,semi-analytical}} = -1.12813$ in agreement with the Monte Carlo result $E_{\text{X,MC}} = -1.1280(3)$ for the same parameters.

Summary

The compact representation of the complicated spin spiral states made possible by the semi-analytical method is summarized in Table 7.1 for all six spin spiral phases of our phase diagram Fig. 7.6. Table 7.1 also summarizes all ten phases of the phase diagram according to the method used to describe each phase, the corresponding ground state symmetry, and corresponding **q** vectors, if any. As a side note we would like to remark that it turns out that these six phases can be divided into three regular ones that possess **q** vectors and three irregular ones, possessing no **q** vectors[5].

---

[5]The **q** vectors originate from generalized Luttinger-Tisza theory [211] and were determined by Heinz-Jürgen Schmidt (co-author of publication [P1]).

phase	symmetry	**q** vectors	semi-analytical			
			N	M	K	# parameters
I	O_h	$(0, \pi), (\pi, \pi)$	–	–	–	–
II	D_4^s	$(0, 0), (\pi, \pi)$	–	–	–	–
III	D_{12}^s	$(-5\pi/6, -5\pi/6), (\pi, \pi)$	864	72	4	3
IV	$D_6^{s,t}$	–	864	228	13	19
V	$\{\text{id}, s\}$	–	864	48	24	47
VI	D_3	$(0, 0), (\pi, \pi)$	–	–	–	–
VII	D_1	$(0, 0), (0, \pi)$	–	–	–	–
VIII	D_{12}	$(\pi/6, \pi)$	864	37	3	3
IX	D_3^σ	–	864	108	18	26
X	D_6^s	$(\pi/3, \pi), (\pi, \pi)$	864	32	4	3

Table 7.1 – **Symmetry characterization of the ten ground state phases** of the phase diagram Fig. 7.6. Given are the ground state symmetry (second column), and the **q** vectors of each phase (if any, third column). For the six semi-analytically described phases (III-V, VIII-X), the compression of the parametrization of the spin spirals via clustering and symmetrization (Fig. 7.18) is given in the four columns on the right. Technically, this semi-analytical description is obtained by starting with a common origin plot with $N = 864$ spins sampled at $T = 10^{-4}$ for a linear system size $L = 12$, and is then given in terms of M, K, and the number of needed parameters (last column) to describe the phase.

7.3.5 Cuboc3 and Pentagonal Order for Mixed Interactions

Finally, we note that one could also consider variations of the model at hand where one changes the sign of the interactions in the original nearest-neighbor (J_1, J_2, J_3) Heisenberg model (see Fig. 7.1 for a reminder of the coupling geometries). Flipping the sign of the bow-tie interactions to ferromagnetic couplings, i.e. $J_2 = J_3 = -1$, while keeping the square interactions antiferromagnetic, i.e. $J_1 = 1$, yields exactly the same phase diagram as shown in Fig. 7.6, up to local spin transformations.

Specifically, since the spins on the bow-ties are coupled via J_2 and J_3 to their nearest neighbors and via J_+ to other bow-tie spins, the total energy remains unchanged if all bow-tie spins are inverted simultaneously while the sign of the triangular couplings is changed, $J_2 \to -J_2$ and $J_3 \to -J_3$. Performing these local spin transformations on the orders of our original phase diagram yields qualitatively new types of orders.

The original cuboctahedral order (Fig. 7.15), for example, becomes a new cuboctahedral order *cuboc3*, where each neighboring pair of spins forms an angle of $2\pi/3$ on the squares and an angle of $\pi/3$ on the triangles (Fig. 7.21). This new cuboc order is different to both *cuboc1* order (where all neighboring pairs of spins form an angle of $2\pi/3$) and to *cuboc2* order (where all neighboring pairs of spins form an angle of $\pi/3$) [39].

The 120° orders (Fig. 7.10) are transformed into new coplanar orders in an analogous way, e.g., into a coplanar *pentagonal* order (Fig. 7.22), that results from flipping the bow-tie spins in the 120° order Fig. 7.10(c). Note that, just as in the original 120° case, at zero temperature there are both coplanar and non-coplanar states degenerate in energy but the coplanar states are selected at finite temperature via thermal order by disorder.
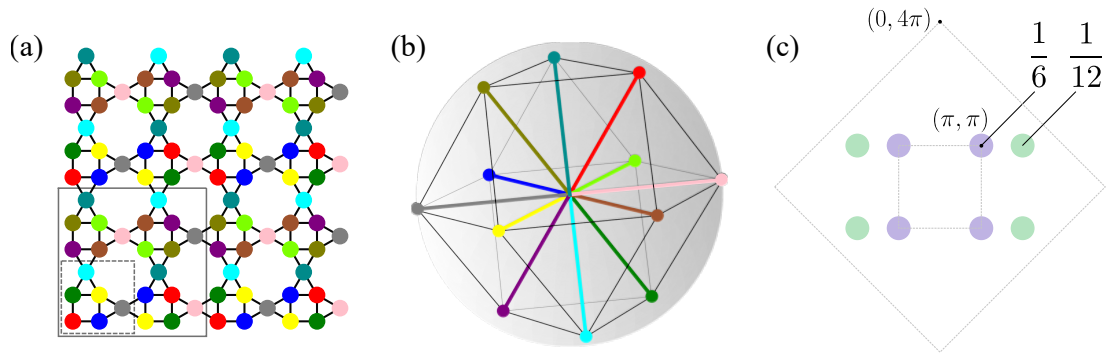
Figure 7.21 – **Cuboctahedral order *cuboc3*.** This variant of a non-coplanar cuboctahedral order is found when flipping the bow-tie interactions J_2 and J_3 of the nearest neighbor model to ferromagnetic (while keeping the square interactions J_1 antiferromagnetic). It is obtained from the original cuboc order (Fig. 7.15) via a local spin transformation (see text). (a) Real space arrangement of spins in the cuboc3 ordered state. There are 12 sublattices (each one corresponding to one color) with a 24-site magnetic unit cell (large gray square), four times larger than the geometric unit cell (small square). (b) Each sublattice of spins points towards a different corner of a cuboctahedron such that each neighboring pair of spins forms an angle of $2\pi/3$ on the squares and an angle of $\pi/3$ on the triangles, making it different from the *cuboc1* and *cuboc2* orders discussed in the literature [39]. (c) First and extended Brillouin zones of the square-kagome lattice showing the positions of the corresponding Bragg peaks. The order breaks C_4 symmetry. Figure taken from [P1].
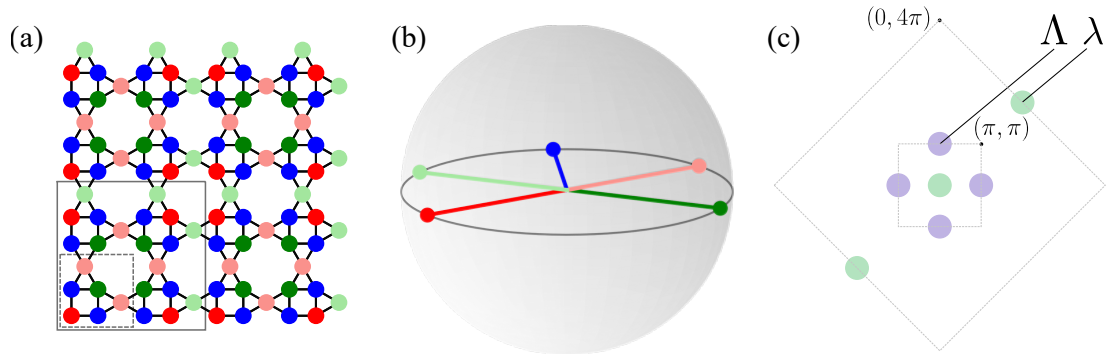

Figure 7.22 – **Pentagonal order.** Coplanar pentagonal order arises when flipping the bow-tie interactions J_2 and J_3 of the nearest-neighbor model to ferromagnetic (while keeping the square interactions J_1 antiferromagnetic). It is obtained from the original 120° order (Fig. 7.10(c)) via a local spin transformation (see text). (a) Real space arrangement of spins in the coplanar pentagonal state. There are five sublattices (each one corresponding to one color) with a 24-site magnetic unit cell (large gray square), four times larger than the geometric unit cell (small square). (b) The spins on the five sublattices point to five out of the six corners of a hexagon. (c) First and extended Brillouin zones of the square-kagome lattice showing the positions of the corresponding dominant and subdominant Bragg peaks. The ratio of the weight of the subdominant peaks λ to the weight of the dominant peaks Λ is $\lambda/\Lambda \approx 85\%$. Figure taken from [P1].

7.3.6 Octagonal and Conical Orders for FM Interactions

Flipping the sign of all three couplings to ferromagnetic in the underlying nearest-neighbor Heisenberg model, i.e. $J_1 = J_2 = J_3 = -1$, the phase diagram for varying cross octagon-plaquette interactions changes its topology substantially. As depicted in Fig. 7.23, there are only three distinct phases. Trivially, there is a large ferromagnetic phase when $J_+, J_\times \leq 0$, which also extents to the other three quadrants in the phase diagram and is bound by the hyperbola defined by $(J_\times - 1)(J_+ - 1) = \frac{1}{2}$. Its ground state energy per site is given by

$$E_{\text{FM}} = -2 + \frac{J_\times + J_+}{3} \, . \tag{7.24}$$

107
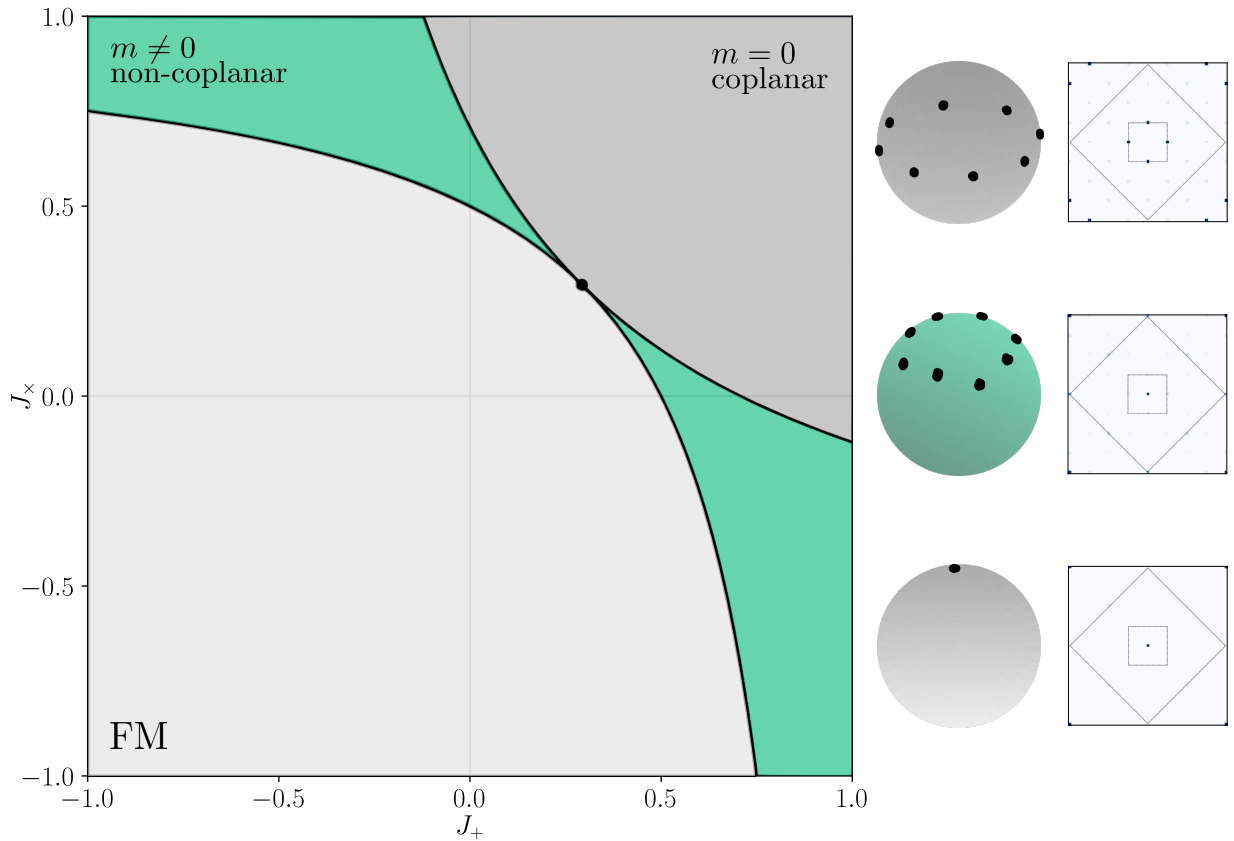
Figure 7.23 − **FM phase diagram.** For fixed $J_1 = J_2 = J_3 = -1$, the model shows a large ferromagnetic phase (light gray), a coplanar phase with octagonal order (dark gray) and non-coplanar umbrella-like double cone states (turquoise) that are an interpolation between octagonal and ferromagnetic states. Ferromagnetic and coplanar phases touch at the single point $J_+ = J_\times = 1 - \frac{1}{\sqrt{2}}$. On the right hand side are corresponding common origin plots and structure factors from Monte Carlo simulations. Figure taken from [P1].

Bound by a second hyperbola, given by $(J_\times + \frac{1}{\sqrt{2}})(J_+ + \frac{1}{\sqrt{2}}) = 1$, there is a coplanar ordered phase with eight sublattices where the spins on each sublattice point to the corners of an octagon. The magnetic unit cell contains 24 sites and is four times larger than the geometric unit cell (cf. Fig. 7.24(a)-(c)). Its ground state has zero magnetization, $m = 0$, and its energy per site is given by

$$E_{\text{octagonal}} = -\frac{1}{3}\left(2 + 2\sqrt{2} + J_+ + J_\times\right). \tag{7.25}$$

Between these two phases, which touch each other only at the point $J_+ = J_\times = 1 - \frac{1}{\sqrt{2}}$, there exist non-coplanar umbrella-like states that smoothly interpolate between octagonal and FM order (cf. Fig. 7.24(d)-(f)). The magnetic unit cell of this phase coincides with the one of the octagonal phase, but the spins are no longer coplanar, but rather the directions in which the spins on the sublattices point form two cones.

The first cone is formed by the four sublattices of spins located on the squares with mutual angles of $\pi/2$, whereas the second cone is formed by the four sublattices of bow-tie spins, again with mutual angles of $\pi/2$ but rotated $\pi/4$ with respect to the first cone. The two polar angles that describe these two cones depend on J_+ and $J_\times$, the ground state energy per site for those
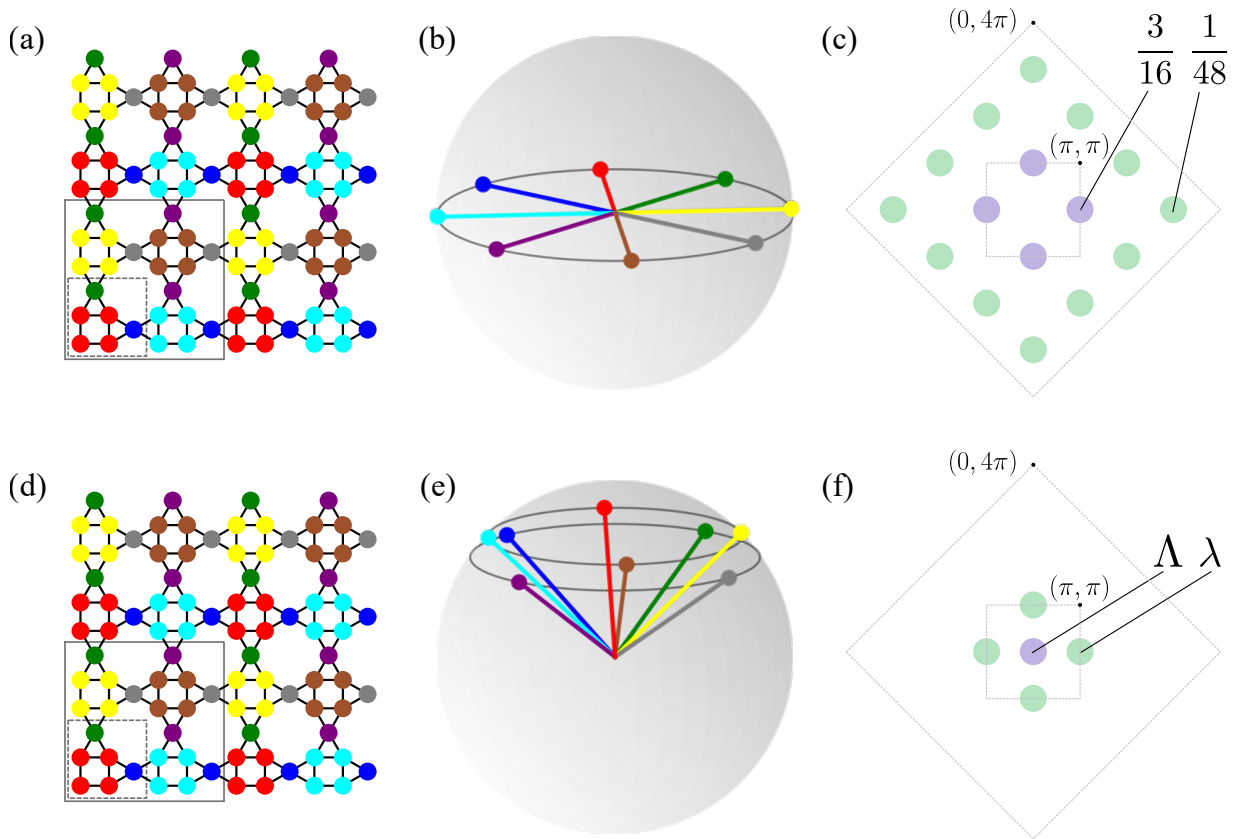
Figure 7.24 – **Octagonal and double-conical orders.** (a) Real space arrangement of spins in the coplanar octagonal ordered state stabilized in the purely ferromagnetic nearest-neighbor model. There are eight sublattices with a 24-site magnetic unit cell (large gray square), four times larger than the geometric unit cell (small square). (b) Each sublattice of spins points towards a different corner of an octagon such that each pair of neighboring spins forms an angle of $\pi/4$. (c) First and extended Brillouin zones showing the positions and the fractions of total spectral weight of the corresponding Bragg peaks. (d) Real space arrangement of spins in the non-coplanar double cone state. The eight sublattices coincide with those of the octagonal state shown in (b). (e) The directions in which the spins on the sublattices point form two cones. The first cone is formed by the four sublattices of spins located on the squares with mutual angles of $\pi/2$, whereas the second cone is formed by the four sublattices of bow-tie spins, again with mutual angles of $\pi/2$ but rotated $\pi/4$ with respect to the first cone. (f) First and extended Brillouin zones showing the positions of the corresponding Bragg peaks. The ratio of the weight of the subdominant peaks λ to the weight of the dominant peaks Λ depends on the two polar angles of the cones and therefore on J_+ and $J_\times$. Figure taken from [P1].

states can be calculated analytically and is given by

$$
E_{\text{conical}} = -\frac{1}{6J_+J_\times}\left(J_+ + J_\times + 4J_+J_\times \right.
$$
$$
\left. \pm (J_+ - J_\times)\sqrt{1 - 12J_+J_\times + 4J_+^2 J_\times^2} \right), \tag{7.26}
$$

where the plus sign applies to the left domain with $J_+ < 1 - \frac{1}{\sqrt{2}}$, and the minus sign to the right domain with $J_+ > 1 - \frac{1}{\sqrt{2}}$. While the ferromagnetic phase has uniform magnetization and the octagonal phase has zero magnetization, the magnetization in the conical phase depends on J_+

and $J_\times$. Analytically, one finds

$$m_{\text{conical}} = \left[(2(J_\times + 4)J_+ \pm \xi) + 1\right]\left[24J_+|J_\times|\right]^{-1}$$
$$\times \sqrt{\frac{\left(2J_\times^2 + 1\right)\xi \pm \left(-4J_\times^3 J_+ + 6J_\times^2 + 6J_\times J_+ - 1\right)}{\xi}}\,, \tag{7.27}$$

where,

$$\xi = \sqrt{4J_\times^2 J_+^2 - 3J_\times J_+ + 1}\,, \tag{7.28}$$

and the plus sign applies to the right domain with $J_+ > 1 - \frac{1}{\sqrt{2}}$, and the minus sign to the left domain with $J_+ < 1 - \frac{1}{\sqrt{2}}$.

7.3.7 Energy and Magnetization

We close this chapter with presenting ground state energy and magnetization Monte Carlo data for selected horizontal and vertical cuts through the phase diagrams of Figs. 7.6 (AFM nearest-neighbor interactions) and 7.23 (FM nearest-neighbor interactions). All data is measured at low temperatures $(T = 10^{-4})$.
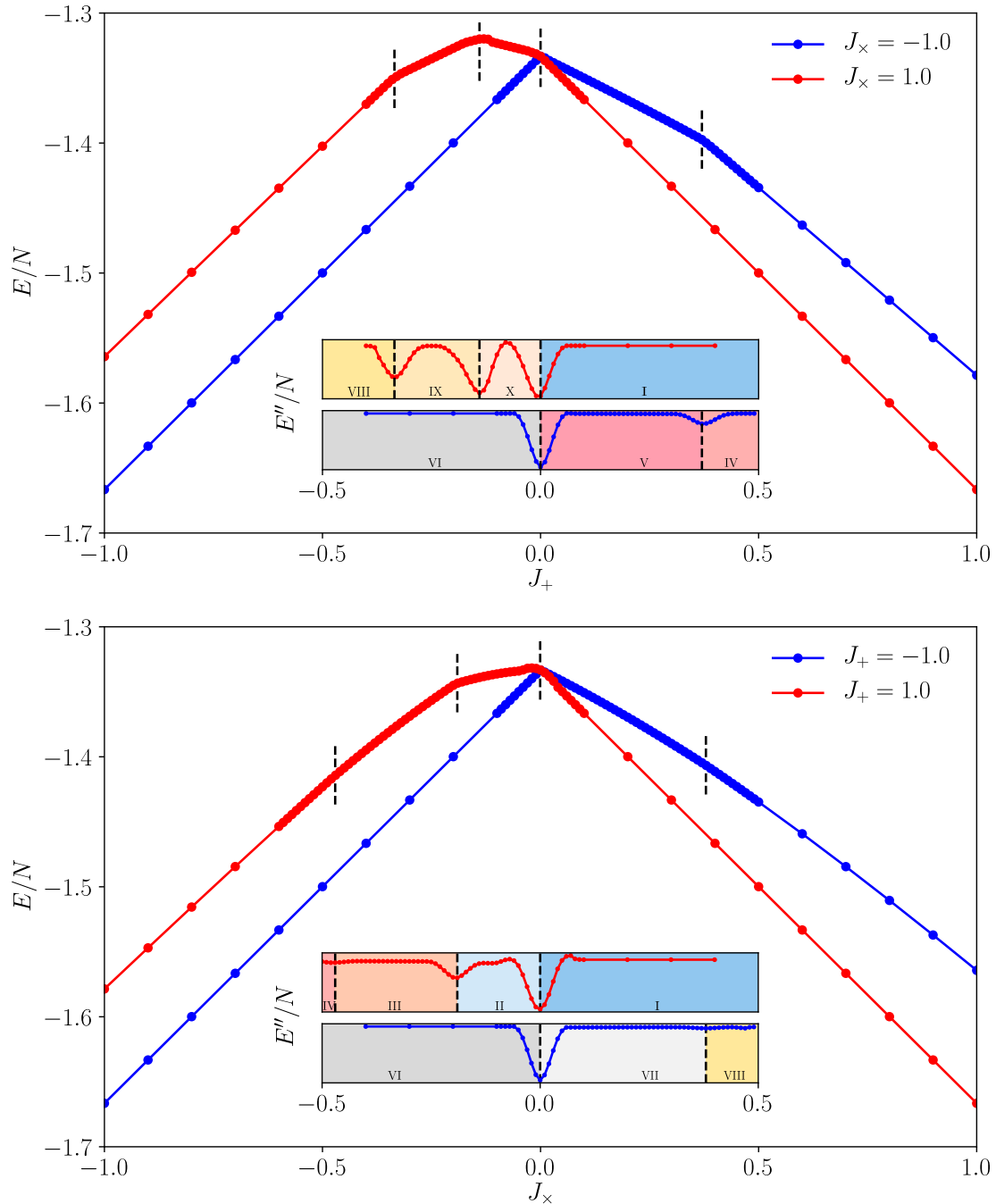
AFM Nearest-Neighbor Interactions

Fig. 7.25 shows Monte Carlo magnetization cuts for fixed $J_+ = -1.0$, and $J_\times = 1.0$, respectively. The only two phases with non-zero magnetization are the 120°-d phase (VII) and the spiral phase VIII. In the deformed 120° phase, the magnetization only depends on $J_\times$ and is given by $m_{120°\text{-d}} = J_\times/(3(2 + J_\times))$.
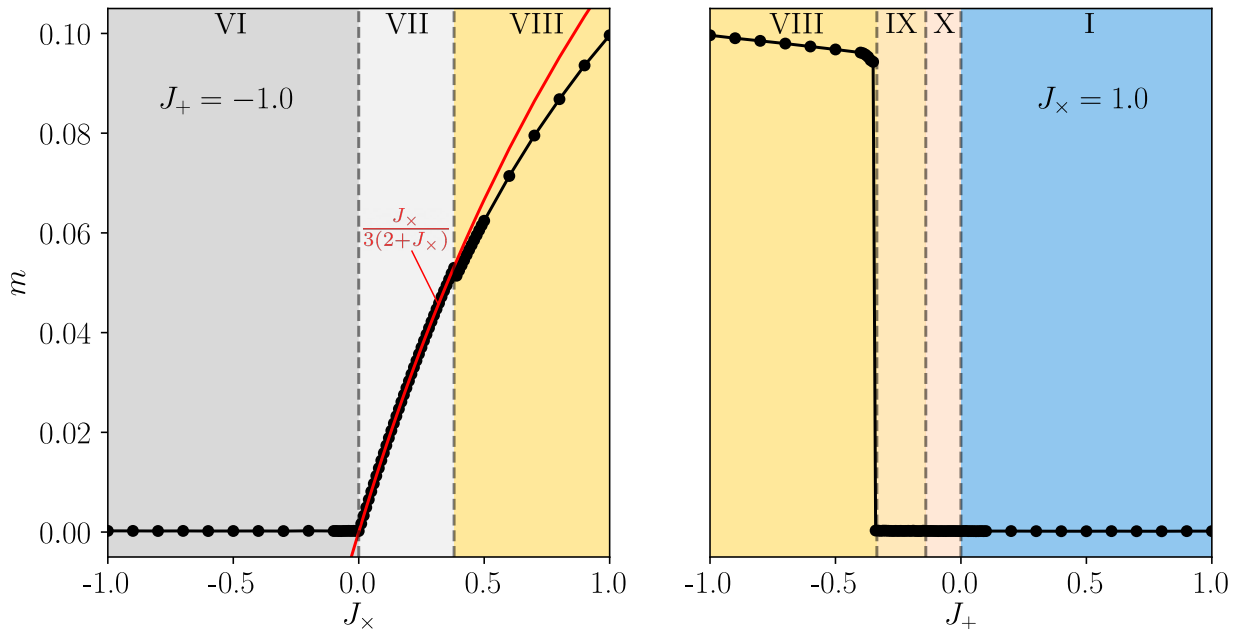
Figure 7.25 − **Magnetization cuts for AFM nearest neighbor interactions.** Magnetization cuts from Monte Carlo simulations for fixed $J_+ = -1.0$ (left) and $J_\times = 1.0$ (right) with the colorcode of the phases shown in Fig. 7.6 in the background. Only the deformed 120° phase (light gray) and the spiral phase with D_{12} symmetry (yellow) have non-zero magnetization. For the deformed 120° phase the magnetization as a function of $J_\times$ can be expressed analytically as $m = J_\times/(3(2 + J_\times))$ (red curve). Figure taken from [P1].

In order to demonstrate the good agreement between the (semi-)analytically derived phase boundaries and Monte Carlo results, we show cuts of E/N for fixed values of $J_+ = \pm 1.0$, and $J_\times = \pm 1.0$, respectively, from Monte Carlo simulations, along with the corresponding second derivatives in Fig. 7.26. The second derivatives of E/N show sharp features exactly at all (semi-)analytically determined phase boundaries.

Figure 7.26 – **Energy cuts for AFM nearest neighbor interactions.** Ground state energy cuts from Monte Carlo simulations for fixed $J_\times = \pm 1.0$ (top) and $J_+ = \pm 1.0$ (bottom). The inset shows the second derivatives of the energy per spin with the phases shown in the phase diagram Fig. 7.6 in the background with the phase boundaries (dashed lines) obtained (semi-)analytically as described in the main text. The second derivatives of E/N show sharp features exactly at all phase boundaries. Figure taken from [P1].

FM Nearest-Neighbor Model

Similarly good agreement between analytically determined phase boundaries and Monte Carlo results we find in the case of FM interactions. Fig. 7.27 shows cuts of E/N for fixed values of $J_+ = 0.0$, and $J_+ = 0.5$, respectively, from Monte Carlo simulations along with the corresponding derivatives in Fig. 7.26. Note that the second derivatives of the energy do not reveal any sharp features (not shown here). Therefore, we present the third derivatives of E/N with the result that these show sharp features at the (semi-)analytically determined phase boundaries. We thus conclude that the phase transitions are of one order higher than in the AFM case considered in Fig. 7.26.
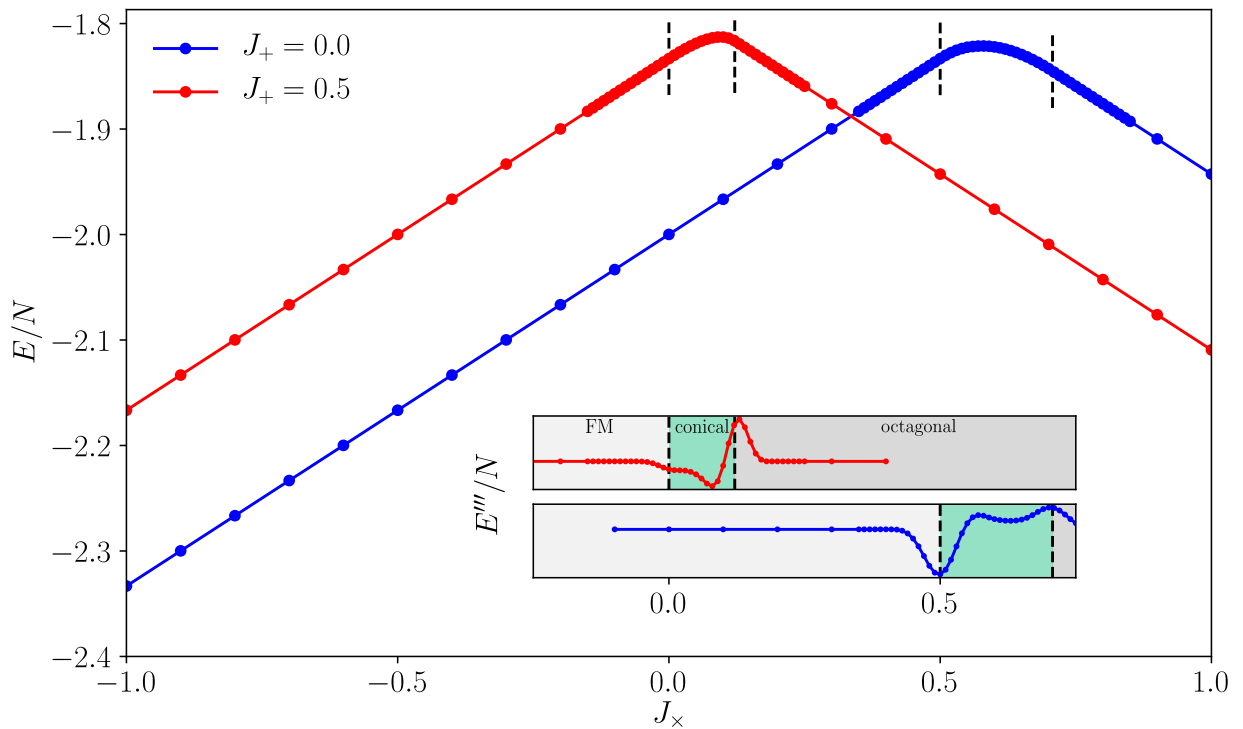
Figure 7.27 – **Energy cuts for FM nearest neighbor interactions.** Energy cuts from Monte Carlo simulations for fixed $J_+ = 0.0$ (blue) and $J_+ = 0.5$ (red). The inset shows the third derivatives of the energy per spin with the phases shown in Fig. 7.23 in the background with phase boundaries (dashed lines) obtained analytically as described in the main text. The third derivatives of E/N show sharp features exactly at the phase boundaries. Figure taken from [P1].

7.4 Discussion and Outlook

Led by the search for non-coplanar magnetic orders, we have indeed found a plethora of non-trivial magnetic textures on the square-kagome lattice. These orders are stabilized by introducing cross-plaquette interactions in addition to the classical nearest-neighbor Heisenberg model, with either antiferromagnetic or ferromagnetic nearest-neighbor interactions, or a combination of both (ferromagnetic on bow-tie bonds and antiferromagnetic on square bonds). By employing large-scale Monte Carlo simulations, we revealed a variety of non-coplanar states including a new type of cuboctahedral order (termed *cuboc3*, Fig. 7.21), as well as highly intricate non-coplanar spirals. The underlying magnetic unit cells of these spin spiral states feature a highly complex structure and large sizes but, remarkably, we were able to provide a semi-analytical construction of these phases based on a symmetry-optimized parametrization with our Monte Carlo results as a starting point. This allowed us to obtain explicit expressions (depending only on a comparably small number of parameters) for their ground state energy as a function of the coupling strengths, which in turn enables us to establish, with high precision, the phase boundaries between these complex spiral phases. The approach established here, in which numerics and semi-analytics go hand in hand, is universal and can be transferred one on one to other lattice geometries, as we will show in the next chapter using the maple-leaf lattice as another example.

Besides the ground state, we also studied the thermodynamics of non-coplanar states employing classical Monte Carlo simulations. By virtue of being chiral, non-coplanar states are expected to feature a symmetry-breaking phase transition at $T \neq 0$. In particular, for the cuboc order we presented the temperature evolution of the specific heat, the chiral order parameter, and its susceptibility, for different system sizes which manifestly exhibits signatures of a chiral phase transition. For the elementary model with only three symmetry inequivalent nearest-neighbor couplings, we showed that, besides the isotropic point, within the entire region occupied by an extensively degenerate manifold of ground states one can always identify three distinct temperature regimes, namely, a high-temperature thermal paramagnet, an intermediate-temperature cooperative paramagnet, and a low-temperature coplanar regime selected via an order-by-disorder mechanism. We showed that upon introduction of ferromagnetic cross-plaquette interactions of just one type, i.e., either J_+ or $J_\times$, the extensive degeneracy is reduced, but there still persists one zero mode per per triangle or per unit cell, respectively. This results in a $T \to 0$ limiting value of specific heat which is less than one, however, the intermediate-temperature cooperative paramagnetic temperature regime disappears.

As motivated earlier, non-coplanar magnetic orders could give rise to chiral quantum spin liquids if quantum fluctuations are introduced and spin rotational symmetry is restored. We thus provided a detailed symmetry analysis for the non-coplanar orders on the square-kagome lattice, paving the way for the systematic classification of possible descendant chiral spin liquid states. The exploration of these exotic phases in the corresponding quantum models employing state-of-the-art numerical quantum many-body approaches constitute an important direction of future research.

In the context of material realizations, it is worth noting that in the copper based compound $Na_6Cu_7BiO_4(PO_4)_4[Cl,(OH)]_3$ [216], the $J_\times$ interactions are mediated by Cu-O-Na-O-Cu superexchange pathways, while the J_+ bonds pass through a chloride group at distances that prevent any Cu-Cl hybridization, and thus not triggering a superexchange. The presence of the non-magnetic Na ions in the center of the octagons is likely to trigger a finite $J_\times$ interac-

tion akin to the scenario realized in the kagome based materials kapellasite and haydeeite [246]. One could think of possible chemical substitutions which are likely to enhance this interactions, e.g., by replacing Na with Cs which has a larger ionic radius. Another route towards strengthening the cross-plaquette couplings would involve preparing the corresponding sulfide version instead of oxides leading to Cu-S-Na-S-Cu type superexchange pathways, similar to the breathing chromium spinels [247]. In $KCu_6AlBiO_4(SO_4)_5Cl$ [213], it is the sulfate SO_4^{2-} that occupies the octagon centers and one may consider the possibility of substituting it with a selenate group SeO_4^{2-} to enhance both the cross-plaquette couplings. These would constitute interesting future explorations on the material synthesis front[6].

---

[6]The last paragraph of the discussion about possible material realizations was written by Yasir Iqbal and taken from Ref. [P1], of which he is a co-author.

Maple-Leaf Antiferromagnets

Recently, a wide range of candidate materials involving quantum spins on the maple-leaf lattice geometry has attracted attention, including the copper minerals bluebellite $Cu_6IO_3(OH)_{10}Cl$ [248, 249], spangolite $Cu_6Al(SO_4)(OH)_{12}Cl{\cdot}3H_2O$ [250], and many more [251–254]. Their potential to host non-trivial quantum ground states such as quantum spin liquids or dimer states led to a number of theoretical studies of quantum antiferromagnets on this very lattice geometry [255–258].

Also from a classical point of view, the maple-leaf lattice is an ideal playground to explore interesting physics. Its non-Bravais property and the possibility of integrating additional cross-plaquette interactions provide the best conditions for finding intricate non-coplanar magnetic orders. To this end, in this chapter we discuss the ground state phase diagram of a classical Heisenberg model on the maple-leaf lattice with further-neighbor interactions based on the methods that have already proven to be fruitful in the previous chapter.

This chapter is based on publication [P2], which is still a work in progress at the time of this writing. The parts of publication [P2] for which the author of this thesis is responsible are presented below.
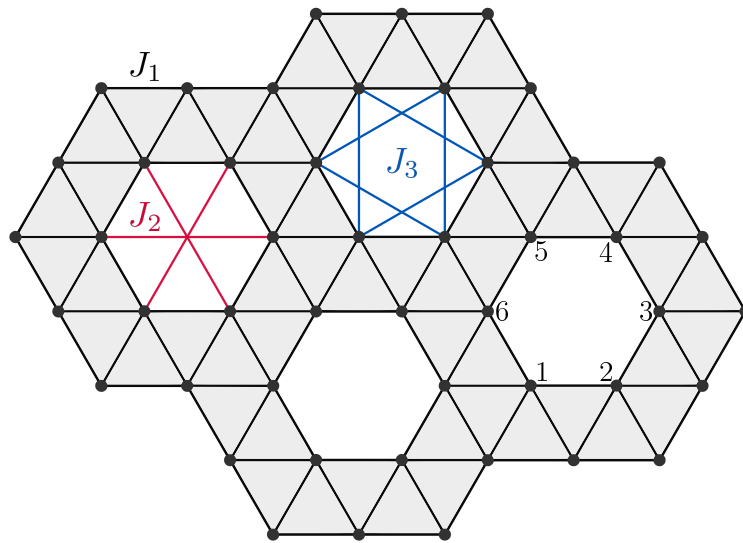
8.1 Maple-Leaf Heisenberg Model

The maple-leaf lattice [259] is an Archimedean lattice that is obtained by a periodic depletion of $1/7$ of the sites of the triangular lattice, as visualized in Fig. 7.1. Its coordination number is $z = 5$ and, therefore, it is intermediately frustrated between the kagome ($z = 4$) lattice and the triangular ($z = 6$) lattice. It can be described by the lattice vectors

$$\mathbf{a}_1 = \left(\frac{3\sqrt{3}}{2}, -\frac{1}{2}\right), \qquad\qquad \mathbf{a}_2 = \left(\sqrt{3}, 2\right),$$

and a unit cell comprising six sites with relative coordinates

$$\delta_1 = (0,0), \qquad\qquad \delta_2 = \left(\frac{\sqrt{3}}{2}, -\frac{1}{2}\right),$$

$$\delta_3 = \left(\sqrt{3}, 0\right), \qquad\qquad \delta_4 = \left(\sqrt{3}, 1\right),$$

$$\delta_5 = \left(\frac{\sqrt{3}}{2}, \frac{3}{2}\right), \qquad\qquad \delta_6 = (0,1).$$

Figure 8.1 – **Maple-leaf lattice and interactions.** Resulting from a 1/7-depletion of the triangular lattice, each site of the maple-leaf lattice belongs to four triangular and one hexagonal plaquette. Next to the nearest-neighbor coupling J_1, cross-hexagon interactions J_2 and J_3 are introduced. The unit cell contains the six sites (labeled 1 to 6) of a single hexagonal plaquette.

Motivated by the stabilization of non-coplanar magnetic orders by cross-plaquette interactions in the previously discussed square-kagome Heisenberg model (SKHM), we introduce further-neighbor cross-hexagon interactions J_2 and J_3 (as indicated in Fig. 8.1) in addition to the nearest-neighbor coupling J_1 to our classical Heisenberg model on the maple-leaf lattice (MLHM).

Numerically, we proceed in exactly the same way as in the SKHM. We again employ Monte Carlo simulations over a range of parameters for the cross-plaquette interactions, performed on finite lattices of size $L \times L$, i.e. $N = 6L^2 = 864$. Also similar to the study of the SKHM, a parallel tempering scheme is employed with 192 logarithmically spaced temperature points between $T_{\min} = 10^{-4}$ and $T_{\max} = 10$ and measurements are performed over $5 \cdot 10^8$ sweeps after a thermalization period of 10^8 sweeps. Where necessary, these simulations are supplemented by the semi-analytical method presented in Sec. 7.3.4[1].

8.2 Ground State Phase Diagram

Upon varying the cross-plaquette interactions J_2 and J_3 (where $J_1 = 1$ is fixed to be antiferromagnetic), we indeed find a number of different ground state phases, including coplanar and non-coplanar magnetic orders as summarized in the phase diagram Fig. 8.2. From the representative common origin plots (and also from static spin structure factors) next to the phase diagram, one can see at first glance that the six phases found (labeled I to VI) are clearly distinct from each other.

The coplanar phases I and III appear in the form of two different six-sublattice ordered states, the first of which has already been described in the context of the quantum model on the maple-leaf lattice without cross-plaquette interactions [258, 260]. The remaining four phases come in

---

[1]As in the SKHM, the semi-analytical results for the MLHM have been worked out in close collaboration with Heinz-Jürgen Schmidt (co-author of [P2]).
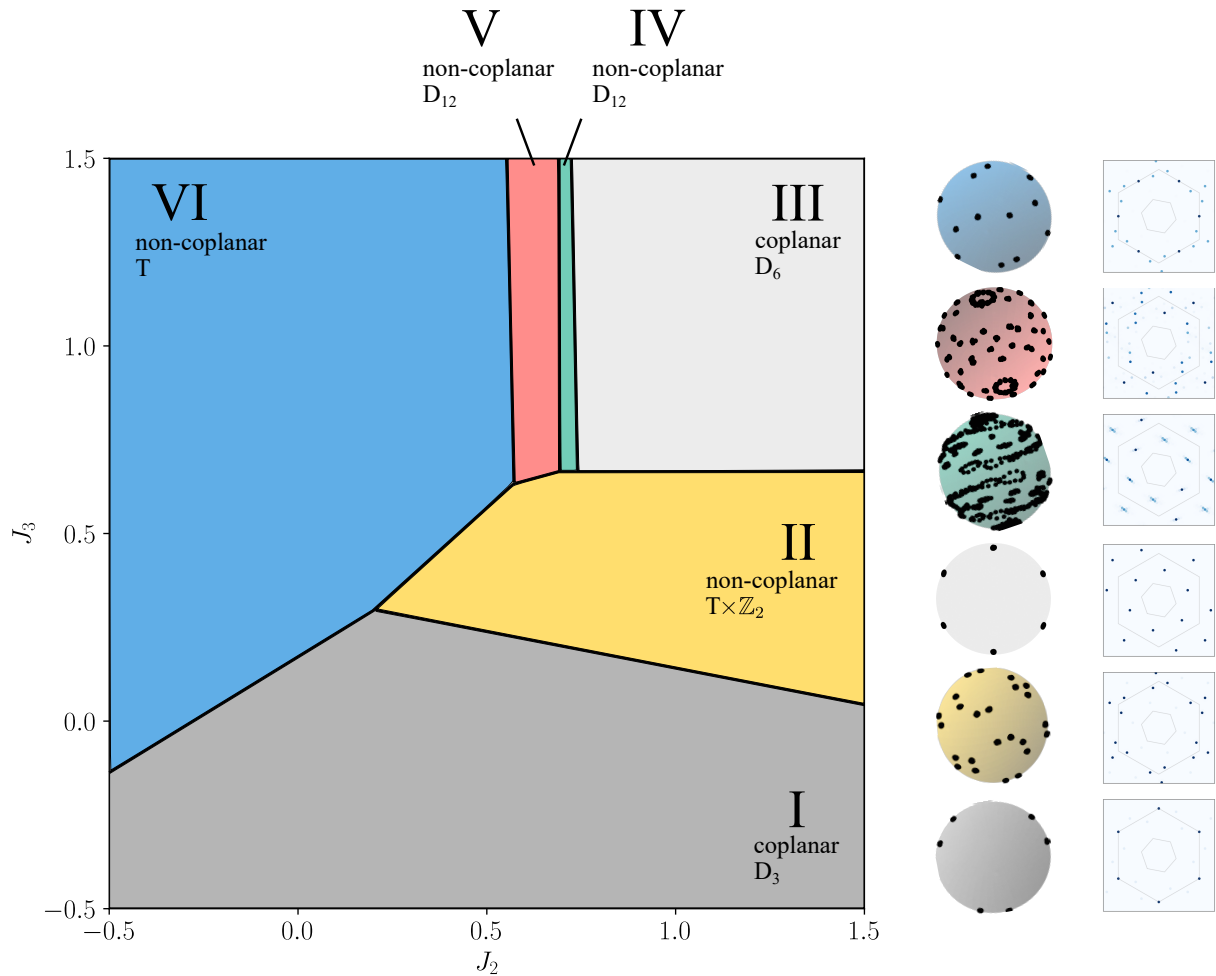
Figure 8.2 – **Classical phase diagram of the maple-leaf lattice** with six different phases (labeled I-VI) as a function of J_2 and J_3 ($J_1 = 1$). Besides indicating the phase boundaries (solid lines), the phases are described by symmetry (with D_n referring to the dihedral group of order n and T to tetrahedral symmetry), and coplanarity. Also, we show Monte Carlo common origin plots and spin structure factors for each phase to the right of the phase diagram.

different non-coplanar orders, including commensurate variants (phases II and VI) as well as incommensurate ones (phases IV and V). We will provide details about each phase in the remainder of this section.

8.2.1 Coplanar Orders

We start with the coplanar ground states of phase I and phase III which make up large parts of the lower half and the upper right corner of the phase diagram Fig. 8.1, respectively.

Coplanar Phase I with D_3 Symmetry

This order has already been described in full agreement with our numerical results as the ground state in the classical limit of the quantum maple-leaf Heisenberg model in Refs. [258, 260]. It consists of six sublattices of spins and a three times larger magnetic unit cell, as indicated in

(a) Phase I

(b) Phase III
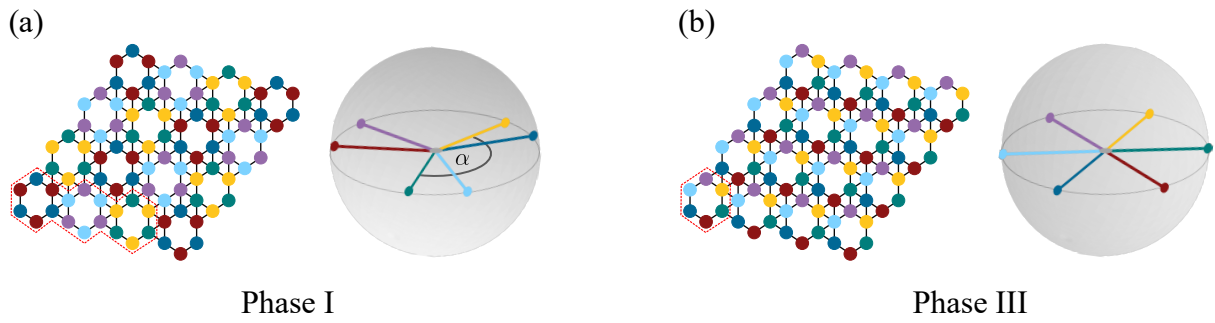
Figure 8.3 – **Coplanar orders.** (a) The ground state of phase I has six sublattices of spins and a 18-site magnetic unit cell (outlined in red). Within one geometrical unit cell, neighboring spins form an angle α (for example, yellow and green spins) while next-nearest neighbors are parallel. Equivalent spins in two neighboring geometric unit cells are rotated by $2\pi/3$ (for example, yellow and light blue spins). (b) In phase III, the ground state has six sublattices as well, but the magnetic unit cell coincides with the geometrical unit cell. Within each unit cell, each spin points to a different corner of a regular hexagon and nearest neighbors (within a unit cell) form an angle of $\pi/3$.

Fig. 8.3(a). Within one geometrical unit cell, neighboring spins form an angle

$$\alpha = \arctan\left(\frac{\sqrt{3}}{3 + 2J_2}\right) + \pi \tag{8.1}$$

while next-nearest neighbors are parallel. Equivalent spins in two neighboring geometric unit cells are rotated by $2\pi/3$. Its energy can explicitly be given as

$$E_{\mathrm{I}} = -\frac{1}{2}\left(1 + \sqrt{3 + 3J_2 + J_2^2} - 2J_3\right). \tag{8.2}$$

The symmetry of this ground state is given by the dihedral group of order 3, D_3. For the special case $J_2 = -2$, the six different spin vectors form a regular hexagon with D_6 symmetry. In the case $J_2 = -1$, on the other hand, the ground state becomes a 120° state which still has D_3 symmetry.

Coplanar Phase III with D_6 Symmetry

The rigid coplanar order of phase III, found in in the upper right corner of the phase diagram, also has six sublattices of spins, but the magnetic unit cell coincides with the geometrical unit cell. Within each unit cell, each spin points to a different corner of a regular hexagon (see Fig. 8.3(b)) and nearest neighbors (within a unit cell) form an angle of $\pi/3$. The corresponding ground state energy is

$$E_{\mathrm{III}} = -\frac{1}{2}\left(1 + J_2 + J_3\right). \tag{8.3}$$

and the symmetry group of the ground state is the dihedral group of order 6, D_6.

8.2.2 Non-Coplanar Orders

We now come to discuss of the various non-coplanar magnetic orders. Our brief introduction of the same starts with the two commensurate structures found in the phases II and IV of the phase diagram. Starting point for all semi-analytical descriptions are numerical Monte Carlo ground states at $T = 10^{-4}$ with fixed $J_1 = 1$.

Phase II   Phase VI
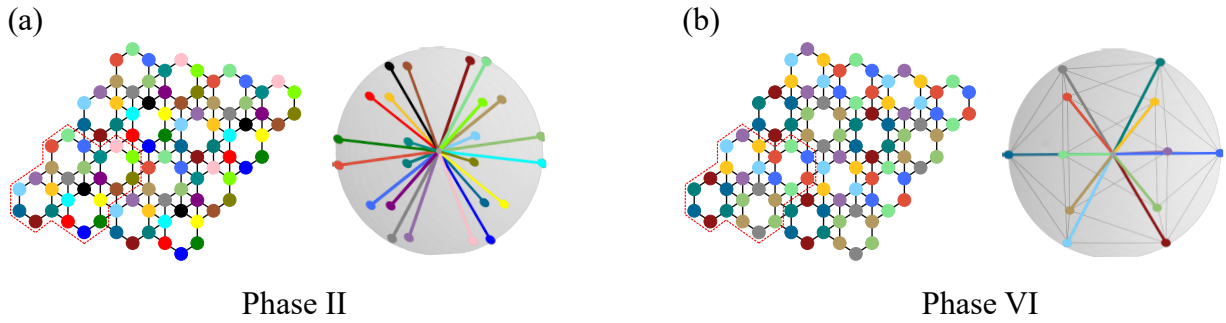
Figure 8.4 – **Non-coplanar orders II and VI.** (a) The ground state of phase II has 24 sublattices of spins and a magnetic unit cell with as many sites (outlined in red in the real-space arrangement on the left). Right: common origin plot of the 24 spin directions. (b) The ground state of phase VI has a 24-site magnetic unit cell as well, but only 12 sublattices of spins. In general, these point to the corners of a deformed icosahedron which becomes regular in the special case $J_2 = -1.0, J_3 = 0.0$ (shown here).

Non-Coplanar Phase II with $T \times \mathbb{Z}_2$ Symmetry

The ground state of phase II consists of 24 sublattices of spins and the magnetic unit cell spans the same amount of sites, as shown in Fig. 8.4(a) exemplarily for $J_2 = 0.5$ and $J_3 = 1.0$. A symmetry analysis of the ground state reveals that its symmetry is described by the symmetry group $T \times \mathbb{Z}_2$, the direct product of the tetrahedral group without reflections T and the group $\{\text{id}, -\text{id}\} \cong \mathbb{Z}_2$. The energy of this state can be expressed as a function of two parameters λ and α as

$$E_{\mathrm{II}} = \frac{1}{6} \Big[-7 - 3J_2 + 12\lambda^2 - 9J_3\lambda^2 + 2\lambda\sqrt{6 - 6\lambda^2}\cos\alpha$$
$$+ 4\lambda^2\cos 2\alpha + 2\lambda\sqrt{2 - \lambda^2}\sin\alpha + 2\sqrt{3}\lambda^2\sin 2\alpha + 6J_3 \Big]. \tag{8.4}$$

Minimizing this expression for $J_2 = 0.5$ and $J_3 = 1.0$ yields $E_{\mathrm{II,semi\text{-}analytical}} = -1.41782$ which fits well with the Monte Carlo result for the same parameters $E_{\mathrm{II,MC}} = -1.417(5)$.

Non-Coplanar Phase VI with T Symmetry

The magnetic order of phase VI also has a 24-site magnetic unit cell, but only 12 sublattices of spins. In general, these point to the corners of a deformed *icosahedron*, which becomes regular in the special case $J_2 = -1.0, J_3 = 0.0$ shown in Fig. 8.4(b). Its symmetry is described by the tetrahedral symmetry group without reflections T (for the aforementioned special case it becomes the icosahedral symmetry group I_h). The general expression for the ground state energy as a function of two parameters λ and α is

$$E_{\mathrm{VI}} = \frac{1}{6} \Big[3 + 3J_2 - 6\lambda^2 - 9J_3\lambda^2 + 4\lambda\sqrt{6 - 6\lambda^2}\cos\alpha$$
$$+ 3\lambda^2\cos 2\alpha - \sqrt{3}\lambda^2\sin 2\alpha + 6J_3 \Big]. \tag{8.5}$$

Minimizing this term for, e.g., $J_2 = -0.5$ and $J_3 = 0.5$, leads to $E_{\mathrm{VI,semi\text{-}analytical}} = -1.60183$ in line with the corresponding Monte Carlo result $E_{\mathrm{VI,MC}} = -1.601(4)$.

In the following, we conclude this report on the various non-coplanar orders on the maple-leaf lattice with the two incommensurate spiral structures of phases IV and V.

119

Non-Coplanar Phase IV with D_{12} Symmetry

In the spiral phase IV, as depicted in the common origin plot on the left of Fig. 8.5(a) for $J_2 = 0.7$ and $J_3 = 1.0$, we are left with $M = 72$ unique spin vectors after grouping those spins that point into the same direction (cf. the corresponding plot on the right of the very same figure). This state is symmetric under actions of the dihedral group of order 12, D_{12}, as well as under mirroring $z \mapsto -z$. The ground state energy E_{IV} can explicitly be expressed analytically as a function of eight parameters (which is too long to be specified here). Its minimization yields $E_{IV,\text{semi-analytical}} = -1.35069$, consistent with the Monte Carlo result $E_{IV,MC} = -1.350(5)$.

Non-Coplanar Phase V with D_{12} Symmetry

For the spiral phase V, we consider the numerical Monte Carlo ground state for $J_2 = 0.6$ and $J_3 = 1.0$, as shown in the common origin plot on the left of Fig. 8.5(b). After grouping the $N = 864$ spin vectors according to their unique directions, we are left with $M = 72$ unique spin vectors, which can be divided into six groups with constant z-component, as visualized on the right of Fig. 8.5(b). Taking into account D_{12} symmetry and invariance under $z \mapsto -z$, the state can be described by three z-components z_1, z_2, and z_3, and the difference angle $\delta\phi$ between the azimuth angles of the spins on the two lower circles on the one hand, and the upper circle on the other. With these parameters, the ground state energy takes the form

$$E_V = \frac{1}{12}\left[-1 - 4z_1^2 - z_2^2 - 2\sqrt{3 - 3z_2^2}\sqrt{1 - z_3^2} - J_2\left(1 + z_1^2 + 2z_2^2 + 2z_3^2\right) \right.$$

$$- 4J_3\left(-z_2z_3 + z_1(z_2z_3) + \sqrt{1 - z_2^2}\sqrt{1 - z_3^2} \right)$$

$$+ \sqrt{1 - z_1^2}\left(\left(2\sqrt{1 - z_2^2} - (2 + \sqrt{3})J_3\left(\sqrt{1 - z_2^2} - \sqrt{1 - z_3^2}\right)\right)\cos\delta\phi \right)$$

$$\left. + \left((-4 + 2\sqrt{3})\sqrt{1 - z_2^2} + J_3\left(\sqrt{1 - z_2^2} - \sqrt{1 - z_3^2}\right)\right)\sin\delta\phi \right)\right]. \tag{8.6}$$

Minimization of this energy yields $E_{V,\text{semi-analytical}} = -1.32311$ in good agreement with and slightly smaller than the Monte Carlo result $E_{V,MC} = -1.322(7)$ for the same parameters.

(a)   (b)
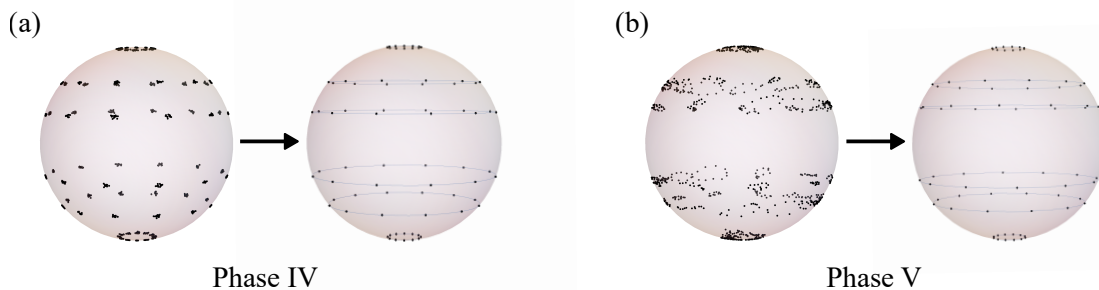
Phase IV   Phase V

Figure 8.5 – **Non-coplanar spiral orders IV and V.** (a) Left: common origin plot of the Monte Carlo ground state of spiral phase IV (for $J_2 = 0.7$ and $J_3 = 1.0$) with $N = 864$ spins. Right: These can be grouped into $M = 72$ unique directions and described analytically (see text). The resulting order has D_{12} symmetry. (b) The same applies in the case of the spiral ground state of phase V, here shown for $J_2 = 0.6$ and $J_3 = 1.0$. The plots of the unique spin directions shown in this figure have been kindly provided by Heinz-Jürgen Schmidt.

8.2.3 Energy and Specific Heat

To conclude this chapter, we present some cuts of the ground state energy as a function of J_2 and J_3, along with selected plots of the specific heat for all six phases of the state diagram. The former are presented in Fig. 8.6 and again underline, as in the SKHM, the good interplay of Monte Carlo numerics on one side, and semi-analytical method on the other. The insets in Fig. 8.6 display the second derivatives of the Monte Carlo ground state energy along with the semi-analytically determined phase boundaries. Note that it is precisely at these boundaries that the Monte Carlo energies have sharp features, which is a confirmation of the accuracy of the phase diagram we have determined.
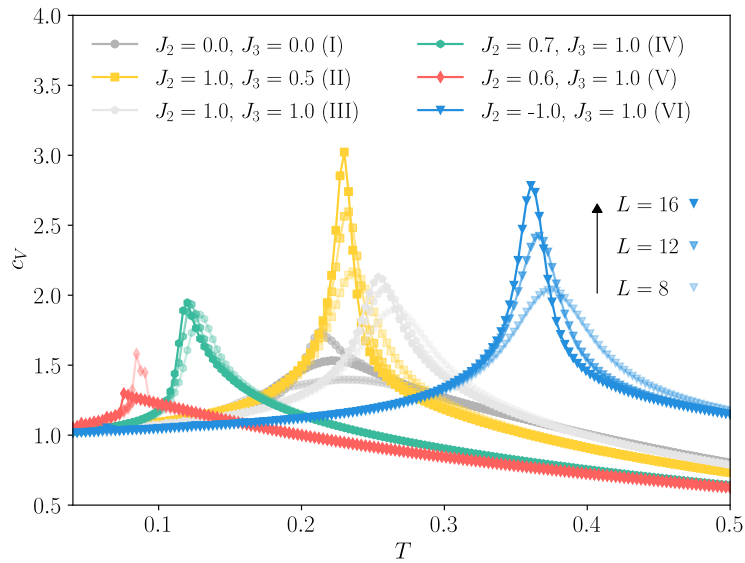
Specific heat traces for the six phases are shown in Fig. 8.7. The spiral phases IV and V show complicated behaviour; due to their incommensurability, these phases depend very sensitively on finite-size effects. In contrast, the three phases II, III, and VI, display single peaks at some finite temperature that scale with the system size—a scaling behaviour that is expected for a thermal ordering phase transition. Phase I is out of line, here. The peak size for $L = 12$ is larger than for $L = 16$. This strange behavior is unexpected and should be investigated further.

8.3 Discussion and Outlook

Motivated by the successful search for non-coplanar magnetic orders on the square-kagome lattice described in the previous chapter, we have here applied our fruitful method to another classical Heisenberg model with nearest-neighbor as well as cross-plaquette interactions on a non-Bravais lattice in the form of the maple-leaf lattice. Using our combined approach of Monte Carlo numerics on the one hand and the semi-analytical method on the other hand, we have again revealed a complex ground state phase diagram with an abundance of coplanar and non-coplanar magnetic structures. The latter include, besides complicated incommensurate spiral structures, a newly type of (deformed) *icosahedral* order (Fig. 8.4(b)).
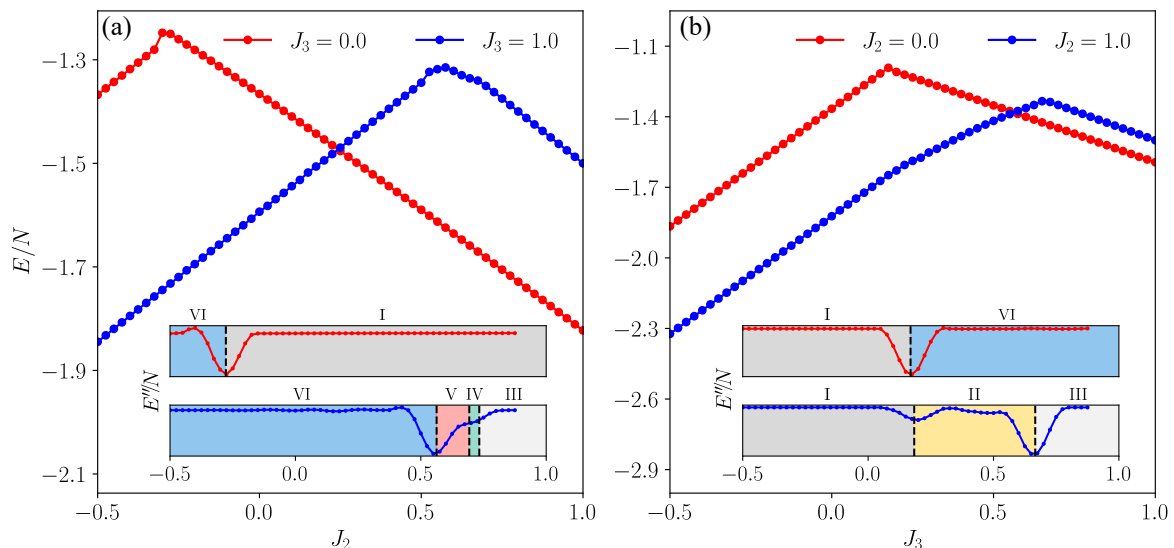
Figure 8.6 – **Ground state energies** from Monte Carlo simulations at low temperatures ($T = 10^{-4}$) for (a) fixed $J_3 = 0.0, 1.0$, and (b) fixed $J_2 = 0.0, 1.0$, respectively. The insets show the corresponding second derivatives, E''/N. These show sharp features exactly at the semi-analytically determined phase boundaries (indicated as vertical dashed lines).

Figure 8.7 – **Specific heat traces** from Monte Carlo simulations for all six phases, color-coded the same way as in the phase diagram Fig. 8.2. The spiral phases IV and V (green and red, respectively) show complicated behaviour indicating a sensitive dependence on finite-size effects. The three phases II (yellow), III (light gray), and VI (blue), display a scaling behaviour that is expected for a thermal phase transition with a single peak that grows with system size. Phase I is out of line, with a peak size for $L = 12$ larger than for $L = 16$.

With the relevance of quantum counterparts of such non-trivial structures in mind, our classical phase diagram can be seen as a foundation for the exploration of quantum models on the maple-leaf lattice. Some of this has already been done in the publication [P2] currently being prepared, of which this classical study forms a part. In it, the exact same model with the exact same couplings is examined by means of pseudo-fermion functional renormalization group (PF-FRG) calculations [261]. These calculations reveal the existence of *quantum disordered states*, indicated by the absence of a flow breakdown in some areas of the phase diagram—especially where classically the spiral phases are located and near the phase boundaries I-VI, II-VI and I-II.

Regarding possible material realizations, our classical study involving cross-plaquette interactions provides a motive to consider ways to generate such couplings for the various maple-leaf materials already available.

General Concluding Remarks

In this thesis, we have studied a variety of classical spin systems that, taken together, exhibit a wide range of the rich phenomenology of frustrated magnetism. For this purpose we have extended existing methods and applied them to uncover various interesting physical phenomena.

We have thus substantially advanced the classical Monte Carlo method by adding to it a dynamical flavor, viz. the interpretation of the Markov chain as time evolution. For the dipolar spin ice system studied in Chapter 4, this allowed us to investigate the dynamics of emergent magnetic monopoles near the monopole liquid-gas transition when applying an external magnetic AC field. We showed that while modulation with a transverse field reveals a critical speeding up, a modulated longitudinal magnetic field yields a critical slowing down, in good agreement with experimental observations. However, the mechanism behind this directional dependence of the dynamics remains an intriguing question. To make the comparison with experimental data systematic, we have gone far beyond the purely phenomenological Arrhenius law ansatz of Takatsu et al., and developed a profound theory for the conversion factor between Monte Carlo time and real time. Eventually, we were able to validate this theory in parts of the phase diagram from zero field up to the kagome ice regime. For the Coulomb spin liquid of the triangular lattice Ising antiferromagnet (TIAFM) described in Chapter 5, we explored the finite-temperature crossover to the paramagnet which is also found to exhibit fluctuation-enhanced dynamics. Moreover, we have shown that the numerical signature of the dynamics in the TIAFM describes well the experimental relaxation times in $Ca_3Co_2O_6$, a system consisting of antiferromagnetically coupled spin chains on a triangular lattice with ferromagnetic intra-chain couplings. Future research should address the question of how these experimental findings, explained by quantum tunneling of magnetization, are related to numerical relaxation times in the classical TIAFM. The numerical observations of Chapters 4 and 5 might indicate that unconventional forms of magnetism often go hand-in-hand with unusual dynamical phenomena – a motif that should warrant further exploration, particularly in quantum magnets.

Also through large-scale Monte Carlo simulations, we then explored in great detail classical Heisenberg models with additional further-neighbor cross-plaquette interactions on non-Bravais lattices in the form of the square-kagome lattice (SKHM, Chapter 7) and the maple-leaf lattice (MLHM, Chapter 8). In the case of the SKHM, we first looked at the pure nearest-neighbor model and encountered a number of concepts that are intimately linked to frustrated magnetism, including a classical spin liquid phase and multiple order-by-disorder mechanisms. Guided by the search for non-coplanar magnetic orders, we then explored the ground state phase diagram for both models, SKHM and MLHM, with further-neighbor interactions by joint forces of numerical simulation results combined with a semi-analytical method. Indeed, we were able to show that in both cases a large number of different ground states constitute the phase diagram. These appear

partly coplanar, but also come in intricate non-coplanar forms and complex incommensurate spiral phases. For the latter, it must be taken into account how much they depend sensitively on the simulated system size. For unit cells comprising hundreds of spins, it cannot be excluded that the found spiral phases may change considerably towards significantly larger systems. This would be a separate question that could be investigated in the future. Among the non-coplanar orders, a novel cuboctahedral order (cuboc3) on the square-kagome lattice and an icosahedral order on the maple-leaf lattice are noteworthy. Our classical studies of these models thus lay the groundwork for future investigations, since exploring the quantum analogs of these phases, either conceptually as in quantum spin-1/2 generalizations of our models, or experimentally, may prove fruitful in identifying chiral quantum spin liquids.

Considering the topics of this thesis as a whole, the verdict is clear: the study of frustrated magnets in the classical realm continues to be an exciting, cutting-edge field. This is not only because it is a playground for the development and extension of numerical and analytical methods of all kinds. More importantly, there is still fascinating new physics to be discovered here—either in the classical systems themselves, or in these systems as precursors to possible new exotic quantum phases of matter. In conclusion, to paraphrase P.W. Anderson, *frustration is STILL the name of the game.*

Appendices

Debye Relaxation from Linear Response Theory and Generalized Debye Models

We review the derivation of Debye relaxation, Eq. (3.42), from linear response theory [107]. In linear response theory, the generalized response function $\chi(t-t')$ describes how a general system shows a generalized displacement

$$x(t) = \int_{-\infty}^{\infty} \chi(t-t')f(t')\mathrm{d}t' \tag{A.1}$$

due to a generalized force $f(t-t')$. Using the convolution theorem, we can rewrite this as a product,

$$x(\omega) = \chi(\omega)f(\omega), \tag{A.2}$$

with the Fourier transform defined as

$$x(\omega) = \int_{-\infty}^{\infty} \mathrm{e}^{-i\omega t}x(t)\mathrm{d}t \tag{A.3}$$

and the corresponding inverse transform

$$x(t) = \frac{1}{2\pi}\int_{-\infty}^{\infty} \mathrm{e}^{i\omega t}x(\omega)\mathrm{d}\omega. \tag{A.4}$$

Assuming causality, that is $\chi(t-t') = 0$ for $t < t'$, we write $\chi(t) = X(t)\theta(t)$ with the Heaviside function $\theta(t)$ and construct $X(t)$ to be odd by choosing

$$X(t) = \begin{cases} \chi(t) & \text{for } t > 0 \\ -\chi(|t|) & \text{otherwise.} \end{cases} \tag{A.5}$$

Consequently, $X(\omega)$ is purely imaginary. By again making use of the convolution theorem, we write the product $X(t)\theta(t)$ as a convolution,

$$\chi(\omega) = \frac{1}{2\pi}\int_{-\infty}^{\infty} \theta(\omega'-\omega)X(\omega')\mathrm{d}\omega', \tag{A.6}$$

and use $\theta(\omega) = \pi\delta(\omega) - i/\omega$ to get

$$\chi(\omega) = \frac{1}{2}X(\omega) - \frac{i}{2\pi}\text{PV}\int_{-\infty}^{\infty}\frac{X(\omega')}{\omega' - \omega}d\omega' \equiv \chi'(\omega) + i\chi''(\omega) \tag{A.7}$$

where the Cauchy principal value (PV) of the second term is taken to avoid any singularities. Since $X(\omega)$ is purely imaginary, we find

$$i\chi''(\omega) = \frac{1}{2}X(\omega) \tag{A.8}$$

and therefore the Kramers-Kronig relation

$$\chi'(\omega) = \text{PV}\int_{-\infty}^{\infty}\frac{\chi''(\omega')}{\pi(\omega' - \omega)}d\omega'. \tag{A.9}$$

We now apply this to the example of a damped harmonic oscillator with equation of motion

$$m\ddot{x} + \alpha\dot{x} + kx = f. \tag{A.10}$$

Plugging this into Eq. (A.2) and writing $\omega_0^2 = k/m$ and $\gamma = \alpha/m$ directly yields

$$\chi(\omega) = \frac{x(\omega)}{f(\omega)} = \frac{1}{m(\omega_0^2 - \omega^2 - i\omega\gamma)} \tag{A.11}$$

Removing the inertial term in Eq. (A.10),

$$\alpha\dot{x} + kx = f, \tag{A.12}$$

and introducing the relaxation time $\tau = \alpha/k$ leads to a susceptibility given by

$$\chi(\omega) = \frac{1/k}{1 - i\omega\tau} \tag{A.13}$$

with real and imaginary parts

$$\chi'(\omega) = \frac{1/k}{1 + (\omega\tau)^2} \tag{A.14}$$

and

$$\chi''(\omega) = \frac{\omega\tau/k}{1 + (\omega\tau)^2}. \tag{A.15}$$

Note that the sign difference in the denominator in Eq. (A.13) compared to Eq. (3.42) results from the differing convention $\chi(\omega) = \chi'(\omega) - i\chi''(\omega)$ for the latter but nevertheless leads to exactly the same equations for the real and imaginary part. At this point it is common to introduce the so-called adiabatic susceptibility $\chi_S \equiv \chi(\infty)$ and isothermal susceptibility $\chi_T = \chi_S + 1/k \equiv \chi(0)$ such that the correct limits at low and high frequencies are recovered. If we take this into account, the following equations result:

$$\chi(\omega) = \chi_S + \frac{\chi_T - \chi_S}{1 + i\omega\tau}, \tag{A.16}$$

$$\chi'(\omega) = \chi_S + \frac{\chi_T - \chi_S}{1 + (\omega\tau)^2}, \tag{A.17}$$

and

$$\chi''(\omega) = \frac{(\chi_T - \chi_S)\omega\tau}{1 + (\omega\tau)^2}.$$ (A.18)

The solution for Eq. (A.12) with $f = 0$ is given by an exponential relaxation with a single relaxation time,

$$x(t) = x_0 e^{-t/\tau}.$$ (A.19)

Therefore, a magnetic system which has a magnetization that relaxes exponentially in time with a single relaxation time, $M(t) = M_0 e^{-t/\tau}$, can be described by the very same equations (A.16) - (A.18).

The derivation of the simple Debye model of Eq. (3.42) from linear response theory is based on the assumption of a magnetization that relaxes exponentially with a single time scale [107]. This assumption completely ignores the complexities in real materials like interaction effects that may lead to a distribution of relaxation times [262]. To overcome this there are several empirical approaches to adjust the simple Debye model in order to take a spread of relaxation times into account. Examples are the generalized Debye model

$$\chi(\omega) = \frac{\chi_0}{1 + (i\omega\tau)^{1-\alpha}},$$ (A.20)

with the phenomenological parameter $0 \leq \alpha \leq 1$ [263], the Cole-Davidson model [264]

$$\chi(\omega) = \frac{\chi_0}{(1 + i\omega\tau)^\beta},$$ (A.21)

or a combination of both, the Havriliak-Negami model [166]

$$\chi(\omega) = \frac{\chi_0}{[1 + (i\omega\tau)^{1-\alpha}]^\beta}.$$ (A.22)

Each of these models parametrizes a spread of relaxation times by introducing the exponents α and/or β and thereby can improve agreement between theoretical model relaxation and data [265], as exemplified in Fig. A.1. Throughout this thesis, when referring to Debye fits, we actually use the more general Havriliak-Negami model.
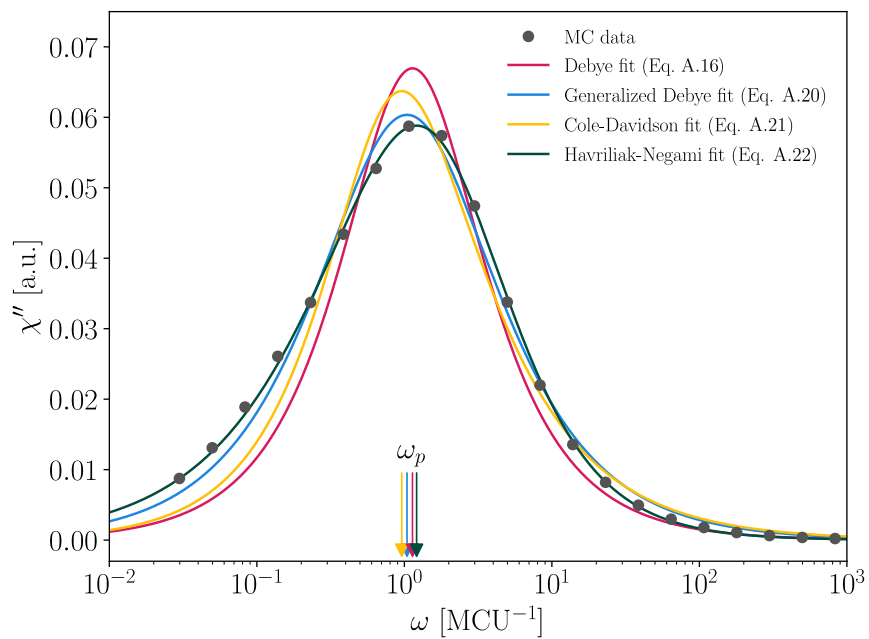
Figure A.1 – **Debye models for relaxation.** Example of Monte Carlo data of the imaginary part of the AC susceptibility and comparison of the different relaxation models mentioned in the text. One can see very well that for this specific set of parameters (spin ice with longitudinal AC field, $T = 1.0$, $H_{DC} = 0.5$), the Havriliak-Negami model gives the best fit to the data.
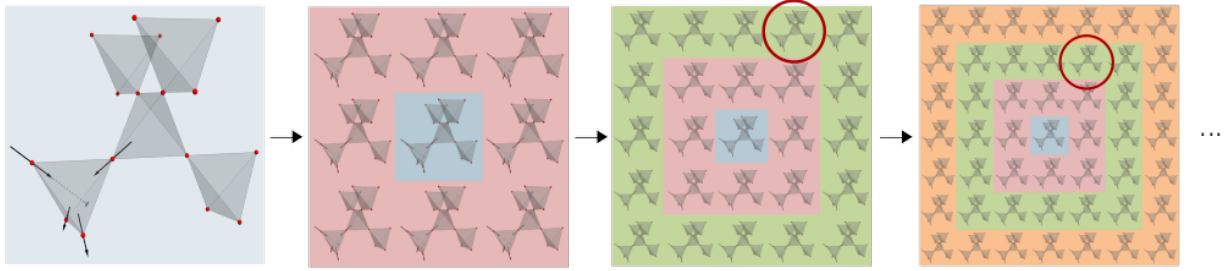
Ewald Summation Technique for Lattice Sums

An efficient way to control the long-ranged dipole-dipole interactions in a simulation is to derive an effective dipole-dipole interaction between spins within the finite simulation cell. This is necessary since the dipolar interaction term in the DSI Hamiltonian, Eq. (4.5), can be determined in principle once the details of the magnetic ions are known, but due to its $|\mathbf{R}_{ij}|^{-3}$ nature such a lattice summation converges, if at all, conditionally and very slowly. By means of the Ewald summation technique the slowly and conditionally convergent dipolar interaction term can be converted into two rapidly absolute converging series [266, 267]. To see how this works we first rewrite the dipole-dipole interaction term, using $\mathbf{S}_i = \sigma_i \hat{\mathbf{z}}_i$, as

$$
\begin{aligned}
\mathcal{H}_{\mathrm{DD}} &= Dr_{\mathrm{nn}}^3 \sum_{i,j} \left[\frac{\mathbf{S}_i \cdot \mathbf{S}_j}{|\mathbf{R}_{ij}|^3} - 3 \frac{(\mathbf{S}_i \cdot \mathbf{R}_{ij})(\mathbf{S}_j \cdot \mathbf{R}_{ij})}{|\mathbf{R}_{ij}|^5} \right] \\
&= Dr_{\mathrm{nn}}^3 \sum_{i,j} \sigma_i \sigma_j \left[\frac{\hat{\mathbf{z}}_i \cdot \hat{\mathbf{z}}_j}{|\mathbf{R}_{ij}|^3} - 3 \frac{(\hat{\mathbf{z}}_i \cdot \mathbf{R}_{ij})(\hat{\mathbf{z}}_j \cdot \mathbf{R}_{ij})}{|\mathbf{R}_{ij}|^5} \right] \\
&= \frac{Dr_{\mathrm{nn}}^3}{L^3} \sum_{i,j} \sum_{\mathbf{n}'} \sigma_i \sigma_j \left[\frac{\hat{\mathbf{z}}_i \cdot \hat{\mathbf{z}}_j}{|\mathbf{r}_{ij} + \mathbf{n}|^3} - 3 \frac{(\hat{\mathbf{z}}_i \cdot (\mathbf{r}_{ij} + \mathbf{n}))(\hat{\mathbf{z}}_j \cdot (\mathbf{r}_{ij} + \mathbf{n}))}{|\mathbf{r}_{ij} + \mathbf{n}|^5} \right] \\
&= \frac{Dr_{\mathrm{nn}}^3}{L^3} \sum_{i,j} \sigma_i \sigma_j \mathcal{A}_{ij}
\end{aligned}
\tag{B.1}
$$

with an interaction matrix $\mathcal{A}_{ij}$, $\mathbf{r}_{ij} = \mathbf{R}_{ij}/L$ with the linear system size L of the simulation cell. The index $\mathbf{n} = (n_x, n_y, n_z)$, $n_{x,y,z} \in \mathbb{Z}$, describes the involvement of dipolar interactions within replicas of the simulation cell that are spherically arranged in shells with radii $L(n_x, n_y, n_z)$ around the simulation cell itself. The summation over $\mathbf{n}'$ indicates that $\mathbf{n} = (0, 0, 0)$—which corresponds to the simulation cell itself—is omitted when $\mathbf{r}_{ij} = 0$. This summation over mirror cells is sketched in Fig. B.1. The interaction matrix $\mathcal{A}_{ij}$ can now be rewritten as follows:

$$
\begin{aligned}
\mathcal{A}_{ij} &= \sum_{\mathbf{n}'} \left[\frac{\hat{\mathbf{z}}_i \cdot \hat{\mathbf{z}}_j}{|\mathbf{r}_{ij} + \mathbf{n}|^3} - 3 \frac{(\hat{\mathbf{z}}_i \cdot (\mathbf{r}_{ij} + \mathbf{n}))(\hat{\mathbf{z}}_j \cdot (\mathbf{r}_{ij} + \mathbf{n}))}{|\mathbf{r}_{ij} + \mathbf{n}|^5} \right] \\
&= -(\mathbf{z}_i \cdot \nabla_{\mathbf{r}})(\mathbf{z}_j \cdot \nabla_{\mathbf{r}}) \left[\sum_{\mathbf{n}'} \frac{1}{|\mathbf{r} + \mathbf{n}|} \right]_{\mathbf{r} = \mathbf{r}_{ij}}
\end{aligned}
\tag{B.2}
$$

Figure B.1 – Sketch of the summation over replica cells in two dimensions. Starting from the simulation cell (blue) on the left, more and more shells of copies of the simulation cell (red, green, and orange) are taken into account for the lattice sum of the dipolar interaction. The red circled replica of the simulation cell corresponds to $\mathbf{n} = (1, 2)$.

The main idea is now to introduce a convergence factor in order to force absolute convergence on the sum. To understand this, consider the conditionally convergent series

$$A = \sum_{i=0}^{\infty} a_i. \tag{B.3}$$

One can now introduce a sequence of numbers $f(n, s)$ that fulfill

(i) $f(n + 1, s) \leq f(n, s) \quad \forall\, s \geq 0 \quad \forall\, n,$

(ii) $0 \leq f(n, s) \leq 1 \quad \forall\, s \geq 0 \quad \forall\, n,$

(iii) $f(n, 0) = 1 \quad \forall\, n.$

It can be shown that inserting these numbers into the series B.3 then leads to some s-dependence

$$A(s) = \sum_{i=0}^{\infty} f(i, s) a_i \tag{B.4}$$

and that taking the limit $s \to 0$ gives back the original series,

$$\lim_{s \to 0} A(s) = A. \tag{B.5}$$

A can then be determined via calculating $A(s)$ with proper $f(n, s)$ enforcing absolute convergence of the series and taking the limit $s \to 0$.

In the present case of determining the interaction matrix $\mathcal{A}_{ij}$, we include a spherical convergence factor $f(\mathbf{n}, s) = e^{-s|\mathbf{n}|^2}$ yielding

$$\mathcal{A}_{ij} = \lim_{s \to 0} \mathcal{A}_{ij}(s) = \lim_{s \to 0} \left\{ -(\mathbf{z}_i \cdot \nabla_{\mathbf{r}})(\mathbf{z}_j \cdot \nabla_{\mathbf{r}}) \left[\sum_{\mathbf{n}'} \frac{e^{-s|\mathbf{n}|^2}}{|\mathbf{r} + \mathbf{n}|} \right]_{\mathbf{r} = \mathbf{r}_{ij}} \right\}. \tag{B.6}$$

By using the Γ-function identity $x^{-2k} = \frac{1}{\Gamma(k)} \int_0^\infty t^{k-1} e^{-tx^2} \mathrm{d}t$ we can rewrite the denominator in expression B.6 as

$$\frac{1}{|\mathbf{r} + \mathbf{n}|} = \frac{1}{\sqrt{\pi}} \int_0^\infty t^{-1/2} e^{-t|\mathbf{r}+\mathbf{n}|^2} \mathrm{d}t \tag{B.7}$$

leading to

$$\begin{aligned}
\mathcal{A}_{ij}(s) &= -(\mathbf{z}_i \cdot \nabla_\mathbf{r})(\mathbf{z}_j \cdot \nabla_\mathbf{r}) \frac{1}{\sqrt{\pi}} \int_0^\infty \mathrm{d}t \left[\sum_{\mathbf{n}'} t^{-1/2} e^{-t|\mathbf{r}+\mathbf{n}|^2} e^{-s|\mathbf{n}|^2} \right]_{\mathbf{r}=\mathbf{r}_{ij}} \\
&= -(\mathbf{z}_i \cdot \nabla_\mathbf{r})(\mathbf{z}_j \cdot \nabla_\mathbf{r}) \left[\bar{\psi}(\mathbf{r}, s) \right]_{\mathbf{r}=\mathbf{r}_{ij}}.
\end{aligned} \tag{B.8}$$

The limit $s \to 0$ for $\bar{\psi}(\mathbf{r}, s)$ can now be taken by splitting the integral into two parts at a suitable chosen boundary α, leaving us with

$$\lim_{s \to 0} \bar{\psi}(\mathbf{r}, s) = \psi(\mathbf{r}) - \frac{2}{3} \pi |\mathbf{r}|^2 \tag{B.9}$$

with the main part

$$\psi(\mathbf{r}) = \sum_{\mathbf{n}'} \frac{\mathrm{erfc}(\alpha|\mathbf{r} + \mathbf{n}|)}{|\mathbf{r} + \mathbf{n}|} + \frac{1}{\pi} \sum_{\mathbf{n} \neq 0} \frac{1}{|\mathbf{n}|^2} e^{-\frac{\pi^2}{\alpha^2}|\mathbf{n}|^2} e^{2\pi i \mathbf{n} \cdot \mathbf{r}} \tag{B.10}$$

where $\mathrm{erfc}(x) = \frac{2}{\sqrt{\pi}} \int_x^\infty e^{-t^2} \mathrm{d}t$ is the complementary error function.

Operating the gradient terms on the above expression then leads to the final expression for the interaction matrix,

$$\begin{aligned}
\mathcal{A}_{ij} &= \frac{4}{3} \pi \hat{\mathbf{z}}_i \cdot \hat{\mathbf{z}}_j + \sum_{\mathbf{n}'} \left[\frac{\hat{\mathbf{z}}_i \cdot \hat{\mathbf{z}}_j}{|\mathbf{r}_{ij} + \mathbf{n}|^2} \left(\frac{2\alpha}{\sqrt{\pi}} e^{-\alpha^2|\mathbf{r}_{ij}+\mathbf{n}|^2} + \frac{\mathrm{erfc}(\alpha|\mathbf{r}_{ij}+\mathbf{n}|)}{|\mathbf{r}_{ij}+\mathbf{n}|} \right) \right. \\
&\quad - \frac{(\hat{\mathbf{z}}_i \cdot (\mathbf{r}_{ij}+\mathbf{n}))(\hat{\mathbf{z}}_j \cdot (\mathbf{r}_{ij}+\mathbf{n}))}{|\mathbf{r}_{ij}+\mathbf{n}|^2} \left(\frac{4\alpha^3}{\sqrt{\pi}} e^{-\alpha^2|\mathbf{r}_{ij}+\mathbf{n}|^2} \right) \\
&\quad \left. - 3\frac{(\hat{\mathbf{z}}_i \cdot (\mathbf{r}_{ij}+\mathbf{n}))(\hat{\mathbf{z}}_j \cdot (\mathbf{r}_{ij}+\mathbf{n}))}{|\mathbf{r}_{ij}+\mathbf{n}|^4} \left(\frac{2\alpha}{\sqrt{\pi}} e^{-\alpha^2|\mathbf{r}_{ij}+\mathbf{n}|^2} + \frac{\mathrm{erfc}(\alpha|\mathbf{r}_{ij}+\mathbf{n}|)}{|\mathbf{r}_{ij}+\mathbf{n}|} \right) \right] \\
&\quad + 4\pi \sum_{\mathbf{n} \neq 0} \frac{(\hat{\mathbf{z}}_i \cdot \mathbf{n})(\hat{\mathbf{z}}_j \cdot \mathbf{n})}{|\mathbf{n}|^2} e^{-\frac{\pi^2}{\alpha^2}|\mathbf{n}|^2} e^{2\pi i \mathbf{n} \cdot \mathbf{r}_{ij}}. \tag{B.11}
\end{aligned}$$

Since the positions of the spins are restricted to fixed lattice points, this has to be calculated only once and can then be stored in a look-up table and be used in a conventional Metropolis algorithm[1].

---

[1]This appendix is taken and slightly modified from M. Gembé, *Dynamical Monte Carlo Simulations with Applications in Dipolar Spin Ice and Open Floquet Systems* [125].

Bibliography

[P1] **M. Gembé**, H.-J. Schmidt, C. Hickey, J. Richter, Y. Iqbal, and S. Trebst, Noncoplanar magnetic order in classical square-kagome antiferromagnets, Phys. Rev. Res. **5** (4), 043204, 2023.

[P2] **M. Gembé**, L. Gresista, H.-J. Schmidt, C. Hickey, Y. Iqbal, and S. Trebst, Noncoplanar orders and quantum disordered states in maple-leaf antiferromagnets, 2024. arXiv: `2402.09400 [cond-mat.str-el]`.

[U1] **M. Gembé**, J. Attig, J. Kunkel, and S. Trebst, Critical Speeding Up in Spin Ice and Spin Liquids, Manuscript in preparation, 2023.

[1] P. W. Anderson, *'Frustration is the name of the game'*, Comment written on blackboard in Aspen, 1976, see [113].

[2] G. Toulouse, Theory of the frustration effect in spin glasses: I, Comm. on Physics **2**, 115–119, 1977.

[3] J. Villain, Spin glass with non-random interactions, Journal of Physics C: Solid State Physics **10** (10), 1717, 1977.

[4] G. Wannier, Antiferromagnetism. The Triangular Ising Net, Physical Review **79** (2), 357, 1950.

[5] G. Wannier, Antiferromagnetism. The Triangular Ising Net, Phys. Rev. B **7** (11), 5017, 1973.

[6] R. M. F. Houtappel, Order-disorder in hexagonal lattices, Physica **16** (5), 425–455, 1950.

[7] P. W. Anderson, Ordering and antiferromagnetism in ferrites, Physical Review **102** (4), 1008, 1956.

[8] W. Giauque and J. Stout, The Entropy of Water and the Third Law of Thermodynamics. The Heat Capacity of Ice from 15 to 273° K. Journal of the American Chemical Society **58** (7), 1144–1150, 1936.

[9] L. Pauling, The structure and entropy of ice and of other crystals with some randomness of atomic arrangement, Journal of the American Chemical Society **57** (12), 2680–2684, 1935.

[10] L. Balents, Spin liquids in frustrated magnets, Nature **464** (7286), 199–208, 2010.

[11] J. Knolle and R. Moessner, A field guide to spin liquids, Annual Review of Condensed Matter Physics **10**, 451–472, 2019.

[12] L. Landau, The theory of phase transitions, Nature **138** (3498), 840–841, 1936.

[13] V. Ginzburg and L. Landau, Theory of superconductivity, Zh. Eksp. Teor. Fiz. **20** (12), 1950.

[14] C. Castelnovo, R. Moessner, and S. L. Sondhi, Spin ice, fractionalization, and topological order, Annu. Rev. Condens. Matter Phys. **3** (1), 35–55, 2012.

[15] L. Savary and L. Balents, Quantum spin liquids: a review, Reports on Progress in Physics **80** (1), 016502, 2016.

[16] Y. Zhou, K. Kanoda, and T.-K. Ng, Quantum spin liquid states, Reviews of Modern Physics **89** (2), 025003, 2017.

[17] C. Broholm, R. Cava, S. Kivelson, D. Nocera, M. Norman, and T. Senthil, Quantum spin liquids, Science **367** (6475), eaay0668, 2020.

[18] A. Y. Kitaev, Fault-tolerant quantum computation by anyons, Annals of physics **303** (1), 2–30, 2003.

[19] C. Nayak, S. H. Simon, A. Stern, M. Freedman, and S. D. Sarma, Non-Abelian anyons and topological quantum computation, Reviews of Modern Physics **80** (3), 1083, 2008.

[20] H. Yan, O. Benton, R. Moessner, and A. H. Nevidomskyy, Classification of Classical Spin Liquids: Typology and Resulting Landscape, 2023. arXiv: `2305.00155 [cond-mat.str-el]`.

[21] H. Yan, O. Benton, A. H. Nevidomskyy, and R. Moessner, Classification of Classical Spin Liquids: Detailed Formalism and Suite of Examples, 2023. arXiv: `2305.19189 [cond-mat.str-el]`.

[22] M. J. Harris, S. Bramwell, D. McMorrow, T. Zeiske, and K. Godfrey, Geometrical frustration in the ferromagnetic pyrochlore $Ho_2Ti_2O_7$, Phys. Rev. Lett. **79** (13), 2554, 1997.

[23] S. T. Bramwell and M. J. Gingras, Spin ice state in frustrated magnetic pyrochlore materials, Science **294** (5546), 1495–1501, 2001.

[24] T. Fennell, P. Deen, A. Wildes, K. Schmalzl, D. Prabhakaran, A. Boothroyd, R. Aldus, D. McMorrow, and S. Bramwell, Magnetic Coulomb phase in the spin ice $Ho_2Ti_2O_7$, Science **326** (5951), 415–417, 2009.

[25] C. L. Henley, The "Coulomb phase" in frustrated systems, Annu. Rev. Condens. Matter Phys. **1** (1), 179–210, 2010.

[26] P. A. M. Dirac, Quantised singularities in the electromagnetic field, Proceedings of the Royal Society of London. Series A, Containing Papers of a Mathematical and Physical Character **133** (821), 60–72, 1931.

[27] C. Castelnovo, R. Moessner, and S. L. Sondhi, Magnetic monopoles in spin ice, Nature **451** (7174), 42–45, 2008.

[28] S. T. Bramwell, S. Giblin, S. Calder, R. Aldus, D. Prabhakaran, and T. Fennell, Measurement of the charge and current of magnetic monopoles in spin ice, Nature **461** (7266), 956–959, 2009.

[29] L. D. Jaubert and P. C. Holdsworth, Signature of magnetic monopole and Dirac string dynamics in spin ice, Nature Physics **5** (4), 258–261, 2009.

[30] D. J. P. Morris, D. Tennant, S. Grigera, B. Klemke, C. Castelnovo, R. Moessner, C. Czternasty, M. Meissner, K. Rule, J.-U. Hoffmann, *et al.*, Dirac strings and magnetic monopoles in the spin ice $Dy_2Ti_2O_7$, Science **326** (5951), 411–414, 2009.

[31] H. Kadowaki, N. Doi, Y. Aoki, Y. Tabata, T. J. Sato, J. W. Lynn, K. Matsuhira, and Z. Hiroi, Observation of magnetic monopoles in spin ice, Journal of the Physical Society of Japan **78** (10), 103706–103706, 2009.

[32] J. N. Hallén, S. A. Grigera, D. A. Tennant, C. Castelnovo, and R. Moessner, Dynamical fractal and anomalous noise in a clean magnetic crystal, Science **378** (6625), 1218–1221, 2022.

[33] A. M. Samarakoon *et al.*, Structural magnetic glassiness in the spin ice $Dy_2Ti_2O_7$, Phys. Rev. Res. **4** (3), 033159, 2022.

[34] H. Takatsu, K. Goto, T. J. Sato, J. W. Lynn, K. Matsubayashi, Y. Uwatoko, R. Higashinaka, K. Matsuhira, Z. Hiroi, and H. Kadowaki, Universal dynamics of magnetic monopoles in two-dimensional kagomé ice, Journal of the Physical Society of Japan **90** (12), 123705, 2021.

[35] L. D. Jaubert and P. C. Holdsworth, Magnetic monopole dynamics in spin ice, Journal of Physics: Condensed Matter **23** (16), 164222, 2011.

[36] J. Villain, R. Bidaux, J.-P. Carton, and R. Conte, Order as an effect of disorder, Journal de Physique **41** (11), 1263–1272, 1980.

[37] J. T. Chalker, P. C. Holdsworth, and E. Shender, Hidden order in a frustrated system: Properties of the Heisenberg Kagomé antiferromagnet, Phys. Rev. Lett. **68** (6), 855, 1992.

[38] M. E. Zhitomirsky, Octupolar ordering of classical kagome antiferromagnets in two and three dimensions, Phys. Rev. B **78** (9), 094423, 2008.

[39] L. Messio, C. Lhuillier, and G. Misguich, Lattice symmetries and regular magnetic orders in classical frustrated antiferromagnets, Phys. Rev. B **83** (18), 184401, 2011.

[40] J.-C. Domenge, P. Sindzingre, C. Lhuillier, and L. Pierre, Twelve sublattice ordered phase in the $J_1 - J_2$ model on the kagomé lattice, Phys. Rev. B **72** (2), 024433, 2005.

[41] H. Takagi, R. Takagi, S. Minami, T. Nomoto, K. Ohishi, M.-T. Suzuki, Y. Yanagi, M. Hirayama, N. Khanh, K. Karube, *et al.*, Spontaneous topological hall effect induced by noncoplanar antiferromagnetic order in intercalated van der waals materials, Nature Physics, 1–8, 2023.

[42] H. Chen, Q. Niu, and A. H. MacDonald, Anomalous Hall Effect Arising from Noncollinear Antiferromagnetism, Phys. Rev. Lett. **112** (1), 017205, 2014.

[43] S. Nakatsuji, N. Kiyohara, and T. Higo, Large anomalous hall effect in a non-collinear antiferromagnet at room temperature, Nature **527** (7577), 212–215, 2015.

[44] A. K. Nayak, J. E. Fischer, Y. Sun, B. Yan, J. Karel, A. C. Komarek, C. Shekhar, N. Kumar, W. Schnelle, J. Kübler, *et al.*, Large anomalous Hall effect driven by a nonvanishing Berry curvature in the noncolinear antiferromagnet Mn_3Ge, Science Advances **2** (4), e1501870, 2016.

[45] C. Hickey, L. Cincio, Z. Papi ć, and A. Paramekanti, Haldane-Hubbard Mott Insulator: From Tetrahedral Spin Crystal to Chiral Spin Liquid, Phys. Rev. Lett. **116** (13), 137202, 2016.

[46] C. Hickey, L. Cincio, Z. Papi ć, and A. Paramekanti, Emergence of chiral spin liquids via quantum melting of noncoplanar magnetic orders, Phys. Rev. B **96** (11), 115115, 2017.

[47] M. Scheffer, J. Bascompte, W. A. Brock, V. Brovkin, S. R. Carpenter, V. Dakos, H. Held, E. H. Van Nes, M. Rietkerk, and G. Sugihara, Early-warning signals for critical transitions, Nature **461** (7260), 53–59, 2009.

[48] A. Kitaev, Anyons in an exactly solved model and beyond, Annals of Physics **321** (1), 2–111, 2006.

[49] C. Lacroix, P. Mendels, and F. Mila, *Introduction to frustrated magnetism: materials, experiments, theory.* Springer Science & Business Media, 2011.

[50] H. Diep *et al.*, *Frustrated spin systems.* World scientific, 2013.

[51] R. Moessner, Magnets with strong geometric frustration, Canadian Journal of Physics **79** (11-12), 1283–1294, 2001.

[52] J. Villain, Insulating spin glasses, Zeitschrift für Physik B Condensed Matter **33** (1), 31–42, 1979.

[53] X. Obradors, A. Labarta, A. Isalgue, J. Tejada, J. Rodriguez, and M. Pernet, Magnetic frustration and lattice dimensionality in $SrCr_8Ga_4O_{19}$, Solid State Communications **65** (3), 189–192, 1988.

[54] A. Ramirez, Strongly geometrically frustrated magnets, Annual Review of Materials Science **24** (1), 453–480, 1994.

[55] D. Bergman, J. Alicea, E. Gull, S. Trebst, and L. Balents, Order-by-disorder and spiral spin-liquid in frustrated diamond-lattice antiferromagnets, Nature Physics **3** (7), 487–491, 2007.

[56] P. W. Anderson, New approach to the theory of superexchange interactions, Physical Review **115** (1), 2, 1959.

[57] A. Auerbach, *Interacting electrons and quantum magnetism.* Springer Science & Business Media, 1998.

[58] U. Nowak, Classical Spin Models, Handbook of Magnetism and Advanced Magnetic Materials, 2007.

[59] J. F. Devlin, Effect of crystal-field anisotropy on magnetically ordered systems, Phys. Rev. B **4** (1), 136, 1971.

[60] I. Dzyaloshinsky, A thermodynamic theory of "weak" ferromagnetism of antiferromagnetics, Journal of Physics and Chemistry of Solids **4** (4), 241–255, 1958.

[61] T. Moriya, Weak ferromagnetism, in *Magnetism*, Elsevier, 1963, pp. 85–125.

[62] I. Bose and U. Bhaumik, Heisenberg Hamiltonian with a Dzyaloshinski-Moriya interaction, Journal of Physics: Condensed Matter **6** (48), 10617, 1994.

[63] S. Palmer and J. Chalker, Order induced by dipolar interactions in a geometrically frustrated antiferromagnet, Phys. Rev. B **62** (1), 488, 2000.

[64] B. C. den Hertog and M. J. P. Gingras, Dipolar Interactions and Origin of Spin Ice in Ising Pyrochlore Magnets, Phys. Rev. Lett. **84** (15), 3430–3433, 2000.

[65] G. Jackeli and G. Khaliullin, Mott insulators in the strong spin-orbit coupling limit: from Heisenberg to a quantum compass and Kitaev models, Phys. Rev. Lett. **102** (1), 017205, 2009.

[66] J. G. Rau, E. K.-H. Lee, and H.-Y. Kee, Generic Spin Model for the Honeycomb Iridates beyond the Kitaev Limit, Phys. Rev. Lett. **112** (7), 077204, 2014.

[67] L. Janssen and M. Vojta, Heisenberg–Kitaev physics in magnetic fields, Journal of Physics: condensed matter **31** (42), 423002, 2019.

[68] S. M. Winter, A. A. Tsirlin, M. Daghofer, J. van den Brink, Y. Singh, P. Gegenwart, and R. Valentí, Models and materials for generalized Kitaev magnetism, Journal of Physics: Condensed Matter **29** (49), 493002, 2017.

[69] J. C. Maxwell, L. on the calculation of the equilibrium and stiffness of frames, Philos. Mag. **27** (182), 294–299, 1864.

[70] R. Moessner and J. T. Chalker, Low-temperature properties of classical geometrically frustrated antiferromagnets, Phys. Rev. B **58** (18), 12049, 1998.

[71] I. Ritchey, P. Chandra, and P. Coleman, Spin folding in the two-dimensional Heisenberg kagomé antiferromagnet, Phys. Rev. B **47** (22), 15342, 1993.

[72] J. D. Bernal and R. H. Fowler, A theory of water and ionic solution, with particular reference to hydrogen and hydroxyl ions, The Journal of Chemical Physics **1** (8), 515–548, 1933.

[73] R. Moessner and J. T. Chalker, Properties of a classical spin liquid: the Heisenberg pyrochlore antiferromagnet, Phys. Rev. Lett. **80** (13), 2929, 1998.

[74] J. T. Chalker, P. C. W. Holdsworth, and E. F. Shender, Hidden order in a frustrated system: Properties of the Heisenberg Kagomé antiferromagnet, Phys. Rev. Lett. **68** (6), 855–858, 1992.

[75] J. N. Reimers and A. Berlinsky, Order by disorder in the classical Heisenberg kagomé antiferromagnet, Phys. Rev. B **48** (13), 9539, 1993.

[76] D. A. Huse, W. Krauth, R. Moessner, and S. L. Sondhi, Coulomb and liquid dimer models in three dimensions, Phys. Rev. Lett. **91** (16), 167004, 2003.

[77] C. Henley, Power-law spin correlations in pyrochlore antiferromagnets, Phys. Rev. B **71** (1), 014424, 2005.

[78] A. Wills, R. Ballou, and C. Lacroix, Model of localized highly frustrated ferromagnetism: The kagomé spin ice, Phys. Rev. B **66** (14), 144407, 2002.

[79] S. Isakov, K. Gregor, R. Moessner, and S. L. Sondhi, Dipolar spin correlations in classical pyrochlore magnets, Phys. Rev. Lett. **93** (16), 167204, 2004.

[80] M. Zinkin, M. Harris, and T. Zeiske, Short-range magnetic order in the frustrated pyrochlore antiferromagnet $CsNiCrF_6$, Phys. Rev. B **56** (18), 11786, 1997.

[81] D. Garanin and B. Canals, Classical spin liquid: Exact solution for the infinite-component antiferromagnetic model on the kagomé lattice, Phys. Rev. B **59** (1), 443, 1999.

[82] T. Fennell, S. Bramwell, D. McMorrow, P. Manuel, and A. Wildes, Pinch points and Kasteleyn transitions in kagome ice, Nature Physics **3** (8), 566–572, 2007.

[83] X.-G. Wen, Topological orders in rigid states, International Journal of Modern Physics B **4** (02), 239–271, 1990.

[84] R. Moessner and S. Sondhi, Irrational charge from topological order, Phys. Rev. Lett. **105** (16), 166401, 2010.

[85] J. von Neumann, Various techniques used in connection with random digits, Appl. Math Ser **12** (36-38), 3, 1951.

[86] N. Metropolis, The beginning of the Monte Carlo method, Los Alamos Science **15**, 125–130, 1987.

[87] R. Eckhardt, Stan Ulam, John von Neumann, and the Monte Carlo method, Los Alamos Science **15**, 131–141, 1987.

[88] N. Metropolis and S. Ulam, The Monte Carlo method, Journal of the American Statistical Association **44** (247), 335–341, 1949.

[89] N. Metropolis, A. W. Rosenbluth, M. N. Rosenbluth, A. H. Teller, and E. Teller, Equation of state calculations by fast computing machines, The Journal of Chem. Physics **21** (6), 1087–1092, 1953.

[90] W. Hastings, Monte Carlo sampling methods using Markov chains and their applications, Biometrika **57** (1), 97, 1970.

[91] R. H. Swendsen and J.-S. Wang, Replica Monte Carlo simulation of spin-glasses, Phys. Rev. Lett. **57** (21), 2607, 1986.

[92] K. Hukushima and K. Nemoto, Exchange Monte Carlo method and application to spin glass simulations, Journal of the Physical Society of Japan **65** (6), 1604–1608, 1996.

[93] D. J. Earl and M. W. Deem, Parallel tempering: Theory, applications, and new perspectives, Physical Chemistry Chemical Physics **7** (23), 3910–3916, 2005.

[94] C. Predescu, M. Predescu, and C. V. Ciobanu, The incomplete beta function law for parallel tempering sampling of classical canonical systems, The Journal of Chem. Physics **120** (9), 4119–4128, 2004.

[95] N. Rathore, M. Chopra, and J. J. de Pablo, Optimal allocation of replicas in parallel tempering simulations, The Journal of Chemical Physics **122** (2), 024111, 2005.

[96] H. G. Katzgraber, S. Trebst, D. A. Huse, and M. Troyer, Feedback-optimized parallel tempering Monte Carlo, Journal of Statistical Mechanics: Theory and Experiment **2006** (03), P03018, 2006.

[97] S. C. Bagui, D. K. Bhaumik, and K. Mehra, A few counter examples useful in teaching central limit theorems, The American Statistician **67** (1), 49–56, 2013.

[98] M. E. Newman and G. T. Barkema, *Monte Carlo methods in statistical physics.* Clarendon Press, 1999.

[99] M. P. Nightingale and H. W. J. Blöte, Dynamic Exponent of the Two-Dimensional Ising Model and Monte Carlo Computation of the Subdominant Eigenvalue of the Stochastic Matrix, Phys. Rev. Lett. **76** (24), 4548–4551, 1996.

[100] R. H. Swendsen and J.-S. Wang, Nonuniversal critical dynamics in Monte Carlo simulations, Phys. Rev. Lett. **58** (2), 86, 1987.

[101] U. Wolff, Collective Monte Carlo updating for spin systems, Phys. Rev. Lett. **62** (4), 361, 1989.

[102] V. Ambegaokar and M. Troyer, Estimating errors reliably in Monte Carlo simulations of the Ehrenfest model, American Journal of Physics **78** (2), 150–157, 2010.

[103] R. G. Miller, The jackknife - a review, Biometrika **61** (1), 1–15, 1974.

[104] K. Binder, D. M. Ceperley, J.-P. Hansen, M. Kalos, D. Landau, D. Levesque, H. Mueller-Krumbhaar, D. Stauffer, and J.-J. Weis, *Monte Carlo methods in statistical physics.* Springer Science & Business Media, 2012, vol. 7.

[105] H. Takatsu, K. Goto, H. Otsuka, R. Higashinaka, K. Matsubayashi, Y. Uwatoko, and H. Kadowaki, AC susceptibility of the dipolar spin ice $Dy_2Ti_2O_7$: Experiments and Monte Carlo simulations, Journal of the Physical Society of Japan **82** (10), 104710, 2013.

[106] H. Takatsu, K. Goto, H. Otsuka, R. Higashinaka, K. Matsubayashi, Y. Uwatoko, and H. Kadowaki, Two-dimensional monopole dynamics in the dipolar spin ice $Dy_2Ti_2O_7$, Journal of the Physical Society of Japan **82** (7), 073707, 2013.

[107] C. Topping and S. Blundell, AC susceptibility as a probe of low-frequency magnetic dynamics, Journal of Physics: Condensed Matter **31** (1), 013001, 2018.

[108] M. Nikolo, Superconductivity: A guide to alternating current susceptibility measurements and alternating current susceptometer design, American Journal of Physics **63** (1), 57–65, 1995.

[109] F. Gömöry, Characterization of high-temperature superconductors by AC susceptibility measurements, Superconductor Science and Technology **10** (8), 523–542, 1997.

[110] M. Bałanda, H.-A. Nidda, M. Heinrich, and A. Loidl, Dynamic susceptibility of magnetic systems, in *Relaxation Phenomena*, Springer, 2003, pp. 89–135.

[111] M. Balanda, AC susceptibility studies of phase transitions and magnetic relaxation: Conventional, molecular and low-dimensional magnets, Acta Phys. Pol. A **124** (6), 964–976, 2013.

[112] G. H. Wannier, The statistical problem in cooperative phenomena, Reviews of Modern Physics **17** (1), 50, 1945.

[113] J. S. Gardner, M. J. Gingras, and J. E. Greedan, Magnetic pyrochlore oxides, Reviews of Modern Physics **82** (1), 53, 2010.

[114] S. Bramwell and M. Harris, Frustration in Ising-type spin models on the pyrochlore lattice, Journal of Physics: Condensed Matter **10** (14), L215, 1998.

[115] A. P. Ramirez, A. Hayashi, R. J. Cava, R. Siddharthan, and B. Shastry, Zero-point entropy in 'spin ice', Nature **399** (6734), 333–335, 1999.

[116] M. Udagawa and L. Jaubert, *Spin Ice.* Springer, 2021.

[117] S. T. Bramwell and M. J. Harris, The history of spin ice, Journal of Physics: Condensed Matter **32** (37), 374010, 2020.

[118] S. Rosenkranz, A. Ramirez, A. Hayashi, R. Cava, R. Siddharthan, and B. Shastry, Crystalfield interaction in the pyrochlore magnet $Ho_2Ti_2O_7$, Journal of Applied Physics **87** (9), 5914–5916, 2000.

[119] Y. Jana, A. Sengupta, and D. Ghosh, Estimation of single ion anisotropy in pyrochlore $Dy_2Ti_2O_7$, a geometrically frustrated system, using crystal field theory, Journal of magnetism and magnetic materials **248** (1), 7–18, 2002.

[120] M. Harris, S. Bramwell, T. Zeiske, D. McMorrow, and P. King, Magnetic structures of highly frustrated pyrochlores, Journal of magnetism and magnetic materials **177**, 757–762, 1998.

[121] S. R. Giblin, M. Twengström, L. Bovo, M. Ruminy, M. Bartkowiak, P. Manuel, J. Andresen, D. Prabhakaran, G. Balakrishnan, E. Pomjakushina, *et al.*, Pauling entropy, metastability, and equilibrium in $Dy_2Ti_2O_7$ Spin Ice, Phys. Rev. Lett. **121** (6), 067202, 2018.

[122] X. Ke, R. Freitas, B. Ueland, G. Lau, M. Dahlberg, R. Cava, R. Moessner, and P. Schiffer, Nonmonotonic zero-point entropy in diluted spin ice, Phys. Rev. Lett. **99** (13), 137203, 2007.

[123] S. Bramwell *et al.*, Spin correlations in $Ho_2Ti_2O_7$: a dipolar spin ice system, Phys. Rev. Lett. **87** (4), 047205, 2001.

[124] A. Cornelius and J. Gardner, Short-range magnetic interactions in the spin-ice compound $Ho_2Ti_2O_7$, Phys. Rev. B **64** (6), 060406, 2001.

[125] **M. Gembé**, *Dynamical Monte Carlo Simulations with Applications in Dipolar Spin Ice and Open Floquet Systems*. Master Thesis, University of Cologne, 2019.

[126] B. C. den Hertog and M. J. Gingras, Dipolar interactions and origin of spin ice in Ising pyrochlore magnets, Phys. Rev. Lett. **84** (15), 3430, 2000.

[127] R. Siddharthan, B. Shastry, A. Ramirez, A. Hayashi, R. Cava, and S. Rosenkranz, Ising pyrochlore magnets: Low-temperature properties,"ice rules," and beyond, Phys. Rev. Lett. **83** (9), 1854, 1999.

[128] R. G. Melko, B. C. den Hertog, and M. J. Gingras, Long-range order at low temperatures in dipolar spin ice, Phys. Rev. Lett. **87** (6), 067203, 2001.

[129] R. G. Melko and M. J. Gingras, Monte Carlo studies of the dipolar spin ice model, Journal of Physics: Condensed Matter **16** (43), R1277, 2004.

[130] J. Reimers, A. Berlinsky, and A.-C. Shi, Mean-field approach to magnetic ordering in highly frustrated pyrochlores, Phys. Rev. B **43** (1), 865, 1991.

[131] M. J. Gingras and B. C. den Hertog, Origin of spin-ice behavior in Ising pyrochlore magnets with long-range dipole interactions: an insight from mean-field theory, Canadian Journal of Physics **79** (11-12), 1339–1351, 2001.

[132] M. Enjalran and M. J. Gingras, Theory of paramagnetic scattering in highly frustrated magnets with long-range dipole-dipole interactions: the case of the $Tb_2Ti_2O_7$ pyrochlore antiferromagnet, Phys. Rev. B **70** (17), 174426, 2004.

[133] J. Li, V. Nield, D. Ross, R. Whitworth, C. Wilson, and D. Keen, Diffuse neutron-scattering study of deuterated ice Ih, Philosophical Magazine B **69** (6), 1173–1181, 1994.

[134] H. Fukazawa, R. Melko, R. Higashinaka, Y. Maeno, and M. Gingras, Magnetic anisotropy of the spin-ice compound $Dy_2Ti_2O_7$, Phys. Rev. B **65** (5), 054410, 2002.

[135] O. Petrenko, M. Lees, and G. Balakrishnan, Magnetization process in the spin-ice compound $Ho_2Ti_2O_7$, Phys. Rev. B **68** (1), 012406, 2003.

[136] R. Higashinaka, H. Fukazawa, and Y. Maeno, Anisotropic release of the residual zero-point entropy in the spin ice compound $Dy_2Ti_2O_7$: Kagome ice behavior, Phys. Rev. B **68** (1), 014415, 2003.

[137] Z. Hiroi, K. Matsuhira, and M. Ogata, Ferromagnetic Ising spin chains emerging from the spin ice under magnetic field, Journal of the Physical Society of Japan **72** (12), 3045–3048, 2003.

[138] R. Moessner and S. L. Sondhi, Theory of the [111] magnetization plateau in spin ice, Phys. Rev. B **68** (6), 064411, 2003.

[139] M. Udagawa, M. Ogata, and Z. Hiroi, Exact result of ground-state entropy for Ising pyrochlore magnets under a magnetic field along [111] axis, Journal of the Physical Society of Japan **71** (10), 2365–2368, 2002.

[140] Matsuhira, Kazuyuki and Hiroi, Zenji and Tayama, Takashi and Takagi, Seishi and Sakakibara, Toshiro, *A new macroscopically degenerate ground state in the spin ice compound* $Dy_2Ti_2O_7$ *under a magnetic field*, Journal of Physics: Condensed Matter **14** (29), L559, 2002.

[141] T. Sakakibara, T. Tayama, Z. Hiroi, K. Matsuhira, and S. Takagi, *Observation of a Liquid-Gas-Type Transition in the Pyrochlore Spin Ice Compound* $Dy_2Ti_2O_7$ *in a Magnetic Field*, Phys. Rev. Lett. **90** (20), 207205, 2003.

[142] Y. Tabata, H. Kadowaki, K. Matsuhira, Z. Hiroi, N. Aso, E. Ressouche, and B. Fåk, *Kagome ice state in the dipolar spin ice* $Dy_2Ti_2O_7$, Phys. Rev. Lett. **97** (25), 257205, 2006.

[143] Z. Hiroi, K. Matsuhira, S. Takagi, T. Tayama, and T. Sakakibara, *Specific heat of kagome ice in the pyrochlore oxide* $Dy_2Ti_2O_7$, Journal of the Physical Society of Japan **72** (2), 411–418, 2003.

[144] H. Aoki, T. Sakakibara, K. Matsuhira, and Z. Hiroi, *Magnetocaloric effect study on the pyrochlore spin ice compound* $Dy_2Ti_2O_7$ *in a [111] magnetic field*, Journal of the Physical Society of Japan **73** (10), 2851–2856, 2004.

[145] H. D. Zhou, C. R. Wiebe, J. A. Janik, L. Balicas, Y. J. Yo, Y. Qiu, J. R. D. Copley, and J. S. Gardner, *Dynamic Spin Ice:* $Pr_2Sn_2O_7$, Phys. Rev. Lett. **101** (22), 227204, 2008.

[146] J. Lago, S. J. Blundell, and C. Baines, *SR investigation of spin dynamics in the spin-ice material* $Dy_2Ti_2O_7$, Journal of Physics: Condensed Matter **19** (32), 326210, 2007.

[147] K. Kitagawa, R. Higashinaka, K. Ishida, Y. Maeno, and M. Takigawa, *High-temperature spin relaxation process in* $Dy_2Ti_2O_7$ *probed by* ^{47}Ti-NQR, Phys. Rev. B **77** (21), 214403, 2008.

[148] G. Ehlers, A. Cornelius, M. Orendac, M. Kajnakova, T. Fennell, S. Bramwell, and J. Gardner, *Dynamical crossover in 'hot'spin ice*, Journal of Physics: Condensed Matter **15** (2), L9, 2002.

[149] G. Ehlers, A. Cornelius, T. Fennell, M. Koza, S. Bramwell, and J. Gardner, *Evidence for two distinct spin relaxation mechanisms in 'hot'spin ice* $Ho_2Ti_2O_7$, Journal of Physics: Condensed Matter **16** (11), S635, 2004.

[150] K. Matsuhira, Y. Hinatsu, and T. Sakakibara, *Novel dynamical magnetic properties in the spin ice compound* $Dy_2Ti_2O_7$, Journal of Physics: Condensed Matter **13** (31), L737, 2001.

[151] J. A. Quilliam, L. R. Yaraskavitch, H. A. Dabkowska, B. D. Gaulin, and J. B. Kycia, *Dynamics of the magnetic susceptibility deep in the Coulomb phase of the dipolar spin ice material* $Ho_2Ti_2O_7$, Phys. Rev. B **83** (9), 094424, 2011.

[152] J. Snyder, B. G. Ueland, A. Mizel, J. S. Slusky, H. Karunadasa, R. J. Cava, and P. Schiffer, *Quantum and thermal spin relaxation in the diluted spin ice* $Dy_{2-x}M_xTi_2O_7$ $(M = Lu, Y)$, Phys. Rev. B **70** (18), 184431, 2004.

[153] J. Snyder, B. G. Ueland, J. S. Slusky, H. Karunadasa, R. J. Cava, and P. Schiffer, *Low-temperature spin freezing in the* $Dy_2Ti_2O_7$ *spin ice*, Phys. Rev. B **69** (6), 064414, 2004.

[154] J. Snyder, B. G. Ueland, J. S. Slusky, H. Karunadasa, R. J. Cava, A. Mizel, and P. Schiffer, *Quantum-Classical Reentrant Relaxation Crossover in* $Dy_2Ti_2O_7$ *Spin Ice*, Phys. Rev. Lett. **91** (10), 107201, 2003.

[155] J. Snyder, J. Slusky, R. Cava, and P. Schiffer, How 'spin ice' freezes, Nature **413** (6851), 48–51, 2001.

[156] K. Matsuhira, Y. Hinatsu, K. Tenya, and T. Sakakibara, Low temperature magnetic properties of frustrated pyrochlore ferromagnets $Ho_2Sn_2O_7$ and $Ho_2Ti_2O_7$, Journal of Physics: Condensed Matter **12** (40), L649, 2000.

[157] K. Matsuhira, C. Paulsen, E. Lhotel, C. Sekine, Z. Hiroi, and S. Takagi, Spin dynamics at very low temperature in spin ice $dy_2ti_2o_7$, Journal of the Physical Society of Japan **80** (12), 123711, 2011.

[158] K. Matsuhira, C. Paulsen, E. Lhotel, C. Sekine, Z. Hiroi, and S. Takagi, Spin dynamics at very low temperature in spin ice $Dy_2Ti_2O_7$, Journal of the Physical Society of Japan **80** (12), 123711, 2011.

[159] L. R. Yaraskavitch, H. M. Revell, S. Meng, K. A. Ross, H. M. L. Noad, H. A. Dabkowska, B. D. Gaulin, and J. B. Kycia, Spin dynamics in the frozen state of the dipolar spin ice material $Dy_2Ti_2O_7$, Phys. Rev. B **85** (2), 020410, 2012.

[160] M. Ruminy, S. Chi, S. Calder, and T. Fennell, Phonon-mediated spin-flipping mechanism in the spin ices $Dy_2Ti_2O_7$ and $Ho_2Ti_2O_7$, Phys. Rev. B **95** (6), 060414, 2017.

[161] D. Khomskii, Electric dipoles on magnetic monopoles in spin ice, Nature Communications **3** (1), 904, 2012.

[162] M. Saito, R. Higashinaka, and Y. Maeno, Magnetodielectric response of the spin-ice $Dy_2Ti_2O_7$, Phys. Rev. B **72** (14), 144422, 2005.

[163] A. Sarkar and S. Mukhopadhyay, Dynamics of electrically polarized magnetic monopoles in spin ice, Phys. Rev. B **90** (16), 165129, 2014.

[164] L. D. C. Jaubert and R. Moessner, Multiferroicity in spin ice: Towards magnetic crystallography of $Tb_2Ti_2O_7$ in a field, Phys. Rev. B **91** (21), 214422, 2015.

[165] C. P. Grams, M. Valldor, M. Garst, and J. Hemberger, Critical speeding-up in the magnetoelectric response of spin-ice near its monopole liquid–gas transition, Nature Communications **5** (1), 1–6, 2014.

[166] S. Havriliak and S. Negami, A complex plane representation of dielectric and mechanical relaxation processes in some polymers, Polymer **8**, 161–210, 1967.

[167] C. Grams and J. Hemberger, *Unpublished*. University of Cologne.

[168] J. Kunkel, *Dynamical Monte Carlo Simulations of the Triangular Ising Model*. Bachelor Thesis, University of Cologne, 2020.

[169] M. E. Fisher, Statistical mechanics of dimers on a plane lattice, Physical Review **124** (6), 1664, 1961.

[170] P. W. Kasteleyn, Dimer statistics and phase transitions, Journal of Mathematical Physics **4** (2), 287–293, 1963.

[171] L. Zhi-Huan, L. Mushtaq, L. Yan, and L. Jian-Rong, Critical behaviour of the ferromagnetic Ising model on a triangular lattice, Chinese Physics B **18** (7), 2696, 2009.

[172] M. Schick, J. S. Walker, and M. Wortis, Phase diagram of the triangular Ising model: Renormalization-group calculation with application to adsorbed monolayers, Phys. Rev. B **16** (5), 2205–2219, 1977.

[173] R. R. Netz and A. N. Berker, Monte Carlo mean-field theory and frustrated systems in two and three dimensions, Phys. Rev. Lett. **66** (3), 377–380, 1991.

[174] C. Hwang, S. Kim, D. Kang, and J. M. Kim, Thermodynamic properties of the triangular-lattice ising antiferromagnet in a uniform magnetic field, J. Korean Phys. Soc. **52**, S203, 2008.

[175] M. Žukovič, M. Borovskỳ, and A. Bobák, Ordering in Triangular Lattice Ising Antiferromagnet Due to Dilution and Magnetic Field, Acta Physica Polonica A **118** (5), 740–741, 2010.

[176] Y. B. Kudasov, Steplike Magnetization in a Spin-Chain System: $Ca_3Co_2O_6$, Phys. Rev. Lett. **96** (2), 027212, 2006.

[177] Y. B. Kudasov, Magnetic structure and phase diagram in a spin-chain system: $Ca_3Co_2O_6$, Europhysics Letters **78** (5), 57005, 2007.

[178] A. Maignan, C. Michel, A. Masset, C. Martin, and B. Raveau, Single crystal study of the one dimensional $Ca_3Co_2O_6$ compound: five stable configurations for the Ising triangular lattice, The European Physical Journal B-Condensed Matter and Complex Systems **15** (4), 657–663, 2000.

[179] V. Hardy, S. Lambert, M. R. Lees, and D. McK. Paul, Specific heat and magnetization study on single crystals of the frustrated quasi-one-dimensional oxide $Ca_3Co_2O_6$, Phys. Rev. B **68** (1), 014424, 2003.

[180] V. Hardy, M. R. Lees, O. A. Petrenko, D. M. Paul, D. Flahaut, S. Hébert, and A. Maignan, Temperature and time dependence of the field-driven magnetization steps in $Ca_3Co_2O_6$ single crystals, Phys. Rev. B **70** (6), 064424, 2004.

[181] A. Maignan, V. Hardy, S. Hébert, M. Drillon, M. Lees, O. Petrenko, D. M. K. Paul, and D. Khomskii, Quantum tunneling of the magnetization in the Ising chain compound $Ca_3Co_2O_6$, Journal of Materials Chemistry **14** (8), 1231–1234, 2004.

[182] V. Hardy, D. Flahaut, M. R. Lees, and O. A. Petrenko, Magnetic quantum tunneling in $Ca_3Co_2O_6$ studied by ac susceptibility: Temperature and magnetic-field dependence of the spin-relaxation time, Phys. Rev. B **70** (21), 214439, 2004.

[183] I. Nekrashevich, X. Ding, F. Balakirev, H. T. Yi, S.-W. Cheong, L. Civale, Y. Kamiya, and V. S. Zapf, Reaching the equilibrium state of the frustrated triangular Ising magnet $Ca_3Co_2O_6$, Phys. Rev. B **105** (2), 024426, 2022.

[184] R. Soto, G. Martínez, M. N. Baibich, J. M. Florez, and P. Vargas, Metastable states in the triangular-lattice Ising model studied by Monte Carlo simulations: Application to the spin-chain compound $Ca_3Co_2O_6$, Phys. Rev. B **79** (18), 184422, 2009.

[185] M. H. Qin, K. F. Wang, and J. M. Liu, Two-step magnetization in a spin-chain system on the triangular lattice: Wang-Landau simulation, Phys. Rev. B **79** (17), 172405, 2009.

[186] B. D. Metcalf and C. P. Yang, Degeneracy of antiferromagnetic Ising lattices at critical magnetic field and zero temperature, Phys. Rev. B **18** (5), 2304–2307, 1978.

[187] L. Gunther and B. Barbara, *Quantum tunneling of magnetization—QTM'94*. Springer Science & Business Media, 2012, vol. 301.

[188] L. Thomas, F. Lionti, R. Ballou, D. Gatteschi, R. Sessoli, and B. Barbara, Macroscopic quantum tunnelling of magnetization in a single crystal of nanomagnets, Nature **383** (6596), 145–147, 1996.

[189] J. M. Hernandez, X. X. Zhang, F. Luis, J. Tejada, J. R. Friedman, M. P. Sarachik, and R. Ziolo, Evidence for resonant tunneling of magnetization in Mn_{12}sacetate complex, Phys. Rev. B **55** (9), 5858–5865, 1997.

[190] D. D. Awschalom, J. F. Smyth, G. Grinstein, D. P. DiVincenzo, and D. Loss, Macroscopic quantum tunneling in magnetic proteins, Phys. Rev. Lett. **68** (20), 3092–3095, 1992.

[191] J. Tejada, X. X. Zhang, E. del Barco, J. M. Hernández, and E. M. Chudnovsky, Macroscopic Resonant Tunneling of Magnetization in Ferritin, Phys. Rev. Lett. **79** (9), 1754–1757, 1997.

[192] F. Jonietz, S. Mühlbauer, C. Pfleiderer, A. Neubauer, W. Münzer, A. Bauer, T. Adams, R. Georgii, P. Böni, R. A. Duine, *et al.*, Spin transfer torques in MnSi at ultralow current densities, Science **330** (6011), 1648–1651, 2010.

[193] A. Fert, V. Cros, and J. Sampaio, Skyrmions on the track, Nature nanotechnology **8** (3), 152–156, 2013.

[194] E. H. Hall *et al.*, On a new action of the magnet on electric currents, American Journal of Mathematics **2** (3), 287–292, 1879.

[195] Y. Taguchi, Y. Oohara, H. Yoshizawa, N. Nagaosa, and Y. Tokura, Spin chirality, Berry phase, and anomalous Hall effect in a frustrated ferromagnet, Science **291** (5513), 2573–2576, 2001.

[196] N. Nagaosa, J. Sinova, S. Onoda, A. H. MacDonald, and N. P. Ong, Anomalous hall effect, Reviews of modern physics **82** (2), 1539, 2010.

[197] C. Sürgers, G. Fischer, P. Winkel, and H. V. Löhneysen, Large topological Hall effect in the non-collinear phase of an antiferromagnet, Nature Communications **5** (1), 3400, 2014.

[198] Y. Machida, S. Nakatsuji, Y. Maeno, T. Tayama, T. Sakakibara, and S. Onoda, Unconventional Anomalous Hall Effect Enhanced by a Noncoplanar Spin Texture in the Frustrated Kondo Lattice $Pr_2Ir_2O_7$, Phys. Rev. Lett. **98** (5), 057203, 2007.

[199] Y. Machida, S. Nakatsuji, S. Onoda, T. Tayama, and T. Sakakibara, Time-reversal symmetry breaking and spontaneous Hall effect without magnetic dipole order, Nature **463** (7278), 210–213, 2010.

[200] V. Kalmeyer and R. B. Laughlin, Equivalence of the resonating-valence-bond and fractional quantum Hall states, Phys. Rev. Lett. **59** (18), 2095–2098, 1987.

[201] X. G. Wen, F. Wilczek, and A. Zee, Chiral spin states and superconductivity, Phys. Rev. B **39** (16), 11413–11423, 1989.

[202] J. Luttinger and L. Tisza, Theory of dipole interaction in crystals, Physical Review **70** (11-12), 954, 1946.

[203] J. Luttinger, A note on the ground state in antiferromagnetics, Physical Review **81** (6), 1015, 1951.

[204] D. Lyons and T. Kaplan, Method for determining ground-state spin configurations, Physical Review **120** (5), 1580, 1960.

[205] N. Niggemann, M. Hering, and J. Reuther, Classical spiral spin liquids as a possible route to quantum spin liquids, Journal of Physics: Condensed Matter **32** (2), 024001, 2019.

[206] M. F. Lapa and C. L. Henley, Ground states of the classical antiferromagnet on the pyrochlore lattice, arXiv preprint arXiv:1210.6810, 2012.

[207] A. Yoshimori, *A new type of antiferromagnetic structure in the rutile type crystal*, Journal of the Physical Society of Japan **14** (6), 807–821, 1959.

[208] Z. Xiong and X.-G. Wen, *General method for finding ground state manifold of classical Heisenberg model*, arXiv preprint arXiv:1208.1512, 2012.

[209] T. Kaplan and N. Menyuk, *Spin ordering in three-dimensional crystals with strong competing exchange interactions*, Philosophical Magazine **87** (25), 3711–3785, 2007.

[210] J. Attig and S. Trebst, *Classical spin spirals in frustrated magnets from free-fermion band topology*, Phys. Rev. B **96** (8), 085145, 2017.

[211] H.-J. Schmidt and J. Richter, *Classical ground states of spin lattices*, J. Phys. A: Math. Theor. **55**, 465005, 2022.

[212] S. R. Sklan and C. L. Henley, *Nonplanar ground states of frustrated antiferromagnets on an octahedral lattice*, Phys. Rev. B **88** (2), 024407, 2013.

[213] M. Fujihala *et al.*, *Gapless spin liquid in a square-kagome lattice antiferromagnet*, Nat. Commun. **11** (1), 3429, 2020.

[214] O. V. Yakubovich, L. V. Shvanskaya, G. V. Kiriukhina, A. S. Volkov, and O. V. Dimitrova, *Hydrothermal synthesis and a composite crystal structure of $Na_6Cu_7BiO_4(PO4)_4[Cl(OH)]_3$ as a candidate for quantum spin liquid*, Inorg. Chem. **60** (15), 11450–11457, 2021.

[215] N. Astrakhantsev *et al.*, *Pinwheel valence bond crystal ground state of the spin-$\frac{1}{2}$ Heisenberg antiferromagnet on the shuriken lattice*, Phys. Rev. B **104** (22), L220408, 2021.

[216] B. Liu, Z. Zeng, A. Xu, Y. Sun, O. Yakubovich, L. Shvanskaya, S. Li, and A. Vasiliev, *Low-temperature specific-heat studies on two square-Kagome antiferromagnets*, Phys. Rev. B **105** (15), 155153, 2022.

[217] M.M. Markina, P.S. Berdonosov, T.M. Vasilchikova, K.V. Zakharov, A.F. Murtazoev, V.A. Dolgikh, A.V. Moskvin, V.N. Glazkov, A.I. Smirnov, A.N. Vasiliev, *Static and resonant properties of decorated square kagome lattice compound $KCu_7(TeO_4)(SO_4)_5Cl$*, arXiv: 2212.11623.

[218] A. F. Murtazoev, K. A. Lyssenko, M. M. Markina, V. A. Dolgikh, A. N. Vasiliev, and P. S. Berdonosov, *New Nabokoite-like Phases $ACu_7TeO_4(SO_4)_5Cl$ (A = Na, K, Rb, Cs) with Decorated and Distorted Square Kagome Lattices*, ChemPhysChem **24** (15), e202300111, 2023.

[219] P. Schmoll, A. Kshetrimayum, J. Naumann, J. Eisert, and Y. Iqbal, *Tensor network study of the spin-$\frac{1}{2}$ Heisenberg antiferromagnet on the shuriken lattice*, Phys. Rev. B **107** (6), 064406, 2023.

[220] R. Siddharthan and A. Georges, *Square kagome quantum antiferromagnet and the eight-vertex model*, Phys. Rev. B **65** (1), 014417, 2001.

[221] O. Janson, J. Richter, and H. Rosner, *Modified Kagome Physics in the Natural Spin-1/2 Kagome Lattice Systems: Kapellasite $Cu_3Zn(OH)_6Cl_2$ and Haydeeite $Cu_3Mg(OH)_6Cl_2$*, Phys. Rev. Lett. **101** (10), 106403, 2008.

[222] O. Janson, J. Richter, and H. Rosner, *Intrinsic peculiarities of real material realizations of a spin-1/2 kagomé lattice*, J. Phys. Conf. Ser. **145** (1), 012008, 2009.

[223] K. Morita and T. Tohyama, *Magnetic phase diagrams and magnetization plateaus of the spin-1/2 antiferromagnetic Heisenberg model on a square-Kagome lattice with three nonequivalent exchange interactions*, J. Phys. Soc. Jpn. **87** (4), 043704, 2018.

[224] F. Wang, A. Vishwanath, and Y. B. Kim, Quantum and classical spins on the spatially distorted kagomé lattice: Applications to volborthite $Cu_3V_2O_7(OH)_2 \cdot 2H_2O$, Phys. Rev. B **76** (9), 094421, 2007.

[225] T. Yavors'kii, W. Apel, and H.-U. Everts, Heisenberg antiferromagnet with anisotropic exchange on the kagomé lattice: Description of the magnetic properties of volborthite, Phys. Rev. B **76** (6), 064430, 2007.

[226] A. P. Schnyder, O. A. Starykh, and L. Balents, Spatially anisotropic Heisenberg kagome antiferromagnet, Phys. Rev. B **78** (17), 174420, 2008.

[227] M. Hering, F. Ferrari, A. Razpopov, I. I. Mazin, R. Valentí, H. O. Jeschke, and J. Reuther, Phase diagram of a distorted kagome antiferromagnet and application to Y-kapellasite, npj Comput. Mater. **8** (1), 10, 2022.

[228] I. Rousochatzakis, R. Moessner, and J. van den Brink, Frustrated magnetism and resonating valence bond physics in two-dimensional kagome-like magnets, Phys. Rev. B **88** (19), 195109, 2013.

[229] P. Chandra, P. Coleman, and I. Ritchey, The anisotropic kagome antiferromagnet: A topological spin glass? J. Phys. I France **3** (2), 591–610, 1993.

[230] E. Lieb and D. Mattis, Ordering Energy Levels of Interacting Spin Systems, J. Math. Phys. **3** (4), 749–751, 1962.

[231] N. D. Mermin and H. Wagner, Absence of Ferromagnetism or Antiferromagnetism in One- or Two-Dimensional Isotropic Heisenberg Models, Phys. Rev. Lett. **17** (22), 1133–1136, 1966.

[232] H.-J. Schmidt and C. Schröder, Thermodynamics of the spin square, Few-Body Syst. **64** (2), 16, 2023.

[233] J. Richter, O. Derzhko, and J. Schnack, Thermodynamics of the spin-half square kagome lattice antiferromagnet, Phys. Rev. B **105** (14), 144427, 2022.

[234] M. Vojta, Quantum phase transitions, Rep. Prog. Phys. **66** (12), 2069, 2003.

[235] J. Richter, J. Schulenburg, P. Tomczak, and D. Schmalfuß, The Heisenberg antiferromagnet on the square-kagome lattice, Cond. Matter Phys. **12**, 507, 2009.

[236] D. A. Huse and A. D. Rutenberg, Classical antiferromagnets on the Kagomé lattice, Phys. Rev. B **45** (13), 7536–7539, 1992.

[237] A. B. Harris, C. Kallin, and A. J. Berlinsky, Possible Néel orderings of the Kagomé antiferromagnet, Phys. Rev. B **45** (6), 2899–2919, 1992.

[238] G.-W. Chern and R. Moessner, Dipolar Order by Disorder in the Classical Heisenberg Antiferromagnet on the Kagome Lattice, Phys. Rev. Lett. **110** (7), 077201, 2013.

[239] S. R. Sklan and C. L. Henley, Nonplanar ground states of frustrated antiferromagnets on an octahedral lattice, Phys. Rev. B **88** (2), 024407, 2013.

[240] V. Grison, P. Viot, B. Bernu, and L. Messio, Emergent Potts order in the kagome $J_1 - J_3$ Heisenberg model, Phys. Rev. B **102** (21), 214424, 2020.

[241] E. Rastelli, A. Tassi, and L. Reatto, Non-simple magnetic order for simple Hamiltonians, Physica B+C **97** (1), 1–24, 1979.

[242] D. H. Lyons, T. A. Kaplan, K. Dwight, and N. Menyuk, Classical Theory of the Ground Spin-State in Cubic Spinels, Phys. Rev. **126** (2), 540–555, 1962.

[243] M. J. Freiser, Thermal Variation of the Pitch of Helical Spin Configurations, Phys. Rev. **123** (6), 2003–2012, 1961.

[244] D. H. Lyons and T. A. Kaplan, Method for Determining Ground-State Spin Configurations, Phys. Rev. **120** (5), 1580–1585, 1960.

[245] T. A. Kaplan and N. Menyuk, Spin ordering in three-dimensional crystals with strong competing exchange interactions, Phil. Mag. **87** (25), 3711–3785, 2007.

[246] Y. Iqbal, H. O. Jeschke, J. Reuther, R. Valentí, I. I. Mazin, M. Greiter, and R. Thomale, Paramagnetism in the kagome compounds $(Zn, Mg, Cd)Cu_3(OH)_6Cl_2$, Phys. Rev. B **92** (22), 220404, 2015.

[247] P. Ghosh, Y. Iqbal, T. Müller, R. T. Ponnaganti, R. Thomale, R. Narayanan, J. Reuther, M. J. P. Gingras, and H. O. Jeschke, Breathing chromium spinels: a showcase for a variety of pyrochlore Heisenberg Hamiltonians, npj Quantum Mater. **4** (1), 63, 2019.

[248] Y. Haraguchi, A. Matsuo, K. Kindo, and Z. Hiroi, Quantum antiferromagnet bluebellite comprising a maple-leaf lattice made of spin-1/2 Cu^{2+} ions, Phys. Rev. B **104** (17), 174439, 2021.

[249] S. J. Mills, A. R. Kampf, A. G. Christy, R. M. Housley, G. R. Rossman, R. E. Reynolds, and J. Marty, Bluebellite and mojaveite, two new minerals from the central Mojave Desert, California, USA, Mineralogical Magazine **78** (5), 1325–1340, 2014.

[250] T. Fennell, J. Piatek, R. Stephenson, G. Nilsen, and H. Rønnow, Spangolite: an s= 1/2 maple leaf lattice antiferromagnet? Journal of Physics: Condensed Matter **23** (16), 164201, 2011.

[251] Y. Haraguchi, A. Matsuo, K. Kindo, and Z. Hiroi, Frustrated magnetism of the maple-leaf-lattice antiferromagnet $MgMn_3O_7 \cdot 3H_2O$, Phys. Rev. B **98** (6), 064412, 2018.

[252] A. R. Kampf, S. J. Mills, R. M. Housley, and J. Marty, Lead-tellurium oxysalts from Otto Mountain near Baker, California: VIII. Fuettererite, $Pb_3Cu_6^{2+}Te^6+O_6(OH)_7Cl_5$, a new mineral with double spangolite-type sheets, American Mineralogist **98** (2-3), 506–511, 2013.

[253] A. Aliev, M. Huvé, S. Colis, M. Colmont, A. Dinia, and O. Mentré, Two-Dimensional Antiferromagnetism in the $[Mn_{3+x}O_7][Bi_4O_{4.5-y}]$ Compound with a Maple-Leaf Lattice, Angewandte Chemie **37** (51), 9393–9397, 2012.

[254] D. Cave, F. C. Coomer, E. Molinos, H.-H. Klauss, and P. T. Wood, Compounds with the "Maple Leaf" Lattice: Synthesis, Structure, and Magnetism of $M_x[Fe(O_2CCH_2)_2NCH_2PO_3]_6 \cdot nH_2O$, Angewandte Chemie **118** (5), 817–820, 2006.

[255] P. Ghosh, T. Müller, and R. Thomale, Another exact ground state of a two-dimensional quantum antiferromagnet, Phys. Rev. B **105** (18), L180412, 2022.

[256] P. Ghosh, J. Seufert, T. Müller, F. Mila, and R. Thomale, Maple Leaf Antiferromagnet in a Magnetic Field, arXiv preprint arXiv:2301.08264, 2023.

[257] P. Ghosh, T. Müller, Y. Iqbal, R. Thomale, and H. O. Jeschke, Effective spin-1 breathing kagome Hamiltonian induced by the exchange hierarchy in the maple leaf mineral bluebellite, arXiv preprint arXiv:2301.05224, 2023.

[258] D. J. J. Farnell, R. Darradi, R. Schmidt, and J. Richter, Spin-half Heisenberg antiferromagnet on two archimedian lattices: From the bounce lattice to the maple-leaf lattice and beyond, Phys. Rev. B **84** (10), 104406, 2011.

[259] D. Betts, A new two-dimensional lattice of coordination number five, Proc. N. S. Inst. Sci. **40** (95), 1995.

[260] D. Schmalfuß, P. Tomczak, J. Schulenburg, and J. Richter, The spin-$\frac{1}{2}$ Heisenberg antiferromagnet on a $\frac{1}{7}$-depleted triangular lattice: Ground-state properties, Phys. Rev. B **65** (22), 224405, 2002.

[261] T. Müller, D. Kiese, N. Niggemann, B. Sbierski, J. Reuther, S. Trebst, R. Thomale, and Y. Iqbal, Pseudo-fermion functional renormalization group for spin models, arXiv preprint arXiv:2307.10359, 2023.

[262] A. Jonscher, A new understanding of the dielectric relaxation of solids, Journal of Materials Science **16** (8), 2037–2060, 1981.

[263] K. S. Cole and R. H. Cole, Dispersion and Absorption in Dielectrics I. Alternating Current Characteristics, The Journal of Chemical Physics **9** (4), 341–351, 1941.

[264] D. W. Davidson and R. H. Cole, Dielectric Relaxation in Glycerol, Propylene Glycol, and n-Propanol, The Journal of Chemical Physics **19** (12), 1484–1490, 1951.

[265] S. Havriliak and S. Havriliak, Results from an unbiased analysis of nearly 1000 sets of relaxation data, Journal of Non-Crystalline Solids **172-174**, 297–310, 1994.

[266] P. P. Ewald, Die Berechnung optischer und elektrostatischer Gitterpotentiale, Annalen der Physik **369** (3), 253–287, 1921.

[267] S. W. de Leeuw, J. W. Perram, and E. R. Smith, Simulation of electrostatic systems in periodic boundary conditions. I. Lattice sums and dielectric constants, Proceedings of the Royal Society of London. A. Mathematical and Physical Sciences **373** (1752), 27–56, 1980.
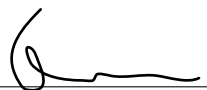
Acknowledgements

Erklärung zur Dissertation

Hiermit versichere ich an Eides statt, dass ich die vorliegende Dissertation selbstständig und ohne die Benutzung anderer als der angegebenen Hilfsmittel und Literatur angefertigt habe. Alle Stellen, die wörtlich oder sinngemäß aus veröffentlichen und nicht veröffentlichten Werken dem Wortlaut oder dem Sinn nach entnommen wurden, sind als solche kenntlich gemacht. Ich versichere an Eides statt, dass diese Dissertation noch keiner anderen Fakultät oder Universität zur Prüfung vorgelegen hat; dass sie – abgesehen von unten angegebenen Teilpublikationen und eingebundenen Artikeln und Manuskripten – noch nicht veröffentlicht worden ist sowie, dass ich eine Veröffentlichung der Dissertation vor Abschluss der Promotion nicht ohne Genehmigung des Promotionsausschusses vornehmen werde. Die Bestimmungen dieser Ordnung sind mir bekannt. Darüber hinaus erkläre ich hiermit, dass ich die Ordnung zur Sicherung guter wissenschaftlicher Praxis und zum Umgang mit wissenschaftlichem Fehlverhalten der Universität zu Köln gelesen und sie bei der Durchführung der Dissertation zugrundeliegenden Arbeiten und der schriftlich verfassten Dissertation beachtet habe und verpflichte mich hiermit, die dort genannten Vorgaben bei allen wissenschaftlichen Tätigkeiten zu beachten und umzusetzen. Ich versichere, dass die eingereichte elektronische Fassung der eingereichten Druckfassung vollständig entspricht.

Teilpublikationen:

[P1] **M. Gembé**, H.-J. Schmidt, C. Hickey, J. Richter, Y. Iqbal, and S. Trebst, Noncoplanar magnetic order in classical square-kagome antiferromagnets, Phys. Rev. Res. **5** (4), 043204, 2023.

[P2] **M. Gembé**, L. Gresista, H.-J. Schmidt, C. Hickey, Y. Iqbal, and S. Trebst, Noncoplanar orders and quantum disordered states in maple-leaf antiferromagnets, 2024. arXiv: 2402.09400 [cond-mat.str-el].

[U1] **M. Gembé**, J. Attig, J. Kunkel, and S. Trebst, Critical Speeding Up in Spin Ice and Spin Liquids, Manuscript in preparation, 2023.

Köln, den 15. Februar 2024

_____
(Carl Martin Gembé)

For decades, physicists have been fascinated by frustrated magnetism. Frustration arises when the pairwise interaction energies between localized magnetic moments in a system cannot be minimized simultaneously. This competition prevents the formation of long range magnetic order even at lowest temperatures and, eventually, leads to the hallmark of frustration in the form of a massive ground state degeneracy accompanied by a finite zero-point entropy. Thus, exotic magnetic analogs of ordinary fluids can be realized, where spins are highly correlated but remain strongly fluctuating. Such spin liquids are linked to remarkable unconventional collective phenomena, most notably emergent gauge fields and fractionalized quasi-particle excitations that can be conceived as magnetic monopoles. In this thesis, we study the dynamics of such quasi-monopoles in the presence of a magnetic field and address the question whether critical fluctuations at a phase transition always slow down equilibration or, conversely, can also help the system to thermalize. Employing large-scale dynamical Monte Carlo simulations, we show that the latter—a critical speeding up—can indeed be observed in two prototypical classical spin systems: dipolar spin ice in pyrochlore magnets and a Coulomb spin liquid in the triangular lattice Ising antiferromagnet. For the former, we also establish a relationship between Monte Carlo time and real time by comparing numerical and experimental data. Another part of this thesis is concerned with systems in which further-neighbor interactions stabilize certain non-coplanar magnetic orders. Such orders are particularly interesting because upon introducing quantum fluctuations, they may possibly melt into a chiral quantum spin liquid. To this end, we study two model systems that turn out to have non-coplanar classical ground states and are motivated by the recent synthesis of a number of Mott insulating square-kagome materials as well as of spin-1/2 maple-leaf lattice antiferromagnets. We explore the rich phenomenology of frustrated magnetism induced by these two lattice geometries, including extensive degeneracies and order-by-disorder mechanisms. For both models, we study an elementary, classical Heisenberg model with nearest-neighbor and additional cross-plaquette interactions and discuss a multitude of non-coplanar orders and spiral spin phases. Using extensive numerical simulations, we also discuss the thermodynamic signatures of these phases, which often show multi-step thermal ordering.

University of Cologne

thp Institute for Theoretical Physics University of Cologne

bcgs

CRC 1238 Control and Dynamics of Quantum Materials